

# Dynamical Influences of Sudden Stratospheric Warmings on Surface Climate

A thesis submitted to the School of Environmental Science of the  
University of East Anglia in partial fulfilment of the requirements for the  
degree of Doctor of Philosophy

Amee Helouise O'Callaghan

June 2016





**© Copyright 2016**

**Amee Helouise O'Callaghan**

This copy of the thesis has been supplied on condition that anyone who consults it is understood to recognise that its copyright rests with the author and that use of any information derived there-from must be in accordance with current UK Copyright Law. In addition, any quotation or extract must include full attribution.



# Abstract

The stratospheric winter polar vortex consists of strong westerly winds; this winter flow regime can undergo a complete breakdown during sudden stratospheric warming events. In the Northern Hemisphere these events are often accompanied by the descent of anomalous flow regimes which can result in extreme surface weather.

The focus of this thesis is to assess sudden stratospheric warmings and their place in the coupled climate system. Portions of this work are dedicated to algorithm development with the aim of quickly and accurately isolating and subcategorising events. A method is successfully created that is computationally cheap, easy to implement, based on dynamically relevant criteria and has error rates clearly outlined.

Impacts on the surface and ocean are assessed with focus on specific subclasses of sudden stratospheric warmings. It is found that there is, on average, stronger surface and oceanic impacts following events that split the polar vortex. The ocean system is impacted via modifications to the implied Ekman heat transport and the net atmosphere-surface heat flux. Furthermore, there is a relationship between the initial location of the disturbed polar vortex and the strength of anomalous flow regime at the surface.

Analysis is conducted predominantly using general circulation model output, with direct comparison between an atmosphere-only model and a coupled atmosphere-ocean model. For the coupled model there is a reduction in the number of simulated sudden stratospheric warmings, a result of altered atmospheric wave dynamics. This is partially attributed to a cold bias over the equatorial Pacific. The frequency of sudden stratospheric warmings is found to be insensitive to North Atlantic sea surface temperature anomalies.



# Table of Contents

<b>Abstract</b>	<b>iii</b>
<b>List of Figures</b>	<b>vii</b>
<b>List of Tables</b>	<b>ix</b>
<b>Acknowledgements</b>	<b>xvii</b>
<b>1 Introduction</b>	<b>1</b>
1.1 Background and Motivation . . . . .	1
1.2 Coupled Climate: Current Scientific Knowledge . . . . .	3
1.3 Synopsis . . . . .	10
<b>2 Sudden Stratospheric Warmings</b>	<b>13</b>
2.1 Introduction . . . . .	13
2.2 Definition . . . . .	14
2.3 Background Literature . . . . .	15
2.4 Hybrid Approach for Isolating SSWs . . . . .	21
2.5 Alternative Classification Techniques . . . . .	25
2.6 Alternative Identification Technique . . . . .	26
2.7 Conclusions . . . . .	30
<b>3 General Circulation Models</b>	<b>33</b>
3.1 Introduction . . . . .	33
3.2 Numerical Methods . . . . .	36
3.3 The IGCM4 . . . . .	38
3.4 Coupling to an Interactive Ocean . . . . .	48
3.5 Conclusions . . . . .	51
<b>4 SSW Effects On Surface Climate And Ocean</b>	<b>53</b>
4.1 Introduction . . . . .	53
4.2 Variable Formulation . . . . .	60
4.3 Results . . . . .	63
4.4 Discussion and Conclusions . . . . .	69



<b>5</b>	<b>EOFs Applied To SSWs</b>	<b>72</b>
5.1	Introduction . . . . .	72
5.2	Mathematical Formulation of EOFs . . . . .	72
5.3	Application of EOF Analysis to SSW Events . . . . .	74
5.4	EOF Analysis Applied to Rotated Fields . . . . .	81
5.5	Assessing Impacts via Disturbed Vortex Trajectory . . . . .	86
5.6	Conclusions . . . . .	90
<b>6</b>	<b>The AMO's Modulation Of The Stratosphere</b>	<b>93</b>
6.1	Introduction . . . . .	93
6.2	Experimental Design . . . . .	98
6.3	Results . . . . .	100
6.4	Discussion and Conclusions . . . . .	111
<b>7</b>	<b>Impacts Of An Interactive Ocean</b>	<b>113</b>
7.1	Introduction . . . . .	113
7.2	FORTE Pre-Industrial Integration . . . . .	114
7.3	IGCM4 forced with FORTE SSTs . . . . .	129
7.4	Conclusions . . . . .	134
<b>8</b>	<b>Conclusions</b>	<b>137</b>
8.1	Simulation Of and Identification Algorithms for SSWs . . . . .	137
8.2	SSWs Interactions with other Climatic Modes . . . . .	139
8.3	Concluding Remarks . . . . .	142
<b>A</b>	<b>Moment Analysis Equations</b>	<b>145</b>
<b>B</b>	<b>SSW Case Studies</b>	<b>147</b>
<b>C</b>	<b>General Circulation Model Vertical Layers</b>	<b>151</b>
<b>D</b>	<b>Acronyms</b>	<b>153</b>
	<b>References</b>	<b>165</b>



## List of Figures

1.1	Annual mean temperature profile as a spatially weighted average . .	2
2.1	Composite plots of Ertel’s potential vorticity during 48 splitting and 65 displacements SSW events . . . . .	15
2.3	Histograms of moments diagnostic values in the IGCM version 3.1 .	25
2.5	Sensitivity of centroid latitude algorithm in identifying SSW displace- ments . . . . .	27
3.2	Example of triangular truncation for spherical harmonic solution. .	37
3.3	IGCM4 $\bar{U}$ climatologies for DJF and JJA with difference to ERA-40 shaded. . . . .	40
3.4	Mean residual vertical velocity at 74.63 <i>hPa</i> in the IGCM4 . . . . .	41
3.5	Climatological meridional heat flux at 100 <i>hPa</i> in the IGCM4 . . .	42
3.6	Scatter plots comparing average 100 <i>hPa</i> $\overline{v'T'}$ to average polar cap temperature for IGCM4 and ERA-40. . . . .	43
3.7	DJF geopotential height eddy field at 500 <i>hPa</i> for ERA-40 and the IGCM4. . . . .	44
3.8	Percentage of ‘blocked days’ as a function of longitude for the IGCM4 and NCEP/NCAR reanalysis . . . . .	45
3.10	Distribution of SSW events in IGCM4 . . . . .	47
3.11	Arakawa-B grid schematic . . . . .	49
4.1	Surface wind stress DJFM climatologies from NCEP/NCAR reanal- ysis spanning 1957 to 2006 . . . . .	57
4.2	The NAM anomaly in the IGCM4 for 90 days surrounding identified SSWs . . . . .	62
4.3	Surface temperature anomaly composites for SSWs in the IGCM4 mature period and CP07 SSWs in NCEP/NCAR reanalysis decay period . . . . .	64
4.4	Surface wind stress DJFM climatologies from IGCM4 data . . . . .	65
4.5	Surface wind stress curl anomaly composites for SSWs in IGCM4 mature period and CP07 SSWs in NCEP/NCAR reanalysis decay period . . . . .	66
4.6	IGCM4 composites for splitting anomalies, displacement anomalies and their difference for the: net atmosphere-surface flux, implied Ekman heat flux and the combined upper ocean energy flux . . . .	67
5.1	Average geopotential height and the leading EOF modes for SSW events . . . . .	76



5.2	Correlations between 10 <i>hPa</i> PCs and daily NAM value at 1000 <i>hPa</i> for various lags . . . . .	77
5.4	Correlations between 10 <i>hPa</i> PCs and daily NAM value at 1000 <i>hPa</i> for splitting and displacement subcategories at various lags . . . . .	80
5.5	Average geopotential height and leading EOF modes created from rotated geopotential height field for SSW events . . . . .	83
5.7	Correlations between 10 <i>hPa</i> rotated analysis PCs and daily NAM value at 1000 <i>hPa</i> for various lags . . . . .	85
5.8	Polar air mass average location as a function of surface NAM . . . . .	87
5.9	Region isolated for the polar vortex trajectory analysis. . . . .	88
5.11	Surface temperature anomaly composites for SSWs grouped via disturbed polar vortex trajectories . . . . .	89
6.1	National Oceanic and Atmospheric Administration AMO index . . . . .	94
6.2	Surface temperature DJF composites minus control for the AMO simulations. . . . .	99
6.3	Zonal mean zonal wind DJF composites minus control and total fields for the AMO simulations. . . . .	101
6.4	SSW frequency comparison across AMO simulations. . . . .	103
6.5	100 <i>hPa</i> meridional heat flux anomaly comparison across AMO simulations. . . . .	103
6.6	10 <i>hPa</i> 60°N zonal wind deceleration associated with SSW event across AMO simulations . . . . .	104
6.7	100 <i>hPa</i> polar cap temperature anomaly associated with SSW events across AMO simulations . . . . .	104
6.8	Histograms of central dates for splitting and displacement events across the control and AMO simulations. . . . .	105
6.9	1000 <i>hPa</i> NAM anomaly averaged from lag 0 to 30 following SSWs across the AMO simulations . . . . .	106
6.10	Splitting minus displacement NAM anomaly composite for AMO simulations. . . . .	107
6.11	Regional surface temperature anomalies from lag 0 to 30 following SSWs across the AMO simulations . . . . .	109
6.12	Geopotential height JFM differences at 500 <i>hPa</i> between AMO warm and cold simulations . . . . .	111
7.1	$\bar{U}$ climatologies of FORTE with difference to ERA-40 and IGCM4. . . . .	114
7.2	$\bar{U}$ at 10 <i>hPa</i> 60 °N and averaged over each calendar day for FORTE and the IGCM4 . . . . .	115



7.3	FORTE climatology of meridional heat flux and the difference to IGCM4. . . . .	116
7.4	DJF climatology of $\rho_0^{-1}\nabla \cdot \vec{F}$ for FORTE and IGCM4. . . . .	117
7.5	FORTE climatology of surface temperature and the difference to IGCM4. . . . .	118
7.6	Surface wind stress curl DJF climatologies for FORTE and IGCM4.	119
7.7	Distribution of SSW events in FORTE . . . . .	120
7.8	The NAM anomaly in FORTE for 90 days surrounding SSWs . . . .	122
7.9	Surface temperature anomaly composites for splitting and displacement events isolated in FORTE. Averaged from event onset up until 30 days later. . . . .	123
7.10	FORTE composites for splitting anomalies, displacement anomalies and their difference from event onset up until 30 days later for the: net atmosphere-surface flux, implied Ekman heat flux and the combined upper ocean energy flux . . . . .	124
7.11	Anomalous rate of change to mixed layer heat budget and anomalous potential temperature from 0 to 120 days following SSWs. . . . .	126
7.12	Anomalous rate of temperature change in the upper ocean layer from full three-dimensional advective terms, cumulative impact over the 120 days following splitting events. . . . .	127
7.14	Surface temperature DJF climatologies minus the IGCM4 for various FORTE based model experiments. . . . .	130
7.15	$\bar{U}$ climatologies of various FORTE based model experiments with difference to IGCM4. . . . .	131
7.16	SSW frequency for various FORTE based model experiments . . . .	132
7.17	Geopotential height 500 <i>hPa</i> eddy field for various FORTE based model experiments . . . . .	133
B1	Case study of displacement SSW event . . . . .	147
B2	Case study of splitting SSW event . . . . .	148
B3	Case study of rotated displacement SSW event . . . . .	149
B4	Case study of rotated splitting SSW event . . . . .	150



## List of Tables

2.2	SSW frequency benchmark applied to the hybrid, CP07 and M13 SSW identification and classification algorithms. . . . .	23
2.4	Comparison of SSW classification due to different moment based binary classification techniques . . . . .	26
2.6	Performance of the different moment based SSW identification algorithms . . . . .	29
3.1	Primitive equation set in Cartesian horizontal coordinates and log-pressure vertical coordinate following Andrews et al. [1987]. . . . .	34
3.9	Modelling benchmarks outlined in Charlton and Polvani [2007] applied to the IGCM4 integration. . . . .	46
5.3	Average PC values for splitting and displacement composites and the average NAM value at 1000 <i>hPa</i> . . . . .	78
5.6	Average rotated analysis PC values for splitting and displacement composites and the average NAM value at 1000 <i>hPa</i> . . . . .	84
5.10	Total number of events and diagnostics for SSWs grouped via the disturbed polar vortex trajectory . . . . .	88
7.13	Acronyms for each 200 year model integration and the source of forcing monthly SST fields . . . . .	129
7.18	ENSO winters based on the Niño 4 Index in FORTE with SSW frequency. . . . .	134
C1	Model layer index for MOMA version coupled to IGCM4. . . . .	151
C2	Model layer index for IGCM4 T42L35 configuration with corresponding $\sigma$ -level with conversions to pressure and log-pressure height . . .	152



# Acknowledgements

Words cannot convey how grateful I am to my wonderful husband Matthew for the limitless support he has provided me over the course of my PhD. He has been my rock, holding me focused and centered when I needed it the most. Always by my side, in the good times and bad, and it is due to his support and love that I have been able to work so hard to make this body of work what it is. Thank you for all the times I have been passionately rambling on about sudden stratospheric warmings, the climate or the IGCM and you have listened, somehow showed genuine interest and participated in the discussion.

I also wish to thank my parents, Paula and Raymond, for their continued support and encouragement. Without their guidance and love I may not have followed my dream of studying mathematics; so thank you for encouraging me to be me.

My advisors, Manoj and Dave, have been amazing sources of support and academic knowledge. They facilitated and encouraged my development as a researcher, always challenging and questioning my concepts and helped me to become a well rounded (less waffly!!) researcher and person. Thank you both for the opportunity of studying such a fascinating topic.

I have also been very lucky to encounter some marvellous people who have provided support during the course of my studies. I wish to thank: Simon Peatman for all of the CDAT guidance; Karin van der Wiel for help with understanding the IGCM coding; Dr Daniel Hodson for the provision of surface temperature fields; Dr Daniel Mitchell for help with the moment analysis coordinate projection; Professor Andrew Charlton-Perez for the help he provided on my sudden stratospheric warming algorithm development; and Dr Adam Blaker and Dr Bablu Sinha for enabling my use of the coupled model.

And Chester, you fill me with so much joy and happiness, I am so lucky to have you in my life.

*Ameesha*

*15.03.2016*



The research in this thesis was carried out on the High Performance Computing Cluster supported by the Research and Specialist Computing Support service at the University of East Anglia.



---

# Chapter 1 - Introduction

## 1.1 Background and Motivation

Historically investigation of atmospheric flow dynamics was mainly constrained to the tropospheric system. There was a general belief that at high altitudes flows were stable and distinct from surface weather systems [Gerber et al., 2012]. In 1952 Richard Scherhag observed an event that radically altered this view and as scientific understanding evolved it has become clear that the stratosphere is not as passive as once assumed. Scherhag discovered a phenomenon known as a sudden stratospheric warming (SSW) where the winter stratospheric polar vortex westerlies become greatly disturbed. During a ‘major event’ these winds reverse and the temperature gradient increases poleward. After investigation and early stratospheric modelling [Matsuno, 1971] it was deduced that the troposphere can affect stratospheric dynamics through the vertical propagation of planetary waves. It is believed that this wave propagation is a necessary, but not sufficient, driving mechanisms for SSW occurrence [Limpasuvan et al., 2004].

As research progressed understanding of a coupled troposphere-stratosphere system emerged (see Figure 1.1 for a schematic depicting these atmospheric layers) with stratospheric anomalies having an observable effect on tropospheric dynamics [Baldwin and Dunkerton, 2001]. Under the World Climate Research Programme a project was initiated to investigate stratosphere-troposphere processes and their role in climate. Complementary to these efforts many studies have been published providing support for stratospheric influences on the Earth’s climate [Baldwin and Dunkerton, 2001, Ripesi et al., 2012, Mitchell et al., 2013a, Gerber et al., 2012, among others]. Research is confirming the role of the stratosphere in facilitating teleconnections in general circulation models (e.g. the El Niño Southern Oscillation and European climate [Bell et al., 2009, Butler et al., 2014]), that stratospheric perturbations can greatly affect the surface climate [Mitchell et al., 2013b, Charlton and Polvani, 2007] and that a well resolved stratosphere can aid model accuracy [Wilcox and Charlton-Perez, 2013]. Furthermore evidence is emerging that the inclusion of SSW simulation could contribute to improved seasonal forecasting skill [Scaife et al., 2016].

Stratospheric influences on oceanic flow is also a developing area of research with studies such as Reichler et al. [2012] emerging which demonstrates a direct link between anomalous stratospheric polar vortex strength and anomalous sea surface temperatures over the North Atlantic. The Earth’s surface comprises of 71% ocean [Siedler et al., 2001] and forms a fundamental component of the climate system due

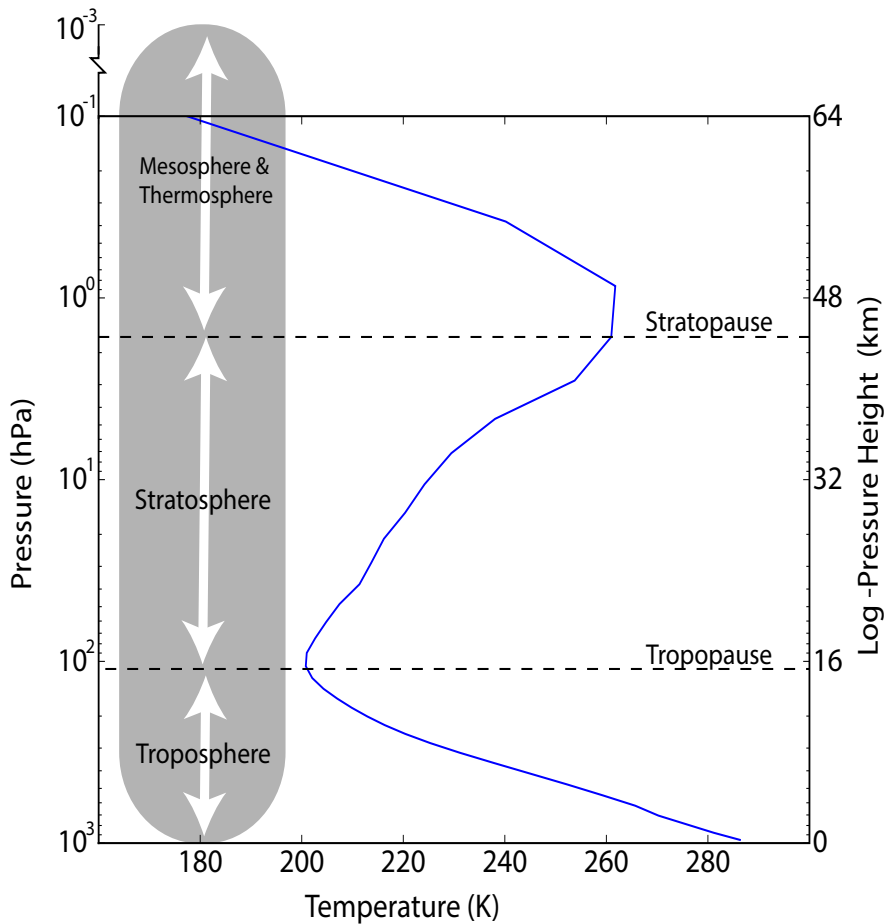


**Figure 1.1:** Annual mean temperature profile (K) as a spatially weighted average over all latitudes and longitudes. Data from the Intermediate General Circulation Model (version 4). Conversion to log-pressure height provided, following Andrews et al. [1987].

to its ability to store and transport heat. A key feature of the oceanic system is the thermohaline circulation which transports significant amounts of heat around the globe, particularly to high latitudes. Understanding how ocean circulation affects climate is of utmost importance, the ocean and atmosphere are coupled at the Earth's surface with both systems being affected by fluxes of wind stress, heat and fresh water. If anomalous stratospheric events can affect the surface climate and cause a significant variation in any of these variables then the stratosphere could have an observable effect on the oceanic circulation.

The main aim of this thesis is to assess SSW interactions within the climate system. Understanding the likelihood into whether specific types of SSW events can impact the surface climate will lead to tangible impacts on society. This will be facilitated by further understanding into the likelihood of extreme Northern Hemisphere

winter conditions following SSW events. This work also aims to increase scientific understanding into the coupled stratosphere-troposphere-ocean system, particularly aiming to advance knowledge into how the ocean and stratosphere can directly influence one another. This will potentially aid advancements into modelling and forecasting efforts.

## 1.2 Coupled Climate: Current Scientific Knowledge

As discussed above there is a vibrant and fruitful scientific community working on understanding the coupled-climate system. Here a brief overview of some research themes (by no means exhaustive) and results are provided as a background to this thesis. Detailed reviews on topics directly investigated in this thesis are provided within the relevant chapters. SSWs are formally introduced in Chapter 2 with understanding on stratosphere-troposphere coupling mechanisms discussed in detail in section 2.3.2.

Often interest resides in changes to the North Atlantic Oscillation Index (NAO) and the Northern Annular Mode Index (NAM). These are indices that represent dominant modes of variability within the atmosphere. The NAO index represents a vacillation in surface pressure over the North Atlantic Ocean with dominant centres of action over the Icelandic and Azores regions [Hurrell et al., 2003]. The NAM index represents the structure of low pressure at high latitudes and high pressure towards the equator [Thompson and Wallace, 2000] and can be calculated at different atmospheric heights. They are statistical measures of the variability within the atmosphere and can be indicative of weather regimes. Particularly the NAO is often associated with anomalous: wind regimes, surface temperature and precipitation, and variability of the storm track [Hurrell et al., 2003]. At the surface the NAM can be considered as the hemispheric counterpart to the NAO [Solomon et al., 2007]. Chapter 4 provides further discussion of these modes.

### 1.2.1 The Solar Cycle

There is a connection between the 11 year solar cycle and stratosphere-troposphere coupling. In the middle atmosphere ozone absorption in the 200-320nm ultraviolet band leads to atmospheric warming. Research has demonstrated the magnitude of warming varies throughout the solar cycle and this can trigger anomalous extratropical flow regimes which can descend through the atmospheric column and affect surface climate.

Haigh [1996] investigated the impact of the combined effects of solar irradiance and ozone changes under solar minimum and solar maximum conditions in the

European Centre for Medium-Range Weather Forecasts (ECMWF) model forced for 3 years with perpetual January conditions. Sea surface temperatures were fixed to allow for isolation of the uncoupled atmospheric response. They found a poleward shift under solar maximum conditions of the Southern Hemisphere tropospheric jet. They linked this to dynamical changes in the atmospheric wind structure as a result of heating in the Southern Hemisphere lower stratosphere under solar maximum conditions. There were stronger stratospheric easterlies which altered the meridional circulation structure and expanded the Hadley cell. They concluded that this led to a poleward shift of the Southern Hemisphere subtropical jet. For the simulation with incorrect ozone profiles the Southern Hemisphere response was dampened, demonstrating the key role interactive ozone played in the process.

Gray et al. [2010] provides a detailed review of solar influences in climate, in this they demonstrate in reanalysis (ECMWF 45-year reanalysis product) during solar minimum years the tropical stratopause region is 2  $K$  cooler than in solar maximum years. This leads to an alteration of the meridional temperature gradient; during solar minimum years there are weaker westerlies over the tropical stratopause region (between 1 and 0.1  $hPa$ ) peaking at values of around  $-4 m s^{-1}$ . Ineson et al. [2011] assessed this mechanism in model simulations. They ran two 80 year experiments in an ocean-troposphere-stratosphere-mesosphere model (HadGEM3) whereby ultraviolet radiation levels in the 200-320nm band were adjusted to be representative of solar minimum and solar maximum periods. Results were compared to reanalysis data. In agreement with Gray et al. [2010] it was found that under solar minimum conditions there was a significant cooling (when compared to the solar maximum simulation) in the tropical stratopause region which led to weaker mid-latitude westerlies in the middle atmosphere. This anomalous flow regime appeared in early winter and, due to alterations of wave dynamics, the anomalies propagated poleward and into the troposphere over the course of the winter. There was a direct influence on the surface climate with a shift to negative NAO conditions over winter (December to February) in the solar minimum simulation, this was also apparent in the reanalysis data. This led to the conclusion that the solar cycle contributed to surface variability through the excitement of stratosphere-troposphere coupling mechanisms (wave-mean flow interactions).

Kodera et al. [2016] extended this solar cycle induced stratosphere-troposphere coupling to include ocean impacts. In reanalysis data (ERA-Interim atmospheric reanalysis and National Oceanic and Atmospheric Administration Extended Reconstructed Sea Surface Temperature v3b) they isolated the same stratospheric zonal mean zonal wind response as discussed by Gray et al. [2010] and Ineson et al. [2011], stressing the radiative source of these anomalies in the upper stratosphere

and their descent into the lower stratosphere and troposphere by dynamical methods. They also isolated an oceanic signal for solar maximum periods where there is mid-latitude warming around ocean frontal zones. They discussed the lagged nature of this signal in observational data (NOAA's Extended Reconstructed Sea Surface Temperatures) over the North Atlantic where there was a lag of 3 to 4 years before sea surface temperature anomalies were large. They argued this time delay was a result of the signal being advected into a region where it could project on the NAO pattern and the signal could potentially be amplified.

Scaife et al. [2013] also discussed the lagged response in the North Atlantic to solar forcing in idealised HadGEM3 model simulations. Similarly to Kodera et al. [2016] there is a 3 to 4 year lag in the sea surface temperature response to prescribed solar irradiance forcing. They demonstrated how a positive feedback can exist in the North Atlantic sea surface temperature as a result of direct atmospheric effect from uv forcing and a delayed feedback from the NAO and related sea surface temperature tripole structure. They develop a simple mechanistic model to isolate the contribution of separate components in this feedback mechanism. Using this simple model they demonstrate an amplification of anomalies associated with solar forcing over the North Atlantic as a result of including the NAO feedback terms. In this study there is no account for white noise forcing but plausible parameters are extracted which can account for the observed results in model output.

### 1.2.2 Eurasian Land Surface Variability

Stratosphere-troposphere coupling has also been linked to Eurasian land surface variability. Cohen et al. [2007] provides a presentation and exploration of this mechanism in the National Centers for Environmental Prediction-National Center for Atmospheric Research (NCEP/NCAR) 40-year reanalysis product. The proposed mechanism is that early winter snow anomalies, particularly over the Eurasian sector, can lead to albedo and short-wave heat flux anomalies that act to excite Rossby wave activity. This can then lead to enhanced stratosphere-troposphere coupling over the following period. They assessed this mechanism by developing a stratosphere-troposphere coupling index based upon wave-activity flux at 100 *hPa* in December and January mean sea level pressure. The index was the first principal component of the multi-variate empirical orthogonal function applied to these fields. It was found that this diagnostic isolated wave activity flux over Eurasia and the mean sea level pressure pattern strongly resembled the Arctic Oscillation. This diagnostic was strongly correlated to midwinter wave activity flux throughout the atmospheric column and polar geopotential height, it was concluded to be a useful

representation of stratosphere-troposphere coupling. Furthermore this stratosphere-troposphere coupling index was strongly correlated to October Eurasian snow cover extent and it was found that early winter wave-activity flux associated with this snow cover could act to precondition the polar vortex to later strong wave activity pulses in December.

A case study of the 2009/10 winter by Orsolini et al. [2015] adds further evidence for a relationship between early winter snow cover extent and a subsequent weakened polar vortex and negative NAM conditions. They ran ensemble ECMWF forecasts, one set with randomised snow cover conditions and one with realistic conditions for December 1<sup>st</sup> 2009, which had anomalously high snow cover extent over the Eurasian sector. They found that for the ensemble with realistic snow conditions there was a sustained negative NAO index throughout December up until mid-January. For the other ensemble there was a quick relaxation back to neutral conditions by mid-December. Upon inspection of zonal mean zonal wind throughout the atmospheric column it appeared that the negative NAO index was sustained through stratosphere-troposphere coupling with easterly anomalies descending from the stratosphere. These studies provide evidence for coupling between the early winter snow extent and later winter geopotential height anomalies that are facilitated via stratosphere-troposphere coupling.

### 1.2.3 El Niño Southern Oscillation

Many studies have reported different coupling pathways for remote El Niño Southern Oscillation (ENSO) teleconnections. The observational study of Butler et al. [2014] highlights the importance of different surface impacts resulting from distinct pathways, which involve either the stratosphere or the troposphere. They utilised NCEP climate prediction center data between 1958 and 2013. They isolated 37 ENSO winters (19 El Niño and 18 La Niña years). 60% of ENSO winters, regardless of phase, also contained at least one SSW event. They composited 500 *hPa* geopotential height anomalies and assessed surface temperature impacts over the winter period and utilised these fields to isolate the stratospheric and tropospheric pathways. To recover the tropospheric pathway they assumed a linear and opposite signed response during El Niño and La Niña periods. They subtracted the anomaly composites from one another and revealed a Pacific/North American wave train in the 500 *hPa* geopotential height field, which was much stronger for winters not containing a SSW event. Assuming a non-linear response due to the stratospheric

pathway<sup>1</sup> they combined the anomalous fields. The 500 *hPa* fields now displayed a negative phase NAM pattern, consistent with SSW surface impacts [Baldwin and Dunkerton, 2001] when a SSW was present. From this observational work it was concluded that there are two distinct pathways, stratospheric and tropospheric, and that the spatial structure of the hemispheric anomalies during ENSO winters depends on which pathway is active. For the stratospheric pathway SSWs were found to be essential in facilitating the ENSO to Europe teleconnection.

In an intermediate model Bell et al. [2009] directly investigated the role of the stratosphere in remote ENSO teleconnection. They ran 40 year simulations with neutral and El Niño Pacific SST climatologies. For the El Niño integration there was an increase in SSW frequency throughout all winter months. There was also increased meridional heat flux throughout the atmospheric column, an indication that more wave activity was entering and travelling through the stratosphere. Easterly zonal mean zonal wind and positive temperature anomalies, for the El Niño simulation compared to the neutral simulation, developed in early winter and descended through the course of the season. Repeated studies with a degraded stratosphere were conducted where the Rayleigh friction scheme was extended down to 10 *hPa*. In this simulation surface anomalies were a response of tropospheric processes only. In the degraded stratosphere simulations the response in geopotential height anomalous spatial structure was more regional and did not project onto a NAM pattern. Overall it was concluded that the stratosphere plays an active role in European impacts following El Niño.

Ineson and Scaife [2009] document the link between European climate and ENSO events and assessed this relationship in a sophisticated high-top general circulation model. They ran an 8 member ensemble simulation in the Met Office Hadley Centre climate model (HagGAM1) from 1961 to 2002 (containing a total 6 El Niño events). During El Niño periods in later winter (January to March) there was a shift to negative NAO regimes. Throughout the atmospheric column the geopotential height structure showed enhancement of the climatological pattern during December to February. The zonal mean zonal wind displayed a descent of negative anomalies from the upper stratosphere into the troposphere. They further subdivided the El Niño winters into seasons that did and did not contain a SSW event. For El Niño winters with a SSW present the hemispheric anomalies project onto a negative NAM pattern, for the remaining winters the anomalies did not project onto this pattern and were similar to the anomalies associated with the troposphere pathway outlined

---

<sup>1</sup>Since both El Niño and La Niña European teleconnections are thought to be facilitated via SSW dynamics and these events have consistent surface spatial impacts if the associated anomalies descend, see Chapter 2.

by Butler et al. [2014].

Overall these studies all provide evidence (in observations, an intermediate and a sophisticated general circulation model) of remote teleconnections between the Pacific and Europe. The nature of response in Europe depends on which pathway is dominant, the stratospheric or tropospheric one, with SSWs being a crucial component in the triggering of the stratospheric pathway.

#### 1.2.4 Quasi-Biennial Oscillation

The quasi-biennial oscillation (QBO) phase is linked to changes in polar vortex strength with reports of a weaker vortex during the easterly QBO phase [Holton and Tan, 1980]. Garfinkel et al. [2012] utilised model output to display how the QBO modulates polar vortex strength during its easterly phase. The introduction of easterly winds in the lower stratosphere (50 *hPa*) led to changes in the mean meridional circulation and affected the quasi-geostrophic refractive index. This led to more wave convergence in the stratospheric polar region and a weaker vortex. They were unable to assess a SSW relation due to the lack of events simulated in WACCM version 3.1.9.

Other studies have assessed the SSW-QBO relationship with model studies generally resulting in SSW events occurring during both easterly and westerly QBO regimes although there may be an increased likelihood of earlier events during the easterly phase [Holton and Austin, 1991]. Pascoe et al. [2006] displayed that improved variability in tropical winds above 45 *km* and a deep QBO led to SSW events earlier in the winter period in the UK Met. Office's Unified Model version 4.5. Richter et al. [2011] hints at the importance of the non-linear interactions between ENSO and the QBO for SSW suppression. In a modelling study (using WACCM3.5) they found that if they removed ENSO or the QBO there was a realistic frequency of SSW occurrence but if they removed both the number of events dropped dramatically. They also reported that the presence of QBO and ENSO were associated with different SSW onsets and strengths, particularly ENSO led to later average SSW onset, in agreement with Ineson and Scaife [2009] and Li and Lau [2013], with stronger polar warming and the QBO was associated with earlier events, in agreement with Pascoe et al. [2006].

#### 1.2.5 Skill of Predictive Models

An area of growing interest is into the relationship between the skill of forecast systems and the presence/complexity of a simulated stratosphere. Tripathi et al. [2015] assessed the potential of sub-seasonal forecast skill in the European Centre for

Medium-Range Weather Forecast system, which was initialised during anomalous stratospheric wind regimes at 10 *hPa* and 60°N. They isolated forecasts that were initialised when the stratospheric zonal winds were anomalous weak (lower than 0 *m s*<sup>-1</sup>) or strong (over 41.2 *m s*<sup>-1</sup>) and compared these to medium strength stratospheric zonal winds (between 14.5 and 36 *m s*<sup>-1</sup>). They found increased skill levels in predicting the NAM index at 100 *hPa* and 1,000 *hPa* in the third and fourth week after forecast initialisation for the anomalous strong and weak conditions. This displays the potential of increased skill in the sub-seasonal time scale for forecast system that have a well resolved stratosphere and can capture wind variability and strength at 10 *hPa* and 60°N.

There is also interest in whether the presence of a fully resolved stratosphere can aid the predictive skill of seasonal forecasts. Scaife et al. [2016] found an interesting correlation between the forecasted risk of a SSW event and enhanced skill in the seasonal prediction of the NAO. They utilised the Met Office Global Seasonal forecast system GloSea (fifth generation) with an ensemble of 24 forecasts initialised in early November for winter seasons between 1992/1993 and 2011/2012. Data from November was discarded so that only forecasting in the seasonal range was assessed. They highlighted the probabilist risk of a SSW or strong polar vortex event in any given winter was between 25% and 90%. This demonstrates potential predictability of these events beyond the deterministic forecast range. In GloSea there was a significant shift in the surface NAO value for winters that contained a SSW or strong polar vortex event when compared to those that did not. This displayed that there is a relationship between the presence of an extreme stratospheric state and the surface climate in GloSea but did not prove any directionality in the signal. Strikingly, when ensemble winters were separated into all members and only those without a SSW event the correlation between the forecasted NAO in GloSea and the observed NAO changed from 0.62 to 0.09 (with the result not due to reduced sample size). For this model there is an enhanced level of probabilistic forecast skill of the NAO when there is a strongly perturbed stratosphere, particularly a SSW, present.

Butler et al. [2016] conducted a multi-model investigation into the more generalised hypothesis that enhanced stratospheric resolution (at least 15 vertical levels between the tropopause and 1 *hPa* and a lid above 1 *hPa*) in a forecast model could lead to increased predictive skill. They focused on ensemble means of monthly mean data; noting the use of an ensemble of opportunity and that the models themselves had different parameter schemes, physics and horizontal resolution scales. Overall they found that the models with enhanced stratospheric resolution simulated stratospheric variability more realistically but this did not necessarily translate into

improved skill in prediction of the NAM value at the surface or at 500 *hPa* on the seasonal timescale. There was little difference in overall skill between the high and low stratospheric resolution model ensembles. Some models stood out as having enhanced skill in predicting the NAM value (e.g. GloSea) and a relationship emerged between increased number of ensemble members in a forecast system and increased skill in predicting the December to February NAO. Differences in forecast skill for models with differing stratospheric resolution were found when Butler et al. [2016] considered winters by ENSO phase. There was increased skill in predicting European surface climate (based upon January to March mean sea level pressure) for the increased stratospheric resolution ensemble during El Niño winters when compared to the low stratospheric resolution ensemble. There was a notable lack in skill, though, over the Western Europe region, attributed to difficulties in simulating Gulf Stream processes and blocking. Overall the models in this ensemble of opportunity display large variability in their behaviour and skill within the subsets of high and low stratospheric resolution. Enhanced stratospheric resolution may be most relevant during winters that contain an El Niño event.

### 1.2.6 Stratosphere-Ocean Coupling

Stratosphere-ocean coupling is an emerging research topic and is a key interest throughout this thesis. As discussed above (section 1.2.3) ENSO events can potentially impact the stratosphere and induce a remote teleconnection. Over the North Atlantic Ocean research is also emerging demonstrating the potential of a signal from the stratosphere into the ocean, facilitated via anomalous surface regimes following extreme stratospheric behaviour. Reichler et al. [2012] directly assessed this pathway during strong stratospheric polar vortex periods in a general circulation model and their results will be discussed in Chapter 4. There is also current work on whether periods with anomalous sea surface temperatures over the Atlantic can lead to shifts in the polar vortex strength, with a mixture of results in the literature [Omrani et al., 2014, Keenlyside and Omrani, 2014, Omrani et al., 2015, Peings and Magnusdottir, 2015], this is discussed in detail in Chapter 6.

### 1.2.7 Concluding Remarks

Overall, there is ongoing research into the coupled climate system due to the positive implications increased understanding can have for seasonal forecasting and understanding remote teleconnection systems. SSWs events display a clear manifestation of stratosphere-troposphere coupling, as discussed in the next Chapter, and increased understanding of this phenomenon and their impacts on and interactions

with the surface climate and ocean motivate the main research aims in this thesis.

### 1.3 Synopsis

In Chapter 2 SSW events are formally introduced. Motivating background literature on interactions with other climatic modes is also provided with a brief overview on the current understanding of stratosphere-troposphere coupling mechanisms. The remainder of Chapter 2 focuses on the technical development of a SSW identification and classification algorithm in preparation for the research conducted in this thesis.

Chapter 3 introduces the general circulation models utilised throughout this thesis. The standalone atmosphere (IGCM4) and ocean models (MOMA) are presented with specification of their technical details. There is a brief overview of combination into an atmosphere-ocean coupled model (FORTE). The atmosphere-only general circulation model is assessed in detail with presentation of its background climatological state. SSW simulation is evaluated using benchmarks from the literature in preparation for work conducted in Chapters 4, 5 and 6.

In Chapter 4 the IGCM4 is used to assess SSW impacts on the surface climate and implied impacts into the ocean. The exclusion of an interactive ocean is overly simplistic but allows for direct isolation of SSW impacts with no complication of coupling features. This isolates one limb, a ‘top down’ perspective, of the coupled climate system.

Chapter 5 presents the exploration, in IGCM4 data, of an objective statistical method to identifying strong surface impacts following SSW events. This Chapter also discusses the possibility of creating a new SSW classification procedure based on Empirical Orthogonal Function analysis.

In Chapter 6 the sensitivity of the stratosphere is assessed in the IGCM4 when configured with different North Atlantic SST climatologies, motivated under a Atlantic Multidecadal Oscillation framework. This provides a complementary ‘bottom up’ perspective to Chapter 4, albeit from the perspective of only one oceanic basin and climatic mode.

Finally in Chapter 7 these two limbs (‘bottom up’ and ‘top down’) are studied as a complete interactive system, as they are in reality. The coupled model integration is discussed with focus on changes to SSW simulation and atmospheric background climatology. The implied results of Chapter 4 are compared to a simulated ocean response to SSW events, providing insight into how coupled and oceanic processes can interact with SSW surface impacts.

Concluding remarks are gathered in Chapter 8 where the key themes of this thesis are drawn together and possible future work outlined.



---

## Chapter 2 - Sudden Stratospheric Warmings

### 2.1 Introduction

Sudden stratospheric warmings are of great academic interest to many people. The motivation behind this interest is that they are dynamically driven events which can greatly disturb the winter stratosphere [Andrews et al., 1987] and manifest strong stratosphere-troposphere coupling [Baldwin and Dunkerton, 2001, Limpasuvan et al., 2004, Mitchell et al., 2013a, and references therein]. Furthermore studies have displayed the potential for a direct downward influence from the stratosphere into the troposphere during these events [Hitchcock and Simpson, 2014]. The effects following SSWs on the surface climate can be persistent and severe [Baldwin and Dunkerton, 2001] with studies reporting a warming over North America and a cooling over North Eurasia associated with a negative NAM regime that can persist for months [Mitchell et al., 2013a]. There is potential for increased understanding of stratosphere-troposphere coupling to aid predictability of Northern Hemisphere extreme cold events [Thompson et al., 2001]. Progress in understanding of SSWs, particularly why only some events manifest strong stratosphere-troposphere coupling, has positive implications for mitigating the impacts of harsh European winter conditions and increased scientific understanding of the coupled climate system.

In an undisturbed winter strong westerly winds develop in the stratosphere, forming the radiatively driven polar vortex and polar night jet. However, in some winters (mainly in the Northern Hemisphere) dynamically driven upward propagating Rossby waves, see section 2.3.2, disturb this typical flow regime and deposit easterly momentum [Matsuno, 1971, Andrews et al., 1987]. This decelerates the polar vortex and can lead to a complete break down of the westerly winds and significant polar warming. Typically events are categorised into either major or minor warmings and, for the major events, can be further sub-categorised into splitting or displacement events.

The academic community has made progress in recent years on the topic of exactly how a SSW should be defined [Butler et al., 2015]. There is ambiguity as to what classification procedure should be implemented which has lead to discrepancies in the literature. For example the study of Palmeiro et al. [2015] suggested that the decadal variability in event occurrence, particularly the lack of events in the 1990's, is a method-dependent feature. As reported by Butler et al. [2015] common methods for identifying and classifying SSW events include: stratospheric zonal wind reversal at one or multiple grid points, empirical orthogonal functions, moment analysis and Northern Annular Mode index (NAM) based methods, among others.

For the purposes of this study a simplified algorithm is developed that is dynamically motivated and computationally efficient.

A brief overview of the different types of events will be provided in section 2.2 followed by a synopsis of stratosphere-troposphere coupling theory in section 2.3. The algorithm development is outlined in section 2.4 and motivated based on a literature review. This new algorithm is then assessed in the context of other moment based techniques in sections 2.5 and 2.6, with conclusions presented in section 2.7.

Overall this Chapter provides an overview of the current understanding of SSW events and stratosphere-troposphere coupling. It also presents a mathematical description of, and physical motivation behind, a new straightforward identification and classification technique which is appropriate for isolating splitting and displacement SSWs and will be used throughout this thesis for studying these events in general circulation model data.

## 2.2 Definition

A major sudden stratospheric warming is commonly identified by two criteria:

1. A reversal of the zonal mean zonal wind ( $\bar{U}$ ) at 10 *hPa* and 60°N.
2. A reversal of the temperature gradient towards the pole.

If criterion (2) is satisfied but (1) is violated then the event is classified as minor. Henceforward only major SSWs shall be discussed due to their greater dynamical relevance and implications for surface climate [Palmeiro et al., 2015]. A further distinction between events can be made from their spatial structure:

- A *splitting event*, Figure 2.1(a), is where the vortex breaks into two smaller ‘daughter’ vortices. Typically these align over the 90°E-90°W axis [Matthewman et al., 2009]. These events are associated with an anomalously high wavenumber-two planetary wave component.
- A *displacement event*, Figure 2.1(b), is where the vortex is shifted off the pole and usually distorts into a ‘comma’ shape. This behaviour is associated with an anomalously high wavenumber-one planetary wave component.

It is important to note that the above statements are based on composite analysis and are therefore representative of generalised SSW behaviour. It is not uncommon for individual events to possess a mixture of splitting and displacement characteristics [Mitchell et al., 2013a]. As highlighted by Ripesi et al. [2012] in some extreme

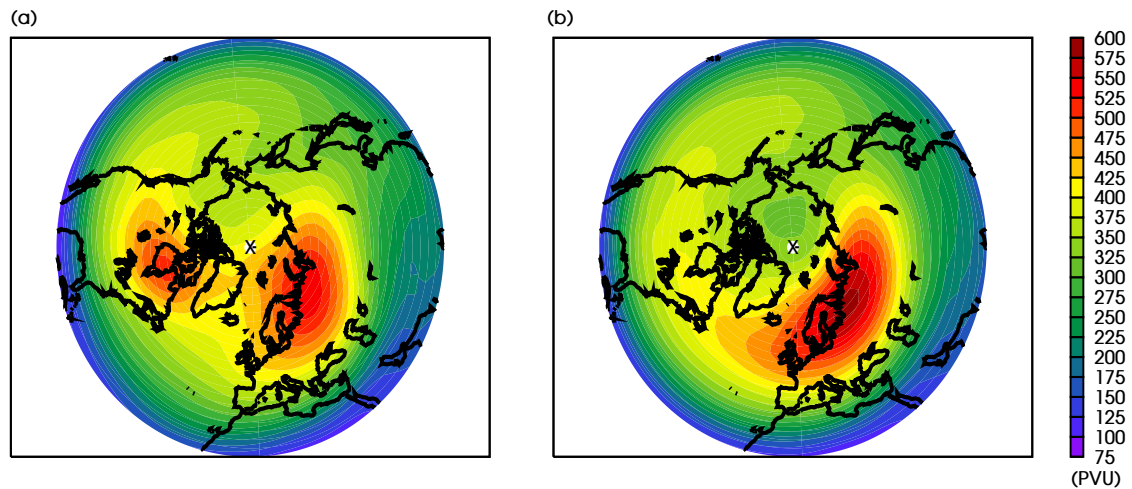


**Figure 2.1:** Composite plots of the 850  $\theta$ -level Ertel's potential vorticity (PVU) during: (a) 48 splitting and (b) 65 displacements SSW events. Individual events are averaged up to 5 days after the identified central date.

cases SSWs are associated with planetary wave numbers larger than one and two and events can also, albeit rarely, occur in the Southern Hemisphere [Barnett, 1975, Varotsos, 2004]. Two case studies of the temporal evolution of a splitting and displacement event are presented in Appendix B

## 2.3 Background Literature

### 2.3.1 Climate System Interactions

Often interest in SSWs is motivated by their interactions with other aspects of the climate system. SSWs are an impressive phenomena in their own right but many bodies of research have emerged which demonstrate how these events are associated with other climatic modes and coupling to the other atmospheric layers. Studying an isolated aspect of the climate system often provides valuable scientific insight, such as simplified mathematical or physical understanding; however, the Earth's climate system is intrinsically non-linear and a result of coupled processes. Coupling must be taken into account if a real working knowledge of the climate system, and improvements in numerical weather prediction, is to be attained.

As discussed in Chapter 1 an active area of research is how the El Niño Southern Oscillation (ENSO) can impact the stratosphere. In particular complementary studies by Ineson and Scaife [2009] and Li and Lau [2013] demonstrate how El Niño events are associated with the onset of late winter SSWs and may account for some of the remote teleconnection pattern associate with ENSO. Bell et al. [2009] shows an increase in SSW frequency in all winter months for El Niño conditions. Evidence

is also emerging that this teleconnection is sensitive to the position and phase of the climatological stationary wave [Fletcher and Kushner, 2011].

Another oceanic mode that may interact with the stratospheric polar vortex is the Atlantic Multidecadal Oscillation [Omrani et al., 2014, Keenlyside and Omrani, 2014]. This mode represents the variability in Atlantic sea surface temperatures and could be linked to the background strength of atmospheric  $\bar{U}$  and modulate upward wave propagation. There are still many open questions regarding the forcing factor(s) behind this mode of variability and whether it can truly impact the stratosphere and European climate. This is discussed in detail in Chapter 6

The QBO is another mode that may modulate SSW occurrence. Holton and Tan [1980] and Garfinkel et al. [2012] report weakening of the polar vortex during QBO easterly phases. Modelling studies of Holton and Austin [1991], Pascoe et al. [2006] and Richter et al. [2011] report an increased likelihood of SSW events earlier in the winter season during the easterly QBO phase. See Chapter 1 for a more detailed review.

There is a complicated relationship between SSWs and blocking events. It is difficult to determine statistically robust trends in blocking frequency and SSW event occurrence due to the fact that blocking is a fairly variable event in the troposphere and different types of blocking may be associated with different SSW types. This is further exasperated by the fact that many models struggle to simulate blocking [Scaife et al., 2011] and there are numerous distinct methodologies for isolating both SSWs and blocking events. However, progress has been made in recent years. Mitchell et al. [2013a] managed to isolate significant relationships between SSWs and a two-dimensional blocking index (based upon Tibaldi and Molteni [1990]) in reanalysis data, see section 2.3.3. Also using reanalysis data Davini et al. [2014] showed that there is a robust link between weak vortex event occurrence and a reduction/enhancement of blocking on the equatorward/poleward side of the Atlantic storm track (again via the Tibaldi and Molteni [1990] based index).

Empirical orthogonal function (hereafter EOF, see Chapter 5) metrics are often utilised to ascertain coupling strength. The NAM (the leading EOF in geopotential height) in the stratosphere is a measure of the strength of the polar vortex and the NAM in the troposphere measures the strength of the mid-latitude jet. There is a strong correlation between these statistical indices and studies often assess the negative NAM associated with SSWs and its descent into the troposphere as a measure of how events impact the surface [Baldwin and Dunkerton, 2001]. Overall examples of stratosphere-troposphere coupling are abundant, although the mechanisms that provide this pathway often remain elusive and will be discussed further in the next section.

### 2.3.2 Tropospheric Coupling

As stated in section 2.3.1 studies often view the descent of NAM anomalies from the stratosphere to the troposphere as an indication of the presence of coupling. It is prudent to note that this is a flawed assumption, as stated by Haynes [2005]. The descent of zonal structures is not sufficient to imply the propagation of information. However studies such as Norton [2003] and Hitchcock and Simpson [2014] have rigorously proven that for SSW phenomena there is a direct downward influence. This aside, it is often better to have an understanding of the potential processes involved in creating pathways between the stratosphere, troposphere and ocean rather than just a proxy view of behaviour through the statistical, and potentially misleading, NAM index.

Theories for mechanisms behind stratosphere-troposphere coupling typically involve linear wave theory, potential vorticity dynamics, eddy driven jet behaviour and wave-mean flow interactions. Many authors appeal to Rossby wave dynamics and their vertical motions (e.g. Limpasuvan and Hartmann [2000]). A brief overview will be provided of some leading theories and then a more detailed description of the mathematical formulation for vertical Rossby wave propagation will be provided.

As outlined by Ambaum and Hoskins [2002] instantaneous geostrophic and hydrostatic adjustment to non-local potential vorticity anomalies in the stratosphere can lead to geopotential height perturbations in the troposphere. For example, if the polar stratosphere experiences wave breaking the climatological westerly winds may decelerate and negative potential vorticity anomalies will appear over the pole. This induces, assuming thermal wind arguments, a warming beneath the region of wind deceleration and a cooling above it resulting in bending of the isentropes away from the potential vorticity anomaly. This reduces the tropopause height and, by conservation of angular momentum, a spin down of the air column beneath it; resulting in negative potential vorticity anomalies in the troposphere. This argument is proven rigorously in Ambaum and Hoskins [2002, and references therein] and Martin [2006].

Studies by Kunz et al. [2009] and Davini et al. [2014], see section 2.3.1, highlight how the behaviour of stratospheric zonal mean windshear can influence Rossby wave breaking. In the presence of a negative stratospheric zonal wind shear Kunz et al. [2009] showed how the wave breaking lifecycle can shift towards a cyclonic tendency causing equatorward shift of the tropospheric jet stream. They noted the nonlinearity of wave dynamics and a sensitivity of the coupling based on the location of the tropospheric jet stream. This dependence on tropospheric jet latitude and the strength of stratosphere-troposphere coupling is also reported by Garfinkel

et al. [2013]. Where they also reported that coupling strength, in an idealized dry dynamical model, was associated only with tropospheric modes of variability. Other authors [Fletcher and Kushner, 2011, Omrani et al., 2015] have highlighted the possibility of constructive or destructive interference in the climatological winter tropospheric stationary wave pattern modulating coupling strength.

Classical arguments of upward wave propagation appeal to linear wave dynamics and have been elegantly outlined by many authors (examples being Andrews et al. [1987] and Holton [2004]). Concepts include; the state of the lower stratosphere modulating the refraction and reflection of upward propagating planetary waves, wave-mean flow interactions and the descent of critical lines leading to alterations of wave dynamics, wave-wave interactions and resonance leading to the amplification of otherwise insignificant anomalies. These theories, and the majority of those in the previous paragraphs, focus on planetary scale Rossby waves. A brief mathematical description of this wave propagation is provided below for a more rigorous derivation see Holton [2004].

To initiate a basic understanding of vertical planetary wave propagation a simple background state of zonal mean zonal flow,  $\bar{U}$ , is assumed. The buoyancy frequency,  $N$ , is assumed to be constant. A mid-latitude  $\beta$ -plane coupled with the quasi-geostrophic potential vorticity equation can then be invoked to show that propagation occurs only if  $\bar{U}$  satisfies

$$0 < \bar{U} - c < \beta \left[ (k^2 + l^2) + \left( \frac{f_0^2}{4N^2H^2} \right) \right]^{-1} = U_c. \quad (2.1)$$

Where  $k$  and  $l$  are zonal and meridional wave numbers respectively and  $c$  is the phase speed.  $f_0$  is a constant mid-latitude reference value of the Coriolis parameter and  $\beta = \frac{\partial f}{\partial y}$ .  $H$  is the mean height scale. This value,  $U_c$ , is the Rossby critical velocity. For a stationary wave the phase velocity,  $c$ , is set to zero. Thus a direct result of Equation 2.1 is that  $\bar{U}$  must be less than the Rossby critical velocity for vertical propagation. From this very simple argument it is evident that Rossby waves with a large wave number will not propagate vertically in a typical winter zonal mean wind profile. Longer waves (wave-one and two) can propagate providing the mean flow is westerly and not too strong. If the polar night jet is unusually poleward or weak then this may allow for the vertical propagation of long planetary waves into higher than usual latitudes. These propagating waves then have the ability to distort and alter the vortex dynamics.

Overall this argument allows for valuable insight into the mechanism behind vertical wave propagation but only accounts for flows under a mid-latitude  $\beta$ -plane approximation. Following the work of Karoly and Hoskins [1982] the propagation

of forced stationary planetary waves can be determined using ray tracing theory in spherical coordinates. A refractive index based upon wavenumber is derived in the vertical-meridional plane that indicates areas in which planetary wave propagation can occur. This is denoted by  $K_s$  and wavenumbers are generally able to propagate in areas of positive values of  $K_s$  that are larger than the wavenumber of interest. Karoly and Hoskins [1982] derived the formula for this index as

$$K_s^2 = \frac{\beta_M}{\bar{u}_M} - \frac{\alpha^2}{4} \quad (2.2)$$

where  $\beta_M$  is  $\cos(\phi)$ ,  $\phi$  is latitude, times the meridional gradient of quasi-geostrophic potential vorticity on the sphere under a Mercator projection and  $\bar{u}_M$  is the Mercator basic zonal flow. A non-dimensional version of the Coriolis force divided by the buoyancy frequency is presented in  $\alpha^2$  such that

$$\alpha^2 = \frac{f_M^2 a^2}{N^2 H_o^2}$$

where  $f_M^2$  is the coriolis parameter in Mercator coordinates,  $a$  is the radius of Earth,  $H_o$  is stratospheric height scale and  $N$  is the buoyancy frequency. Furthermore it has also been assumed here that the buoyancy frequency is a constant. Karoly and Hoskins [1982] showed that rays are always refracted toward the direction of  $\nabla K_s$ . This theory is useful for a zonal mean based view of stratosphere-troposphere coupling and allows for wave tracing on given background flow states. It is worth recalling, though, that as stated above evidence is emerging for a non annular component to stratosphere-troposphere coupling and simple linear wave dynamics are a very useful starting point but should not be used as a complete theory.

### 2.3.3 Surface Impacts of Splitting and Displacement SSW

As understanding into SSWs has evolved investigation has shifted to encompass how different types of major events behave. A classical distinction is into splitting and displacement events (see section 2.2). Areas of interest include whether they lead to noticeably different anomalies and, if so, what the subsequent impact on tropospheric flow and surface climate is. One paper investigating this in reanalysis data (combined National Centers for Environmental Prediction-National Center for Atmospheric Research, NCEP/NCAR, reanalysis dataset [Kalnay et al., 1996] and the European Centre for Medium-Range Weather Forecasts (ECMWF) 45-year reanalysis product, ERA-40, Uppala et al. [2005]) has been published by Mitchell et al. [2013a], hereafter M13. This study found that there was a dependence on the

type of SSW event and the subsequent effects on surface climate. Overall the main features discovered were:

#### Vortex Displacement Events

- The Mean Sea-Level Pressure (MSLP) has a strong wave-one-like structure preceding the event consistent with enhanced wave-one propagation.
- There are large stratospheric NAM anomalies which are positive preceding the event and negative for up to 60 days afterwards. This anomaly does not descend beneath the tropopause.
- The surface impact appears to be due to cold air outbreaks over North America. This impact is largest in the month following the event and low temperatures are observed over North America of up to 1.5K below average. An increase in blocking accompanies this.

#### Vortex Splitting Events

- Before the event the MSLP has a wave-two-like pattern but this doesn't project well onto the NAM.
- The NAM stratospheric signal is generally weaker than in the displacement events with positive anomalies preceding it and negative anomalies afterwards. However, in this case the negative NAM anomalies do propagate into the troposphere.
- Two months after the event the negative surface NAM anomaly is still observed and there is high latitude blocking occurring in the Atlantic and Pacific basins. The blocking frequency is decreased over Europe and Western Eurasia.
- There is a warming over North America and a cold anomaly over North Eurasia. This is associated with the negative NAM.

In contrast to M13 the study of Charlton and Polvani [2007], hereafter CP07, reported a lack of difference in surface impact for subcategories of events based on their spatial structure in ERA-40 reanalysis data. They discovered that the splitting events had, on average, more hemispheric anomalies in the geopotential height field following events, averaged up until 60 days after event onset, at 1000 *hPa* with a strong positive anomaly over central Eurasia and the Pacific Ocean. The anomalies associated with displacements appeared to be more localised to the North Atlantic sector. However the difference in these anomaly patterns was present before the

onset of SSW events and therefore unlikely to be a result of downward influence. CP07 attempted to ascertain any differences between the impacts following splitting and displacement events via the surface NAM and area-weighted RMS geopotential height anomaly from 20 to 90°N. There was no significant difference in these indices following event. The overall conclusion was that there is no difference in hemispheric impacts in the troposphere following the two SSW types, in contrast with the results of M13.

There is clearly a need for further research into this topic to investigate whether there is a dependence on the surface impact based on spatial structure of the disturbed polar vortex. It is clear that the relatively short timespan available in reanalysis data leads to difficulties in isolating robust results. Another potential source of this apparent discrepancy could be the different methodologies employed by the two aforementioned studies. For large datasets it is necessary to formulate a numerical method which is computationally cheap and accurately locates and classifies the major SSW events. Here a hybrid method is developed that utilises features from the two studies in an attempt to consolidate their apparently contradictory results.

## 2.4 Hybrid Approach for Isolating SSWs

To analyse typical SSW behaviour, and any difference between the splitting and displacement subsets, it is important that there is an algorithm that can reliably locate and classify these events. A hybrid method is developed in sections 2.4.1 and 2.4.2. A key function of this algorithm is to quickly and reliably locate SSW splitting and displacement events in general circulation models. The hybrid nature allows for comparison to the CP07 and M13 studies. Its accuracy is assessed in section 2.4.3.

### 2.4.1 Identification

To identify SSWs the event central date is defined as the day where  $\bar{U}$  at 10 *hPa* and 60°N becomes easterly, following CP07, between the months of December and March (DJFM) following M13. Note that the CP07 implementation of wind reversal at 60°N is justified as this marks the lower bound of where a latitude is representative of a coherent reversal over the entire poleward region [Butler et al., 2015].

The CP07 study neglects the temperature gradient reversal criterion in their algorithm. To conform to historic literature [McInturff, 1978] events that do not have a strong polar warming are discarded. To achieve this spatial averages of the temperature field are calculate for the regions 50-70°N ( $\mathcal{R}1$ ) and 70-90°N ( $\mathcal{R}2$ ) at 10 *hPa*. The difference  $\mathcal{R}1$  minus  $\mathcal{R}2$  is calculated. If this is positive then there is

no polar warming and the central date is removed. It is found that this additional step does not slow the algorithm and leads to only a few events being removed.

Duplicates of the same event should be avoided. This is achieved by ensuring there is no occurrence of a central date within 20 days before the identified wind reversal. This is approximately equal to two radiative time-steps in the middle stratosphere. Furthermore only mid-winter warmings are of interest so any final warmings captured by the algorithm must be removed. This is achieved by removing central dates where  $\bar{U}$  does not return to a westerly state for at least 10 consecutive days before the 30<sup>th</sup> of April.

### 2.4.2 Classification

To classify events into either splittings or displacements a moment analysis technique is developed. The equations employed follow the algorithm developed in Mitchell et al. [2011], which is based upon works by Waugh and Randel [1999] and Matthewman et al. [2009]. Mathematically a moment is the quantitative measure of the shape of a set of points in a two-dimensional data set. Waugh [1997] showed that the quantities needed to capture the shape of the polar vortex (namely the elliptical area, centroid location and aspect ratio) could be directly calculated using the moment equations.

Moments are performed over potential vorticity (PV) fields on isentropic surfaces for the 20 days surrounding an identified central date. This is advantageous because PV is conserved under frictionless, adiabatic flow on isentropic surfaces, thus enabling it to be accurately tracked over them. Following this method allows for detailed study of the vortex temporal evolution.

Matthewman et al. [2009] further developed the moment analysis to include kurtosis<sup>2</sup>, which is a measure of the peakedness of the 2D dataset distribution. A very low or negative value of kurtosis indicates a low distribution around the mean value (i.e. a high bipolarity of the PV field) and this is indicative of a splitting of the polar vortex [Matthewman et al., 2009, Mitchell et al., 2011]. The condition set by Matthewman et al. [2009] to define a major SSW splitting event is that the kurtosis drops below -0.1 and this criterion will also be adopted here. Furthermore, in Matthewman et al. [2009] it was shown that the splitting of the polar vortex occurs almost instantaneously over the atmospheric column and Mitchell et al. [2011] found that the distribution of kurtosis over isentropic levels was fairly similar. The exact criterion used to define a splitting event will be a drop in kurtosis below -0.1 on the 850 K potential temperature surface. It is assumed that this will be representative

---

<sup>2</sup>Note that this is labelled as ‘excess kurtosis’ in their literature.

**Table 2.2:** SSW frequency benchmark,  $SSW \text{ year}^{-1}$ , applied to the hybrid, CP07 and M13 SSW identification and classification algorithms. Parentheses indicate standard error.

Dataset/Method	All SSW	Vortex displacement	Vortex splitting
IGCM/Hybrid	0.57(0.07)	0.33(0.05)	0.23(0.05)
NCEP/NCAR/CP07	0.6 (0.1)	0.33 (0.07)	0.27 (0.07)
ERA-40/M13	0.82 (0.1)	0.40 (0.08)	0.42 (0.08)
ERA-40/Hybrid	0.6 (0.1)	0.22 (0.07)	0.37 (0.08)

of the entire atmospheric column. For identified splitting events the central date (event onset) is set as the date that the kurtosis threshold is met as this is the most dynamically relevant date. Hereafter this  $\bar{U}$  based identification and moment based classification technique will be referred to as the ‘hybrid method’.

A mathematical description of the moment analysis equations is contained in Appendix A.

### 2.4.3 Algorithm Verification

To assess the hybrid identification and classification method, data from a preliminary atmosphere-only general circulation model integration are utilised. This model is the Intermediate General Circulation Model (IGCM) version 3.1 (note that version 4 is presented in Chapter 3) which is a hydrostatic, multilevel, primitive equation atmospheric model with spherical geometry. The primitive equations are solved using the spectral method with triangular truncation at wave number 42, there is a  $2.8^\circ$  horizontal grid and 35 vertical levels. There is a model lid at  $0.1 \text{ hPa}$  with 13 vertical levels in the stratosphere. This intermediate model has prescribed boundary conditions (sea surface temperature and solar insolation) with fixed greenhouse gas and prescribed ozone concentrations. There is no inclusion of atmospheric gravity waves, Rayleigh-Friction is applied in the upper most levels to ensure no spurious Rossby wave behaviour, see Forster et al. [2000] for technical model details. Here interest resides in the hybrid methods’ ability to accurately locate and separate SSWs into splitting and displacement subsets. The speed and ease at which integrations are performed by the IGCM 3.1 provides a convenient learning platform on which SSW classification and identification techniques can be performed.

In 110 years of model data the algorithm locates 56 events in total. The kurtosis threshold classifies 23 events as splitting the polar vortex which leaves 33 as displacements. Table 2.2 presents the frequency of SSW events, in SSWs per year, for the hybrid method applied to IGCM data, the CP07 algorithm applied to NCEP/NCAR data and the M13 algorithm applied to ERA-40 data. These figures

provide a somewhat insightful benchmark to assess how the different algorithms are behaving, although the use of three difference datasets does makes cross-comparison ambiguous. It is worth noting, however, that the study of M13 also undertook analysis of NCEP/NCAR and found that there was little change to their results. CP07 also presents events captured by their algorithm in ERA-40 data. The frequency of events for the hybrid method and the CP07 algorithm are within standard error of each another for all three categories of SSWs (Table 2.2). The hierarchical clustering algorithm of M13 locates more events per year than both the CP07 and the hybrid methods. In particular it isolates more splitting events. Explanations for this could be this could include; the M13 algorithm does not remove final warmings whereas the other algorithms do, the M13 algorithm is overly sensitive or that the methods that identify events based upon  $\bar{U}$  reversal at 10 *hPa* and 60°N are too stringent.

Comparison of SSW frequencies across three different datasets (that is the IGCM, NCEP/NCAR and ERA-40) and 3 different algorithms has limited usefulness due to the fact that it is not really known, to the authors knowledge, how accurate the CP07 and M13 algorithms are and, at this stage, whether the IGCM simulates SSW events in a similar manner to how they occur in reanalysis data. For a clearer comparison to methodologies outlined in the literature the hybrid method is applied to ERA-40 data<sup>3</sup>. This is directly compared to the identified dates in ERA-40 by CP07 (their Table 1). This allows for any differences in the algorithms to be directly assessed and the hybrid methods accuracy in reanalysis data to be estimated (based on the subjective ‘Type Subject’ provided by CP07). SSW frequencies in ERA-40 reanalysis from the hybrid method are presented in Table 2.2 row 4. The hybrid method discards three dates identified by CP07 as violating the polar warming criterion and also identifies two central dates not captured by CP07. These two dates are close to a SSW which occurs earlier in the season (23 and 22 days prior) and are most likely removed as duplicates in the CP07 analysis. The overall frequency and standard error is similar to that of CP07, as one would expect. Event classification by the hybrid method is not in agreement with the CP07 algorithm for 7 events. Assuming the ‘Type Subject’ identified by CP07 is correct there are a total of 6 out of 25 events miscategorised by the hybrid method. The sample is small and these values are sensitive to the temporal boundaries used. However, it would appear that more algorithm development would be required to enable confident application of the hybrid method to reanalysis data.

To assess the hybrid algorithms accuracy in differentiating between splitting and displacement events in model data the daily evolution of the polar vortex PV field

---

<sup>3</sup>downloaded from <http://apps.ecmwf.int/datasets/data/era40-daily/levtype=pl/> between 1958 to 2002

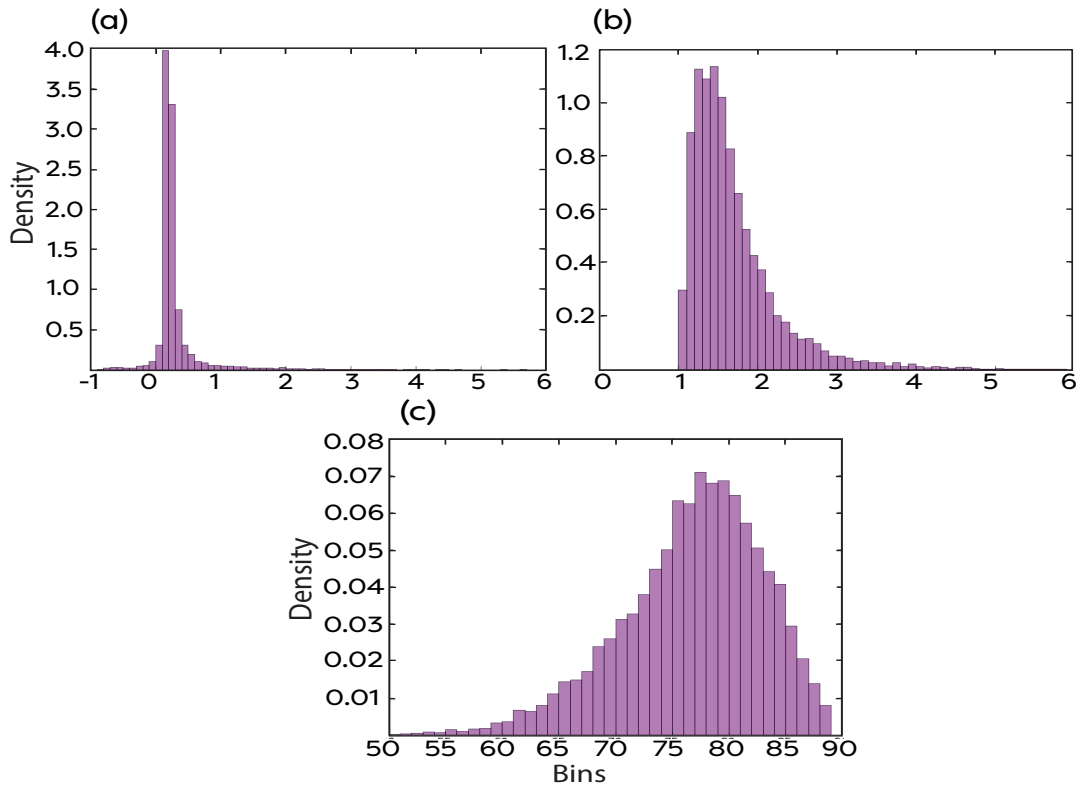


**Figure 2.3:** Histograms of moments diagnostic values in the IGCM version 3.1 over winter (DJFM) period for: (a) kurtosis, (b) aspect ratio (both dimensionless) and (c) centroid latitude ( $^{\circ}$ N). Bins are normalised to yield a total integral of one; thus being representative of a probability distribution function.

over the 20 days prior to and up until 20 days after the identified  $\bar{U}$  reversal is assessed. The 56 case studies are checked by eye to see if the algorithm accurately captures the splitting of the vortex or not.

Out of the 23 ‘splitting’ events one event contains only a partial separation of the vortex core and does not form two completely separate daughter vortices. The remaining 22 events all display a coherent splitting of the polar vortex. Out of the 33 ‘displacement’ events 5 events contain a splitting. These events are missed by the kurtosis parameter because one daughter vortex is considerably smaller than the other resulting in the kurtosis not dropping below the threshold value as the majority of PV is still distributed around the larger daughter vortex. This is a 10.7% error rate.

It is difficult to contextualise this error due to the lack of published error rates of SSW classification in the literature. The CP07 study does present a comparison of their algorithms classification of events in NCEP/NCAR and ERA-40 to the consensus of observed event classifications from the literature. Extrapolating from

their Table 1 it appears that the CP07 algorithm has a 9% error rate in classification for NCEP/NCAR and a 7% error rate in classification for ERA-40. However it is doubtful that these errors are robust due to the short period of reanalysis data available.

Overall it is likely that in IGCM data the hybrid method developed here will miscategorise 1 in 10 SSW events with the majority of these being splittings with one very small daughter vortex which are mislabelled as displacements.

## 2.5 Alternative Classification Techniques

Mitchell et al. [2011] showed that moment diagnostics behave in statistically significantly different manners during splittings and displacements and Hannachi et al. [2011] has developed a hierarchical clustering algorithm based upon moment analysis that can locate major SSWs. Could a criterion be set that captures splitting and displacement events more reliably than the kurtosis parameter method? Mitchell et al. [2011] found that aspect ratio is, on average, significantly larger for splitting than displacement events. The centroid latitude is statistically significantly lower, on average, for displacement events when compared to splitting events. It may be possible to set a threshold value for aspect ratio and centroid latitude to classify splitting and displacement events respectively.

Histograms are compiled of the moment diagnostics applied to the IGCM, Figure 2.3, over the entire winter period to assess their typical and extreme values. The values contained within bins are normalised so that the total area contained within the plot is equal to one and the histograms are representative of a probability density function.

It is observed that the moment diagnostics behave in a sensible manner by comparing the IGCM based mean values and standard deviation to that of diagnostics from ERA-40 presented in Mitchell et al. [2011] Figure 3. It is decided that, for aspect ratio and centroid latitude, threshold values will be set that are 2 standard deviations away for the mean value. This corresponds to a value of 2.8 for aspect ratio and 64°N for centroid latitude. The criteria that is applied to classify splitting and displacement events is:

- If the aspect ratio exceeds 2.8 in the 20 day period surrounding the  $\bar{U}$  reversal then the SSW event is a splitting. Otherwise the event is a displacement.
- If the centroid latitude becomes equatorward of 64°N in the 20 day period surrounding the central date then the SSW event is a displacement. Otherwise the event is a splitting.

An overview of the results from these binary classification procedures are presented in Table 2.4. The errors associated with using aspect ratio and centroid latitude as a binary classification tools are larger than that associated with kurtosis. It is clear that the use of aspect ratio and centroid latitude as a threshold based binary classification tool is inappropriate in the IGCM.

## 2.6 Alternative Identification Technique

At this juncture it is a useful academic experiment to remove the CP07 identification technique and use the moment diagnostics independently as an identification tool (as in M13 and in similar fashion to Seviour et al. [2013]). This would enable events to be located with no zonal averaging and may lead to more events captured which would help improve composite statistics.

An algorithm is developed to identify SSW events in the IGCM based solely upon the moment diagnostics of the winter (DJFM) polar vortex. Key issues in this algorithm development include; accuracy and sensitivity to threshold values, if any particular moment diagnostic is advantageous and if/how final warmings should be removed.

### 2.6.1 Threshold And Timespan Sensitivity

The moment diagnostics were run over the winter period in the IGCM 3.1 integration. Here the vortex edge is taken to be the spatial average poleward of  $45^{\circ}\text{N}$  on the winter climatology of PV.

To identify splitting events kurtosis and aspect ratio are used. The algorithm is developed so that a ‘splitting’ event is identified if the relative *threshold value* is exceeded for a minimum of  $n$  days, where  $n$  is the timespan prescribed. A ‘displacement’ event is identified if the centroid latitude remained equatorward of the *threshold value* for  $n$  days. For all identification algorithms the event date was

**Table 2.4:** Comparison of SSW classification due to different moment based binary classification techniques. The first column documents the procedure used. The number of splitting(displacement) events classified in column two(four) with the error in column three(five).

Diagnostic	Splittings	Error	Displacements	Error
Manually Checked	27	n/a	29	n/a
Kurtosis	23	1	33	5
Aspect Ratio	36	13	20	4
Centroid Latitude	23	10	33	14

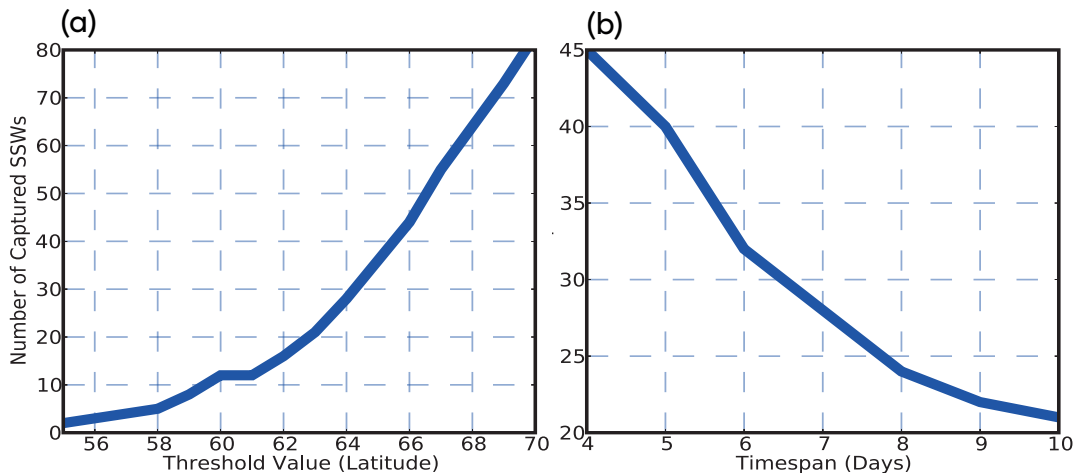


**Figure 2.5:** Sensitivity of centroid latitude algorithm in identifying SSW displacements: (a) The number of events captured with varying threshold values ( $^{\circ}N$ ) with timespan held at 7 days. (b) As in (a) but now with varying timespans with the threshold value held at  $64^{\circ}N$ .

recorded as the first day that the criteria was fulfilled and duplicates were removed if an event date existed within 20 days prior to it.

It is postulated that a complete set of SSWs can be presented by combining the identified displacement events with either the kurtosis or aspect ratio based splitting events. Algorithms are executed with varying timespans and threshold values. The number of SSWs captured is found to be sensitive to the threshold values implemented. An example of this sensitivity is displayed in Figure 2.5.

To proceed with analysis thresholds for aspect ratio and centroid latitude values are taken as 2 standard deviations from their mean winter value and timespans are taken to be 7 days. This period corresponds to the results in Mitchell et al. [2011] where composites of aspect ratio and centroid latitude for splitting and displacement events remained statistically significantly different for just over a week following event onset. The kurtosis threshold of -0.1 is retained as this is the value used by Matthewman et al. [2009]. A timespan of 5 days is implemented that is the length of time that kurtosis remained below -0.1 in the composite of splitting SSWs identified in ERA-40 in the study of Mitchell et al. [2011]. It is far from straightforward to come to an objective criteria for such SSW identification algorithms.

A further issue arises with final warming removal. An additional criterion of the moment diagnostic not satisfying the threshold for at least 10 consecutive days before April 30<sup>th</sup> was also introduced. This should represent a coherent re-establishment of the polar vortex and ensure that the event is not a final warming. Unfortunately up to half of the identified events did not satisfy this criteria and were

labelled as final warmings. This is either an inaccurate method or the moments are extremely biased to capturing final warmings. To preserve the dataset this moment based final warming criteria will not be implemented; after all it does not matter for this experiment if the event is a final or mid-winter warming. However, to allow for direct comparison to the hybrid method it was decided that the CP07 final warming criteria, see section 2.4, would be applied to filter out any final warmings that would have been removed in the original method.

### 2.6.2 Performance and Accuracy of Moment Identification Methods

The criteria implemented to identify SSWs are:

- A *displacement event* occurs if the *centroid latitude* remains lower than  $64^{\circ}\text{N}$  for at least 7 days. This isolates **20** displacement events.
- A *splitting event* occurs if the *aspect ratio* remains higher than 2.8 for at least 7 days. This yields a total of **27** splitting events.
- A *splitting event* occurs if the *kurtosis* remains lower than -0.1 for at least 5 days. This yields a total of **17** splitting events.

Duplicates are removed if an event date occurred within 20 days of a preceding event and it is found that the number of events removed is not sensitive to this time period. The identified splitting and displacement events are combined to form a total set of SSWs. The resulting sets are compared directly to the hybrid algorithm in Table 2.6.

The accuracy of the methods is once again analysed by checking the evolution of the 850  $\theta$  PV field 20 days around the identified event date. Five splitting events located by the aspect ratio algorithm do not split. One event located by the kurtosis algorithm does not displaying a coherent separation of the polar vortex. For the centroid latitude algorithm 4 out of the 20 identified ‘displacement’ events display a splitting that is not captured by the other algorithms.

Interestingly the aspect ratio and kurtosis method only agree for 10 splitting events. Overall, the kurtosis method is more accurate than aspect ratio but captures less events and is biased to events occurring in March. The fact that there is a low level of agreement between the two methods appears to render it inappropriate to try and combine them into one identification algorithm.

### 2.6.3 Conclusions

Overall the moment diagnostics are capable of independently capturing SSWs. Displacement events can be located using the centroid latitude diagnostic and splitting

**Table 2.6:** Performance of different moment based SSW identification algorithms. For algorithm details see text.

	Binary Kurtosis	Centroid/Aspect	Centroid/Kurtosis
Total SSW Events	56	47	37
Displacement Events	33	20	20
Split Events	23	27	17
Error	10.7%	19.1%	13.5%

events can be identified using aspect ratio or kurtosis. The total number of events captured appears to be sensitive to the configuration of the algorithm and biased to late winter events. It is very difficult to find an objective moment based algorithm for SSW identification.

The originally proposed hybrid method, section 2.4, identifies the most events and has a low error rate (see Table 2.6). This method will be implemented hereafter for identifying and classifying SSWs. This will also allow investigation into the apparently contradictory results discussed in section 2.3.3.

## 2.7 Conclusions

Isolating and classifying SSW events is by no means a straightforward task. There are many different methodologies outlined in the literature that can be utilised, all with their own strengths and weaknesses. Here a straightforward and computationally efficient algorithm is presented and motivated by previous studies. It is found that in utilising a hybrid method ( $\bar{U}$  based identification of events and moment analysis based classification) the algorithm successfully locates SSWs and has an error rate similar to that of the CP07 method and better than other algorithms using moment based identification techniques. The choice of a kurtosis based threshold is simplistic but dynamically meaningful and the majority of the error associated with the hybrid algorithm is a result of splitting events being missed by kurtosis due to one daughter vortex being considerably smaller than the other.

The hybrid method is suitable for isolating and classifying SSW events in an intermediate general circulation model and will be used hereafter for capturing SSWs in model data. Once SSWs are isolated their impact on and interactions with other components of the climate system can be analysed, as is conducted in Chapters 4, 6 and 7.

As a reference the hybrid methods steps consist of:

Hybrid Method Identification (CP07 based)

1.  $\bar{U}$  extracted as a daily average at 10 *hPa* and 60°N.
2. Central dates identified where  $\bar{U} \leq 0$  during DJFM.
3. Duplicates within 20 day period removed.
4. Final warmings identified and removed. Identified by no consistent return to westerly flow for 10 consecutive days before April 30<sup>th</sup>.
5. Events with no polar warming removed. Identified when the area-weighted average temperature between 70-90°N is cooler than 50-70°N.

Hybrid Method Classification (moment analysis based)

1. Moment analysis (Appendix A) performed over polar Ertel's potential vorticity on the 850  $\theta$ -level for the 20 day period surrounding the identified central date.
2. Splitting events located when the kurtosis reaches a -0.1 threshold [Matthewman et al., 2009]. Central date set as the date when the kurtosis threshold is initially satisfied.
3. If the kurtosis remains above -0.1 the event is classified as a displacement.



## Chapter 3 - General Circulation Models

*Portions of this Chapter also appear in the paper ‘IGCM4: a fast, parallel and flexible intermediate climate model’ by Joshi et al. and was published in the Journal of Geoscientific Modelling Development in April 2015 under a creative commons license (CC-BY).*

### 3.1 Introduction

To understand climate dynamics and atmosphere-ocean coupling a multitude of different sources of information types can be accessed. This includes, but is not limited to: observations, numerical model simulations, direct analytical solutions for simplified mathematical concepts and a hybrid of numerical model solution with assimilated observational fields (reanalysis). All methods have their particular strengths and weaknesses, observational data may be seen as a strong candidate for understanding Earth’s climate system but data sets often span limited temporal periods are limited in geometric space and can contain errors from problematic calibration or instrument accuracy.

A popular way to simulate the climate system and to aid scientific understanding is to numerically solve the governing set of equations for climate, the primitive equations, with appropriate boundary conditions and numerical methods. A primitive equation set is presented in Table 3.1 as presented in Andrews et al. [1987]. Only a basic breakdown of this simple set of primitive equations is provided, see Andrews et al. [1987] for complete description and presentation in other coordinate systems. This set is formulated using Cartesian coordinates in the horizontal plane, which encapsulates the large scale fluid dynamics on the Earth without being encumbered by complications introduced from the spherical coordinate system. It is often easier to work in log-pressure coordinates ( $z$ ) than with geometric height ( $z^*$ ) in the atmosphere, due to the fact that this simplifies the momentum equation via the removal of an inverse density term. In Table 3.1 the terms are: three dimensional velocity  $\vec{U}$  such that  $\vec{U} = (u, v, w)$ ;  $\vec{V}$  the two dimensional horizontal velocity such that  $\vec{V} = (u, v)$ ;  $\Phi$  is the geopotential;  $\vec{X}$  is nonconservative horizontal mechanical processes/friction;  $\rho$  is density with  $\rho_0$  a reference density profile;  $z$  represents the log-pressure height scale;  $f$  is Coriolis force;  $H$  is reference height scale;  $R$  is the ideal gas constant;  $T$  is temperature and  $\theta$  is the potential temperature. The material derivative is defined as  $\frac{D}{Dt} = \frac{\partial}{\partial t} + \vec{V} \cdot \nabla$  and is interpreted as the rate of change of a fluid parcel following its flow. In the thermodynamic equation  $Q$  is the

**Table 3.1:** Primitive equation set in Cartesian horizontal coordinates and log-pressure vertical coordinate following Andrews et al. [1987].

Name	Equation
Horizontal Momentum Eq.	$\frac{D\vec{V}}{Dt} + f(\vec{k} \times \vec{U}) = -\nabla\Phi + \vec{X}$
Hydrostatic Balance	$\frac{\partial\Phi}{\partial z} = H^{-1}RT$
Continuity of Mass	$\frac{\partial}{\partial x}(u) + \frac{\partial}{\partial y}(v) + \rho_o^{-1} \frac{\partial}{\partial z}(w\rho_o) = 0$
Thermodynamic	$\frac{D\theta}{Dt} = Q$

adiabatic heating term.

The momentum equation represents how the material rate of change of momentum in the horizontal plane is a result of Coriolis force, pressure gradient force along with frictional and non-conservative terms. To a rough first approximation in the mid-latitudes scale analysis for synoptic systems<sup>4</sup> lead to scale analysis leads to the first term and last terms being negligible (order  $10^{-4}$  and  $10^{-12}$  respectively) when compared to the pressure gradient and geostrophic terms (both of order  $10^{-3}$ ), resulting in a steady state geostrophic flow. In the midlatitudes this approximate geostrophic wind is often within 15% of the observed large scale flow [Martin, 2006]. Under accelerating, equatorial or non-conservative fluid flow the ageostrophic wind is an important component and cannot be neglected. For example, following Holton [2004] in a spherical coordinate system the full form of the momentum equation in the  $y$ -direction is

$$\frac{Dv}{Dt} + \frac{u^2 \tan \phi}{a} + \frac{vw}{a} = \frac{\partial\Phi_y}{\partial y} - fu + \vec{X}_y$$

①
②
③
④
⑤
⑥

For notational simplicity  $x$  and  $y$  now represent eastward and northward distance (note we are no longer in Cartesian coordinates) where  $Dx = a \cos(\phi)D\lambda$ ,  $Dy = aD\phi$  with the spherical coordinates such that  $\phi$  is latitude and  $\lambda$  is longitude. In this  $a$  is the radius of the Earth and terms involving this are denoted as curvature

<sup>4</sup>following Holton [2004] the scale analysis approximations are: horizontal velocity  $\sim 10 \text{ m s}^{-1}$ , vertical velocity  $\sim 1 \text{ cm s}^{-1}$ , length  $\sim 10^6 \text{ m}$ , depth scale  $\sim 10^4 \text{ m}$ , horizontal pressure fluctuation scale  $\sim 10^3 \text{ m}^2 \text{ s}^{-2}$ , time scale  $\sim 10^5 \text{ s}$ .

terms and arise from the spherical coordinate system. Subscript  $y$  denotes a vector term in the  $y$ -direction. It is interesting to note that along with the geostrophic balance outlined above a variety of other steady-state flows can be achieved [Martin, 2006]. Terms 3 and 6 are both typically small for synoptic scale mid-latitude systems, of order  $10^{-8}$  and  $10^{-12}$  respectively. When the centrifugal force (term 2 above) balances pressure gradient force (term 4) the result is cyclostrophic wind, where circular fluid motion has pressure gradient force directed in towards the center and this is balanced by an outward centrifugal force. This balance commonly holds for large Rossby number scenarios, such as tornadoes. Inertial flow can occur for motions under weak pressure gradient force, here the centrifugal force (term 2) balances the Coriolis force (term 5). For inertial flows the motion is typically anticyclonic and small scale. Overall a variety of flow dynamics, far more than is discussed here, can be modelled using the primitive equation set, which depend on the scales of interest and complexity of retained terms.

Within the group of general circulation models a hierarchy exists in the sense that general circulation models (GCMs) that solve the primitive equations vary greatly in complexity and computational demand. More complex models for the atmosphere typically strive to include detailed climatic features above and beyond what the primitive equations capture. This is typically achieved via offline routines and inclusion of other numerical models which can simulate features such as: interactive chemistry; glacial fields; groundwater; interactive ocean dynamics; complicated chemical processes; and so on, in an attempt to realistically simulate what is experienced on Earth. The issue is that, in running such complicated simulations there is a high computational demand, integrations take longer to complete (often resulting in shorter/fewer simulations) and it can be difficult to separate out different climatic processes. Intermediate models that resolve the primitive equations but neglect certain, more complex, climatic features often have lower computational demand. This enables long integrations and multiple simulations to be obtained more readily (often resulting in better statistics and hypothesis testing) at the sacrifice of processes which may prevail in Earth's climate system.

Here an intermediate atmosphere-only general circulation model, the IGCM4, is presented and its climatology analysed. The IGCM4 provides a good testing ground for various hypotheses, the relative ease in which long simulations can be performed enables appropriate numbers of SSWs to be captured and for their impacts on the surface climate to be assessed, as conducted in Chapter 4. The IGCM4 also utilises prescribed sea surface temperatures (SSTs), as outlined in section 3.3.1, making it well suited for assessing the impacts of various SST climatologies, or particular persistent SST anomalies, on climate as is achieved in Chapter 6 and section 7.3.

The IGCM4 also has the benefit of being coupled to an interactive ocean model, the modular ocean model array processor version (MOMA) as described in section 3.4.1. This enables comparison of climatologies and SSW simulation in coupled and uncoupled models that have the same atmospheric component. This facilitates direct traceability to the impacts of an interactive ocean model on atmosphere simulation, as in conducted in Chapter 7.

For completeness a quick, generalised outline of the numerical methods utilised in the IGCM4 and MOMA are presented in section 3.2. Technical details of the IGCM4 are presented in section 3.3 with its climatology and SSW simulation assessed. MOMA and its coupling to the IGCM4 is briefly discussed in section 3.4 with the coupled model being analysed in detail in Chapter 7

## 3.2 Numerical Methods

Finite difference schemes approximate a solution to a function locally by utilising the definition of a derivative and Taylor series expansion. The rate of convergence of the approximation can be determined by comparison to Taylor series, this is called the *order* of the scheme. Finite differences are useful for solutions on grids with irregular domain boundaries such as the ocean.

A key note is that when applying finite differences to equations which have a wave type solution, such as the momentum equations in the primitive equation set, then the Courant, Friedrichs and Lewy (CFL) criterion must be considered [Washington and Parkinson, 2005]. The wave will be stable only if  $|\frac{c\Delta t}{\Delta x}| \leq 1$ , where  $c$  is the wave speed,  $\Delta t$  is the time-step and  $\Delta x$  is the spatial step. Issues occur at high latitudes where the spatial step becomes increasingly small resulting in the need for smaller and smaller time-steps for stable solutions.

Other issues with the finite differences, when applied to the primitive equations, include phase error with wave speeds being underestimated [Washington and Parkinson, 2005]. This error can be reduced by including more gridpoints; often eight gridpoints per wave is seen to combat this. When using a centered scheme problems can occur due to oscillations between even and odd time-steps leading to a separation in these solutions.

The spectral method is particularly suited to spherical coordinate systems where solutions are found on a global basis via spherical harmonics. This makes the method more computationally efficient when compared to finite differences with errors being introduced from the truncation of the spherical harmonics. Due to horizontal atmospheric levels being spherical with no physical boundaries (on  $\sigma$ -levels, see section 3.3.1) this results in the horizontal momentum equation being

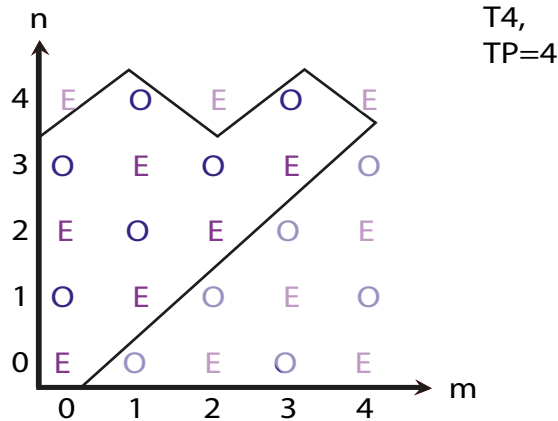


**Figure 3.2:** Example of  $T_4$  jagged triangular truncation ( $TP = 4$ ) for spherical harmonic solution. Odd and even terms denoted by ‘O’ and ‘E’ respectively. Non-opaque terms within the black lines are retained.

particularly well suited to the spectral method. Bourke [1972] provides a thorough explanation of the application of the spectral method to the primitive equations. Here a general outline of their paper is presented.

The equations of interest, the primitive equations, need to be presented in a suitable form to allow spectral method application. The variables should be represented as scalars to allow for straightforward representation in spherical harmonics. Particularly the momentum equation (e.g. see Table 3.1 row 1) is manipulated into a prognostic equation comprising of horizontal vorticity,  $\xi$  and divergence,  $D$ , via vector calculus manipulations.

Once equations for  $\frac{D}{Dt}(\xi)$  and  $\frac{D}{Dt}(D)$  are derived they can be presented in terms of scalars by the introduction of  $\psi$ , the stream function, and  $\chi$ , the velocity potential. Helmholtz’s theorem,

$$\vec{V} = (u, v) = (\vec{k} \times \nabla\psi) + \nabla\chi \quad (3.1)$$

allows for derivation of the relationships  $\xi = \nabla^2\psi$  and  $D = \nabla^2\chi$ . This is substituted into the momentum equation and solutions can be found in terms of the scalars  $\psi$  and  $\chi$ . This solution can then be represented in terms of  $\xi$  and  $D$  or  $u$  and  $v$  (via Equation 3.1), whichever is more appropriate.

Now that the equations of interest are represented in terms of scalars, namely  $\psi$  and  $\chi$ , the spectral method can be applied. The variables are assumed to take the form of orthogonal spherical harmonics. A suitable horizontal spectral representation, for variable  $X$ , takes the form

$$X(\mu, \lambda) = \sum_m \sum_n X_n^m P_n^m(\mu) e^{im\lambda} \quad (3.2)$$

where  $\lambda$  is the longitude and  $\mu = \sin(\phi)$ , where  $\phi$  is latitude.  $X_n^m$  is the time dependent expansion coefficient which needs to be calculated.  $P_n^m(\mu)$  is the first type Legendre polynomial providing a solution for the Laplacian operator when expanded in spherical coordinates. For feasible numerical calculation summations must be finite, so a truncation must be applied with maximum wavenumber given as the truncation parameter,  $TP$ . The IGCM4 uses a triangular truncation where  $TP \geq n \geq m$ , the even terms on the maximum retained  $n$  are discarded to enable the same number of odd and even terms to remain, see Figure 3.2 for an example.

The equations are resolved by the substitution of the spectral representations of scalar variables. This is only non-trivial for non-linear terms. As shown by Orszag [1970] non-linear terms are tackled by transforming each separate component onto a two-dimensional spatial grid. The computed gridpoint values are then multiplied and transformed back into spectral space. To do this the gridpoint values are represented as truncated Fourier series at each latitude with the Fourier coefficients being derived using the fast Fourier transform. These Fourier series, representing the non-linear products, are then substituted back into the prognostic equations and the solution is integrated forward in time.

### 3.3 The IGCM4

#### 3.3.1 Technical Configuration

The IGCM4 is an intermediate model with lineage descending from the ‘‘Reading IGCM’’ models. It is based upon the dynamical core of Hoskins and Simmons [1974], general programme description is provided by Blackburn [1985] and version 4 is presented in Joshi et al. [2015] where technical model details are provided. Here only a breakdown of the most relevant information is provided.

The stratosphere resolving version of the IGCM4 is employed. This has a model lid at 0.1 *hPa* and 35 vertical  $\sigma$  levels (where  $\sigma$  is a vertical coordinate system such that  $\sigma = \frac{P}{P_0}$ ,  $P$  is pressure and  $P_0$  is surface pressure) and assumes hydrostatic balance. There are 3  $\sigma$  levels above 1 *hPa*, 13 in the stratosphere and 19 in the troposphere, see Table C2 in Appendix C. A new feature of the fourth version is parallelisation of the model code, which enhances computational efficiency. As reported in Joshi et al. [2015] running with a 15 minute time-step across 32 processors yields approximately 75 years of model data in 24 hours.

To numerically solve the primitive equations presented in Hoskins and Simmons

[1974] the model utilises finite differences in the vertical and the spectral method in the horizontal with jagged-triangular truncation at wavenumber 42 (T42). The model utilises a semi-implicit time-step as discussed in Hoskins and Simmons [1974], which increases stability and allows for a longer time-step when compared to explicit time-step discretisation. The horizontal grid has 64 latitudinal and 128 longitudinal points, approximately a  $2.8^\circ$  grid cell.

SSTs are prescribed as climatologies of monthly means based upon ERA-40 reanalysis [Forster et al., 2000]. Surface temperature over land evolves freely and there are 8 distinct surface types (ice, inland water, forest, grassland, agriculture, tundra, swamp and desert) all with relative albedos and roughness length scales. Simple snow and soil moisture routines are included. Sea ice forms for oceanic grid points with temperate less than  $-2^\circ\text{C}$  and melts at  $0^\circ\text{C}$ . Between  $0^\circ\text{C}$  and  $-2^\circ\text{C}$  there is linear interpolation of surface values (albedo, roughness length scale, saturated vapor pressure) between the open water and sea ice to avoid spurious jumps in these values. Surface wind stress ( $\vec{\tau}$ ) is calculated using a Richardson number dependent bulk aerodynamic formula, assuming a no-slip condition at the surface, as presented in Forster et al. [2000]

$$\vec{\tau} = -C_D \rho \vec{V} \|\vec{V}\| + 3 \quad (3.3)$$

where  $C_D$  is the drag coefficient and is 0.001 in the IGCM4. In the above bulk-aerodynamic formula the term 3 represents  $3 \text{ m s}^{-1}$  and is a ‘gustiness factor’ to account for sub-grid scale processes that lead to surface wind stresses.

The Morcrette radiation scheme [Zhong and Haigh, 1995] is used and ozone is prescribed as a fixed climatology of monthly means from Li and Shine [1995]. In the model  $\text{CO}_2$ ,  $\text{CH}_4$ ,  $\text{N}_2\text{O}$ , CFC-11 and CFC-12 are radiatively active species that are assumed to be well mixed throughout the model domain.  $\text{H}_2\text{O}$  is advected beneath the seasonal tropopause and above this is parameterised by the oxidation of methane added to a background value of  $3 \text{ ppmv}$ . Standard configuration mixing ratios are set as:  $360 \text{ ppmv}$  for  $\text{CO}_2$ ,  $1.72 \text{ ppmv}$  for  $\text{CH}_4$  and  $314 \text{ ppbv}$  for  $\text{N}_2\text{O}$ , and 0 for CFCs. The values are all easily altered when running the model. The current configuration is representative of an late 20<sup>th</sup> century climate with fixed SSTs and ozone.

In the IGCM4 there is a simple inclusion of gravity wave drag based upon Lindzen [1981] which conserves angular momentum. There is one orographic gravity wave mode with an initial amplitude equal to the lowest model level wind multiplied by standard deviation of sub-grid scale topography. There are two non-orographic gravity wave modes with initial amplitudes equal to the lowest model level wind

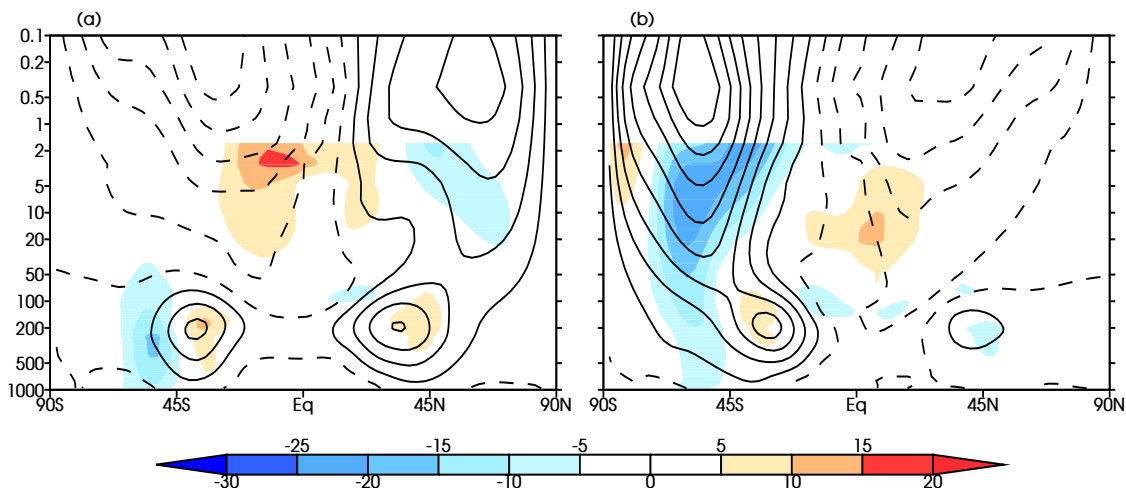


**Figure 3.3:** IGCM4  $\bar{U}$  ( $m s^{-1}$ ) climatologies for: (a) DJF and (b) JJA. IGCM4 minus ERA-40 in solid colours. Total IGCM4 field in contour lines. Contour interval of  $10 m s^{-1}$ . Solid contours for positive values, zero and negative values dashed.

multiplied by  $90m$  (a tunable parameter), phase speeds are the lowest model level wind  $\pm 10 m s^{-1}$ . The magnitude of the profile of deceleration between the breaking level (dependant on initial wave amplitude) and the critical level is a tunable parameter which is set to 1.2 in the IGCM4. The gravity wave drag has been tuned so that the climatological zonal mean zonal wind profile is similar to that in NCEP/NCAR, with a particular focus on the Northern Hemisphere westerly wind structure during winter. At the upper most model levels a cubic drag is applied to ensure there is no spurious wave reflection at the model lid, satisfying the no-normal flow and no-slip boundary condition here.

The remainder of this section presents the climatological state of the IGCM4 from a 200 model year integration. This simulation provides the data analysed in Chapters 4 and 5 and used as a control data set in Chapters 6 and 7.

### 3.3.2 Climatological Assessment

To provide insight into the average behaviour of large scale atmospheric features climatologies of  $\bar{U}$  are created for December to February (DJF) and June to August (JJA), this is compared to 44 years of ERA-40 data (spanning 1958 to 2002) with results presented in Figure 3.3. Overall IGCM4 climatological  $\bar{U}$  is in agreement with the reanalysis data. The largest differences to ERA-40 occur in the southern hemisphere (SH). In DJF (panel (a)) the SH tropospheric jet is slightly equatorward and in JJA (panel(b)) the SH midlatitude zonal winds are more easterly. The latter feature could potentially be caused by the simplicity of the gravity wave drag

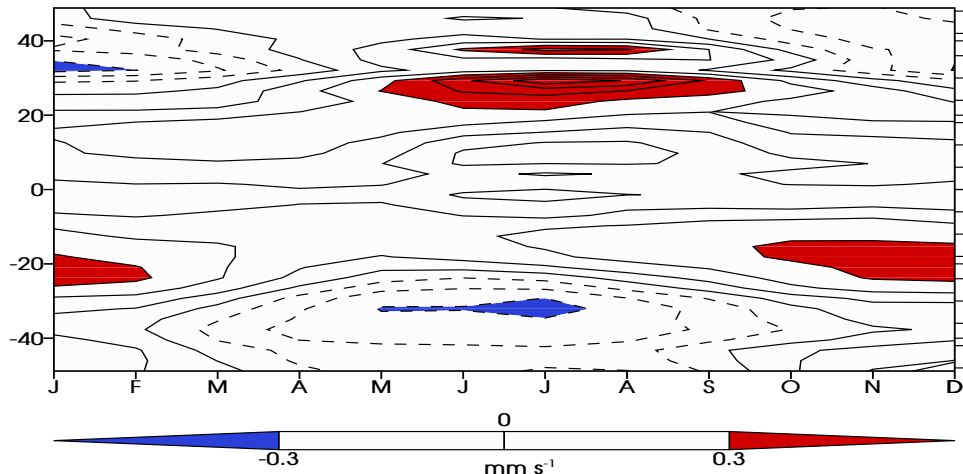


**Figure 3.4:** Mean residual vertical velocity in  $\text{mm s}^{-1}$  at  $74.63 \text{ hPa}$ . Calculated as a daily climatology from IGCM4 data. Month labelled on x-axis, latitude in degrees North on y-axis. Contour intervals of  $0.1 \text{ mm s}^{-1}$ , negative values dashed.

scheme. In DJF the magnitude of Northern Hemisphere (NH) stratospheric westerly winds are closer to reanalysis, displaying reasonable behaviour of the gravity wave and Rossby wave drag that modulates the flow here. The NH winter tropospheric jet is stronger on the poleward flank. Over the equator in the stratosphere there are perpetual easterlies most likely due to the lack of QBO in this intermediate model. This is not particularly surprising since it is well known that general circulation models struggle to simulate the QBO without careful consideration of the parameterisation of nonorographic gravity waves [Scaife et al., 2000].

As with some features of the zonal wind profile the residual mean meridional circulation, the ‘Brewer-Dobson circulation’ is a wave-driven circulation. Butchart [2014] provides a complete review of the history, driving mechanisms and features of this circulation. The Brewer-Dobson circulation consists of a shallow cell of upwelling (from the troposphere into the lower stratosphere) over the equator, poleward transport and sinking in the polar regions. There is a deeper cell from the upper stratosphere into the mesosphere with upwelling in the summer hemisphere, transport across the equator and sinking near to the winter pole. The circulation, away from the equator, is controlled by wave drag from dissipating upwardly propagating waves. For the shallow branch (from the troposphere into the lower stratosphere) upwardly propagating planetary-scale Rossby waves deposit easterly momentum, to conserve angular momentum there is rising over the equator and poleward transport of air masses. The deeper branch (from the upper stratosphere into the mesosphere) consists of transport from the summer to winter hemisphere poles, in this branch the forcing is dominated by momentum deposition from gravity waves in the mesosphere, with their phase speed being filtered by the underlying

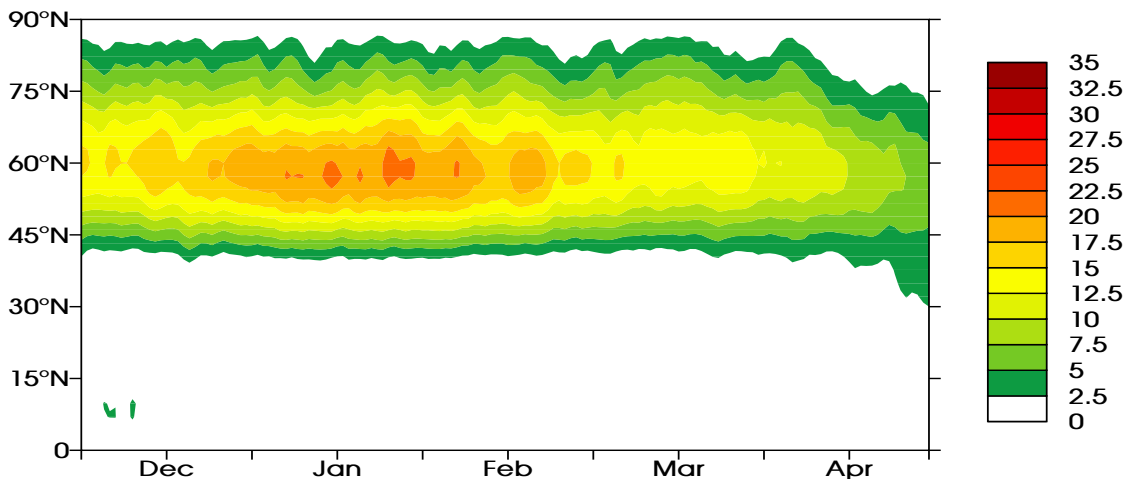


**Figure 3.5:** Climatological meridional heat flux ( $\overline{v'T'}$ ) in  $K m s^{-1}$  at 100 hPa. Calculated as a daily climatology from IGCM<sub>4</sub> data, designed to be comparable to Figure 2 in Charlton et al. [2007].

stratospheric winds. In the winter hemisphere the stratospheric westerly  $\overline{U}$  structure leads to only easterly gravity wave acceleration in the mesosphere, resulting in a net poleward transport to conserve angular momentum. In the summer hemisphere stratospheric easterlies lead to only westerly gravity wave acceleration in the mesosphere and a net equatorward transport. In the IGCM4 the vertical residual mean meridional circulation is assessed at one atmospheric level.

The vertical residual mean meridional circulation component is formulated as in Andrews et al. [1987] at 74.63 hPa and presented in Figure 3.4. There is a local maximum in upwelling in the summer subtropics with the boundary between upwelling and downwelling being seasonally displaced by appropriately 20°. This is within the envelope of model behaviour as presented in Butchart et al. [2006] and displays that the IGCM4 is simulating the meridional mass residual circulation as well as other models.

The meridional heat flux ( $\overline{v'T'}$ ) in  $K m s^{-1}$  at 100 hPa is a proxy for the vertical component of the Eliassen-Palm flux. Multi-model comparisons of this field are provided by Charlton et al. [2007] (their Figure 2) and Figure 3.5 is directly comparable to their results. This field is useful because the Eliassen Palm Flux, under a transformed Eulerian mean framework (as discussed by Andrews et al. [1987]) is a vector field that has vertical and meridional components which can be interpreted as planetary wave activity with its divergence completely representing eddy acceleration on mean flow. Thus Figure 3.5 provides a representation of the seasonality of planetary wave activity entering the stratosphere. The peak strength of  $\overline{v'T'}$  is just over 20  $K m s^{-1}$  and occurs in late January. The timing is consistent with NCEP/NCAR reanalysis and slightly lower in magnitude.  $\overline{v'T'}$  is largest in the

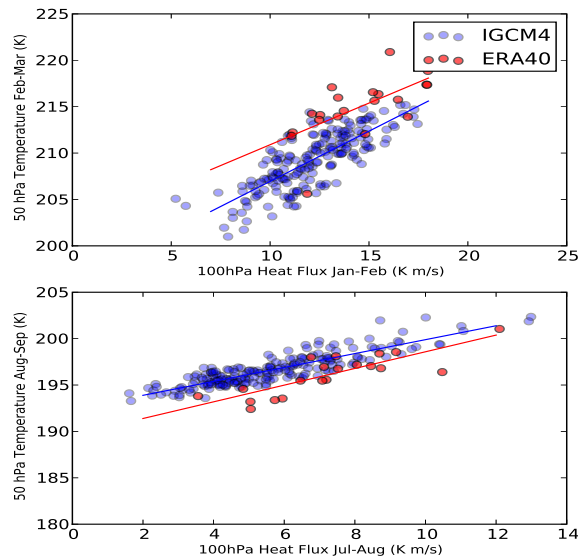


**Figure 3.6:** Scatter plots comparing average 100 hPa  $\overline{v'T'}$  to average polar cap temperature for IGCM4 (blue) and ERA-40 (red). Top panel compares 100 hPa  $\overline{v'T'}$  averaged between  $40^\circ\text{N}$  and  $80^\circ\text{N}$  over January-February months to 50 hPa temperature averaged poleward of  $60^\circ\text{N}$  over the following February-March months. Bottom panel compares the same fields but for the southern hemisphere, July-August meridional heat flux is compared to August-September polar cap temperature.

midlatitudes, centered around  $60^\circ\text{N}$ , also in good agreement with NCEP/NCAR. Early and late winter wave activity is slightly suppressed in IGCM4 when compared to reanalysis but well within the behaviour of models presented in Charlton et al. [2007]. Overall this field compares well with other models and NCEP/NCAR reanalysis, displaying a good level of wave activity entering the stratosphere.

To test the IGCM4's stratospheric sensitivity to planetary scale wave breaking a scatter plot is created comparing average winter 100 hPa  $\overline{v'T'}$  and comparing this to 50 hPa temperature. This is created following Eyring et al. [2006] and presented in Figure 3.6 along with ERA-40 data (from 1980 to 1999, as in Eyring et al. [2006]) for direct comparison, NH/SH results are in top/bottom panel.

As would be expected, increased heat flux is followed by warmer average stratospheric temperatures. The sensitivity of the stratosphere to heat flux in both hemispheres is similar to the behaviour in ERA-40. For NH winter the polar cap temperature is on average lower than in ERA-40, a feature that could be related to the prescribed ozone. This 5-10 K difference is within the range of model biases presented in Eyring et al. [2006].

The geopotential height eddy field at 500 hPa is presented in Figure 3.7. This represents the typical NH winter standing wave pattern in the mid-troposphere

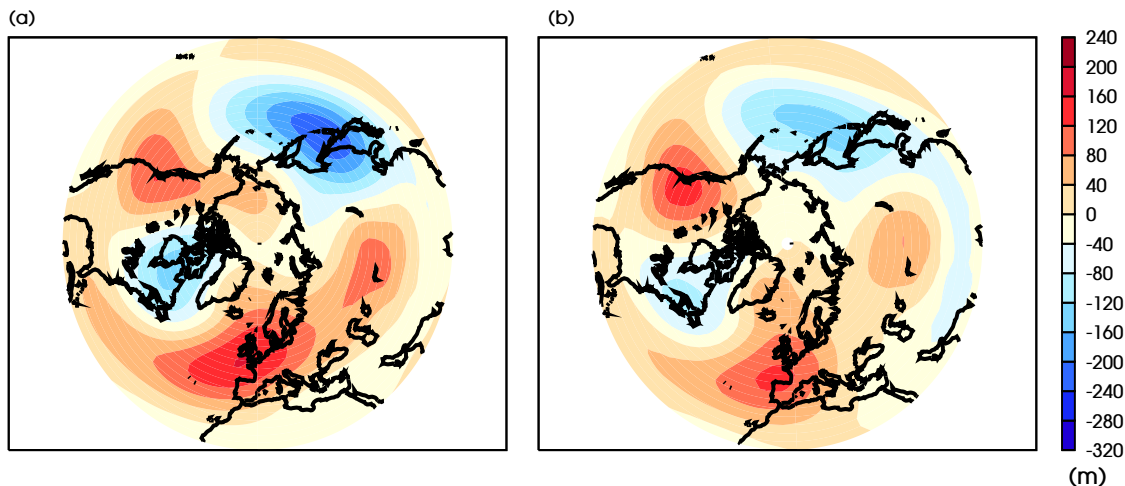


**Figure 3.7:** DJF geopotential height eddy field ( $m$ ) at 500  $hPa$  for: (a) 44 years of ERA-40 data (1958-2002) and (b) 200 years of IGCM4 data.

and provides a two dimensional representation of the tropospheric structure in the IGCM4. The overall standing wave structure is similar between ERA-40 and the IGCM4 with local maxima and minima being coherent in space between the two datasets but variable in magnitude. Particularly the IGCM4 has weaker local minima over the Eastern Pacific and a stronger local maximum over the Western Pacific. Over the Atlantic the strength of the eddy field is more similar to reanalysis, with the overall structure being slightly weaker in the IGCM4. Similarly, the local maximum over Eurasia is weaker in the IGCM4.

Blocking is an important atmospheric phenomenon which leads to the stagnation of weather patterns, resulting in the persistence of weather types over a region [Tibaldi and Molteni, 1990, Berckmans et al., 2013a]. Simulation of this phenomenon is important for accurate forecasting and understanding of the climate system. It is often found that general circulation models can struggle with the simulation of blocking. As discussed by Scaife et al. [2010] this is often attributed to coarse horizontal resolution leading to a lack of small scale eddies that can maintain the blocked weather patterns; however they also demonstrated that biases in the climatological state of a model attribute to issues in blocking simulation. It is likely that improvements in blocking at high resolutions are due to a combination of improved mean state and small scale eddy simulation.

Blocking is formulated on a daily basis over the NH following the Tibaldi and Molteni [1990] definition, utilising the geopotential height ( $m$ ) at 500  $hPa$ . The percentage of blocked day at each longitude over the DJF period is then created and compared to the same metric formulated for NCEP/NCAR reanalysis data (50 years of data downloaded from 1957 to 2006) and presented in Figure 3.8. Overall

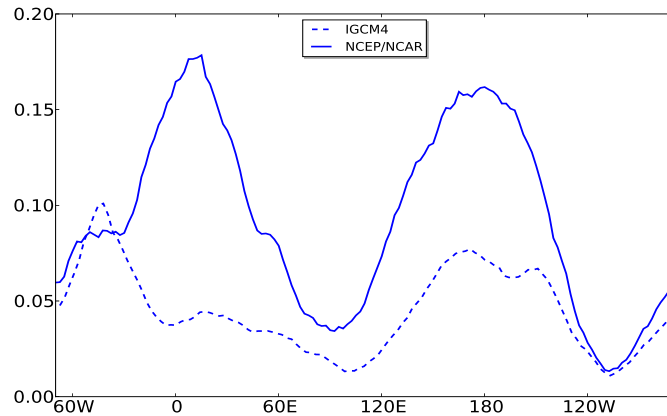


**Figure 3.8:** Percentage of ‘blocked days’ as a function of longitude for the IGCM4 (dashed) and NCEP/NCAR reanalysis (solid). Calculated from daily DJF data in the Northern Hemisphere.

the frequency of ‘blocked days’ in the IGCM4 is lower than when compared to reanalysis. The peak in blocking over the Atlantic is more westward in the IGCM4. Over the Pacific the longitudinal structure is more coherent between the model and reanalysis, but underestimated in the IGCM4. This behaviour is not altered upon subdivision of IGCM4 data into shorter temporal periods. Improvements in blocking could be attained by further model development; areas of focus could include improving the mean state [Scaife et al., 2010] along with the horizontal resolution and orography [Berckmans et al., 2013b].

### 3.3.3 SSW Simulation

In the 200 years of IGCM4 data SSWs are identified and classified following the hybrid approach outlined in section 2.4. To assess the model’s ability to simulate these events the benchmarks of CP07, created from NCEP/NCAR reanalysis, are utilised. The benchmarks of interest are formulated for the entire set of SSWs, and the splitting and displacement subclasses, with results presented in Table 3.9. Black values correspond to the IGCM4 and blue values to the CP07 benchmarks. The diagnostics evaluated in the IGCM4 are:

1. SSW frequency: in total number of events per year.
2.  $\Delta T_{10}$ : 10 hPa polar cap temperature anomaly (K). Area-weighted average between 90°N and 50°N. Temporal average 5 days around the central date. This gives an indication of the magnitude of average event strength in the middle stratosphere.

**Table 3.9:** Modelling benchmarks outlined in Charlton and Polvani [2007] (CP07) applied to the IGCM4 200 year simulation. Black font represents IGCM4 statistics. Blue font represents the CP07 benchmarks. Standard error in parenthesis. For benchmark definitions see text.

Benchmark	All SSW	Vortex displacement	Vortex splitting
Frequency	0.57(0.05) 0.6 (0.1)	0.33(0.04) 0.33 (0.07)	0.24(0.03) 0.27 (0.07)
$\Delta T_{10}$	4.93(0.27) 7.4 (0.8)	4.67(0.35) 6.8 (1.2)	5.28(0.40) 8.1 (1.1)
$\Delta T_{100}$	1.89(0.08) 2.0 (0.3)	1.86(0.11) 1.7 (0.4)	1.93(0.12) 2.4 (0.3)
$\Delta U_{10}$	20.21(0.73) 26.2 (1.8)	19.59(0.95) 22.5 (2.0)	21.05(1.14) 30.9 (2.5)
$\overline{\Delta v'T'}_{100}$	7.07(0.41) 8.5 (1.0)	6.65(0.66) 8.6 (1.4)	7.64(0.51) 8.2 (1.4)

3.  $\Delta T_{100}$ : 100 hPa polar cap temperature anomaly (K). Area-weighted average between 90°N and 50°N. Temporal average 5 days around the central date. This gives an indication of whether coupling processes between the middle and lower stratosphere are adequate.
4.  $\Delta U_{10}$ :  $\bar{U}$  ( $m s^{-1}$ ) at 60°N and 10 hPa, 15–5 day average prior to the central date minus 0–5 day average after the central date. This represents the magnitude of average  $\bar{U}$  deceleration.
5.  $\overline{\Delta v'T'}_{100}$ : meridional heat flux ( $K m s^{-1}$ ) at 100 hPa averaged 20–0 days before the central date and between 45°N and 75°N. This is a proxy for the average upward wave propagation proceeding SSWs, a reasonable magnitude should be observed if events are being driven by upwardly propagating planetary-waves.

SSW frequencies are all well within the modelling benchmarks. Statistical testing of the SSW frequency and type as outlined in Appendix A and B of Charlton et al. [2007] leads to the null hypotheses of ‘The mean frequency of SSWs in the GCM and NCEP–NCAR reanalysis is equal’ and ‘The frequency distributions of vortex displacement and splitting events in the GCM and NCEP/NCAR reanalysis are the same’ being accepted, both at the 5% confidence level.

The average event magnitude at 10 hPa is weaker than what is observed in reanalysis, particularly it is outside the benchmark standard error for splitting events. The overall magnitude of polar cap warming at 100 hPa is within the model benchmark, so even though the typical event strength in the middle stratosphere is weaker

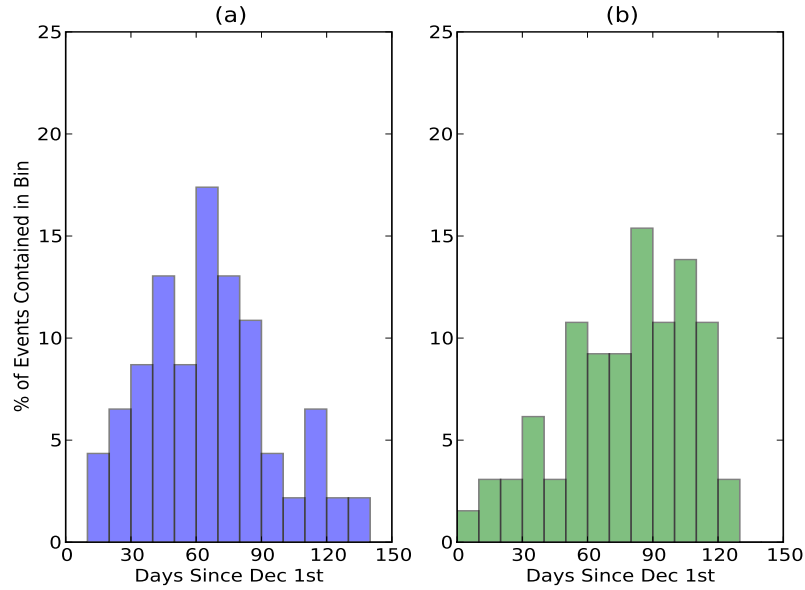


**Figure 3.10:** Distribution of SSW event onset in IGCM4 separated into 10 day bins from December the 1st onwards for: (a) splitting events and (b) displacement events.

than reanalysis the impacts in the tropopause region are of a similar magnitude. This is, in a sense, in agreement with the results of Charlton et al. [2007] who found that models tend to couple too strongly between the middle and lower stratosphere and have  $\Delta T_{100}$  values that are larger than that found in NCEP/NCAR reanalysis.

The average magnitude of meridional heat flux prior to event onset is slightly lower than the benchmark but within the standard error, so it is reasonable that SSW are occurring as a result of upward wave propagation. Inspection of Eliassen-Palm flux divergence (divided by density, figure omitted) over the 10 days prior to event onset reveals negative values in the middle stratospheric polar regions. These values peak at around  $-8$  and  $-10 \text{ m s}^{-1} \text{ day}^{-1}$  (between  $5$  and  $10 \text{ hPa}$ ,  $55^\circ\text{N}$  and  $80^\circ\text{N}$ ) for splitting and displacement composites respectively, supporting the conclusion that the event onset is a result of planetary wave forcing.

The distribution of SSW event onset throughout the winter season for splitting and displacement events is presented in Figure 3.10. This is complementary to Figure 10 in Joshi et al. [2015] where the seasonal distribution of: all events; displacement and splittings, is compared directly to NCEP/NCAR data. The IGCM4 has a seasonal distribution of SSWs that is similar to NCEP/NCAR, the magnitudes in monthly occurrence is similar and the model is able to simulate event occurrence in December. There is a slight tendency for displacement events to occur later in the season that what is seen in NCEP/NCAR. This behaviour is well within the

range of high-top CMIP5 models as analysed in Seviour et al. [2016].

Overall the IGCM4 produces a good number of SSW events that are slightly weaker than reanalysis in the middle stratosphere but have a reasonable magnitude at 100 *hPa*. The seasonal distribution of event occurrence is very similar to reanalysis and it is highly likely that the events are being driven by the breakdown of upwardly propagating planetary-waves. The IGCM4 is a suitable GCM for use in assessing SSW impacts on the surface and SSW interactions with other climatic modes, as is conducted throughout the rest of this thesis.

### 3.4 Coupling to an Interactive Ocean

Implied impacts into the ocean can be achieved through the study of the atmosphere-only IGCM4 with results interpreted in the context of analytical theory and published research, as in Chapter 4. It is also useful to repeat the analysis when an interactive ocean is incorporated to create a coupled model. This enables comparison between the implied impacts and a simulated response (which include feedbacks between the atmosphere and ocean) allowing for a deeper understanding of the dynamics involved. The procedure of coupling the IGCM4 to an interactive ocean also allows for assessment of changes to the background climatological atmospheric state and whether SSW simulation is altered when in the presence of an interactive ocean.

#### 3.4.1 MOMA

The modular ocean model array processor version (MOMA) in the coarse resolution used in this thesis is appropriate for coupling to the IGCM4 due to its relatively low computational demands and similar horizontal resolution scale. A brief breakdown of the model is provided here following Webb [1996].

The model utilises the primitive equations set, similar to Table 3.1, formulated for ocean dynamics in geometric height ( $z^*$  coordinates). It is assumed the ocean is incompressible, small changes in density can be neglected when not included in a term involving gravity and that in the vertical momentum equation vertical velocities are small. The resulting horizontal momentum equation is

$$\frac{\partial \vec{V}}{\partial t} + \left( \vec{V} \cdot \nabla \right) \vec{V} + w \frac{\partial \vec{V}}{\partial z^*} + f \times \vec{V} = -\frac{1}{\rho_0} \nabla p + F_{\vec{V}}.$$

Note that here  $w$  is the vertical velocity in  $z^*$  coordinates and  $p$  is pressure. The forcing and dissipation terms are represented as  $F_{\vec{V}}$ . Along with the above horizontal momentum equations further equations are required to close the system,

including: incompressibility given by  $\nabla \cdot \vec{V} + \frac{\partial w}{\partial z^*} = 0$ ; hydrostatic balance  $\frac{\partial p}{\partial z^*} = -\rho g$  and an equation of state such that  $\rho = \rho(\theta, S, p)$  where  $S$  is salinity.

Advection-diffusion for salinity and potential temperature are

$$\begin{aligned} \frac{\partial \theta}{\partial t} + (\vec{V} \cdot \nabla)\theta + w \frac{\partial \theta}{\partial z^*} &= F_\theta \\ &\text{and} \\ \frac{\partial S}{\partial t} + (\vec{V} \cdot \nabla)S + w \frac{\partial S}{\partial z^*} &= F_S. \end{aligned}$$

In MOMA the prognostic variables are the horizontal velocity, potential temperature, salinity and free surface height. The diagnostic variables are pressure, density and vertical velocity.

The first boundary condition is that of no-slip, so  $\vec{V} = 0$  on all solid sidewalls. The second boundary condition is that gradients of salinity and potential temperature normal to all solid boundaries are zero. Mathematically this is represented as  $\frac{dS}{d\hat{n}} = 0$  and  $\frac{d\theta}{d\hat{n}} = 0$ , where  $\hat{n}$  is the vector normal to solid boundaries. At the air-sea interface there is daily exchange of heat, fresh water and surface stress between the IGCM4 and MOMA.

The MOMA version implemented in FORTE has a  $2^\circ$  square horizontal grid and 15 non-uniform vertical levels. In the upper ocean the vertical resolution is around 30 *m* and this increases with depth up to around 800 *m* in the abyssal layers, see Table C1 in Appendix C. All grid boxes are either land or sea. To solve the governing equations advective and diffusive terms are transformed into fluxes through the boundaries of the grid box, all other terms are averaged over the box. This is then solved using finite differences on an Arakawa-B grid, Figure 3.11, which has the best wave dispersion properties for coarser resolution ocean models [Beckers, 2002].

MOMA uses discrete time-steps with data being held asynchronously. The barotropic and baroclinic velocity time-steps are every 45 model seconds and 45 model minutes respectively. MOMA utilises a leapfrog scheme in time with the diffusive terms being lagged by one time-step. To combat computational issues and splitting of solutions a periodic Euler backward step is used. To prevent spurious transfers of vertical flux when these terms appear at Arakawa-B grid points they are replaced by the average flux of the four surrounding tracer points.

A further important component of the physical ocean system is the mechanical energy transfer from the conversion of potential energy into kinetic energy via oceanic eddies. It is approximated that the kinetic energy contained within meso-scale eddies over the entire ocean is 100 times larger than the kinetic energy of

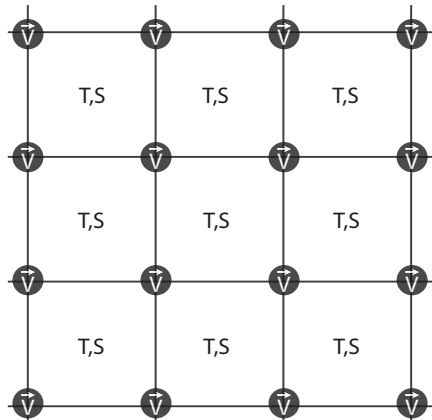


**Figure 3.11:** Arakawa-B grid schematic for prognostic variables; horizontal velocity on grid corners, temperature and salinity on grid centres.

the time-mean flow [Huang, 2010]. Coarse horizontal ocean models do not directly resolve these eddies (they are not ‘eddy permitting’) and their associated tracer transport. To include this important component of the mechanical energy cycle this process is parameterised. MOMA implements the Gent-McWilliams Skew-flux scheme outlined by Griffies [1998].

### 3.4.2 FORTE

The combination of IGCM4 outlined in section 3.3.1 and MOMA outlined above results in a fully coupled atmosphere-ocean GCM. This is the latest version of FORTE. Previous versions of FORTE have utilised the IGCM3 coupled with MOMA and have been implemented in modelling studies including Wilson et al. [2009], Atkinson et al. [2009] and Blaker et al. [2006]. The key difference in this latest FORTE version is the updated IGCM4, which is now (among many other improvements outlined in Joshi et al. [2015]): parallelised, includes gravity wave drag, improved solar irradiance and has updated surface and cloud schemes.

Air-sea surface fluxes (heat, fresh water, momentum) are exchanged daily and the resolution makes this coupled model an ideal candidate for longer integrations and the study of large scale teleconnections and atmosphere-ocean coupling. However, it must be remembered that there is no simulation of more computationally expensive features, for example the diurnal cycle and interactive ozone. FORTE utilises OASIS coupler software version 2.3 as outlined by Terray et al. [1999].

The bulk aerodynamic formula of Forster et al. [2000] (equation 3.3) now uses relative lower model layer wind values, where  $\vec{V}$  is taken as the IGCM4 lowest model

velocity minus MOMA top level current strength. The sea ice field is modified from the standalone IGCM4, sea ice in FORTE is formed when the ocean temperature reaches  $-0.5^{\circ}\text{C}$  and has an albedo value of 0.6. When ice is present the atmospheric lower level air temperature is diagnosed as that of the ice. Sea ice albedo increases with decreasing surface temperature to a maximum value of 0.8, to parameterise snow cover. Ice melts when the air temperature reaches  $0^{\circ}\text{C}$ .

FORTE and the stand-alone IGCM4 have been configured to be as similar as feasibly possible to allow for a comparison of the background climatologies and SSW simulations between the two models, as is conducted in Chapter 7. This is advantageous because it allows for attribution of any difference to the presence of an interactive ocean. This approach also facilitates assessment of the implied ocean impacts discussed in the next Chapter.

### 3.5 Conclusions

This Chapter has presented the IGCM4, an intermediate atmosphere GCM, and MOMA, a coarse resolution ocean GCM, in preparation for the modelling experiments conducted throughout the rest of this thesis. The climatological state and SSW simulation of the IGCM4 is assessed and it is found that this model is appropriate for the study of atmosphere-ocean interactions and SSW impacts. The middle atmosphere climatological state sits well within the envelope of current GCMs. There is a reasonable number of SSWs simulated (for both splitting and displacement subsets), these events are slightly weaker than NCEP/NCAR reanalysis at 10 *hPa*, couple appropriately in the tropopause region and are forced by the breakdown of upward wave propagation.

In Chapter 4 the IGCM4 is used to assess SSW impacts on the surface climate and implied impacts into the ocean. The exclusion of an interactive ocean is overly simplistic but allows for direct isolation of SSW impacts.



---

## Chapter 4 - Sudden Stratospheric Warming Effects On The Surface Climate And Ocean

*This Chapter is based upon the paper ‘The Effects of Different Sudden Stratospheric Warming Type on the Ocean’ by O’Callaghan et al. and was published in the Journal Geophysical Research Letters in October 2014 under a creative commons license (CC-BY).*

*Figures 4.2, 4.5 and 4.6 and some portions of text have been directly extracted from this manuscript and reproduced with permission from the Journal.*

### 4.1 Introduction

As discussed in Chapter 2 recent studies have shown that sudden stratospheric warming (SSW) events have a direct impact on the surface climate [Charlton and Polvani, 2007, Mitchell et al., 2013b] with increased knowledge into these phenomena potentially leading to lengthened timescales of accurate forecast and understanding of stratospheric-tropospheric coupling. A debated issue is whether the surface response is dependent on the spatial type of SSW, typically separated into splitting and displacement events, see section 2.2. The first aim of this chapter is to assess the impact of splittings and displacements on the surface in the IGCM4. The results will be compared to literature and, where appropriate, reanalysis data. This enables assessment of the performance of the IGCM4 and whether there is a dependence on the surface response due to the type of SSW.

The second aim of this chapter is to explore the potential influence from the stratosphere into the ocean system. There is a confirmed link between SSW events, see Chapter 2, and the descent of negative Northern Annular Mode index (NAM) anomalies [Baldwin and Dunkerton, 2001] which can modify the surface climate at middle to high latitudes. It is also known that phase of the North Atlantic Oscillation (NAO) directly interacts with the North Atlantic Ocean. The NAO is very closely related to the surface NAM [Solomon et al., 2007] but has different centres of action. It is, therefore, a logical step to investigate whether the surface NAM anomaly, that frequently persists following SSWs, can be communicated into the ocean on timescales associated with SSW events.

Overall the scientific aim of this chapter is to answer the question: how do anomalies associated with SSWs make their way into the ocean system and is the response dependent on SSW type? To achieve this focus will be on SSW induced NAM

anomalies that lead to changes in the surface wind stress and the net atmosphere-surface fluxes which, in turn, modify the mixed layer heat budget. This work follows that of Reichler et al. [2012] but from a new perspective of the influence of different SSW types on the ocean. An atmosphere only general circulation model is utilised to isolate the direct influence of SSW events.

#### 4.1.1 Literary Background of NAO Impacts on the Ocean

The NAO index represents a vacillation in surface pressure over the North Atlantic Ocean with dominant centres of action over the Icelandic and Azores regions. In the high index phase the low pressure center over Iceland deepens and the high pressure over Azores intensifies with a weakening of both in the low index phase. The structure of this high-low pressure dipole over the North Atlantic affects many dynamical processes including the storm track and North Atlantic gyre system. Marshall et al. [2001], Visbeck et al. [2003] and Zhai et al. [2014] all demonstrate a link between the phase of the NAO and ocean circulation typically communicated from the atmosphere into the ocean through Ekman dynamics and downwelling rates. These works predominantly focused on annual timescales.

Visbeck et al. [2003] provides a complete overview of oceanic responses to NAO variability. They covered; local rapid responses, longer processes associated with large scale geostrophy and the overturning circulation and finally they evaluated potential impacts on the climate on decadal timescales. Visbeck et al. [2003] cautioned against trying to identify ‘typical’ ocean/climatic responses to NAO behaviour as these can vary greatly depending on: the background state of the climate system, other teleconnection patterns [Moore and Renfrew, 2012] and variables such as sea-ice extent and cloud cover. The analysis presented here isolates the ocean and climate responses associated with SSW induced NAM anomalies, caution must be taken if applying these findings to individual observational periods as other processes that may modulate the behaviour are not accounted for here.

Marshall et al. [2001] discussed the response of the ocean, mainly gyre and thermohaline components, to NAO-like forcing and coupled atmosphere-ocean interactions on decadal timescales. In observational data, provided by Martin Visbeck, they assessed the dynamical Ekman response to anomalous wind forcing associated with NAO phases and assessed the short-term (typically locally damped) direct ocean response in sea surface temperature patterns. They then analysed the decadal behaviour in a simple mathematical model where it was found that the North-Atlantic gyre system responded to meridional shifts in the zero wind stress curl line. The gyre system advected warm/cold waters via an anomalous inter-gyre gyre circula-

tion (anticyclonic for positive NAO phases and cyclonic for negative NAO phases). This heat redistribution dampened the zonal winds associated with the NAO phase.

Zhai et al. [2014] extended the study of Marshall et al. [2001] by focusing on the interplay between the gyre and thermocline response to idealised NAO regimes using a simple ocean general circulation model. It was found that the sign of basin wide heat content anomalies in the Atlantic Ocean varied depending on whether the gyre or thermohaline response was dominant. Under negative NAO conditions there were less cold air outbreaks in the Labrador sea which lead to less deep water formation and a general increase in the Atlantic thermocline depth. Simultaneously the gyre system was weakened by the wind stress associated with NAO negative conditions and this lead to an increase in thermocline depth over the subpolar gyre and a decrease in thermocline depth over the subtropical gyre. The gyre and thermohaline basin-wide anomalies in ocean heat content (and thermocline depth) were found to oppose one another, especially at low frequencies. It was concluded that the temporal evolution of the basin-wide ocean heat content depended on the interplay between these two mechanisms.

The confluence of the subtropical and subpolar gyres is demarked by the zero wind stress curl line, and has a south-west to north-east tilt. The position and tilt of the zero wind stress curl line is influenced by the NAO phase. Marshall et al. [2001] and Zhai et al. [2014] showed that during negative NAO phases the zero wind stress curl line became more zonal and an anomalous cyclonic flow appeared across the boundary of the two gyres, with the opposite behaviour in positive phases. For the negative phase there was a weakening of the strength of the climatological surface wind stress and a southward shift in the pattern. This reduced surface Ekman transport and the downwelling/upwelling rates in the subtropical/subpolar gyres were also weakened. Zhai et al. [2014] demonstrated that this in turn affected the thermocline depth and triggers anomalous Rossby waves which travel along the pycnocline and eventually propagated into the wider ocean system. It is unlikely that relatively short lived anomalies associated with SSWs would have the influence to substantially alter the thermocline depth but the anomalies may have the ability to impact on the mixed layer heat budget due to their direct influence on the Ekman heat transport and potentially impact the atmosphere-surface heat fluxes. This is what is investigated here.

#### 4.1.2 Ekman Theory

The basin scale anomalies associated with negative NAO regimes are communicated into the ocean through air-sea fluxes of heat, momentum and fresh water [Visbeck

et al., 2003, Marshall et al., 2001]. On the timescale associated with SSW anomalies only a local rapid ocean response is directly relevant. This component of ocean circulation is wind driven and captured by Ekman dynamics.

The Ekman layer is a thin upper ocean boundary layer that was hypothesised in the seminal work of Ekman [1905]. A thorough explanation of Ekman theory is provided by Huang [2010] and brief over-view of this work is provided here. The Ekman layer is a shallow boundary layer with a thickness proportional to  $HE^{1/2}$ , where  $H$  is the ocean depth and  $E$  is the Ekman number. This layer is typically of the order of 30  $m$ . In this boundary layer the velocity term in the momentum equation is balance by the frictional and pressure gradient terms; it is assumed that the fluid motion is large scale, quasi-steady, linear and incompressible. The momentum equations in the horizontal plane become

$$-fv = -\frac{1}{\rho_0} \frac{\partial p}{\partial x} + \frac{\partial}{\partial z} \left( A \frac{\partial u}{\partial z} \right), \quad (4.1a)$$

$$fu = -\frac{1}{\rho_0} \frac{\partial p}{\partial y} + \frac{\partial}{\partial z} \left( A \frac{\partial v}{\partial z} \right). \quad (4.1b)$$

In this;  $\vec{V} = (u, v)$  is the horizontal current,  $p$  is pressure,  $\rho_0$  is the reference density of the ocean,  $f$  is the Coriolis force and  $A$  is a turbulence parameter. The boundary condition at the bottom of the surface Ekman layer is that frictional stress vanishes, I.e.  $u = v = 0$ . At the surface the only stress is a direct result of the wind forcing. Mathematically the surface boundary condition is

$$A \frac{\partial \vec{V}}{\partial z} = \vec{\tau} \quad \text{at} \quad z = 0 \quad (4.2)$$

where  $\vec{\tau} = (\tau_x, \tau_y)$  is the surface wind stress. Due to the large scale motion it is assumed the fluid velocity satisfies an ageostrophic solution of the form

$$u = u_g + u_E = -\frac{1}{f\rho_0} \frac{\partial p}{\partial y} + u_E \quad (4.3a)$$

$$v = v_g + v_E = \frac{1}{f\rho_0} \frac{\partial p}{\partial x} + v_E \quad (4.3b)$$

Upon substitution of 4.3 into 4.1 the Ekman velocities are

$$u_E = \frac{1}{f} \frac{\partial}{\partial z} \left( A \frac{\partial v_E}{\partial z} \right) \quad (4.4a)$$

$$v_E = -\frac{1}{f} \frac{\partial}{\partial z} \left( A \frac{\partial u_E}{\partial z} \right) \quad (4.4b)$$

It is assumed that  $A \frac{\partial u_g}{\partial z} \approx A \frac{\partial v_g}{\partial z} \approx 0$  due to the small vertical length scale. To formulate the transport over the Ekman layer Equation 4.4 is integrated over depth and upon substitution of Equation 4.2 the Ekman transport,  $\vec{U}_E$ , is

$$\vec{U}_E = - \left( \vec{k} \times \frac{\vec{\tau}}{f\rho_0} \right). \quad (4.5)$$

The transport in the Ekman layer is directed  $90^\circ$  to the right (in the Northern Hemisphere) of the surface wind stress. Figure 4.1 displays the surface wind stress from the National Centers for Environmental Prediction National - Center for Atmospheric Research (NCEP/NCAR) reanalysis dataset (daily data at T62 with 28 vertical levels) [Kalnay et al., 1996]. Winter climatologies are calculated to assess Ekman transport over a typical winter period.

Focusing on meridional transports over the North Atlantic Ocean provides a qualitative understanding of the north-south heat transport. The meridional term in Equation 4.5 is  $v_E = -\frac{\tau_x}{f\rho_0}$ , Ekman dynamics lead to equatorward transport in regions of positive  $\tau_x$  and poleward transports elsewhere. Figure 4.1(a) displays that climatologically there is poleward transport equatorward of  $30^\circ\text{N}$  and poleward of  $60^\circ\text{N}$  (where  $\tau_x$  is negative) and equatorward transport between  $30^\circ\text{N}$  and  $60^\circ\text{N}$ .

There is also vertical transport between the surface Ekman layer and the ocean interior which is called Ekman pumping, or suction, for flow into, and out of, the ocean interior. Assuming that geostrophic flow is uniform in space the continuity equation becomes

$$w_I \Big|_{z=0} = w_E = \int_{-H}^0 \frac{\partial u}{\partial x} + \frac{\partial v}{\partial y} dz^*.$$

Again assuming an ageostrophic solution, Equation 4.3, the Ekman pumping velocity is

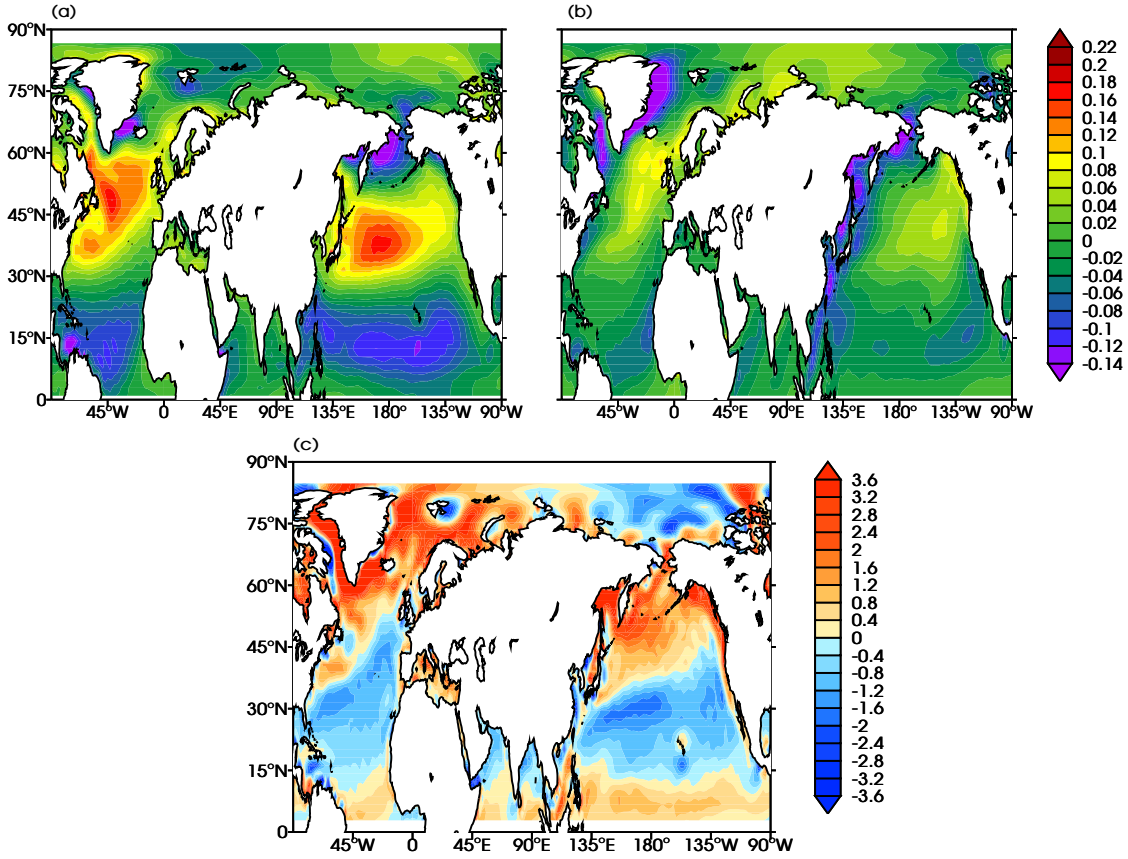


**Figure 4.1:** Surface wind stress fields from NCEP/NCAR reanalysis spanning 1957 to 2006 (50 years). December–March climatologies of: (a) zonal wind stress, (b) meridional wind stress ( $\text{Nm}^{-2}$ ) and (c) surface wind stress curl ( $10^{-7} \text{Nm}^{-3}$ ).

$$\begin{aligned}
 w_E &= \int_{-H}^0 \frac{\partial U_E}{\partial x} + \frac{\partial V_E}{\partial y} dz \\
 &= \frac{\partial}{\partial x} \frac{\tau_y}{f\rho_0} - \frac{\partial}{\partial y} \frac{\tau_x}{f\rho_0} \\
 &= \frac{1}{f\rho_0} k \cdot \nabla \times \vec{\tau} + \frac{\beta \tau_x}{f^2 \rho_0}.
 \end{aligned} \tag{4.6}$$

Areas of positive wind stress curl induce upwelling and negative wind stress curl induce downwelling in the Northern Hemisphere. Ekman pumping velocities can also be a result of the beta effect, the second term in Equation 4.6, this is a result of the change in the Coriolis parameter with latitude.

The surface wind stress curl from NCEP/NCAR reanalysis is presented in Figure 4.1(c). In the North Atlantic, between  $65^\circ\text{N}$  and  $15^\circ\text{N}$ , positive (negative) curl corresponds to the subpolar (subtropical) gyre and is region of climatological upwelling (downwelling). This agrees with the qualitative zonal wind stress arguments

where areas of convergent meridional Ekman transport lead to downwelling and vice versa.

The transport induced by the surface wind stress,  $\vec{U}_E$ , advects heat in the upper ocean. Marshall et al. [2001] provides a formula, their equation (1), for this implied Ekman heat transport which is

$$H_E = \rho_0 c_o \vec{U}_E \cdot \nabla SST. \quad (4.7)$$

In this  $c_o$  is the specific heat of sea water ( $4181 \text{ J / kg K}$ ) and  $\nabla SST$  is the gradient of climatological sea surface temperature. Equation 4.7 represents a pseudo air-sea Ekman induced heat flux from the advection of SST gradients by Ekman transport. Here the units are such that a positive flux is into the planet and  $H_E$  is the implied Ekman heat flux in this study.

The implied Ekman heat flux can rapidly adjust on the time-scale of days and often provides a significant forcing on the upper ocean [Visbeck et al., 2003]. From Equation 4.7 it can be qualitatively stated that a weakening of the zonal surface wind stress would lead to less relatively warm (cool) water being advected poleward (equatorward) in regions of negative (positive)  $\tau_x$ . This could lead to a warming (cooling) in the upper ocean over the subpolar (subtropical) gyre. Exact quantification of variations to upper ocean heat content requires the inclusion of the meridional wind stress and the net atmosphere-surface flux over the ocean from other heat flux terms. Screen et al. [2010] provides a simplified mixed layer heat budget, their Equation (4), of the form

$$\frac{\partial T}{\partial t} = \frac{Q_S + H_E}{\rho c_o D}. \quad (4.8)$$

Where  $Q_S$  is the net atmosphere-surface flux and consists of: net shortwave radiation, net longwave radiation, latent heat flux and sensible heat flux terms. Equation 4.8 simply states that changes to temperature over time are proportional to the sum of the net atmosphere-surface flux and implied Ekman heat flux divide by the mixed layer depth. This simplified budget makes the assumptions that the effects of advection and mixing are negligible, often true for wind driven ocean dynamics, and also assumes that the Ekman layer depth is less than or equal to the mixed layer depth.

Following a SSW it is known that there are impacts on  $\vec{\tau}$  communicated through the negative NAM they are associated with. There is a tangible link between the stratosphere and ocean through modification to Ekman dynamics as outlined above and through the generalised NAO impacts on the ocean which were reviewed in Section 4.1.1. The study of Reichler et al. [2012] confirms this theoretical link

through the evaluation of strong polar vortex events.

### 4.1.3 Stratospheric Impacts on the Ocean

Reichler et al. [2012] demonstrated the interaction of strong polar vortex events with the North Atlantic Ocean through surface wind stress anomalies and latent and sensible heat flux. They discovered significant anomalies in the surface wind stress for the 60 days following strong polar vortex events and this lead to surface temperature anomalies over the Atlantic Ocean which impacted the deep ocean over the following years. The temperature anomalies in the deep ocean fluctuated in phase with the models overturning circulation displaying a potential link to the Atlantic meridional overturning circulation. This was conducted in a model with low stratospheric variability when compared NCEP/NCAR reanalysis.

Strong polar events are in a sense a comparable phenomenon to SSWs but of the opposite magnitude with a strong intensification of the strength of the NH polar vortex, often due to a lack of vertical planetary wave propagation allowing radiative thermal relaxation [Davini et al., 2014]. Reichler et al. [2012] explicitly isolated the connection between the Northern hemisphere stratospheric polar vortex, the surface NAM anomaly and subsequent ocean variations. The work presented in this chapter provides a more detailed analysis of the air-sea heat flux (including longwave and shortwave radiative terms) following anomalous polar vortex behaviour and determines the difference in ocean impact depending on SSW type.

## 4.2 Variable Formulation

### 4.2.1 Northern Annular Mode Index

To view the descent of anomalies associated with SSW events NAM anomaly height against time plots are derived following the works of Baldwin and Dunkerton [2001] and Mitchell et al. [2013b]. The NAM throughout the entire atmosphere is formulated to provide insights into the temporal behaviour of anomaly descent. In this study the NAM anomaly is formulated from daily zonal mean geopotential height anomalies poleward of  $20^{\circ}\text{N}$ . This methods follows the work of Baldwin and Thompson [2009] and is optimized to assess daily stratosphere-troposphere coupling.

To formulate the NAM anomaly field at each model level the following algorithm is applied:

- [1] The daily zonal geopotential height anomaly field is formulate poleward of  $20^{\circ}\text{N}$

- [2] The covariance matrix of [1] is extracted
- [3] Empirical orthogonal functions of the covariance matrix are formulated (see Chapter 5). These are the eigenvalues and eigenvectors of the covariance matrix. The eigenvector represents the spatial mode and the corresponding eigenvalue displays the percentage of variance accounted for.
- [4] The leading eigenvector is extracted, this is the vector with the highest eigenvalue. The leading principal component is formulated by projecting this eigenvector onto the 2D geopotential height anomaly field poleward of 20°N. The leading principal component represents the temporal variability of the dominant spatial mode.
- [5] The NAM anomaly is the standardised leading principal component. This ensure the field has unit variance at each atmospheric level and is directly comparable throughout the entire atmospheric column.

When formulating the NAM anomaly for the IGCM4 it is found that the leading eigenvalue is clearly distinct from the second and third and the leading empirical orthogonal function accounts for a large amount of the spatial variability. This is around 80% at the uppermost atmospheric levels and 50% in the troposphere.

### 4.2.2 Surface Variables

The surface fields of principal interest are the surface wind stress, net atmosphere-surface flux (which includes long wave radiation, short wave radiation, latent heat flux and sensible heat flux) and surface temperature. Due to the derivation of surface wind stress, see below, it is only valid over oceans. In the IGCM4 the surface temperature only freely evolves over land. Combined analysis of these two fields provides a global perspective of the surface impacts following a SSW in the IGCM4.

To derive the surface wind stress the bulk aerodynamics formula, Equation 3.3 is applied to the lowest model level  $u$  and  $v$  fields. The surface wind stress curl is then derived as  $\vec{k} \cdot \nabla \times \vec{\tau}$ . It is assumed that the atmospheric surface density is equal to 1, this is only valid over the oceans.

### 4.2.3 Climatological and Anomaly Fields

Climatologies are calculated by averaging over individual calendar days and anomalies are taken as departures from the climatology to remove seasonality. To view the surface impacts following SSWs the surface anomaly fields are averaged over

two periods. The first is the *mature stage* and is an average from event onset (lag 0) until 30 days after (lag +30). The second stage is assessed from 30 to 60 days (lag +60) following the events and is the *decay stage*.

#### 4.2.4 Statistical Methods

To determine the average behaviour following a SSW composites of anomaly fields are produced for the identified splitting and displacement events from the 200 year IGCM4 integration presented in Chapter 3. A paired students t-test (or a Welch's test for unequal sample variances) is used to assess the probability that the anomalies would occur given that the null hypothesis was true. For anomaly fields the null hypothesis states that there is no difference between the anomaly data surrounding a SSW event (for the time frame of interest) and the anomaly data averaged for each winter season. This test assesses the probability that the anomalies surrounding the SSW events are typical of winter behaviour and could have occurred randomly. If this chance is less than 5% the data is stippled and not insignificant.

Difference fields of the composites are formulated to assess the explicit difference in the impacts following splitting and displacement SSWs. For these difference fields (splitting composite minus displacement) a paired t-test is used with a null hypothesis that there is no difference between the splitting and displacement composites, again p-values of less than 0.05 are stippled.

In all instances where t-tests are applied the data is first checked to ensure it is likely to be Gaussian in nature; a  $\chi^2$  test is performed with a null hypothesis stating the data is normally distributed. In all cases presented in this chapter the fields returned p-values higher than 0.35 and the null hypothesis was accepted.

### 4.3 Results

#### 4.3.1 NAM Anomaly

The descent of NAM anomalies associated with splitting and displacement SSWs is presented in Figure 4.2 and should be compared to Figure 4 of M13 who investigated surface impacts following SSWs in ERA-40 reanalysis [Uppala et al., 2005]. The results show similarities with M13. In the stratosphere there is a positive anomaly leading up to event onset, lag 0, which is stronger for displacements. The negative anomaly appears before lag 0 in both cases and peaks just after event occurrence in the middle stratosphere.

The difference between splitting and displacement composites is displayed in Figure 4.2(c). The negative anomaly leading up to lag 0, throughout the entire

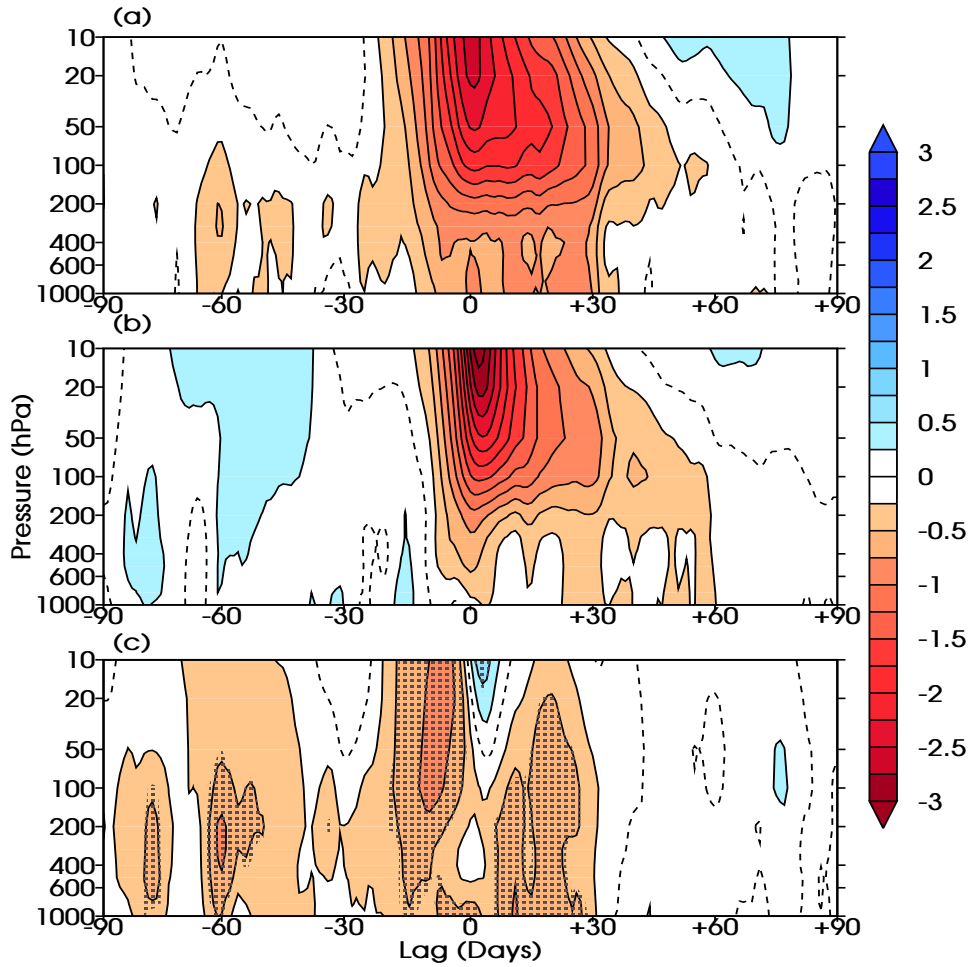


**Figure 4.2:** The NAM anomaly (unitless) in the IGCM4 for 90 days surrounding identified SSWs as a function of height against time for: (a) 48 splitting events composite and (b) 65 displacement events composite. (c) splitting composite minus displacement composite where stippling represents a  $p$ -value of less than 5%. The dashed line represents the zero contour. The NAM index anomaly is both unitless and dimensionless.

atmospheric column, is stronger for the splitting composite. The maximum strength in the middle stratosphere at lag 0 is around -3 for displacements and -2.5 for splittings which is not insignificantly different. The displacement composite may have more impact in the middle stratosphere, at lag 0, but possesses less ability to descend to the surface. For the splitting composite there is a persistent negative surface anomaly appearing prior to event onset and remains for over 30 days. It has a peak strength of around -1. The surface impact in the displacement composite is weaker and more intermittent. The displacement peak impact occurs in the decay period (lag +30 to +60).

Splitting events have a heightened ability to affect the surface climate in the

IGCM4, this is: insensitive to the number of ensemble members; the inclusion or exclusion of events occurring in March; and shows similar, albeit noisier, behaviour when composite plots are created using SSW events with central dates from a given winter month. The analysis is also repeated with central dates that were originally removed as final warming events. There is no qualitative change to the results. It can be stated with confidence that the apparent contradiction between the results of CP07 and M13 is not a result of how their respective algorithms treat final warming events.

Negative NAM anomalies have similar life spans in the stratosphere for both types of SSW, although lasts slightly longer for splitting events. In both cases there is a return to normal conditions 60 days after an event. These results are in agreement with the results of M13 where here a simple GCM is employed and an independent identification and classification method is utilised. The first scientific aim of the Chapter can be concluded; in the IGCM4 it is more likely for the anomalies associated with splitting SSWs to descend into the troposphere and affect the surface climate.

The NAM anomaly behaviour in the IGCM4 is similar to the findings of M13. However, there is one interesting difference. For the splitting composite the anomaly descent from the tropopause to the surface is faster in the model than in ERA-40, where NAM anomalies take 15 days to reach the surface. The peak negative anomalies occur in the decay phase in the reanalysis and it is evident that the timescales for descent in the IGCM4 is faster than in ERA-40. The timescales associated with anomaly descent in the IGCM are within the range of variability of CMIP5 models [Gerber et al., 2010].

### 4.3.2 Surface Temperature

M13 and CP07 both assessed the tropospheric and surface impacts following SSWs, see Section 2.3.3. The impact on surface temperature over land following SSWs is assessed in the IGCM4 and is directly compared to NCEP/NCAR reanalysis utilising SSWs isolated in CP07. There are a total of 27 NCEP/NCAR SSW events between 1957 and 2006 with one occurring in November which is discarded for continuity to the hybrid method.

Figures 4.3(a) and (b) display surface temperature anomalies for SSW composites in the IGCM4 and NCEP/NCAR reanalysis respectively. Once again the timescale for anomaly onset is faster in the model. The period with the strongest anomalies is presented (when averaging over lag 0 to +60 the anomaly pattern is still evident and significant but weaker). The broad spatial patterns present in the

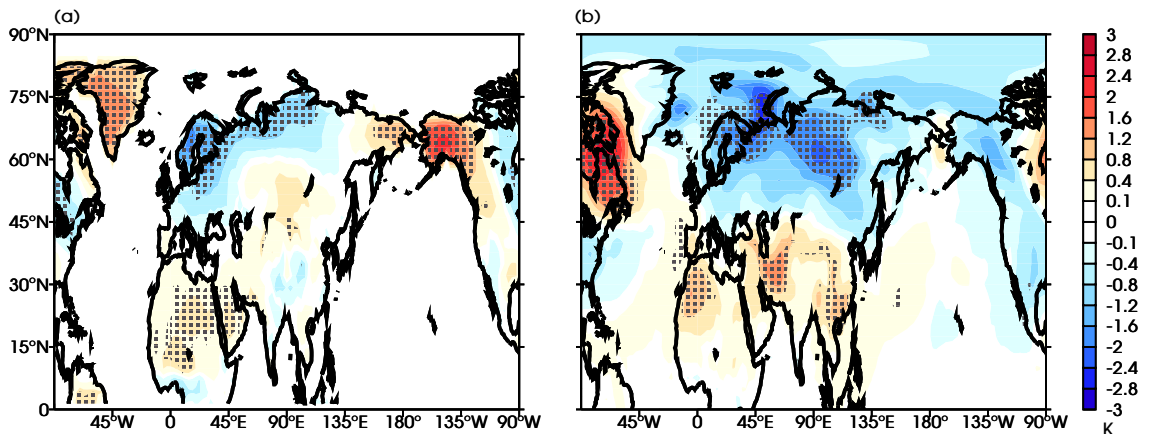


**Figure 4.3:** Surface Temperature anomaly composites (K) for: (a) 113 SSWs in IGCM4 mature period (lag 0 to lag +30) and (b) 26 CP07 SSWs in NCEP/NCAR reanalysis decay period (lag +30 to lag +60). Stippling represents a  $p$ -value of less than 5%.

model and reanalysis are generally similar. There are cold anomalies over western Europe and central Eurasia which are accompanied by warm anomalies over east Alaska/Greenland. This cold/warm pattern is also reported in the literature [Mitchell et al., 2013a]. The anomalies appear to be stronger and extend further eastward into the Eurasian continent for the NCEP/NCAR composite., there is warming beneath this that is not observed in the IGCM4. There is warming over Africa in both the model and reanalysis. Over the Aleutian region there is warming in the IGCM4 which is not in the reanalysis, the warming appears strongly in the period leading up to SSW onset and could be a precursory signal.

### 4.3.3 Surface Wind Stress

The IGCM4 surface wind stress fields are presented in Figure 4.4 and have been formulated to be directly comparable to the winter surface NCEP/NCAR wind stress fields presented in Figure 4.1. The IGCM4 wind stress generally compares favourably with the large scale features seen in the NCEP/NCAR reanalysis. There is a strong north-west stress, Figures 4.4(a) and (b), present over 30°N to 55°N attributed to the midlatitude westerlies that reside here. The IGCM4 is able to simulate the overall wind stress magnitude and structure well. When focusing on smaller structures it is noted that the peak zonal stress is shifted eastward in the model when compared to reanalysis which could be a result of differences in the storm track simulated by the IGCM4. The zero wind stress curl line that separates the subtropical and subpolar boundary is more zonal in the IGCM4, Figure 4.4(c),

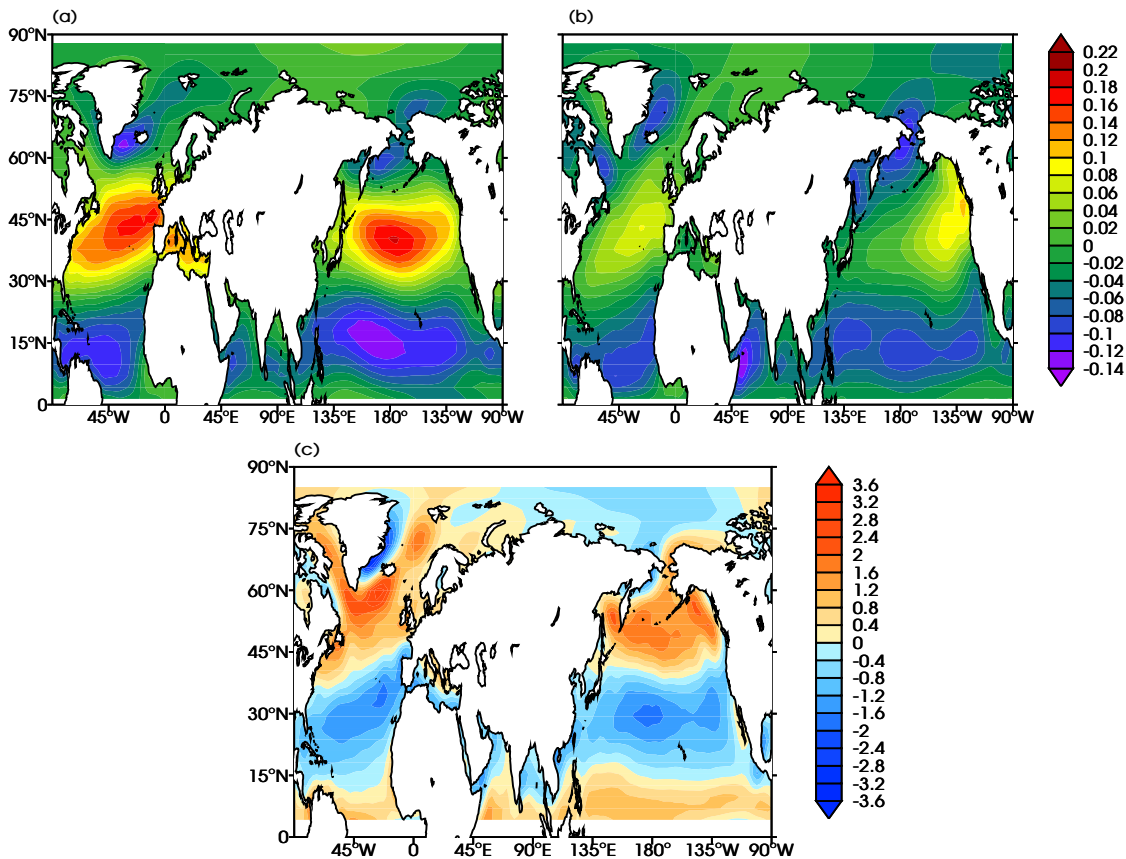


**Figure 4.4:** Surface wind stress fields from IGCM4 (200 years). December-March climatologies of: (a) zonal wind stress, (b) meridional wind stress ( $Nm^{-2}$ ) and (c) surface wind stress curl ( $10^{-7}Nm^{-3}$ ).

than what is observed in NCEP/NCAR reanalysis, Figure 4.1(c). The large scale features are captured over the majority of the ocean in the IGCM4 but care must be taken in interpreting fine scale IGCM4 behaviour especially over coastal regions and specifically around Greenland where the model fails to reproduce the variations in surface orography that leads to strong wind stresses in reanalysis.

The post-SSW surface state is analysed in the IGCM4 and also in NCEP/NCAR reanalysis [Kalnay et al., 1996], the latter again using event dates isolated in CP07. The surface wind stress curl anomaly fields are presented in Figure 4.5(a) and (b) for the IGCM4 and NCEP/NCAR reanalysis respectively. The surface wind stress fields shows good agreement between model and reanalysis with both displaying negative NAM type responses primarily over the North Atlantic Ocean. This acts to weaken the climatological pattern (by around 30% in the IGCM4) and pulls the zero wind stress curl line equatorward in both the model and reanalysis. A cyclonic anomaly across the boundary between the sub-polar gyre and sub-tropical gyre appears in agreement with the work of Marshall et al. [2001], see Section 4.1.1. The

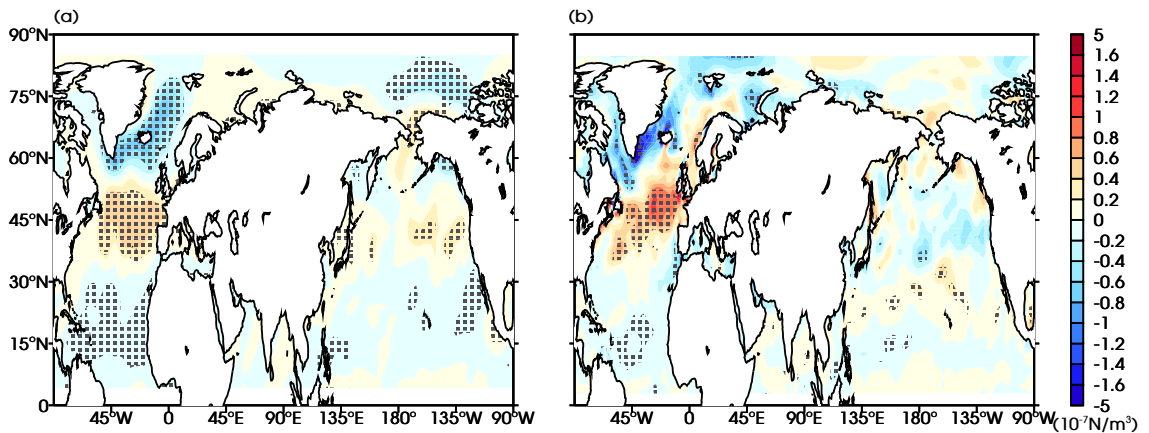


**Figure 4.5:** Surface wind stress curl anomaly composites ( $10^{-7} \text{ N m}^{-3}$ ) for: (a) 113 SSWs in IGCM4 mature period (lag 0 to lag +30) and (b) 26 CP07 SSWs in NCEP/NCAR reanalysis decay period (lag +30 to lag +60). Stippling represents a  $p$ -value of less than 5%.

shift in the zero wind stress curl line could result in a more zonal North Atlantic Current and has implications for the ocean as highlighted in section 4.1.1.

#### 4.3.4 Surface Energy Flux

The anomalous surface regime following SSWs is communicated into the ocean on short timescales both dynamically (through Ekman transport induced heat flux) and thermodynamically through net atmosphere-surface fluxes (including: the longwave radiation, shortwave radiation, latent heat flux and sensible heat flux), see Sections 4.1.1 and 4.1.2. The implied Ekman heat flux and the net atmosphere-surface flux are both modified following a SSW and their sum is labelled the combined upper ocean energy flux.

The anomalous net atmosphere-surface flux for the mature period in the IGCM4 is shown in Figure 4.6. Behaviour in the decay period is similar and weaker. It is now determined if the surface response is different between the two types of SSW in the IGCM4. Composite anomalies following 48 splitting events are presented in the left hand column of Figure 4.6 and for 65 displacement events in the central column. The anomalies in the North Atlantic Ocean have similar spatial patterns for the splitting and displacement composites; however, the magnitude is different with the displacement composite anomalies being, at most, half the strength when compared to the splitting events. This difference is not insignificant between  $45^{\circ}\text{N}$  and  $75^{\circ}\text{N}$  for all three flux fields, as shown in Figures 4.6(c), (f) and (i). This shows that when considering surface impacts in the IGCM4 splitting and displacement SSWs should be considered as distinct events. This is consistent with the conclusions of

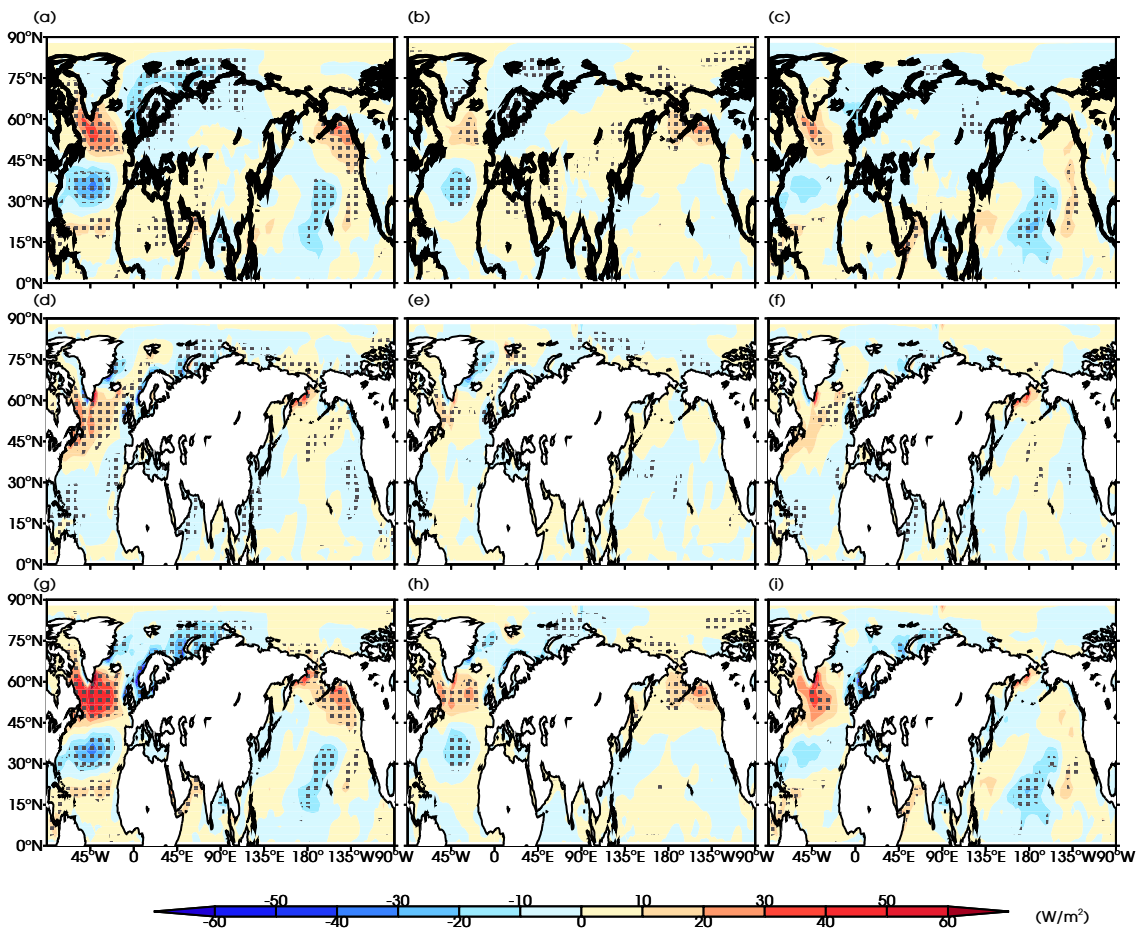


*Figure 4.6:* Mature period (lag 0 to lag +30) IGC4 composites for splitting anomalies, displacement anomalies and their difference (splittings minus displacements) in columns one, two and three respectively for: (a)-(c) net atmosphere-surface flux, (d)-(f) implied Ekman heat flux and (g)-(i) the combined upper ocean energy flux. Positive fluxes are into the planet (downwards) units are in  $Wm^{-2}$ . There are 48 splitting events (left column) and 65 displacement events (middle column). Stippling represents  $p$ -values of less than 5%.

M13 who found that there was a need to identify vortex splitting and displacement events individually if an accurate understanding of influence on the surface climate in reanalysis was to be achieved.

For the splitting SSWs the surface fluxes in the North Atlantic Ocean following event onset are strong. As displayed in Equation 4.8 under a simplified ocean framework the rate of change to the mixed layer heat budget is proportional to the combined upper ocean energy flux,  $Q_s + H_E$ , divided by mixed layer depth,  $D$  the anomalies associated with splitting SSWs are strong and more likely to modify the mixed layer heat budget when compared to the displacement composite. The net atmosphere-surface flux, Figure 4.6(a), displays anomalous fluxes into the ocean over

the sub-polar gyre and out of the ocean over the sub-tropical gyre. This anomalous pattern is slightly different in the implied Ekman heat flux, Figure 4.6(d), which is weaker and shifted equatorward. The implied Ekman heat flux provides a non-negligible contribution. The combined upper ocean energy flux, Figure 4.6(g), has strong anomalous fluxes, over  $50 \text{ W m}^{-2}$ , into the ocean between  $65^\circ\text{N}$  and  $45^\circ\text{N}$  and anomalous fluxes out of the ocean, up to  $40 \text{ W m}^{-2}$ , from  $45^\circ\text{N}$  to  $25^\circ\text{N}$ . Note that once the net atmosphere-surface flux is considered in conjunction with the implied Ekman heat flux the transition between anomalous positive and negative flux is shifted equatorward, particularly near to the western boundary current region. This is important because the Ekman response acts to ‘pull’ the positive flux into the ocean towards regions of shallower mixed layer depth, potentially enabling the anomaly to have a more significant impact on the ocean heat budget. Overall the signal is one of cooling in the sub-tropical gyre and warming in the sub-polar gyre with exact magnitude of change being dependent on the local mixed layer depth.

It is worthwhile noting that the thermocline depth will more than likely respond to changes associated with surface negative NAM regime following SSWs (for those events that do have anomalies which descend) as highlighted by Zhai et al. [2014]. There will also be variations in Ekman suction and pumping when there are strong implied Ekman heat transport anomalies. For more detailed and accurate quantification of the oceanic impact following SSWs a coupled atmosphere-ocean general circulation model is required, see Chapter 7, that takes into account both dynamic and thermodynamic ocean heating, as well as spatial variations in thermocline depth. A model which fails to simulate variations in thermocline depth will not accurately capture the rates of change to the mixed layer heat budget.

## 4.4 Discussion and Conclusions

This chapter has investigated the impacts of splitting and displacement sudden stratospheric warmings on the surface climate and ocean in the IGCM4; a model which represents the stratospheric circulation and SSW behaviour well. There is a heightened ability for anomalies associated with splitting events to descend into the troposphere and reach the surface. There are negative NAM anomalies in the troposphere for the splitting composite which persist for over 30 days. This behaviour is consistent with the findings of Mitchell et al. [2013a] but the timescales are different. Anomalies in the IGCM4 rapidly travel through the atmospheric column and reach the surface whereas this takes up to 15 days in reanalysis. This timescale difference is also observed in the surface fields.

In both the IGCM4 and NCEP/NCAR reanalysis datasets there is a weakening

of the climatological winter surface wind stress patterns following SSW events. In the IGCM4 there are strong anomalies following splitting SSWs in the surface wind stress providing a pathway for SSWs to interact with ocean dynamics. The surface wind stress anomalies generate anomalous implied Ekman heat transport which, once combined with the net atmosphere-surface flux, alter the mixed layer heat budget. The displacement events do not have the same impact on the surface climate and ocean; this is consistent with the results of Mitchell et al. [2013a]. When considering ocean impacts splitting and displacement SSWs should be considered as separate phenomena. Reichler et al. [2012] assessed the surface and ocean responses following strong polar vortex events. This study finds a similar spatial pattern in the anomalous surface fluxes but also includes the radiative and implied Ekman heat transport terms to provide a more complete understanding of the surface flux behaviour.

These results highlight the need for different SSW types to be simulated in coupled stratospheric/tropospheric/ocean models. Due to the explicit use of an uncoupled atmosphere general circulation model to isolate the stratospheric influence on the ocean the change in mixed layer heat budget can be qualitatively inferred but not quantitatively presented. A coupled model that resolved the thermocline depth in both spatial and temporal dimensions is required to achieve a detailed understanding of how the mixed layer heat budget responds to SSW events. However, this will also introduce feedback and oceanic mechanisms that will impede the attribution of the response to the stratospheric anomalies. Very speculatively,  $D$  is extremely large during Boreal winter over high latitudes, it is likely that any changes in the mixed layer heat budget poleward of  $55^{\circ}\text{N}$  would be negated by the large mixed layer depths found here. It is more likely that anomalies equatorward of  $55^{\circ}\text{N}$  and in regions near to the coast would have an impact on the mixed layer heat budget. Simulated changes to mixed layer heat budget in a coupled atmosphere-ocean general circulation model following SSW events is directly assessed in Chapter 7.

As discussed above this chapter has presented the findings that splitting events have a heightened ability to impact the surface climate in the IGCM4, a result that also appears in Mitchell et al. [2013a]. However, there is no investigation into the mechanism(s) that could be leading to this. As Gerber et al. [2012] discussed key pathways which control stratosphere-troposphere coupling are difficult to isolate and thus it makes it hard to state with confidence any mechanism which would lead to the difference in average impact on the surface climate. The purpose of this work was to investigate the apparent contradiction in the literature and assess potential oceanic impacts following SSW events. A useful next step would be to investigate

whether a specific stratosphere-troposphere coupling mechanism can be attributed to the results. A few speculate concepts are presented for the interested reader:

1. An initial note is that in the IGCM4 the descent of the NAM anomaly associated with SSWs is barotropic in nature, see Figure 4.2. The timeframe associated with anomaly descent is therefore in accordance with the mechanism outlined by Ambaum and Hoskins [2002], which appeals to instantaneous geostrophic and hydrostatic adjustment to potential vorticity anomalies (discussed in section 2.3.2)
2. Another possible influencing factor is that splitting events are typically associated with an anomalously high wavenumber-two planetary wave component and displacement events are associated with an anomalously high wavenumber-one planetary wave component. The Rossby critical velocity for wavenumber-two planetary waves is lower than that for wavenumber-one planetary waves, see equation 2.1. This could lead to differences in the nature of wave-breaking, reflection and refraction associated with splitting events; for example planetary waves could be reflected at a lower stratospheric level. This could then lead to differences in the nature of average coupling with the troposphere during these events. Nath et al. [2016] displayed that planetary wave reflection was a crucial component to the stratosphere-troposphere coupling which occurred during the SSW of January 2013.

As a final note the relative importance of stratosphere-troposphere coupling mechanisms is an open question for the scientific community and more work needs to be done in this field, beyond the limited discussion above. If progress could be made into the generalised impacts following different coupling pathways this would be useful for forecasting and modelling communities.

## Chapter 5 - Empirical Orthogonal Function Analysis Applied To Sudden Stratospheric Warmings

### 5.1 Introduction

Climate science data sets are often large in size, contain high frequency signals and are affected by many forcing factors. This can make it difficult to isolate the important modes of variability. Statistical methods are often employed to reduce the dimensionality of the data and provide useful, objective methods by which to analyse it. One such method is empirical orthogonal function (EOF) analysis which isolates vectors that are orthogonal and linearly project onto the data of interest. The maximal amount of variability is retained by the leading modes which allows for reduction of the dimensionality of the data, making it more straightforward to analyse, whilst minimising the amount of information lost when truncating the modes of variability.

It is apparent that SSW events are highly variable in nature with only some events leading to strong stratosphere-troposphere coupling. In Chapter 4 it was concluded that on average in the IGCM4 splitting SSWs had a stronger impact on the surface climate than displacements; although the mechanisms behind this are unknown. EOF analysis is now applied to extract the different spatial modes of variability between SSW events and assess whether any particular mode is linked to enhanced surface impacts. If this is the case then this mode may prove useful as an early indicator of a heightened probability for strong surface impacts. If there are different spatial modes associated with splitting or displacement events then this may also provide a more formal and less subjective distinction between the two classes of events.

### 5.2 Mathematical Formulation of EOFs

EOF analysis is often conducted on one pressure level where the data matrix is in a three-dimensional form consisting of time, latitude and longitude. Mathematically the dataset is a matrix in the form  $\mathbf{D}_{np_y p_x}$  which represents a  $n \times p_y \times p_x$  matrix. Here  $n$  is the number of independent temporal data points,  $p_y$  is the number of latitudinal data points and  $p_x$  the longitudinal data points ( $n, p_y, p_x \in \mathbb{N}$ ). This is then collapsed into a two dimensional matrix for the EOF analysis such that  $\mathbf{D}_{np_y p_x} \equiv \mathbf{X}_{np}$  where  $p = p_y \times p_x$  and

$$\mathbf{X}_{np} = \begin{array}{c} \xrightarrow{\text{space}} \\ \left[ \begin{array}{cccccc} x_{11} & x_{12} & x_{13} & \dots & x_{1p} \\ x_{21} & x_{22} & x_{23} & \dots & x_{2p} \\ \vdots & \vdots & \vdots & \ddots & \vdots \\ x_{n1} & x_{n2} & x_{n3} & \dots & x_{np} \end{array} \right] \\ \downarrow \text{time.} \end{array}$$

The data is then centred in time to formulate the anomaly matrix, where the temporal average is

$$\langle \mathbf{X}_p \rangle = \frac{1}{n} \sum_{k=1}^n x_{kp} = \left[ \langle x_1 \rangle \quad \langle x_2 \rangle \quad \langle x_3 \rangle \quad \dots \quad \langle x_p \rangle \right]$$

and the anomaly matrix is  $\mathbf{X}_{np}^* = \mathbf{X}_{np} - \langle \mathbf{X}_p \rangle$ . Anomaly data are weighted by the cosine of latitude to stop poleward data-points artificially influencing the EOFs [Hannachi, 2004]. From the anomaly matrix,  $\mathbf{X}^*$ , the covariance matrix,  $\mathbf{A}$ , is formed which is a  $p \times p$  matrix where entry  $ab$  contains the covariation between spatial point  $a$  and spatial point  $b$ . This matrix is symmetric and entries on the diagonal are the variance of the corresponding spatial point.

The EOFs are the eigenvectors,  $\mathbf{v}$ , of the anomaly data covariance matrix with the total variance captured by each EOF represented by its eigenvalue,  $\lambda$ , which are positive by construction and usually converted into a percentage. The EOFs are then ordered by the amount of variance explained such that the leading mode accounts for the most variance. In this context the eigenvectors can be interpreted as orthogonal modes of spatial covariability within the data [Dawson, 2011].

The sign of eigenvectors are arbitrary due to their satisfying

$$\mathbf{A}\mathbf{v} = \lambda\mathbf{v}$$

which captures the inherent nature of eigenvectors. Under the transformation of matrix  $\mathbf{A}$  (recall that  $\mathbf{A}$  is the covariance matrix) the eigenvectors directionality is preserved, thus the mapping is a linear transformation of the eigenvector.

The covariance matrix can be reconstructed from the set of eigenvalues and eigenvectors [Dawson, 2011] as

$$\mathbf{A} = \lambda_1 \mathbf{v}_1 \mathbf{v}_1^T + \lambda_2 \mathbf{v}_2 \mathbf{v}_2^T + \dots + \lambda_p \mathbf{v}_p \mathbf{v}_p^T$$

where the subscript now represents the  $k^{\text{th}}$  eigenvector or eigenvalue such that  $k \in \{1, \dots, p\}$ .

Principal components, PCs, represent the temporal evolution of the eigenvectors. They are formulated by projecting the EOF structures back on to the weighted anomaly matrix [Hannachi, 2004], more specifically

$$\mathbf{C}_k(t) = \sum_{s=1}^p \mathbf{X}^*(t, s) \mathbf{v}_k(s),$$

where  $t$  is time,  $s$  is space and  $\mathbf{C}_k$  is the principal component series associated with the  $k^{\text{th}}$  EOF. Quite often it is useful to standardise the principal components for ease of inter-comparison.

The anomaly field can be reconstructed from the EOFs and (unstandardised) PCs such that

$$\mathbf{X}^*(t, s) = \sum_{k=1}^p \mathbf{C}_k(t) \mathbf{v}_k(s).$$

Due to the statistical nature of EOF analysis, particularly due to the orthogonality constraint, eigenvectors can sometimes turn out to be mathematical artefacts rather than meaningful physical modes. Such a statistical analysis should therefore always be supported by a plausible physical interpretation.

A sensible precaution is to also ensure that the eigenvectors are distinct physical modes of spatial variability. North's rule of thumb [North et al., 1982] can be applied which assesses whether eigenvectors account for similar amounts of variability and are likely to be mixed. If the difference in variance accounted for between an eigenvector and its closest neighbour is less than the error associated with its eigenvalue then it is likely that the two eigenvectors are mixed and the EOF analysis is degenerate from that mode onwards.

### 5.3 Application of EOF Analysis to SSW Events

To isolate the modes of variability between different sudden stratospheric warmings the total geopotential height at 10 *hPa* is averaged from the date of zonal mean zonal wind reversal at 10 *hPa* and 60°N, hereafter denoted by lag 0, up until 15 days afterwards. This provides a representation of the average structure of each event in the stratosphere independently from the classification procedure and removes high frequency noise that leads to computational issues in the EOF analysis. There is one temporal sample for each event with all samples being independent from one another. From the total geopotential height data the anomaly matrix is formulated and weighted as outlined in section 5.2. This is then used to create the EOF structures, assess their degeneracy and create the associated PCs.

To quantify whether any particular EOF mode is associated with surface climate impacts the correlation between the PC temporal series and a temporal series formulated from the surface NAM is calculated. If any spatial mode displays a strong

correlation with the surface NAM then this may imply enhanced stratosphere-troposphere coupling when this spatial mode is present in the SSW evolution.

To assess if one spatial mode of variability is associated on average with either splitting or displacement SSWs the average PC values are formulated for both subsets of events and the total field is reconstructed using these values.

This methodology is constructed specifically to isolate variability between different SSW events. If a specific spatial mode is found to be related to strong surface impacts then this may have the potential to be incorporated into forecasting efforts to aid predictive skill of extreme NH winter conditions. Furthermore it could lead to insights into the mechanism behind SSW stratosphere-troposphere coupling, i.e. whether it is linked to specific spatial structures in the geopotential height anomaly field.

### 5.3.1 Results

The six leading EOF modes and mean field are presented in Figure 5.1. These are presented together to aid physical interpretation of the EOF modes. Application of North's rule of thumb reveals that the EOF analysis is degenerate in mode 17 with the first 6 modes being particularly well separated and, in order from EOF1 to EOF6, they account for; 32%, 21%, 16%, 10%, 6% and 4% of the variance. Overall these leading modes account for 89% of the variance in the anomaly data. The mean structure of the 113 SSW events displays an average shift of the polar vortex into the 0 to 90°E quadrant with a tail wrapping across the Atlantic and into the Americas ( Figure 5.1(a)). There is a local maximum in geopotential height over the Aleutian region.

The mean field is somewhat illuminating, it provides the basic structure that the EOF modes are contributing to, but it does not capture the variability between events which may be more dynamically relevant. This is captured by the PC values and EOF structures, Figure 5.1(b)-(g), which can be used to reconstruct the anomaly field associated with each event (see section 5.2). One physical interpretation of these EOFs is that the three leading structures influence the general location of the disturbed polar vortex air-mass. EOF1 (Figure 5.1(b)) will shift the vortex structure either towards the European-Atlantic region and deepen the geopotential height field over Europe (for negative PCs) or shift the vortex structure towards Russia (for positive PCs). EOFs 2 and 3 can be interpreted in a similar manner. The fourth EOF structure could be linked to the magnitude of displacement towards the equator or general longevity of the disturbance of the polar vortex breakdown, with positive PC values potentially indicating a longer disturbance/more equator-

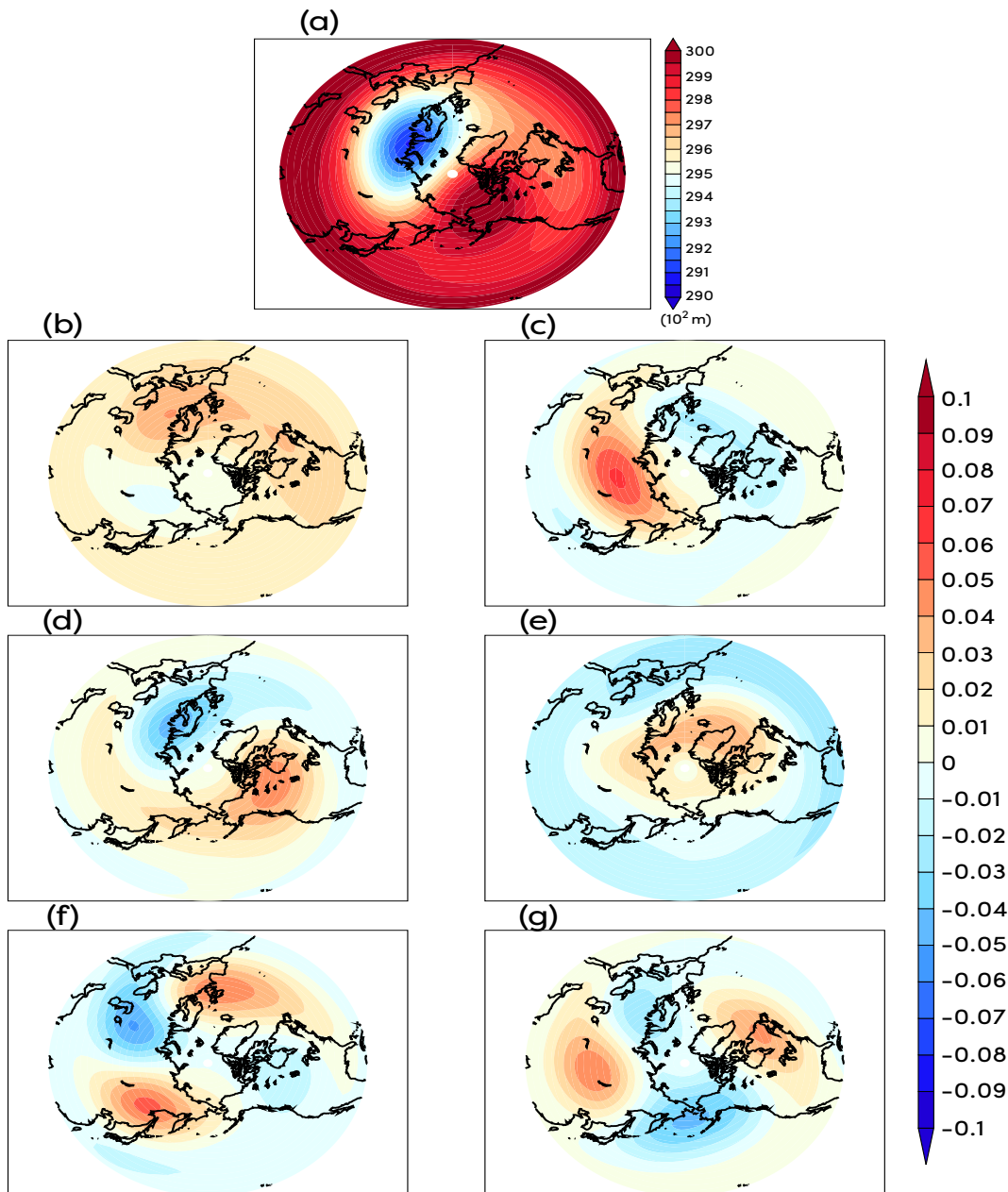


**Figure 5.1:** EOF modes and the mean geopotential height at 10 hPa created from data averaged over 0-15 days for each SSW event: (a) the mean field ( $10^2$  m) and (b)-(g) the six leading EOF modes.

ward displacement. EOF4 could represent the relaxation back to a typical flow regime for each event. It is postulated that the fifth and sixth EOFs reconstruct some of the finer scale features associated with splitting events.

To assess whether a particular mode is associated with stratosphere-troposphere coupling correlations between PC values and the surface NAM index are analysed. The NAM index at 1000 hPa is isolated for each SSW event at lag 0; resulting in a temporal series with length 113. The linear correlation between this and the strato-

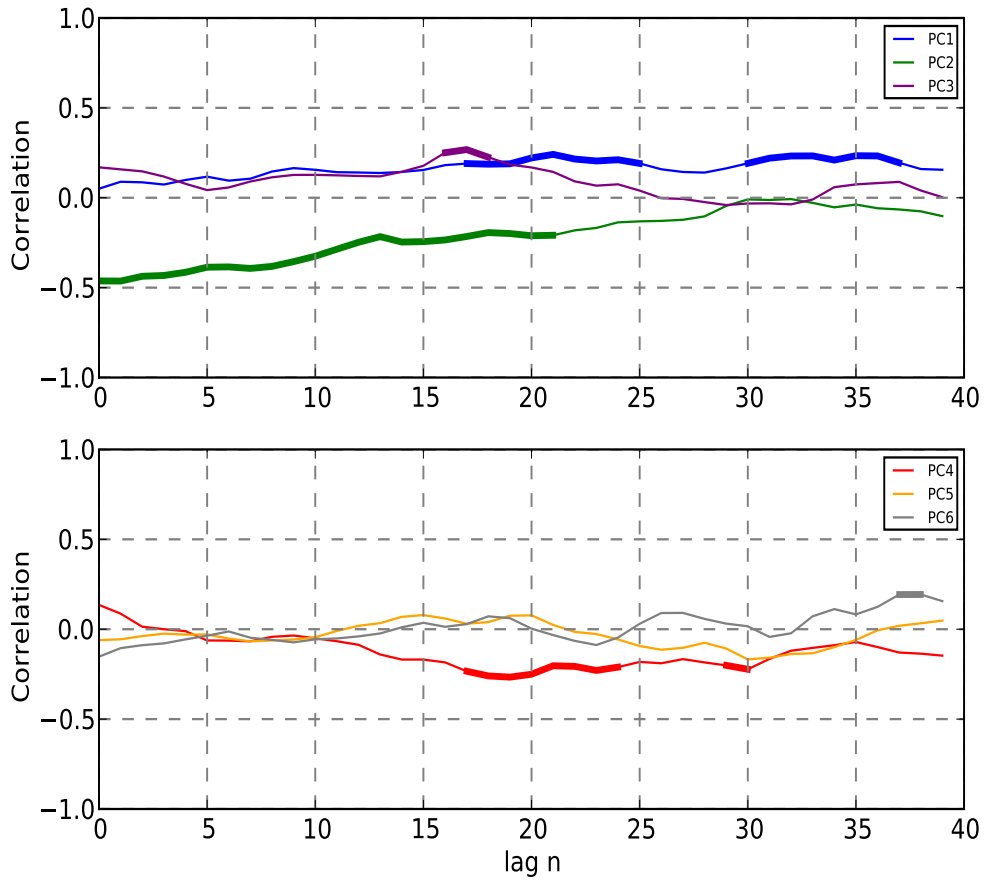


**Figure 5.2:** Correlations between 10 hPa PCs and daily NAM value at 1000 hPa for various lags. Lag  $n$  indicates  $n$  days after zonal mean zonal wind reversal at 10 hPa and  $60^\circ\text{N}$ . If the correlations have  $p$ -values of less than 0.05 then the line is emboldened.

spheric PC values is formulated using a Pearson correlation test if both series are likely to be normally distributed, otherwise a Spearman correlation test is applied<sup>5</sup>. This is then repeated using temporal NAM series calculated at lag 1, I.e. one day after the stratospheric zonal mean zonal wind reversal, up to lag 40. This assesses the temporal evolution of the correlations between daily surface NAM values and the different stratospheric spatial modes. Correlation values are presented in Figure 5.2. If there is a less than 5% chance that the correlation could have occurred from uncorrelated series then the line is emboldened ( $p$ -values are less than 0.05).

It is clearly evident that PC2 has a large correlation with the surface NAM which

<sup>5</sup>The use of different correlation tests could potentially lead to artificial jumps in the correlations evolution over time. The method was repeated using only the Spearman correlation test and it was found that the quantitative results remained similar (no artificial jumps are introduced by the inclusion of the Pearson test).

is consistently strong from the zonal mean zonal wind reversal in the stratosphere up until 21 days afterwards. The correlation is negative implying a negative NAM value at the surface is associated with a positive EOF2 structure and vice versa. Physically this indicates that when the polar vortex is disturbed and shifted towards the Atlantic/Canadian region (on average over the 15 days following the wind reversal) then it is often associated with a negative surface NAM. It could also imply that if the polar vortex is shifted towards the Russian region then it is associated with positive surface NAM values. It is worth noting that the correlations only indicate the covariance of the two timeseries, it does not necessarily imply strong anomalies at the surface or strong PC values in the stratosphere. Also there is no way to determine the directionality of the signal, the only conclusion that can be firmly stated is there is an anti-correlation between the series.

The other noteworthy, significant correlations occur for PC1 (between lag 17 to 25 and lag 30 to 37) and PC4 (between lag 17 to lag 24). The positive correlation for PC1 could indicate that negative surface NAM values are associated with a disturbed stratospheric polar vortex situated towards the European region in the 15 days following zonal mean zonal wind reversal (or equally positive NAM values being associated with a disturbed stratospheric polar vortex situated towards the Russian region). For this to make physical sense it is likely that the directionality of the signal is from the stratosphere into the troposphere although the correlation could also be due to some external forcing factor that is affecting both series. The negative correlation for PC4 could indicate that events which are consistently strong or particularly displaced equatorward over the 15 day period following zonal mean zonal wind reversal are more often associated with negative surface NAM values 17 to 24 days following the zonal mean zonal wind reversal.

To assess whether a specific spatial mode separates the variability between splitting or displacement events average PC values for both subsets are formulated and presented in Table 5.3 along with the 1000 *hPa* surface NAM value averaged from lag 0 to lag 30 for each event and then averaged for both subclasses of SSW. The averaged total geopotential height is reconstructed from these PC values and it is found that the leading 6 modes reproduce the large scale field reasonably well (fig-

**Table 5.3:** Average PC values for splitting and displacement composites and the average NAM value at 1000 *hPa* from lag 0 until lag 30.

	NAM	PC1	PC2	PC3	PC4	PC5	PC6
Splitting	-0.74	-0.29	0.19	-0.11	0.04	0.11	-0.01
Displacement	-0.22	0.22	-0.14	0.08	-0.03	-0.08	0.01

ures omitted). There is no PC which stands out as being strongly associated with splitting or displacement events (at least when they are averaged over the 15 day period implemented). The 15 day average splitting composite has a ‘tail’ which is located from Western Europe across the Atlantic and into the Americas. This is most likely a smeared out representation of the Canadian daughter vortex and is reconstructed via the negative PC1 value and positive PC2 value. As would be expected from the results of Chapter 4 the average surface NAM value is stronger for the splitting composite. This ‘tail’ is not evident, unsurprisingly, in the displacement composite and the polar vortex is localised towards the Eurasian sector, reconstructed mainly through the positive PC1 and negative PC2 values.

The anti-correlation between PC2 and the surface NAM may be a result of splitting events being associated with stronger tropospheric and surface NAM values and also typically containing daughter vortices that lead to more negative PC2. In other words the anti-correlation could occur coincidentally. To verify whether this is likely the 10 events that are associated with the most negative NAMs at the surface (averaged from lag 0 up until 30 days afterwards) are isolated and reconstructed from their associated PC values. There are 5 splitting and 5 displacement events in this set where 8 out of the 10 have negative PC1 values and 9 out of 10 have positive PC2 values. The mean PC2 is 0.86 with a standard deviation of 0.6. It is evident that all events are individual and reconstruction should be done on a case by case basis; however, there does appear to be some pattern in behaviour for these 10 events with stronger surface NAM values which have a shift of the polar vortex towards the Atlantic sector. Importantly displacement events that have a strongly positive PC2 are associated with negative surface NAM values.

To provide a quantitative interpretation on how PC values for splitting and displacement events are associated with the surface climate, the correlation to the surface NAM for PCs subcategorised into just splitting and displacement events is formulated and the results are displayed in Figure 5.4. The anti-correlation between PC2 and the surface NAM persists from lag 0 to lag 16 for the displacement events but decays quickly for the splitting events which becomes weak and dismissible by lag 6. This is interesting since on average the splitting events are associated with stronger surface climate impacts. Explanations for this could include;

1. Upon subcategorisation the smaller data sets leads to less signal being evident.
2. The correlation is stronger for displacements but it is less likely for displacements to project onto a positive PC2 and hence have a weaker average surface climate impact.

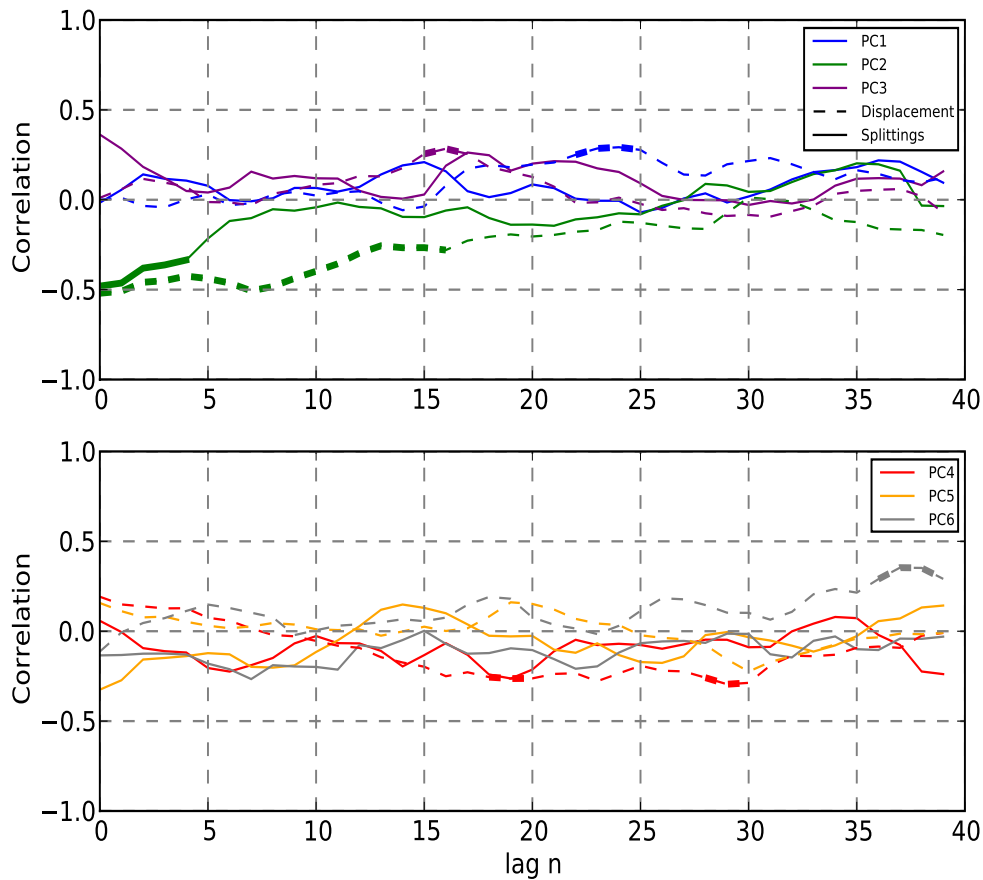


**Figure 5.4:** Correlations between 10 hPa PCs and daily NAM value at 1000 hPa for splitting and displacement subcategories for various lags. Layout as in Figure 5.2 where solid/dashed lines represent the splitting/displacement event data.

3. The utilisation of zonal mean zonal wind reversal as ‘lag 0’ is inappropriate for the spatial covariability associated with splitting events since on average the zonal mean zonal wind reverses at 10 hPa and 60°N 2-3 days prior to the splitting of the vortex.

To address the third point the analysis was repeated with ‘lag 0’ set to when the kurtosis threshold is met for splitting events, see Chapter 2, and kept as zonal mean zonal wind reversal for the displacement events. Overall the broad scale features of the leading EOF structures are generally similar, with some subtle differences in the smaller scale features. These modes are degenerate, by North’s rule of thumb, in mode 5. The correlation analysis between the surface NAM and the PCs for these new EOF structures is repeated. In the splitting composite there is now an increased correlation between PC3 and the surface NAM. This correlation is around +0.4 and

not insignificant between lag 3 and 22. This correlation suggests that for a negative surface NAM there is an increased local minimum over Canada. For displacement events there is sustained not insignificant correlation between PC2 and the surface NAM between lag 0 and 21, initially with a value of around -0.5 and reducing to -0.3 by lag 21. In using kurtosis as a basis in the formulation of EOF structures there is more separation in the spatial modes associated with splitting and displacement events. However, these modes have a higher degeneracy and are less objective in their construction violating the initial aims of the EOF methodology.

### 5.3.2 Discussion

Overall the current EOF analysis does not isolate a particular spatial mode that could be helpful in creating an objective classification technique for splitting and displacement SSWs. There is a negative correlation between the second PC and surface NAM indicating that for negative surface NAM regimes the disturbed polar vortex is situated towards the Atlantic/W.Europe/Canadian sector. This relationship is evident for splitting and displacement events with the displacement subset contributing to the majority of the longer term (up to lag +21) correlation signal. Due to the statistical nature of the EOF analysis and limitations of correlation analysis it would be practical to assess the geographic influence on surface impacts in an independent manner from the methodologies utilised here, see section 5.5.

The EOF methodology is adjusted to create EOFs from rotated geopotential height fields in an attempt to isolate modes of variability distinct to splitting and displacement events. This also removes any geographic dependence in the EOF modes and has the potential to capture covariability in spatial structures and the surface NAM more clearly.

## 5.4 EOF Analysis Applied to Rotated Fields

The polar vortex disturbance associated with SSW events is a complex phenomenon where the vortices spatial structure is distorted whilst often simultaneously being displaced off the pole. Once displaced away from the pole the vortex can then follow an atypical trajectory, often in a retrograde fashion [Matthewman et al., 2009]. In creating EOF structures from 15 day averaged fields, as in the previous section, small to medium scale spatial features can be averaged out; particularly if the vortex is rotating quickly around the pole. This could lead to important features inadvertently being removed from the analysis.

To create a methodology that does not lose coherent spatial features EOFs are created from geopotential height fields rotated such that the center of the polar

vortex remains in the same spatial location. To construct these new ‘rotated’ EOFs the total geopotential height field at 10  $hPa$  is isolated for each event from the zonal mean zonal wind reversal, lag 0, up until 15 days afterwards, lag 15. This is a slice containing 15 daily averages. At each time-step the total geopotential height field is rotated so that the longitude containing the minimum geopotential height, representative of the centroid of the polar vortex, is now situated at  $47^\circ E$  (this is the centroid of the composite of all events). From these rotated geopotential height fields the 15 day averages are calculated. This again results in one temporal sample for each event, alleviating computational issues from high frequency noise and ensures all samples are independent. The analysis then proceeds as in Section 5.3. Two case studies of the rotated geopotential height fields are presented in Appendix B.

This new methodology has the primary advantage that any consistent spatial structures, that may be transient in space but coherent in time, are preserved even after the 15 day averaging. The other advantage is that the new EOF structures will have no longitudinal dependence, they will only represent the covariability in the spatial structure of the disturbed polar vortex and the magnitude of any displacement towards the equator.

An issue in the new EOF methodology is introduced by the use of the geopotential height minimum as a proxy for vortex centroid location. The vortex is rotated daily from this identified centroid longitude and unphysical jumps in the rotation occur when there are two daughter vortices that switch dominance in the 15 days following lag 0. This occurs in 11 out of the 48 splitting events. It is also observed that artificial jumps also occur in 4 out of the 65 displacement events, during the breakdown of the disturbed vortex and filamentation leading to sudden changes in the ‘centroid’ location. A more complicated algorithm could be used that tracks the centroid more smoothly to stop these artificial jumps. This analysis is beyond the scope of this work but could provide an interesting test of the robustness of the modes isolated here.

#### 5.4.1 Results

The new leading EOF structures are presented in Figure 5.5. The composite of 15 day averaged total geopotential height at 10  $hPa$  for all 113 SWSs is presented in panel 5.5(a) with the six leading EOF modes in panels 5.5(b) to (g). By North’s rule of thumb the EOF structures are degenerate in mode 6, signified by a line across panel 5.5(g), and account for 41%, 15%, 14%, 11%, 4% and 3% of the variability respectively. Figure 5.5 is directly comparable to Figure 5.1 which presents the

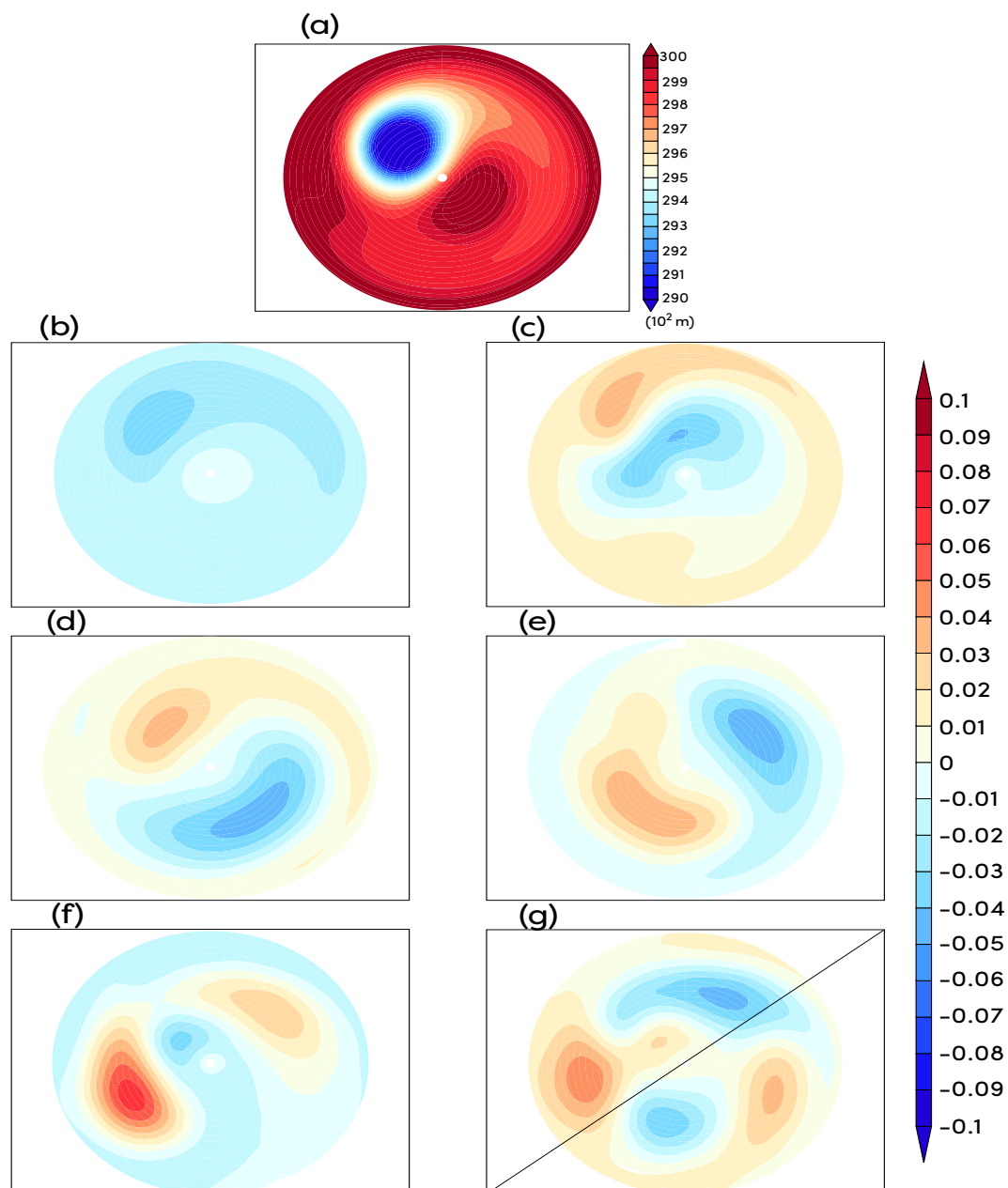


**Figure 5.5:** EOF modes from rotated fields and mean geopotential height at 10 hPa created from data averaged over 0-15 days for each SSW event: (a) the mean field ( $10^2$  m) and (b)-(g) the six leading EOF modes.

modes from the EOF analysis from unrotated fields.

The spatial structures captured by the EOFs created from rotated geopotential height fields are now notably different from the previous analysis. One reasonable physical interpretation of these modes would be that the leading mode captures the variability in the overall magnitude of the geopotential height field. The second mode is a measure of the equatorward shift of the polar vortex. The third and fourth modes could be used to reconstruct a second daughter vortex and the fifth

**Table 5.6:** Average rotated analysis PC values for splitting and displacement composites and the average NAM value at 1000 hPa from lag 0 until lag 30.

	NAM	PC1	PC2	PC3	PC4	PC5	PC6
Splitting	-0.74	0.21	-0.16	0.35	0.19	0.01	-0.07
Displacement	-0.22	-0.15	0.12	-0.26	-0.14	-0.01	0.05

mode could be used to construct a splitting structure that is orthogonal to mean field.

As before the PCs are formulated and averaged for splitting and displacement subsets to assess whether any particular mode forms a clear distinction between the two classes of events and could be used for classification purposes. The results are presented in Table 5.6. PC3 appears to show some promise, having an averaged value of 0.35 and -0.26 for the splitting and displacement subsets respectively, however the averaged magnitude of PC3 is not large enough to be confidently separated from any background noise or round-off errors. Additionally PC2 appears to indicate that splitting events are, on average, more equatorward than the displacement events in the 15 days following zonal mean zonal wind reversal. However, this behaviour is not observed in the 850 K Ertel’s potential vorticity (EPV) field, taken as an average from lag 0 to 15 with no rotation.

The PCs associated with the 10 events that have the strongest surface NAM, averaged from lag 0 to lag 30, have low values for all PCs apart from PC2 which has an averaged value of -0.62. The correlation between the PC values and daily NAM values is presented in Figure 5.7, particularly PC2 has a strong correlation to the surface NAM between lag 13 to lag 30. PC3 also has a strong correlation to surface NAM between lag 0 and lag 21. Upon subcategorisation into splitting and displacement events (figure omitted) the strong correlation between PC3 and the surface NAM disappears leading to the conclusion that this correlation is not robust. The correlation observed between PC2 and the surface NAM is mainly attributable to the splitting event. This positive correlation would lead to the conclusion that for negative surface NAM values the disturbed polar vortex would be more equatorward. If this correlation was meaningful for interpretation of a negative NAM response following SSWs it seems surprising that more equatorward splitting events are associated with stronger surface impacts whereas their displacement counterparts have no perceptible relationship between their magnitude of displacement and the surface impacts.

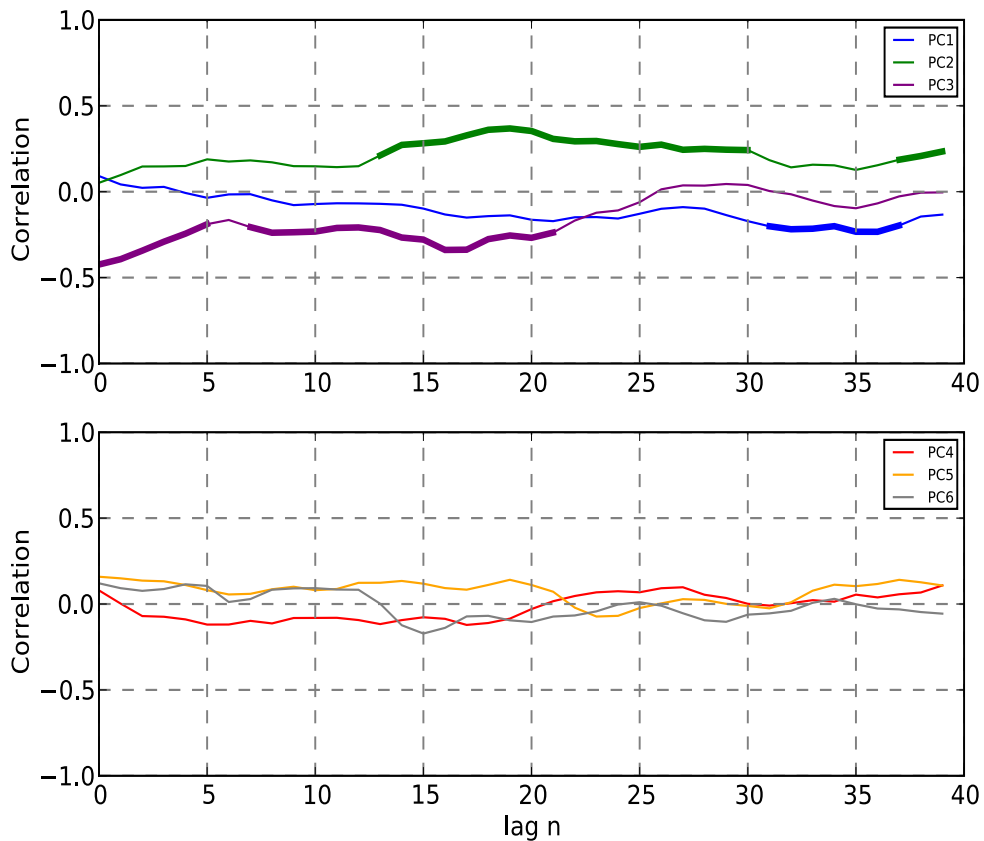


**Figure 5.7:** Correlations between 10 hPa rotated analysis PCs and daily NAM value at 1000 hPa for various lags. Lag  $n$  indicates  $n$  days after zonal mean zonal wind reversal at 10 hPa and  $60^\circ N$ . If the correlations have  $p$ -values of less than 0.05 then the line is emboldened.

#### 5.4.2 Discussion

Overall, EOFs created from rotated geopotential height fields have not led to any spatial mode being isolated which could be used to objectively classify splitting and displacement SSWs. The second PC appears to indicate that events which are displaced further equatorward than the average SSW event could be associated with stronger surface impacts. Due to the fact that this behaviour is not observed in the mean EPV field at 850 K this calls into question the validity of this interpretation.

This new EOF analysis still contains many of the limitations discussed in the previous analysis, such as the use of correlations and the statistical nature of EOF modes. The artificial jumps introduced by the rotated EOF algorithm only adds to the complications of interpreting meaningful results. Moreover; even this methodology does not provide any advantage in isolating a spatial structure that provides an objective distinction between splitting and displacement events. This leads to the conclusion that it is unlikely EOF analysis employed in this manner could be

used to formulate an objective classification procedure.

It is somewhat ironic that even when trying to create a methodology that minimises geographical dependence, the only mode which appears to contain this dependence (that is how far equatorward the vortex is initially displaced over the 0-15 day period) contains the only strong, robust and not insignificant correlation to the surface. Results from the EOF analysis from unrotated fields, section 5.3.1, also showed promise in a relationship between the geographic location of the disturbed polar vortex and the strength of stratosphere-troposphere coupling. It is worth investigating this point further as it could potentially lead to an enhanced understanding of stratosphere-troposphere coupling and why only some SSWs impact the surface climate.

## 5.5 Assessing Impacts via Disturbed Vortex Trajectory

In the previous analysis there was emerging evidence for a relationship between the geographical location of the disturbed polar vortex and strong surface impacts. In section 5.3 it appeared that events which were initially displaced towards the Atlantic/W.Europe/Canadian sector were associated with negative NAM regimes at the surface for up to a month following event occurrence in the stratosphere. Deducing relationships between the surface NAM regime and the behaviour of PC values at 10 *hPa* was troublesome due to conclusions being equally valid for negative NAM and positive NAM regimes. Furthermore the correlations implied no directionality of the signal and EOF structures are highly statistical in nature. This all led to difficulty in physical interpretation. To assess the conclusions of sections 5.3 a highly simplified algorithm is developed with the aim of independently assessing surface impacts following SSW grouped by the disturbed polar vortex trajectories.

To initially test the validity of this approach the opposite statement of *'where is the polar vortex situated for events grouped via their surface impacts?'* is assessed. The type of surface impact is evaluated by averaging surface NAM values from lag 0 to lag 30. Groups are then constructed from this averaged NAM value where it is positive; between 0 and -1; between -1 and -2 and less than -2. The location of the polar vortex is then quantitatively represented by the total fraction of polar air contained at each longitude. The polar air mass is formulated as outlined in Appendix A. The mean fraction of polar air at each longitude (displayed as a percentage) and the standard deviation is presented in Figure 5.8. The data are separated for the splitting and displacement subcategories. Figure 5.8 displays a westward shift in the location of the disturbed polar air mass with increasingly negative average surface NAM values, in agreement with the results of section 5.3. This trend is

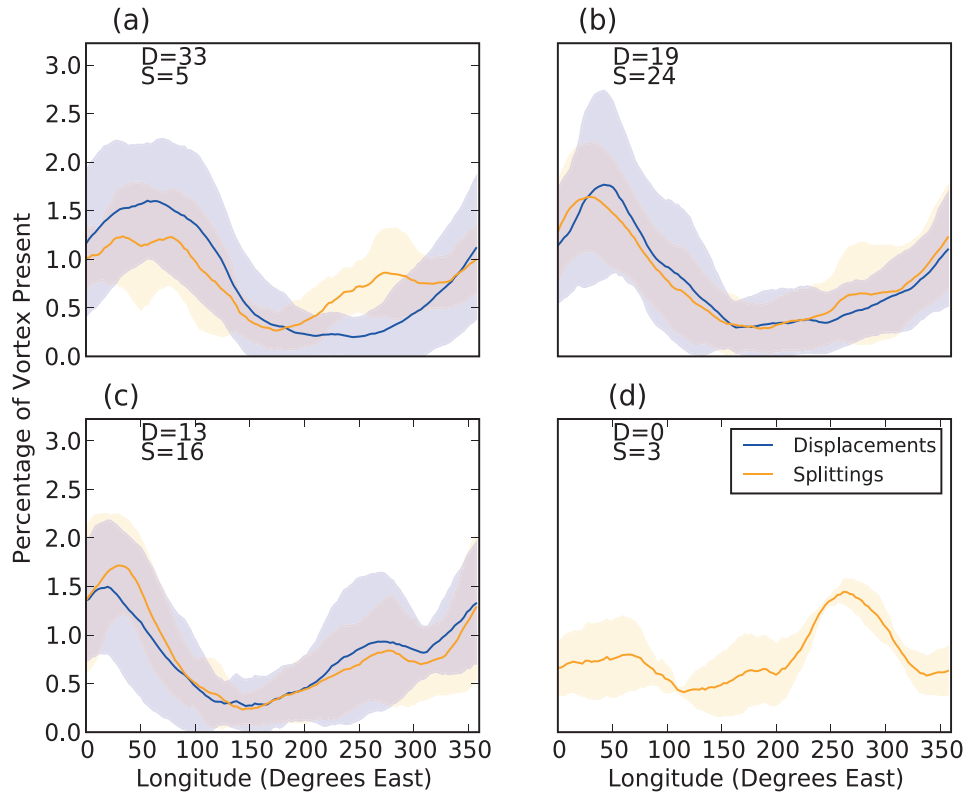


**Figure 5.8:** Polar air mass average location, between lag 0 to 15, as a function of surface NAM. NAM averaged from lag 0 to lag 30 and categories created from events with values that are: (a) positive, (b) between 0 and -1, (c) between -1 and -2 and (d) less than -2. Standard deviation at each longitude is represented by shading. Number of displacements,  $D$ , and splittings,  $S$ , in each samples displayed in top left of each panel.

also observed when the subcategories are created from a NAM averaged from lag 0 to 15 and lag 5 to 35. There are not enough sample members in panel 5.8(d), for the results to be meaningful. These preliminary results suggest that assessing the surface response based on the initial trajectory of the disturbed polar vortex may lead to isolating events which have a greater probability of strongly impacting the surface climate.

Motivated by the previous results a simple algorithm is created to isolate events that pass through a specific geographic region. This region is taken as a box from 125°W to 30°E and between 50°N to 80°N, see Figure 5.9. The region is justified as; it matches the negative centre in the EOF2 structure (isolated from the unrotated analysis) as depicted in Figure 5.1(c) and it is a boundary of separation between the subclass of events in 5.8(a) and 5.8(c). This analysis is also repeated with the region expanded and reduced by 5° with the results not displaying sensitivity

to these variations.

An event is isolated as ‘passing through’ the region presented in Figure 5.9 if at least 50% of the region contains polar air for five consecutive days between lag 0 and 15 days. A balance must be achieved between stringent enough criteria to ensure the disturbed polar vortex travels through the region of interest and isolating enough events for to allow meaningful results. A total of 20 events were isolated as travelling through the region in the 15 days following zonal mean zonal wind reversal in the stratosphere. EPV fields of the daily evolution of the SSWs were then assessed subjectively to check the disturbed polar vortex trajectories. It was found that one event started in the region but then travelled in a cyclonic direction towards Russia. The 19 other events all had trajectories as expected. The results presented are not sensitive to the exact algorithm criteria used.

In addition, events that ‘did not pass through’ the region presented in Figure 5.9 were also isolated. These are taken as events that have less than 20% of the region containing polar air for at least 10 consecutive days following zonal mean zonal wind reversal. Again this was assessed manually and all events had trajectories as expected. A total of 18 events were isolated.

**Table 5.10:** Total number of events and diagnostics for SSWs grouped via the disturbed polar vortex trajectory. The average PC2 value is from unrotated analysis. 1000 hPa composite NAM values averaged from lag 0 to lag 30. Standard error in parenthesis.

	Total	Splittings	Displacements	PC2	NAM
Do Pass Through	20	10	10	0.76 (0.18)	-0.7 (0.19)
Do Not Pass Through	18	3	15	-1.05 (0.18)	0.19 (0.13)

### 5.5.1 Results

The total number of events captured by the simple algorithm, along with the number of splitting and displacement events is presented in Table 5.10. For events with a disturbed polar vortex trajectory that passes through the region of interest there is no bias in whether splitting or displacement events are captured. However, for

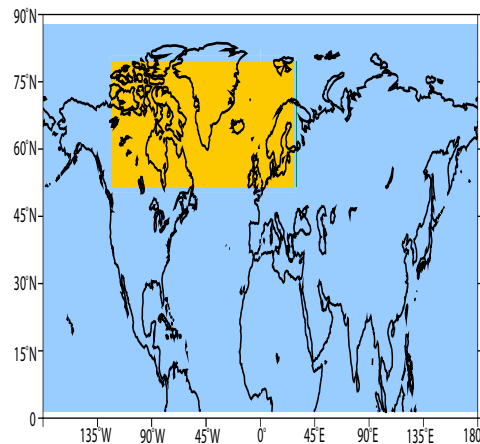


**Figure 5.9:** Region isolated for the polar vortex trajectory analysis.

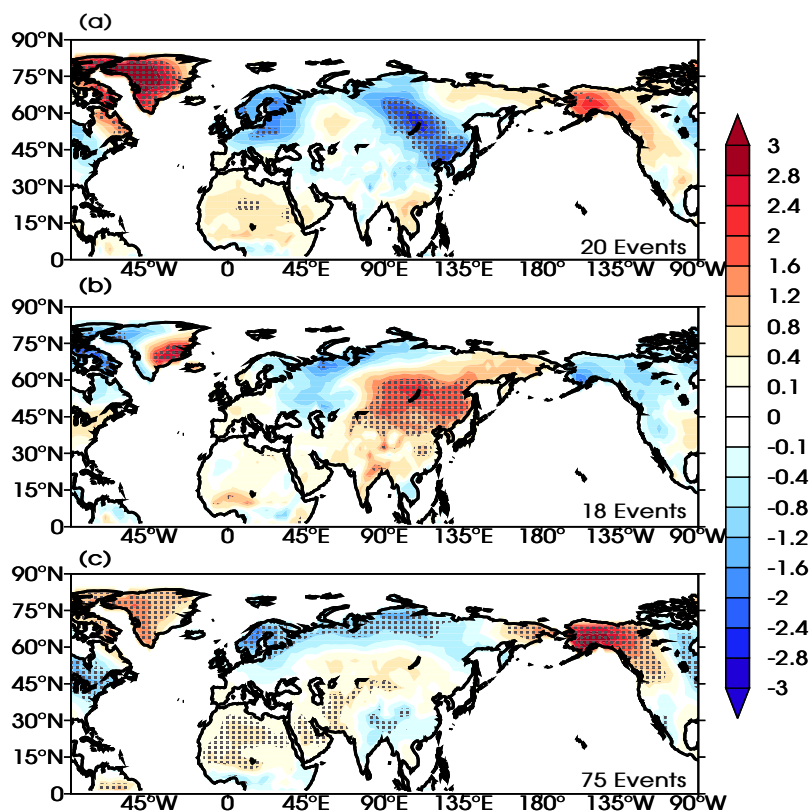


**Figure 5.11:** Surface temperature anomaly composites for SSWs that: (a) do and (b) do not pass through the region presented in Figure 5.9. Composite for all other SSW events presented in panel (c). Number of events in each subset displayed in the lower right corner of each panel. *P*-values less than 0.1 stippled.

events with a trajectory that do not pass through there are far more displacement events captured. As one would expect the events that pass through the region project positively onto the EOF2 structure. To assess the average impact on the surface climate following these SSW events the surface NAM value is isolated and averaged from lag 0 to lag 30. Events that have a trajectory which pass through the EOF2 negative region have a stronger average negative NAM value at the surface. For events with a trajectory that do not pass through the region the average NAM value is weakly positive. This indicates a clear difference in the average surface climate following the two classes of events isolated by the algorithm.

The NAM value is a good indicator of average surface regimes; however it is also illuminating to inspect two dimensional surface variables. The surface temperature anomaly composite is presented in Figure 5.11. For the SSW events that have a displaced polar vortex trajectory which pass through the region there is a surface temperature pattern which is associated with a negative NAM regime and SSW surface impacts [Mitchell et al., 2013a]. When this is subdivided into splitting and displacement events both groups display the warm Greenland/cold western

European pattern with no statistically significant differences at any grid point. For the events with a trajectory that do not pass through the regions the average surface temperature response is not typical of a SSW impacts at the surface.

### 5.5.2 Discussion

The average response following SSW events which pass through the EOF2 negative region is one of a positive PC2 and negative surface NAM regime, with the associated surface temperature response being evidence. It appears as though the algorithm is able to isolate events which are accompanied by enhanced stratosphere-troposphere coupling and strong surface climate impacts. However, it is noted that there is variability between events and although the average response is very promising not all events lead to a positive PC2 and/or the negative NAM type surface impacts. It is clearly evident that using averaged response as a measure of predictability is an oversimplification.

Another noteworthy point is that this approach only isolates one set of events which are accompanied by enhanced stratosphere-troposphere coupling. There are clearly events that are not captured by this algorithm that strongly impact the surface climate as shown in Figure 5.11(c). It is worth remembering that this is not the only subcategory of SSWs that are related to enhance stratosphere-troposphere coupling. What is interesting is that splitting and displacement events isolated by this algorithm have very similar surface impacts, whereas on average in the IGCM4 splitting events are associated with stronger surface impacts. This leads to the speculative hypothesis that the average geographic location and trajectory of the disturbed polar vortex may be more important for stratosphere-troposphere coupling mechanisms than the spatial structure of the event. It could be that splitting events are, on average, more likely to travel through this region. This is a tentative assertion that requires more work to test.

## 5.6 Conclusions

This Chapter had two primary scientific aims. The first aim was to investigate whether EOF analysis could be applied to objectively isolate splitting and displacement events based on their modes of spatial covariability. The second aim was to assess if any particular EOF mode was associated with enhanced stratosphere troposphere coupling.

It has been shown that EOF analysis applied in this manner is not useful for creating an objective distinction between splitting and displacement SSWs, even when a rotated method that removes longitudinal dependence is developed. However, this

method is open to improvement, particularly the algorithm applied to rotating the daily geopotential height fields.

The EOF analysis indicated that there is a relationship between the geographical location of the disturbed polar vortex (between lag 0 and lag 15) and surface climate impacts. This was interpreted as events which are shifted towards the Atlantic/W.Europe/Canadian region are associated with negative NAM regimes at the surface<sup>6</sup>. This hypothesis has been supported by further scientific study. There is a westward shift in the location of the disturbed polar vortex for events grouped by increasingly negative averaged surface NAM values. Events were then isolated with a trajectory passing through the region of interest and on average they are found to have strong surface impacts, which are clearly distinct from events that do not pass through the region. Next research steps should include a more thorough analysis of the precursors leading to events with/without a disturbed polar vortex trajectory over the Atlantic/W.Europe/Canadian region and the mechanism(s) behind the increased stratosphere-troposphere coupling. It would also be prudent to repeat this analysis in a much longer integration, particularly as the sample sizes in section 5.5 are low. Overall this is promising initial work which could aid forecasting efforts

---

<sup>6</sup>Note that event magnitude in the middle stratosphere is not indicative of the strength of associated surface impacts. Therefore this relationship is not a result of stronger events possessing faster retrograde motion and tracking into this region more frequently.



---

## Chapter 6 - The Atlantic Multidecadal Oscillation And Its Modulation Of Stratospheric Behaviour

### 6.1 Introduction

In Chapter 4 a pathway for stratosphere-ocean communication is explored through SSW events. This was conducted in an atmosphere-only general circulation model which was forced with prescribed sea surface temperatures. Configuring the experiment in this manner was beneficial because it enabled the mechanisms in this section of the climate system to be isolated. However, this experimental design is artificially simplistic due to the coupled nature of Earths climate system. Many climatic features will have been over-simplified/neglected; most notably the ocean which is a crucial component of the climate system providing large scale heat and momentum transport and is intrinsically linked to atmospheric dynamics. It is well known that the troposphere is constantly interacting with the ocean. Another area of study is the sensitivity of the stratosphere to oceanic configuration.

Studies have confirmed that the El Niño Southern Oscillation can impact the stratosphere [Ineson and Scaife, 2009, Bell et al., 2009, Manzini, 2009, Li and Lau, 2013]. It is also known that the Atlantic Ocean can fluctuate between warm and cold surface conditions on a multidecadal scale; termed the Atlantic Multidecadal Oscillation (AMO). As discussed in section 6.1.2 the directionality of the AMO-NAO correlation is a debated issue. Furthermore studies that do find a NAM regime response to AMO phase do not agree on whether the stratosphere is necessary to facilitate this response. Particularly Omrani et al. [2014] and Omrani et al. [2015] appeal to shifts in SSW frequency (increased SSW frequency under AMO warm conditions and vice versa) as a mechanism behind the tropospheric NAM response. However, this argument is only implied and there is no direct demonstration of shifts in SSW frequency under specific AMO forcing.

The purpose of this chapter is to explore the sensitivity of the IGCM4 (Chapter 3) to the AMO phase. Cold and warm AMO configurations are implemented with varying strengths to asses any non-linearity in the IGCM4s response. Focus is on the frequency and nature of SSW events under AMO warm and cold conditions. The surface response following a SSW event is also assessed to see whether it is modulated by Atlantic Ocean configuration. The experimental design is discussed further in section 6.2 with general results being presented in section 6.3 and compared to Omrani et al. [2014] in section 6.3.5.

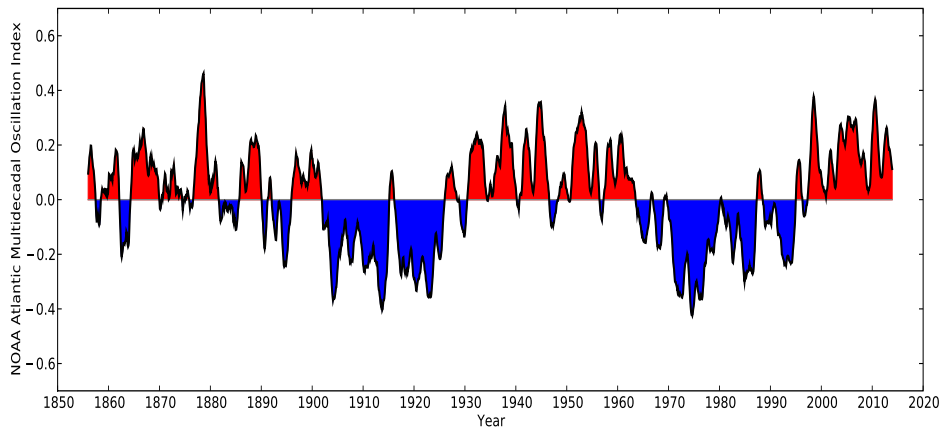


*Figure 6.1: National Oceanic and Atmospheric Administration AMO index, 1856 to 2014, smoothed using a 121 month filter.*

### 6.1.1 The Atlantic Multidecadal Oscillation

Observations suggest that the Atlantic Ocean fluctuates between warm and cold surface conditions with an approximate 60-70 year periodicity. The source of this variability has not yet been rigorously established [Hodson et al., 2010, Omrani et al., 2014], with possible drivers being natural internal variability, such as variations in the Atlantic meridional overturning circulation [Wang and Zhang, 2013], or externally forced by anthropogenic phenomena such as aerosols [Booth et al., 2012]. The decadal timescale of the AMO and the relatively short observational record makes it difficult to determine governing mechanisms. Irrespective of the source of the AMO there have been distinct shifts in its regime over the last 50 years.

The AMO index between 1856 and 2014 is presented Figure 6.1 using the National Oceanic and Atmospheric Administration AMO index [Enfield et al., 2001], downloaded from <http://www.esrl.noaa.gov/psd/data/timeseries/AMO/>. This index is formulated using the Kaplan SST dataset which is in turn created using observational data [Kaplan et al., 1998, Reynolds and Smith, 1994]. After downloading the index has been smoothed using a 121 month running average.

The multidecadal variability in the AMO is evident with the 1930 to 1960 period being dominated by warmer sea surface temperatures and the 1960 to 1990 period containing persistent cold sea surface temperatures. Prior to 1900 there is little discernible multidecadal variability, which may be due to the lack of observational data available from this period.

### 6.1.2 Literary Background

Hodson et al. [2010] conducted a multimodel comparison into the climatic impacts resulting from changes in the AMO phase. They assessed five atmosphere general circulation models, which did not explicitly resolve the stratosphere, and found consistent responses in the climate system over the Americas. During warm AMO conditions there was an increase in Northern Hemisphere summer land temperatures over the United States and a reduction in mean sea level pressure. There was little coherent signal in rainfall over the United States but over northern South America there was an increase/reduction in Southern Hemisphere summer/winter rainfall in all five models with large inter-model variation in the magnitude of this signal. Hodson et al. [2010] did not find any consistent climatic response away from the Americas and particularly not in the winter NAO Index (see section 4.1.1 for a discussion on the NAO).

Peings and Magnusdottir [2014] investigated AMO fluctuations and their connection to winter North Atlantic weather regimes. A particular focus was on the negative correlation they found between the NAO and the AMO. The anticorrelation of these two modes is also reported by Omrani et al. [2014] and Li et al. [2013]. In Peings and Magnusdottir [2014] they assessed this correlation in the 20<sup>th</sup> century reanalysis and found it varied between -0.5 and -0.7 when the AMO led the NAO by 0 to 15 years and was found to be not insignificant at the 95% level. Peings and Magnusdottir [2014] also analysed two 50 year Community Atmosphere Model (CAM5) simulations, one with AMO positive and one with AMO negative surface forcings, along with the 20<sup>th</sup> century reanalysis data and a linkage between NAO-like weather regimes and the AMO phase was detected. During AMO negative conditions there was an increase in the frequency of NAO positive type weather regimes during the December to March period. Under AMO positive conditions there was an increase in the frequency of NAO negative type regimes for the February to March period. This shift in the frequency of weather regimes was attributed to the AMO SST anomalies. In the area where the Atlantic storm track emerges the AMO SST anomalies are greatest and alter the meridional temperature gradient. For AMO warm periods there is more latent heat flux released into the atmosphere which reduces the atmospheric baroclinicity. This in turn leads to a reduction in synoptic scale wave activity which maintains the westerly winds. The peak westerlies are weakened and shift equatorward, leading to the negative NAO regime.

In a study of observational data (HadSST3 SST data; HadCRUT4 land and SST data; NCAR sea level pressure data) by Li et al. [2013] different conclusions

were drawn when assessing the AMO-NAO relationship. Overall they concluded the NAO led the AMO and could potentially be used as a predictor of the AMO phase. They found a strong positive correlation, which was within a 98% confidence level, when the NAO led by  $\sim 15$  years. An anticorrelation when the AMO led was also discovered and was of a similar magnitude to that reported by Peings and Magnusdottir [2014], but was not within a 98% confidence level. The studies of Li et al. [2013] and Peings and Magnusdottir [2014] utilise different reanalysis and observational datasets for both the AMO and NAO index formulation. The sign of covariance agrees between the two studies, so there is a level of consistency in the results, but when the NAO leads the magnitude of covariation is much stronger in the study of Li et al. [2013] and this results in the differences emphasis in their conclusions. Overall in the literature there is some dispute in the direction of the casual relationship between the AMO and NAO. The two modes appear to be correlated but there may also be some level of interaction between them with a direct cause and effect relationship being overly simplistic.

Omrani et al. [2014] also assessed AMO interactions with the atmosphere by comparing model simulations that included and neglected the stratosphere in the standalone Atmospheric General Circulation Model ECHAM5 (the high top version being MAECHAM). This study focused on AMO warm conditions restricted to the  $40^{\circ}\text{S}$  to  $66^{\circ}\text{N}$  region of the Atlantic. The high top AMO warm and control experiments were run forward in time for 100 model years. The low top experiments were run forward in time for 40 model years. They found that there was a shift to NAO negative type surface conditions but only when the stratosphere was resolved. An explanation was put forward where under AMO warm conditions there is an increase in winter zonally averaged poleward eddy heat flux that leads to a deceleration of the stratospheric zonal mean zonal winds and hypothesised that there would be more major SSW events. This in turn promotes a negative surface NAO pattern through the downward NAM anomaly descent that is often associated with SSW events. The opposite argument should hold for AMO cold conditions. In this study they do not explicitly identify changes in SSW frequency in the model experiments.

The above study is extended by further work of Omrani et al. [2015] in a fully coupled atmosphere-ocean model, MPI-ESM which is ECHAM6 coupled to the MPI-OM (see paper for full model details). Here a 500 year pre-industrial control integration is assessed and three further sensitivity experiments performed. The AMO warm and cold phases are identified in the control simulation as one standard deviation from a computed AMO index (this index is an detrended average over  $0^{\circ}\text{N}$  to  $60^{\circ}\text{N}$  and  $75^{\circ}\text{W}$  to  $7.5^{\circ}\text{W}$  over the January-March period). The North Atlantic SST and ice fields from  $40^{\circ}\text{S}$  to  $66^{\circ}\text{N}$  are extracted from periods where the ocean

is neutral, AMO positive and AMO negative. This is then used to force, as a climatology of monthly means, the stand-alone ECHAM6 to create control, AMO warm and AMO cold simulations. All other forcing factors such as green-house gases, ozone and aerosols are kept as in the coupled model control integration. These AMO experiments are run forward in time for 40 years each. Under AMO warm conditions there is a negative NAM shift throughout the atmospheric column over the January to March period and this is twice as strong in the atmosphere-only GCM when compared to the coupled simulation. Under AMO cold conditions there is no consistent response in atmospheric NAM between the coupled and uncoupled versions of the model. In the coupled version there is a tropospheric shift to positive NAM regime in early winter. Again SSW arguments are invoked to explain the observed response. They argue that the influence of anomalies in the 500 *hPa* geopotential height field may go some way to consolidate the results. There is a strong negative anomaly over the Aleutian low for the AMO cold uncoupled experiment which could potentially act to enhance the climatological wave structure and promote upward Rossby wave propagation. This could mitigate the AMO signal by increasing the likelihood of SSW activity in the AMO cold experiment. Overall they conclude that there is the potential for the AMO phase to impact the stratosphere/troposphere coupled system but factors such as interference from other oceanic basins, modes such as the QBO, and model configuration could mitigate this signal. Again there is no presentation of actual SSW frequencies from the experiments.

The work of Omrani et al. [2014] stresses the importance of the stratosphere to facilitate a response in NAM regime to AMO phase. Peings and Magnusdottir [2015] extended the work of Peings and Magnusdottir [2014] to assess the sensitivity of AMO impacts on NAM regime to stratospheric representation. They used a ‘low-top’ (lid at 2.2 *hPa*) atmosphere only GCM, CAM5, and a ‘high top’ (lid at  $5.1 \times 10^{-6}$  *hPa*) chemistry-climate model, WACCM (again see paper for full model details), with year 2000 aerosols and green-house gases, and a nudged QBO. They ran 80 year AMO warm and cold simulations, forced with HadISST observations in the region, 0°N to 85°N, for CAM5 and WACCM. They also conducted an experiment where CAM5 was coupled to a slab-ocean model activated in the Atlantic ocean northward of 40°S where AMO forcing was created by perturbing Q-flux values. They find that there is a shift to negative NAM regime throughout the atmospheric column for AMO positive simulations when compared to AMO negative simulations. This is predominantly in early winter (December-January) in the CAM5 prescribed SST experiments, in later winter (February-March) for the WACCM experiments, and through-out winter for the slab-ocean CAM5 experiments. Importantly, there

is a response in surface NAM regime in these experiments in the 'low-top' CAM5 simulations and, particularly, there is a strong surface response in the slab-ocean configuration with no significant response observed in the stratosphere. They argue that the stronger response in their 'low-top' model, when compared to Omrani et al. [2014], may be enhanced due to the inclusion of a turbulent mountain stress parameterisation that enhances SSW frequency. Overall, in these experiments it appears that the stratosphere is not necessary to facilitate surface perturbations.

Clearly in the literature it is still a debated issue whether the AMO leads the NAO or vice versa and whether the stratosphere is necessary to facilitate the covariance of the two modes. Current papers invoke SSW arguments, but fail to demonstrate actual frequencies and characteristics of the SSWs the model experiments simulate. These studies appear to demonstrate that the nature of response could be a model dependant feature and may be non-linear, particularly Omrani et al. [2015] only finds a consistent response under AMO warm configurations. The key scientific aim of this chapter is to determine whether SSW simulation is sensitive to AMO phase. Specific focus is in on the frequency and nature of SSW events under AMO warm and cold conditions. The surface response following a SSW event is also assessed to see whether it is modulated by the Atlantic Ocean configuration.

## 6.2 Experimental Design

The IGCM4 is configured as outlined in section 3.3. The two hundred year simulation from Chapter 4 is used as a control experiment with which to compare the new simulations. A further six model configurations are created for warm and cold North Atlantic Ocean conditions of varying strengths applied between 40°S and 90°N. The new model integrations vary from the control simulation only by the SST and surface saturation vapor pressure, which are prescribed monthly.

SST anomalies associated with the distinct AMO warm and cold periods are provided by Dr Daniel Hodson. The Hadley Centre SST and Sea Ice Coverage datasets, HadISST, is utilised [Rayner et al., 2003] with the long term 1890-2003 climatology being subtracted from the 1951-1960 and 1960-1990 composites to create the warm and cold anomaly profiles. For implementation in the IGCM4 these anomalies are then multiplied by a factor of 1, 2 or 4 and added to the basic climatological SST field that is used in the control simulation. This allows for a direct comparison between the control run and AMO simulations. The multiple strengths of anomalies allows for any non-linearity in the IGCM4 response to be assessed. It is acknowledged that the double and quadruple anomalies are unrealistically strong but they should be useful for interpreting any underlying mechanisms. In the IGCM4 the

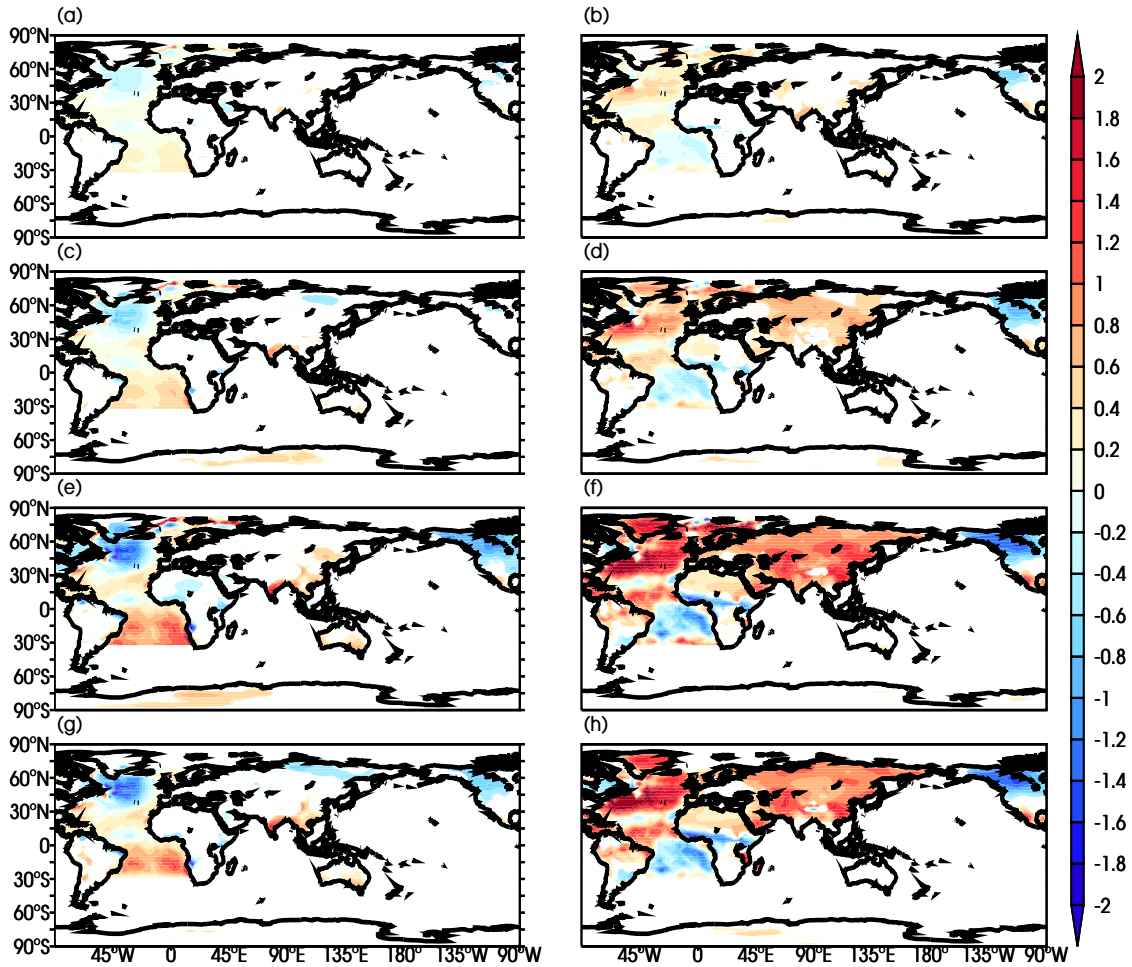


**Figure 6.2:** Surface temperature DJF composites minus control ( $^{\circ}\text{C}$ ) for: (a), (c), (e) and (g) AMO cold simulations and (b), (d), (f) and (h) AMO warm simulations. The anomalies are single strength in (a) and (b), double strength in (c) and (d) and quadruple strength in (e), (f), (g) and (h). Differences that have a  $p$ -value less than 0.05 are shaded (methodology outlined in section 4.2.4).

surface saturation vapour pressure is formulated using results of the August-Roche-Magnus formula, a rough approximation to the Clausius–Clapeyron relation, where each  $1^{\circ}\text{C}$  rise in temperature accrues a 7% rise in the saturated vapour pressure value.

Winter, DJF, anomalies of the surface temperature field for the six two hundred year AMO simulations are presented in Figure 6.2 (a)-(f). These are differences from the control DJF field. The structure of the anomalous warming and cooling for the different AMO regimes contain the distinctive quadrupole structure over the North Atlantic with a maximum in anomaly strength over the Gulf Stream as expected and reported in the literature [Hodson et al., 2010, Omrani et al., 2014]. There are also some interesting variations in the surface temperature over land that

appear mainly in the double and quadruple strength AMO warm simulations, Figure 6.2 (c)-(f), which display warming over the Eurasian land mass and a cooling over Alaska.

The anomaly region in these six simulations is the same as what is utilised in the multimodel study of Hodson et al. [2010], albeit they applied a smoothing at the anomaly boundary. It was also decided to configure the quadruple strength experiment with a reduced domain, between 20°S to 60°N as in Omrani et al. [2014]. At this stage it was also decided to implement a cosine squared smoothing, as in Hodson et al. [2010], at the anomaly boundaries that reduced from a factor of one to zero over four grid points. These final two configurations are used to assess the sensitivity of results to the anomaly domain (particularly the inclusion/exclusion of anomalies over the polar sea-ice region). The DJF anomalies of the surface temperature field are presented in Figures 6.2 (g) and 6.2 (h) for the reduced domain quadruple strength cold and warm simulations respectively. Overall there are a total of eight different AMO simulations, with the main focus of this chapter being on the six 40°S to 90°N experiments.

### 6.3 Results

To assess the sensitivity of the IGCM4 to the Atlantic Ocean configuration three main areas are investigated. Initially the background climatological state is assessed to see if the atmospheric zonal wind structure is sensitive to the Atlantic Ocean state. Following this SSWs are isolated to see if there is any modification to the frequency or behaviour of SSWs under the distinct AMO regimes. Finally tropospheric and surface impacts following SSW events are assessed to see if the AMO phase can modulate the surface response to SSW events.

#### 6.3.1 Winter Climatological State

The winter, DJF, climatology of zonal mean zonal wind provides reasonable insight into the background state of the six AMO configurations. The structures of these fields are a result of the interplay between many mechanisms including: radiative balance and relaxation scales, atmospheric circulation and transport, atmospheric wave propagation and breakdown, and atmospheric chemistry (noting this is not interactive in the IGCM4). The winter climatological state could be altered due to changes in: the behaviour of the jet streams, upward wave propagation and changes in the specific humidity at the surface altering the hydrological cycle. Omrani et al. [2014] and Keenlyside and Omrani [2014] both discuss a mechanism where SSTs associated with the warm phase of the AMO cause a reduction in mid-latitude

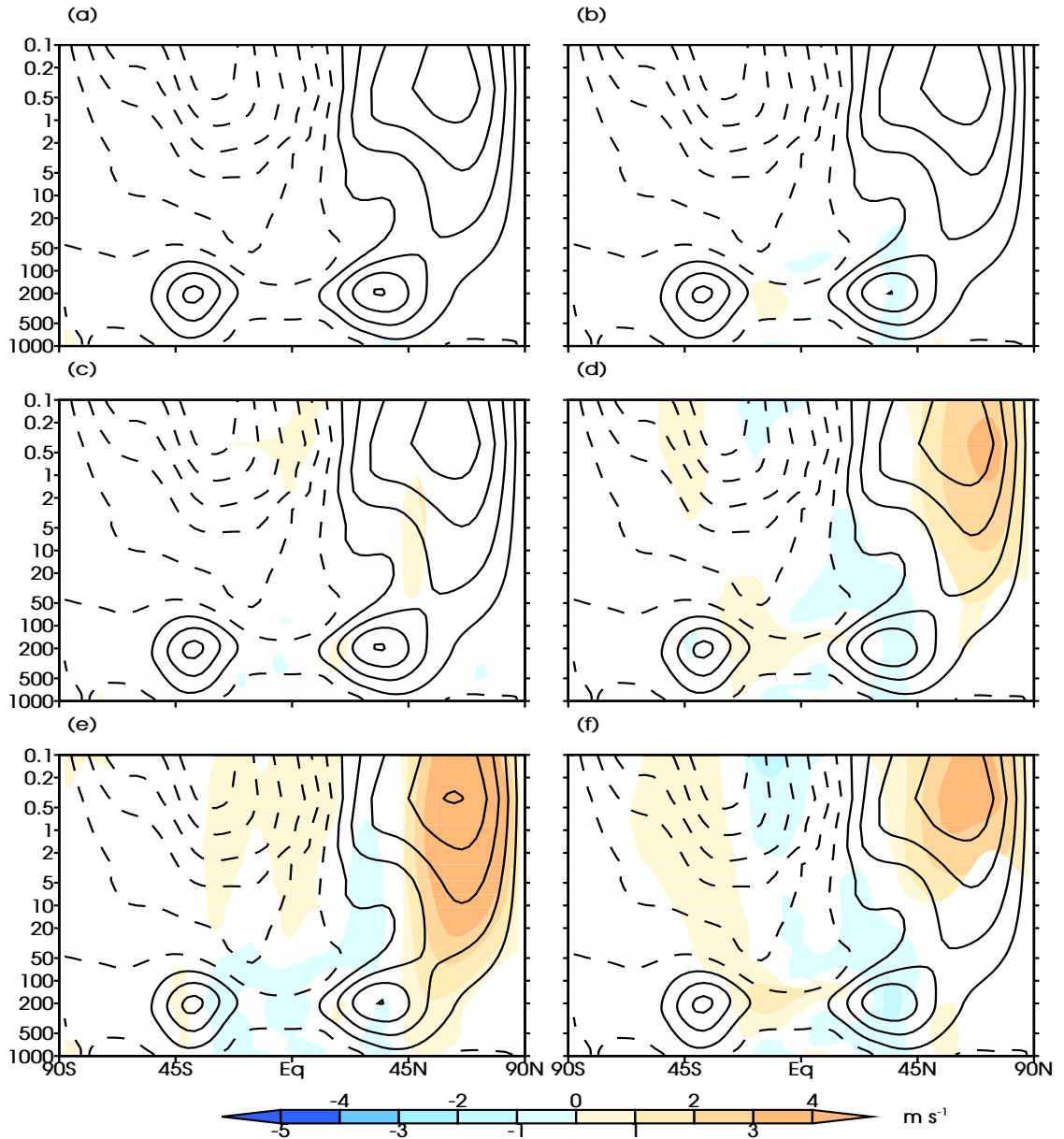


**Figure 6.3:** DJF zonal mean zonal wind climatologies (contour lines) and composites minus control (shading) ( $\text{m s}^{-1}$ ) for: (a), (c) and (e) AMO cold simulations and (b), (d) and (f) AMO warm simulations. The anomalies are single strength in (a) and (b), double strength in (c) and (d) and quadruple strength in (e) and (f). Contour intervals are  $10 \text{ m s}^{-1}$  with values equal to or below zero dashed. Only areas with  $p$ -values less than 0.05 are shaded.

atmospheric baroclinicity. This in turn leads to a weakening of the mid-latitude westerlies which can then result in a weakening of the stratospheric polar vortex due to increased SSW activity. It seems reasonable to expect some variation in the winter climatological state between the six AMO simulations.

In contrast to the two aforementioned studies the climatological state of the

IGCM4 is insensitive to the North Atlantic SST configuration when single strength anomalies are applied. Figure 6.3 displays the climatological (contour line) and anomalous (shaded) DJF zonal mean zonal wind fields ( $m s^{-1}$ ) as a function of latitude against height. Anomalies are calculated as differences from the control where positive (negative) values indicate more westerly (easterly) winds. In the single strength AMO cold configuration, Figure 6.3 (a), there are no differences with p-values lower than 0.05. For the single strength AMO warm configuration, Figure 6.3 (b), there is a very slight weakening through the sub-tropical jet centre, in agreement with the mechanism outlined by Peings and Magnusdottir [2014] and Keenlyside and Omrani [2014] but this difference is no greater than  $1 m s^{-1}$ . This weakening is also present in the AMO warm double and quadruple strength simulations, panels (d) and (f), but remains consistently weak. The climatological strength of the polar night jet is accelerated in the AMO warm double and AMO warm quadruple simulations which is in contrast with the mechanism of Omrani et al. [2014] and Keenlyside and Omrani [2014]. There is little notable variation in the AMO cold double strength simulation Figure 6.3 (c). For the AMO cold quadruple strength simulation, Figure 6.3 (e), there is a general acceleration of the westerly winds poleward of  $45^{\circ}N$  and deceleration equatorward of this up to the zero contour line. This could be in agreement with the aforementioned mechanism but for cold SST forcing. The fact that there is a slight strengthening of the polar vortex under both warm and cold AMO quadruple strength configurations is unexpected. To check the likelihood that this is a result of internal variability the simulations are performed again with perturbed initial atmospheric states. The strengthening of the polar vortex in both simulations is still apparent, leading to the conclusion that this result may not be internal variability. The exact mechanism behind this result is beyond the scope of this work and requires further investigation to isolate.

As in the original analysis of the IGCM4, section 3.3, the meridional heat flux and refractive index for stationary Rossby waves are also assessed in the six AMO simulations. There is very little variation in the structures of these fields and it appears as though the wave propagation is invariant between these six AMO simulations.

It should be noted here that the overall zonal mean zonal wind climatological structure is a result of many processes which include SSW dynamics. Just because there appears to be little variation in the overall climatological state between AMO simulations this does not necessarily imply that there will be little variation in the behaviour and frequency of SSWs.

### 6.3.2 Sudden Stratospheric Warmings

SSWs are identified and classified as outlined in section 2.4. The frequency of SSW events in each model integration is calculated as the total number of SSWs divided by the total number of winters. The SSW frequencies are presented in Figure 6.4 where the AMO warm quadruple (W4), double (W2) and single (W1) is presented to the left of the control simulation (C) with AMO cold quadruple (C4), double (C2) and single (C1) on the right. A least squares regression is also applied to assess any trends over the 7 simulations. This technique fits a straight line to the data points which minimizes the sum of the squared vertical residuals between the regression line and data points. The gradient of this line is also presented in Figure 6.4 as  $M$  and the correlation coefficient, which is the amount of variance explained in the data by the regression with 1 stating that all variance is accounted for, as  $CC$ . Analysis is performed on all, splitting and displacement SSWs categories and is presented in purple, blue and green respectively. For all sets of frequencies there is a slight upward trend with cooler Atlantic SST configuration. However, this trend is small, with a regression gradient of 0.013 for all SSW events and is comparable to the standard error magnitude. The least squares regression explains half of the variability in the displacement frequencies and 61% in the splitting frequencies. Overall there is little notable trend in SSW frequency across the 7 model simulations. There are consistently more displacement than splitting SSWs in agreement with CP07. The slight reduction in the number of SSW events for the AMO warm quadruple and AMO warm double events could be associated with the climatological acceleration of the polar night jet in Figure 6.3 (d) and (f).

As mentioned in the previous section there is little variation in the winter meridional heat flux climatologies across the AMO simulations. This climatological average provides little information into the wave forcing leading up to SSWs. Figure 6.5 presents the 100  $hPa$  meridional heat flux anomaly prior to SSW onset (as introduced in section 3.3.3). Five of the simulation have a stronger average wave forcing prior to splitting events when compared to the wave forcing prior to displacement events. Notably there is no observable trend in this data with the magnitude of wave forcing prior to events remaining similar across all six simulations.

The polar vortex deceleration at 10  $hPa$  and 60°N is an indication of the typical stratospheric disturbance due to a SSW event. A scatter-plot is presented in Figure 6.6, that is again constructed in a similar manner to Figure 6.4. Deceleration is calculated as in section 3.3.3. The strength of the average stratospheric disturbance is generally similar across most of the model simulations with the exception of the AMO cold quadruple simulation which has a stronger deceleration for splitting

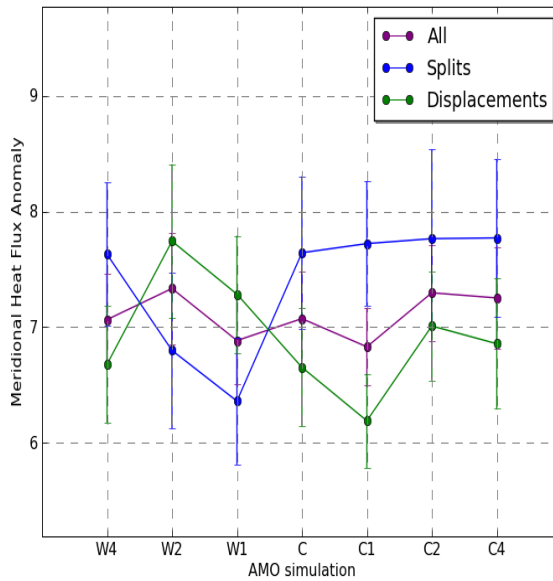
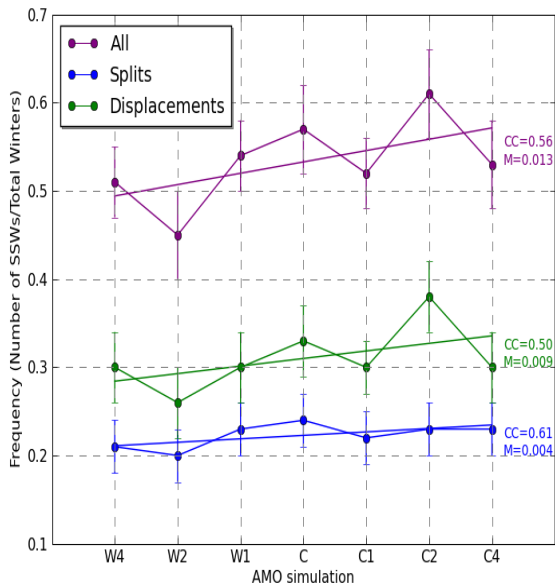


**Figure 6.4:** SSW frequency calculated as the total number of events divided by the total number of winters in the 200 year simulations. AMO warm simulations presented to the left of the control (C) with AMO cold simulations on the right. Bars represent standard errors and a least squares regression is applied.

**Figure 6.5:** Meridional heat flux anomaly ( $K m s^{-1}$ ) averaged between lag -20 to 0 and  $45$  to  $75^{\circ}N$ . x-axes layout as in Figure 6.4, least square regression lines omitted.

events, around  $24.5 m s^{-1}$ . There could be a slight upward trend in this data with the regression lines possessing a weak positive gradient (0.34 for splitting data, 0.02 for displacement data and 0.16 for all events combined). However if you remove the most extreme AMO simulations there is no discernible trend in average SSW strength at  $10 hPa$ . Overall the trend is not robust and most likely the results of random internal variability. This data does confirm that splitting events have a stronger magnitude at  $10 hPa$  than displacements as found in CP07.

The strength of middle to lower stratosphere coupling for anomalies associated with SSWs is portrayed by the  $100 hPa$  polar cap temperature anomaly, Figure 6.7. This field is also invariant to AMO configuration in the IGCM4 displaying a consistent coupling strength between the middle and lower stratosphere.

There is little variation in the overall frequency, tropospheric forcing associated with or strength of SSWs at  $10 hPa$  across the various AMO simulations. The other main characteristic that could be altered is the seasonality of SSWs. Histograms of event occurrence are presented in Figure 6.8. In the control run, Figure 6.8 (a), it appears as though the distribution of splitting SSW central dates could be skewed

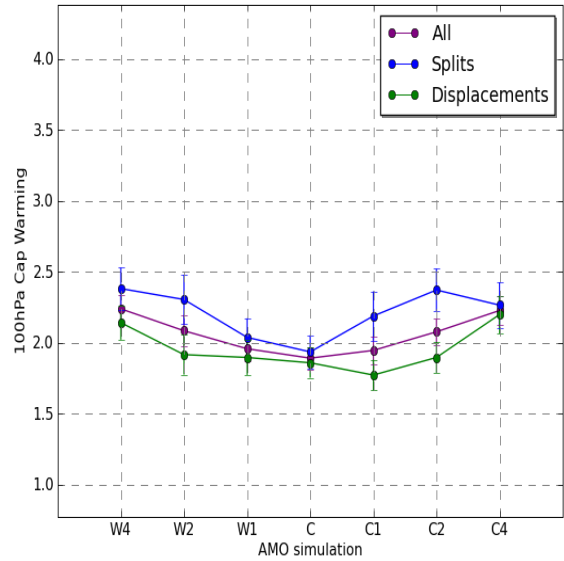
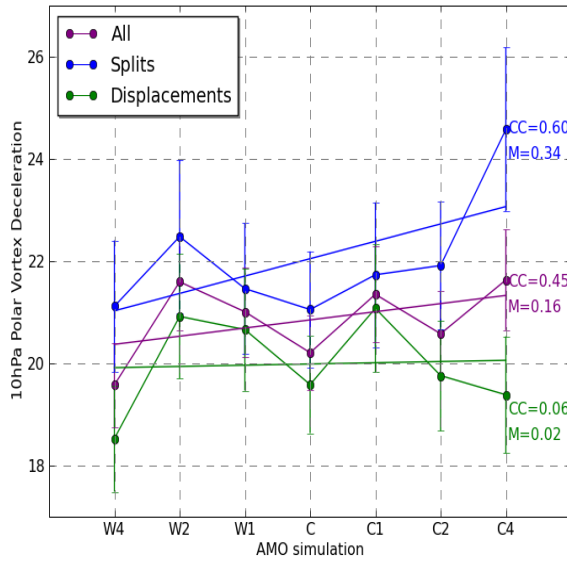


**Figure 6.6:** 10 hPa 60°N zonal wind deceleration ( $m s^{-1}$ ) associated with SSW events. Calculated as the difference between averages over lag -15 to -5 and lag 0 to +5. Layout as in Figure 6.4

**Figure 6.7:** 100 hPa polar cap temperature ( $^{\circ}C$ ) anomaly associated with SSW events. Averaged over lag -5 to lag +5 and 50 to 90°N. Layout as in Figure 6.5.

towards early winter and displacements towards late winter. The mean and standard deviation of event onset for the two datasets is calculated and it is revealed that the average central dates are surprisingly similar with a large standard deviation, especially for the splitting composite. There does not appear to be a consistent shift in the mean date of SSW onset over the AMO simulations, Figure 6.8 (b)-(g).

In the IGCM4 the wave forcing, frequency, seasonality, stratospheric strength and coupling at the tropopause associated with SSWs are all insensitive to the AMO phase. It still remains to be seen whether the AMO can modulate the surface response to SSW events.

### 6.3.3 NAM Anomaly

To assess the strength of typical surface impact following SSWs the NAM anomaly is averaged from lag 0 to lag +30 for the splitting composite, displacement composite and all events for the six AMO simulations. This is presented in Figure 6.9 and is laid out as in Figure 6.6. For all simulations, except AMO cold single (C1), the average surface impacts following splitting events are stronger than the impacts associated with displacements. Any overall trends in the least squares regression line are small, however it does appear that the impact following splitting events in the AMO cold simulations are, on average, weaker than the splitting impacts in the

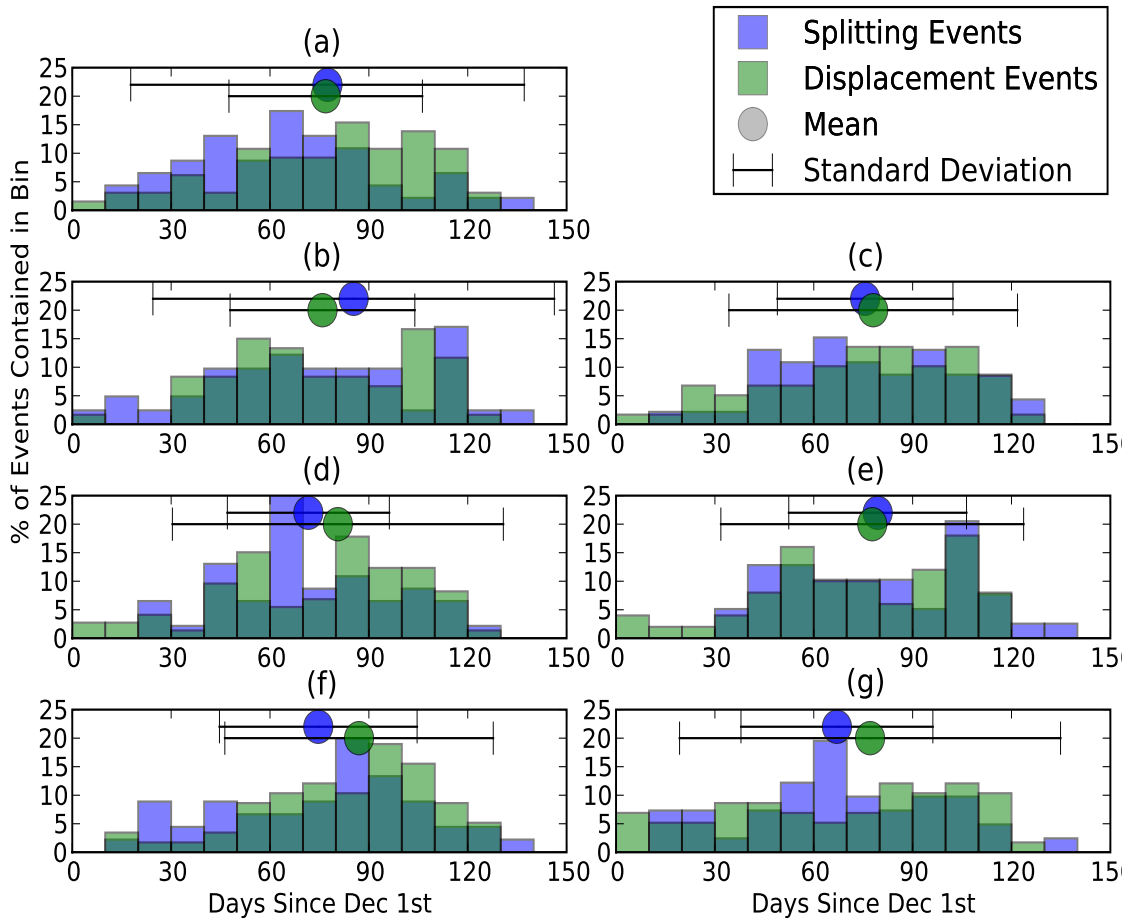


**Figure 6.8:** Histograms of central dates for splitting and displacement events for: (a) the control simulation, (b), (d) and (f) AMO cold and (c), (e) and (g) AMO warm simulations for: (b) and (c) single, (d) and (e) double, and (f) and (g) quadruple strength simulations. Central dates measured as days from December the 1st. Bar height represents the percentage of events contained in the 10 day bin period. Mean and standard deviation of central dates presented above the histograms as a circle and bar lines respectively. Green represents displacement SSW data, blue represents splitting SSW data and turquoise is where they overlap.

AMO warm simulations, which are comparable to the control with the exception of the double strength warm (W2) simulation.

An indicator into the behaviour of anomaly descent following SSWs is by means of a paint dripping plot [Baldwin and Dunkerton, 2001] which presents composites of the NAM anomaly, section 4.2.1, as a function of height against time. The typical disturbance following SSWs project onto the negative NAM mode and if these anomalies descend into the troposphere this is often captured by the NAM index. To synthesize the data throughout the atmospheric column for the six AMO experiments the difference between the splitting and displacement NAM anomaly

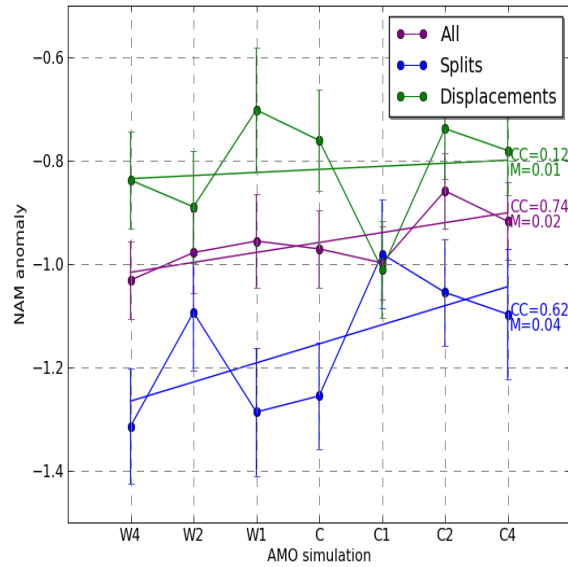


**Figure 6.9:** 1000 hPa NAM anomaly averaged from lag 0 to 30 following SSWs across the AMO simulations. AMO warm simulations presented to the left of the control (C) with AMO cold simulations on the right. Bars represent standard errors and a least squares regression is applied.

composites for each model configuration is presented in Figure 6.10. This is directly comparable to Figure 4.2 (c) which presents the NAM anomaly difference for the control data. The difference is calculated as splitting composites minus displacement where the red/blue spectrum represents a stronger negative NAM anomaly associated on average with splitting/displacement events. In the control experiment splitting SSWs had a stronger impact on the troposphere and surface climate over lag 0 (the central date) to lag +30 (30 days after the central date). There is some variability in the average NAM anomaly descent across the AMO simulations. The splitting composite is not significantly stronger than the displacement for the majority of the cold Atlantic configurations between lag 0 to lag +60, Figure 6.10 (a), (c) and (e), in agreement with Figure 6.9. The splitting composite has a stronger surface NAM anomaly in the double strength cold Atlantic simulation, Figure 6.10 (c), but this is found to be sensitive to the splitting central date definition (I.e. whether kurtosis reaching -0.1 or zonal mean zonal wind reversal at 10 hPa and 60°N is utilised). For the warm configurations the single, Figure 6.10 (b), and quadruple, Figure 6.10 (f), strength simulations display a stronger average tropospheric anomaly in the response period, lag 0 to +60. The AMO warm double strength simulation, Figure 6.10 (d), generally has negative NAM values for both splitting and displacements throughout the troposphere, total fields omitted, with the splitting composite being only slightly stronger and not significantly different.

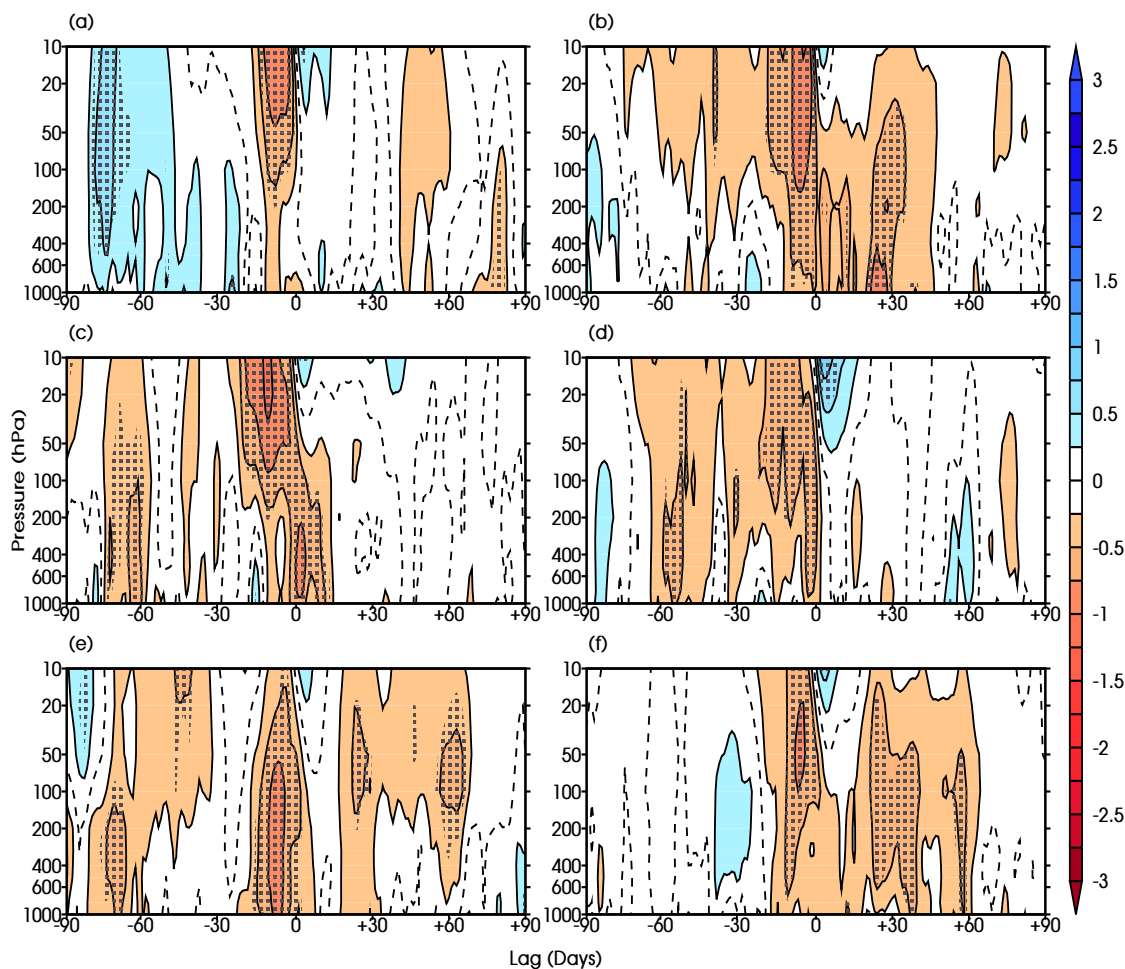


**Figure 6.10:** Splitting minus displacement NAM anomaly composite for: (a), (c) and (e) AMO cold simulations and (b), (d) and (f) AMO warm simulations. The anomalies are single strength in (a) and (b), double strength in (c) and (d) and quadruple strength in (e) and (f).  $p$ -values less than 0.05 stippled. Lag 0 is the SSW central date Lag  $-/+90$  being 90 days prior to/after event onset.

This is also reflected in the surface NAM values, Figure 6.9. Finally it is worth noting that the stronger anomaly for splitting composites prior to event onset that is observable across all of the AMO simulations in Figure 6.10 is sensitive to the central date definition and disappears when the zonal mean zonal wind reversal criteria is implemented.

Overall there could be an indication that tropospheric and surface impacts associated with splitting events is stronger during AMO warm regimes when compared to AMO cold regimes.

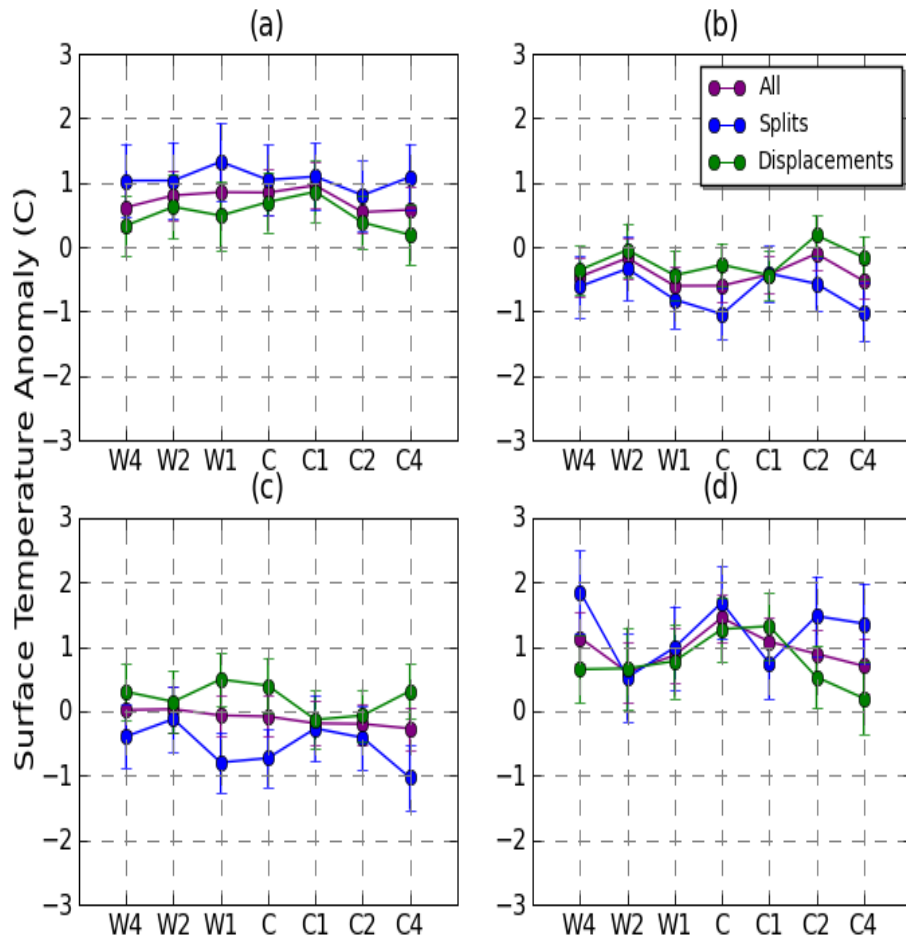


**Figure 6.11:** Regional surface temperature anomalies ( $^{\circ}\text{C}$ ) averaged from lag 0 to 30 following SSWs across the AMO simulations for: (a) Greenland sector, (b) western Europe sector, (c) central Eurasian sector and (d) Aleutian sector. AMO warm simulations presented to the left of the control (C) with AMO cold simulations on the right. Bars represent standard error of the mean. Anomalies are calculated as differenced from daily climatological values.

### 6.3.4 Surface Temperature

To assess the direct surface impact following SSWs across the AMO simulations the surface temperature anomalies are calculated over land and averaged over the mature (lag 0 to lag +30) and decay (lag +30 to +60) periods. These anomalies are then averaged over specific geographic regions to display the average surface temperature anomalies over; Greenland, Western Europe, Central Eurasia and the Aleutian sectors. The results for the mature period are presented in Figure 6.11. Analysis was found to be insensitive to the bounding box limits. Overall there is no trend in the surface temperature anomalies over the 6 AMO simulations. For the mature period the behaviour in the IGCM4 is similar to what is reported by M13 with a consistent

warming over Greenland, Figure 6.11 (a), and a cooling over western Europe, 6.11 (b), which are both stronger for the splitting composites. There is also a warming over the Aleutian region, 6.11 (d), for both splitting and displacement events and weak warming/cooling for displacement/splitting events over central Eurasia, 6.11 (c). The impacts associated with splitting events in the AMO warm simulations are no different to those from the AMO cold simulations. Overall the surface response is consistent over the AMO simulations with a warm/cold dipole appearing over Greenland/western Europe as one would expect during a negative NAM regime. In the decay period, figure omitted, there is less distinction between the splitting and displacement composites with the anomalies over Greenland and Western Europe generally dissipating.

### 6.3.5 Comparison to Literature

In contrast to the study of Omrani et al. [2014] the stratosphere in IGCM4 is insensitive to the North Atlantic SST state, in agreement with the results of Peings and Magnusdottir [2015]. The winter zonal mean zonal wind profiles display insensitivity in their structure for the single strength forcing simulations. Over all six simulations there is no discernible shift in the climatological winter meridional heat flux profile or the refractive index associated with quasi-stationary Rossby waves. The frequency of SSWs remains similar for all six AMO simulations. The mechanism put forward in the study of Omrani et al. [2014] (also discussed by Peings and Magnusdottir [2014] and Keenlyside and Omrani [2014]) appears to be ineffective/non-existent in the IGCM4.

Could the differences in results between this study and that of Omrani et al. [2014] be due to the experimental design? The high-top standalone atmospheric general circulation in use in Omrani et al. [2014] is ECHAM5 with 35 vertical levels and a lid at 0.01 *hPa*, the IGCM4 has 35 vertical levels and a lid at the lower level of 0.1 *hPa*. The experiments performed in Omrani et al. [2014] were performed at T63 whereas the experiment here utilise a T42 truncation. Both GCMs invoke gravity wave drag parametrisations and ozone is not interactive. A stark difference in the experimental design is the treatment of the Northern Hemisphere high latitudes. Both studies simulate the AMO using HadISST with the warm phase consisting of the 1951-1960 period; however, Omrani et al. [2014] limits the anomaly domain to between 40°S and 66°N to avoid perturbing the sea-ice field.

To assess whether the exclusion of sea-ice variations leads to a difference in stratospheric response in the IGCM4 a further two AMO simulations are performed with the anomalies at four times observational strength and restricted to the same

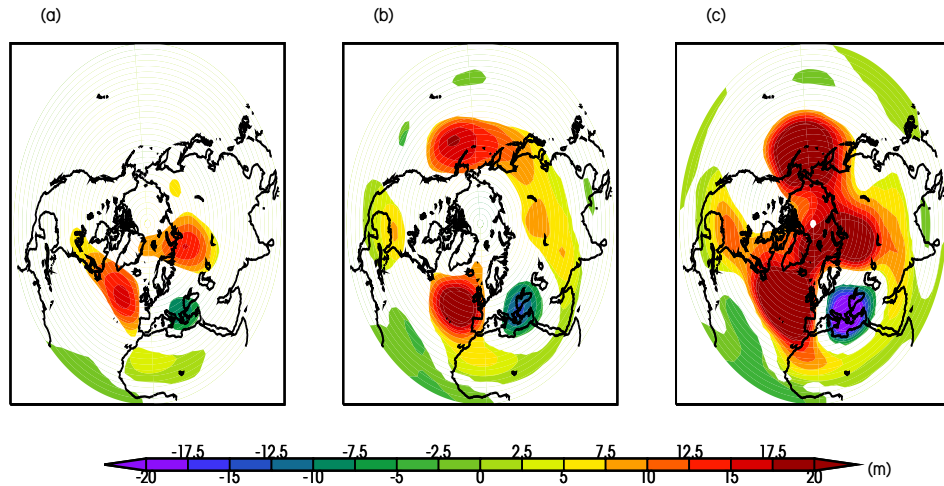


**Figure 6.12:** Geopotential height JFM differences at 500 hPa (m) between AMO warm and cold simulations for: (a) single strength, (b) double strength and (c) quadruple strength simulations. AMO warm minus AMO cold. Only differences with  $p$ -values less than 0.05 shaded.

domain used in Omrani et al. [2014], see section 6.2. It is found that there is a slight change in the zonal mean zonal wind structure where the upper and lower Northern Hemisphere jets are now connected by a  $20\text{--}25\text{ m s}^{-1}$  contour interval and the isolines have a sharp angular incline at  $\sim 50\text{ hPa}$ . There is no modification to the frequency, strength, forcing or NAM anomaly descent associated with SSWs in these new reduced domain AMO simulations. It is unlikely that the difference in results presented here and in Omrani et al. [2014] is due to the SST anomaly domain. The lack of impact from the inclusion of ice perturbations is in agreement with Peings and Magnusdottir [2015], who found the exclusion of sea ice anomalies in their low-top experiments did not affect the sea level pressure response.

Omrani et al. [2015] hypothesised that the lack of positive NAM regime response to the negative AMO SST forcing in their uncoupled experiment may have been associated with a deepened climatological Aleutian low which could lead to enhanced likelihood of SSW occurrence. This mechanism would counteract the expected reduction in SSW frequency under AMO negative conditions. Figure 6.12 displays that in the IGCM4 there is no significant difference in winter (JFM) 500 hPa climatologies for the single strength AMO warm and cold simulations over the North Pacific, panel (a). For the double, panel (b), and quadruple strength, panel (c), simulations there are significant differences. In both AMO warm and cold experiments there is more positive climatological geopotential height values over the North Pacific when compared to the control simulation. This implies a weakened Aleutian low in all four experiments. This is significantly stronger in the AMO warm exper-

iments when compared to the AMO cold experiments. If the mechanism proposed in Omrani et al. [2015] was evident in the IGCM4 then it would be expected that there would be a reduction in SSW frequency, particularly for the warm double and quadruple configurations. This could potentially mitigate the AMO warm impacts on SSW frequency, as is observed in the IGCM4. This could also increase the likelihood of reduced SSW frequency under AMO cold conditions, which is not observed in the IGCM4. Overall these speculative arguments could go some way to resolving the stratospheric insensitivity to warm AMO phases under double and quadruple forcing, but not for the AMO cold experiments. Ultimately, the lack of difference over the Pacific in the single strength simulations calls into question the validity of this hypothesis.

## 6.4 Discussion and Conclusions

Overall it is found that the winter climatological state and SSW simulation in the IGCM4 is insensitive to the North Atlantic SST configuration. Even with a surface SST field that is four times stronger than observations there is little modification to the background climatological state and SSW behaviour for surface conditions that replicate both the AMO warm and cold phases. Furthermore these results are insensitive to the inclusion or exclusion of perturbations to the sea-ice fields but the winter zonal mean zonal wind profile is smoother and more realistic when the polar anomalies are included.

These results appear to be in contrast with the work of Omrani et al. [2014] who found that under AMO warm conditions there is an increase in mid-winter poleward eddy heat flux and a shift to more SSWs. There is more coherence with the work of Peings and Magnusdottir [2015] who found that it was unlikely that the surface NAM response to AMO phase was a result of stratospheric anomaly descent.

One possible explanation of the differences with Omrani et al. [2014] is that the model configuration affects the sensitivity of the stratosphere to the ocean state. Why this should be the case remains unclear and will require further research. The version of IGCM used here has a coarser resolution and slightly lower lid than the high-top general circulation model used by Omrani et al. [2014]. Other possible sources of the differences could be; the nature of simulated SSWs in MAECHAM5, the treatment of gravity waves and tuning of the associated drag scheme, the climatological ozone profile, treatment of greenhouse gasses and the SST climatologies used in other ocean basins. If the source of this difference is isolated this would be useful for modelling efforts and for understanding the mechanisms behind ocean-stratosphere coupling.

---

## Chapter 7 - Impacts Of An Interactive Ocean

### 7.1 Introduction

Much can be learned about the climate system under the simplified framework of studying individual components of this system independently from one another. In Chapter 4 the downward influence of SSWs was investigated. Surface impacts associated with splitting events were, on average, stronger than those of displacements and a pathway into the ocean was highlighted. Isolating the atmosphere-only branch of the system in an intermediate model was beneficial because it allowed the signal to be directly isolated free from other climatic processes (for example: ENSO, solar variability, the QBO phase) which could lead to difficulties in clearly isolating SSW impacts. However, while this leads to scientific advances it has limited validity in Earth's climate system due to the processes neglected which could interact with and modulate this behaviour. Understanding interactions between different climatic elements is important for realistic forecasting.

In an attempt to assess how coupling between the atmosphere and ocean could modulate SSW surface impacts the IGCM4 is combined with an ocean model to develop an atmosphere-ocean general circulation model. This is designed so that the atmospheric component of the coupled model, FORTE, is comparable to the atmosphere-only IGCM4.

The first scientific aim of this chapter is to assess how an interactive ocean changes the climatological basic state of the model. This is achieved by directly comparing FORTE and IGCM4 200 year control integration configured to be as similar as realistically possible (see section 7.2). As in Chapter 3 the Northern Hemisphere stratospheric winter state, upward wave propagation and surface climatologies are analysed. This work directly contributes to scientific understanding on how studies utilising atmosphere-only general circulation models may be affected by the presence of an interactive ocean.

The second scientific aim is to isolate how the presence of an interactive ocean impacts SSW simulation and modulates their surface and oceanic impacts. In the study of Hansen et al. [2014] it was found that in the Community Earth System Model (atmospheric component WACCM 4, 56 year integration) upon suppressing SST variability, by replacing it with climatological monthly means, there was a reduction in SSW frequency attributed to less tropospheric wave forcing. In this experiment there was a nudged QBO and 1960 level greenhouse gases. It is reasonable to assume that in FORTE there may be some alteration to SSW frequency due to the presence of an interactive ocean when compared to the stand-alone IGCM4.

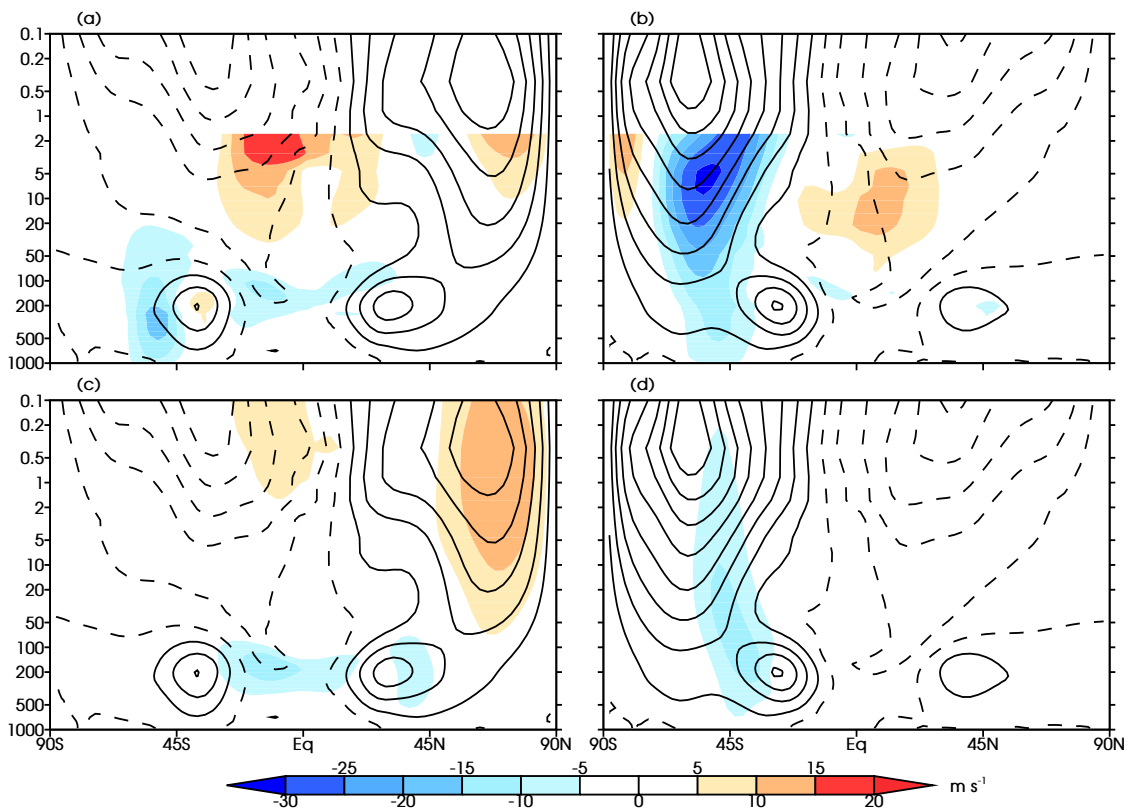


**Figure 7.1:**  $\bar{U}$  ( $m s^{-1}$ ) climatologies of: (a) and (c) DJF, and (b) and (d) JJA. Total FORTE field in contour lines. Contour interval  $10 m s^{-1}$ . Solid contours for positive values, zero and negative values dashed. Solid colours are: (a) and (b) FORTE minus ERA-40, (c) and (d) FORTE minus IGCM4.

If this is the case then the behaviour will be extracted free from QBO influence enabling further understanding into how an interactive ocean can directly interact with SSW simulation.

## 7.2 FORTE Pre-Industrial Integration

To assess the scientific topics outlined in section 7.1 the IGCM4 is combined with an ocean model, MOMA. The technical model details are summarised in Chapter 3. The result of this is a fully coupled atmosphere-ocean GCM, referred to as ‘FORTE’. The atmospheric component of this coupled model is comparable to the standalone IGCM4. FORTE is spun up for 1,000 years and integrated forward in time for a further 200 years for analysis. The coupled model output is compared to the control IGCM4 200 year integration as utilised in the previous Chapters and introduced in section 3.3.

Key points to recall from the earlier model discussion is that the only routines which have been altered in FORTE, when compared to the IGCM4, are the bulk-aerodynamic formula and the treatment of the snow and ice fields (section

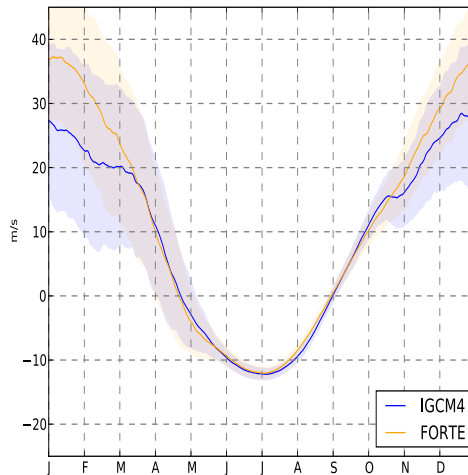


**Figure 7.2:**  $\bar{U}$  at 10 hPa 60°N and averaged over each calendar day for FORTE and the IGCM4. One standard deviation represented by shading. Calendar month along the x-axis, wind magnitude along the y-axis in  $m s^{-1}$ .

3.4.2). Surface data (SST, currents, radiative fluxes, wind stress, precipitation) are exchanged daily between MOMA and the IGCM4. Importantly there is now day-to-day variability in SST which is generated by FORTE. Pre-Industrial mixing ratios are set as: 285 ppmv for  $CO_2$ , 0.7 ppmv for  $CH_4$  and 270 ppbv for  $N_2O$ .

### 7.2.1 Background Climatological State

To assess the overall changes to the large scale atmospheric flow in FORTE DJF and JJA climatologies of zonal mean zonal wind ( $\bar{U}$ ) are presented in Figure 7.1. Recall that a comparison to ERA-40 for the IGCM4 is presented in Figure 3.3 and also appears in Joshi et al. [2015]. Many of the differences when compared to reanalysis remain similar in FORTE (Figure 7.1 top row). The exception being the DJF Northern Hemisphere tropical jet stream, panel (a), which was too strong by approximately  $5 m s^{-1}$  in the IGCM4 is now closer to reanalysis in FORTE. The easterly bias across the upper tropospheric equatorial region when compared to both ERA-40 and the IGCM4 could indicate a weaker Walker circulation in FORTE. The westerly bias across the stratospheric equator in both JJA and DJF when compared to reanalysis could be attributed to the simplicity of the treatment of gravity wave drag in this intermediate model and the lack of a QBO. Particularly interesting is the strengthening of the DJF Northern Hemisphere stratospheric westerlies when compared to the IGCM4, panel (c). This displays a stronger, and potentially less disturbed, polar vortex in FORTE. When compared to reanalysis the polar vortex is also poleward and stronger.

To assess the climatological behaviour of the polar night jet in FORTE  $\bar{U}$  is

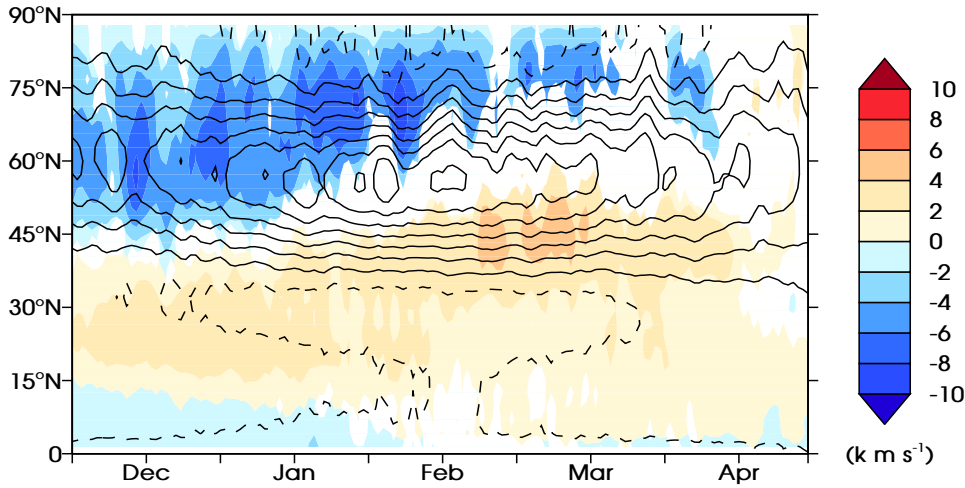


**Figure 7.3:** Climatology of meridional heat flux ( $\overline{v'T'}$ ) in  $K m s^{-1}$ , calculated as averages over calendar days. FORTE minus IGCM<sub>4</sub> in solid colours, total FORTE field in contour lines. Solid contours for positive values, zero and negative values dashed. Contour interval of  $2.5 K m s^{-1}$ . Only differences that have  $p$ -values less than 0.05 are displayed.

isolated at 10  $hPa$  60°N. This is then averaged for each calendar day and compared to the same field created from IGCM4 data. The mean value and standard deviation is presented in Figure 7.2, which indicates the typical temporal evolution of the polar vortex over winter and the magnitude of interannual variability in its strength. The winter transition to westerlies and spring transition to easterlies are similar between both model configurations, displaying similar behaviour in the radiatively driven onset of the polar vortex and its breakdown in spring. The typical strength of the polar vortex during NH winter is clearly distinct between the stand-alone and coupled version of the model. In FORTE the typical strength of the polar night jet is around  $10 m s^{-1}$  stronger than in the IGCM4. This agrees favourably with the conclusions from the climatological  $\overline{U}$ , that the polar vortex in FORTE is less disturbed on average during Northern Hemisphere winter.

The 100  $hPa$  meridional heat flux ( $\overline{v'T'}$ ) is used as a proxy for the vertical propagation of upward wave activity following Polvani and Waugh [2004] and Charlton et al. [2007]. A direct comparison to the IGCM4 is presented in Figure 7.3. Recall that, as discussed in Chapter 3, the IGCM4 has a meridional heat flux field that is within the behaviour of models analysed by Charlton et al. [2007] and compares favourable to NCEP/NCAR reanalysis. Upon the inclusion of an interactive ocean this field has been substantially altered. Peak values of the flux are now shifted equatorward of 60°N and occur approximately a month later in the season. There is a general reduction of the heat flux through December and January poleward of 45°N and increased heat flux towards the equator.

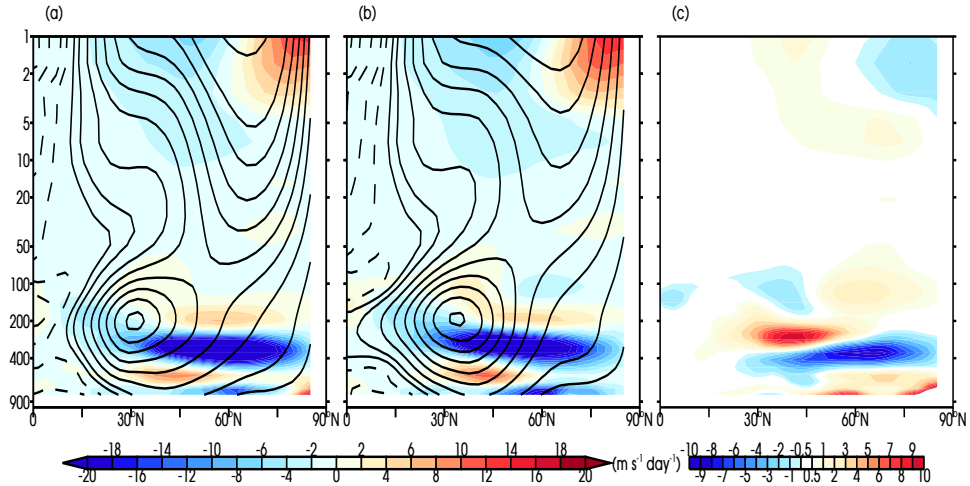


**Figure 7.4:** DJF climatology of  $\rho_0^{-1} \nabla \cdot \vec{F}$  ( $\text{m s}^{-1} \text{ day}^{-1}$ ) in solid colours for: (a) FORTE (b) IGCM4, with  $\bar{U}$  in countourlines as in Figure 7.1. (c) Difference in DJF  $\rho_0^{-1} \nabla \cdot \vec{F}$ , FORTE minus IGCM4.

The contribution to acceleration/deceleration of  $\bar{U}$  from resolved eddy forcing (under a transformed Eulerian mean framework) is captured by  $\rho_0^{-1} \nabla \cdot \vec{F}$ , where  $\vec{F}$  is the Eliassen-Palm flux [Andrews et al., 1987]. The boreal winter climatological  $\rho_0^{-1} \nabla \cdot \vec{F}$  for FORTE and the IGCM4 is presented in Figure 7.4 for the northern hemisphere. In both simulations there is deceleration from wave convergence on the equatorward flank of the polar night jet, and acceleration from wave divergence within the polar vortex region. This climatological behaviour represents the expected modification to  $\bar{U}$  from breaking Rossby waves. The difference between FORTE and the IGCM4 is presented in Figure 7.4 (c). Notably in FORTE there is less climatological wave breaking activity in the polar stratosphere and enhanced wave breaking on the poleward flank of the subtropical jet. These features are both evident in the differences in the DJF  $\bar{U}$ , Figure 7.1(c), and indicate a reduction in wave activity entering the stratosphere. Overall there are different climatological atmospheric wave dynamics in FORTE.

Upon checking the relationship between the meridional heat flux at 100 *hPa*, averaged from January to February, and the polar cap temperature anomaly at 48 *hPa* averaged from February to March (as in Eyring et al. [2006] (their Figure 3) and conducted for the IGCM4 in Figure 3.6) the temperature response in the stratosphere following anomalous wave flux is similar in FORTE, IGCM4 and ERA-40. FORTE has a reasonable sensitivity to upward wave flux in the stratosphere.

The surface temperature is an interesting field to study due to the fact that it is a result of the interplay of many different processes including physical and dynamical mechanisms. The winter, DJF, and summer, JJA, fields are presented

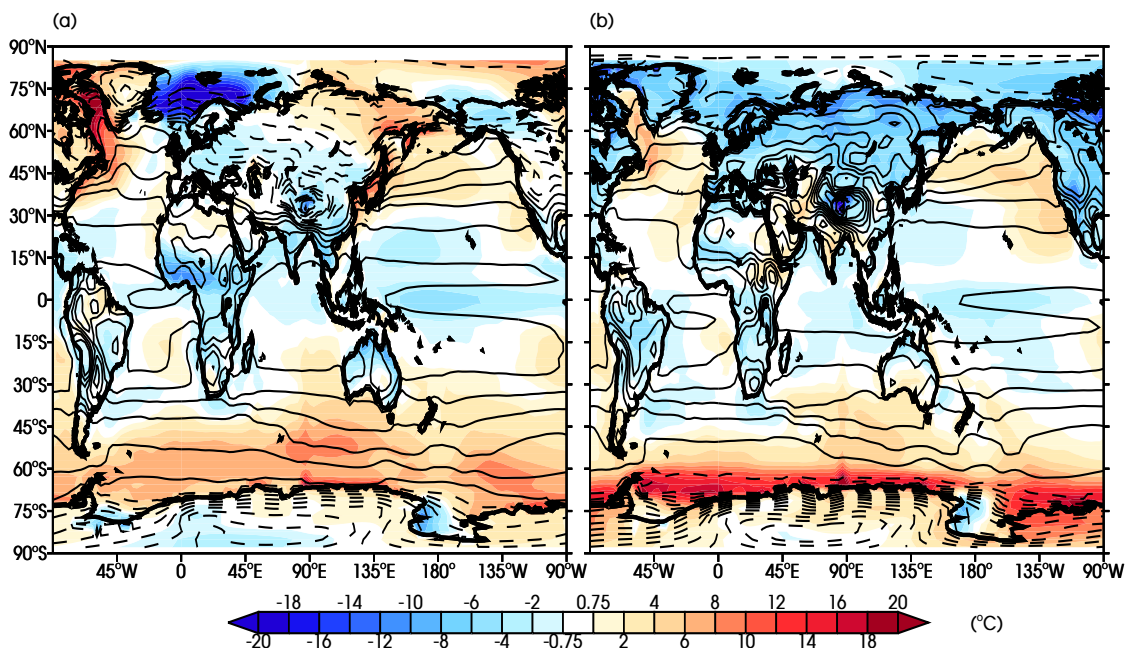


**Figure 7.5:** Climatology of surface temperature ( $^{\circ}\text{C}$ ) for: (a) DJF and (b) JJA. FORTE minus IGCM4 in solid colours, total FORTE field in contour lines. Solid contours for positive values, zero and negative values dashed. Contour intervals of  $4^{\circ}\text{C}$ .

in Figure 7.5(a) and (b) respectively. In the figure red/blue tones indicate where FORTE is warmer/cooler than the IGCM4. Over the ocean there are many large scale biases in FORTE (recalling that the SST field is prescribed from reanalysis in the IGCM4). There is an equatorial cold bias, particularly notable in DJF over the Western Pacific. The Atlantic Circumpolar Current region has a year round warm bias, peaking in Austral Summer. These are both common ocean model biases [Flato et al., 2013]. The North Atlantic and North Pacific both display warm tendencies, most likely a result of changes to the behaviour in the oceanic western boundary currents and storm tracks. Particularly along the East Coast of America/Canada and in the Labrador Sea there are much warmer SSTs in FORTE. There is a strong cooling over the Nordic sea, possibly a consequence of the lack of deep water formation here in FORTE.

Upon inspection of the surface energy balance field (including long and short wave radiation and sensible and latent heat terms, figures omitted) there is more heat loss to the atmosphere over this region and less heat loss where the North-Atlantic current should be situated. This implies that the Gulf Stream is not separating adequately and the North Atlantic Current path is too far poleward, a common problem in coarse resolution viscous ocean models [Bryan et al., 2007].

It would be expected that the cooling over the equatorial Pacific could lead to

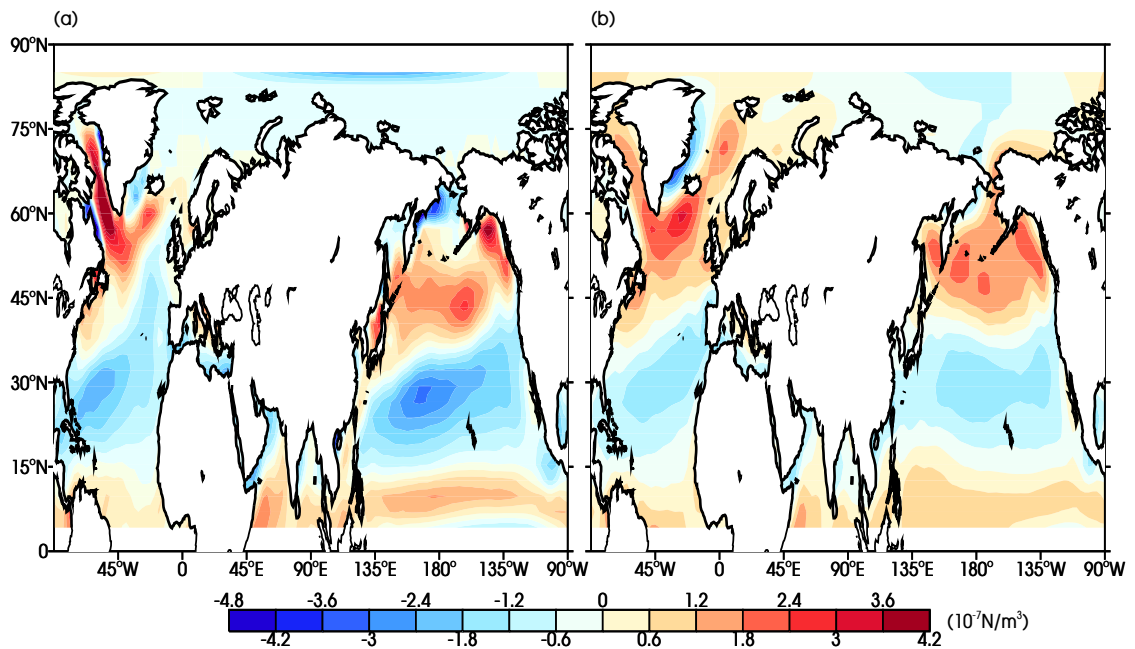


**Figure 7.6:** Surface wind stress curl ( $10^{-7} \text{Nm}^{-3}$ ) DJF climatologies for: (a) FORTE and (b) IGCM4.

changes in atmospheric dynamics such as deep convection and wave propagation [Sardeshmukh and Hoskins, 1988]. This could be related to (but not the only factor influencing) the differences observed in  $\bar{U}$  and the Eliassen-Palm flux as outlined above. To assess any quantitative changes in deep convection the difference in divergence at 200 hPa between FORTE and the IGCM4 is analysed. The region above the equatorial West Pacific is starkly different between the coupled and uncoupled versions of the model. In FORTE there is weaker divergence over the equatorial West Pacific and the structure is more zonal, especially in the Southern Hemisphere. The walker circulation also displays a year round reduction in strength, figures omitted.

The surface wind stress is an important field for atmosphere-ocean coupling, see section 4.1, and the wind stress curl provides insight into the structure of the wind driven gyre system. The DJF surface wind stress curl climatologies for FORTE and the IGCM4 are presented in Figure 7.6 panels (a) and (b) respectively<sup>7</sup>. Recall that NCEP/NCAR DJFM surface wind stress curl is presented in Figure 4.1. Between 70°N and 15°N positive/negative wind stress curl indicates the location of the wind driven subpolar/subtropical gyre. In FORTE the surface wind stress curl large scale

<sup>7</sup>In FORTE this was formulated using the total wind stress field as in Equation 3.3 to enable direct comparison to the IGCM4 results. Note that the use of a relative wind stress may lead to the reduction in stress felt by the ocean [Munday and Zhai, 2015]. This analysis was also conducted using the relative wind stress directly archived by FORTE, 10 day averaged fields, which led to no qualitative difference in the overall results presented in this Chapter.

features are in general agreement with what is observed in NCEP/NCAR reanalysis. The North Atlantic gyre system displays an enhanced South-West to North-East tilt when compared to the IGCM4 and NCEP/NCAR reanalysis. The strength of peak wind stress curl over the gyres is improved in FORTE when compared to the IGCM4. Over the Labrador Sea there is a local maximum in wind stress curl in FORTE, which is not observed in NCEP/NCAR reanalysis or the IGCM4.

Overall the inclusion of an interactive ocean has substantially altered the atmospheric climatological state. The Northern Hemisphere polar vortex is stronger and there is less wave activity entering the stratosphere, particularly in early winter. Some common ocean model biases are evident in the SST, e.g. the warm Antarctic Circumpolar Current and cold tongue over equatorial Pacific. It is a reasonable assumption that the behaviour of prominent currents such as the Gulf Stream and Kuroshio Current are poorly represented in FORTE, leading to some of the SST biases. It is likely that biases in SST are contributing to the changes in stratospheric behaviour. Given that SSW simulation in the IGCM4 was reasonably insensitive to prescribed North Atlantic conditions based on the AMO, see Chapter 6, it will be interesting if SSW simulation is impacted by the inclusion of an interactive ocean. If this is the case then either; coupling processes, increased day-to-day variability, or potentially the new climatological surface state has led to these variations.

### 7.2.2 Simulation of Sudden Stratospheric Warmings

The stratospheric climatological state of FORTE is different during boreal winter when compared to the IGCM4. This could both result in and be caused by changes in SSW simulation. SSWs are identified in FORTE and classified as outlined in section 2.4. In the 200 years of model data there are a total of 50 SSWs identified, yielding a frequency of 0.25 events per year with a standard error of 0.04. This is outside the benchmark of 0.6 with standard error of 0.1 presented in Charlton and Polvani [2007]. Applying the statistical testing for SSW frequency outlined in Charlton et al. [2007] it is found that the null hypothesis of ‘the mean frequency of SSWs in FORTE and NCEP-NCAR is equal’ is rejected at the 10% confidence level. Out of these 50 events 33 are classified as displacement and 17 as splitting, yielding a splitting to displacement ratio of 0.52. There are comparatively less splitting events in the coupled configuration with the frequency of both classes of event being outside of the standard error of Charlton and Polvani [2007] benchmarks.

The seasonal distribution of SSW occurrence is presented in Figure 7.7 which is directly comparable to Figure 3.10. There is now a higher proportion of events occurring in later winter in FORTE (when compared the the IGCM4), with over

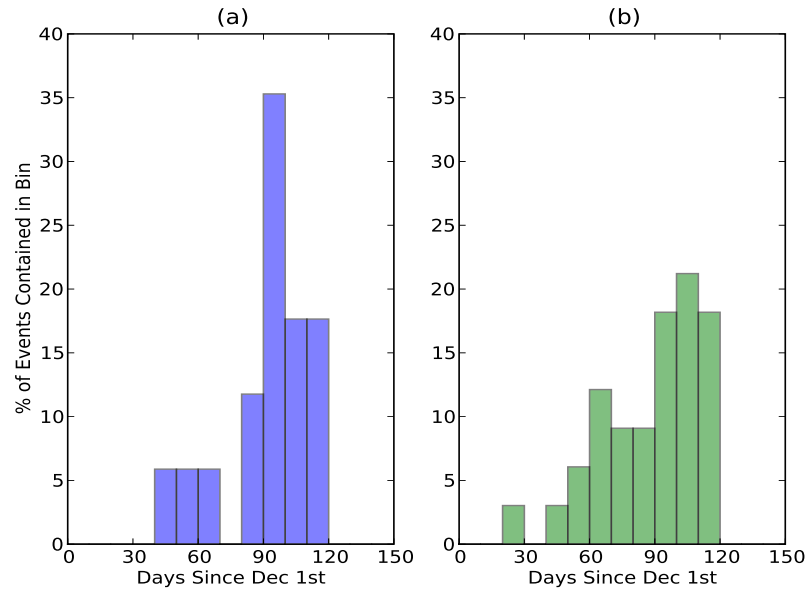


**Figure 7.7:** Distribution of SSW event onset in FORTE separated into 10 day bins from December the 1st onwards for: (a) splitting events and (b) displacement events.

70% of splitting and 57% of displacement events occurring after March 1st. For the IGCM4 17% of splitting and 39% of displacement events occurred after March the 1st.

As in Chapter 3 the CP07 benchmarks are used to assess the typical strength of zonal wind deceleration associated with SSW onset and coupling to the tropopause. It is found that the coupling between the middle and lower stratosphere is too strong, especially for splitting events. The zonal wind deceleration associated with displacement events is within standard error of the benchmark and similar to the IGCM4. The deceleration for splitting events in FORTE is far lower (by approximately  $15 \text{ m s}^{-1}$ ) than the benchmark. In the IGCM4 the deceleration associated with splitting events was approximately  $8 \text{ m s}^{-1}$  lower than the benchmark value. The  $100 \text{ hPa}$  meridional heat flux preceding events is within standard error for both classes of SSW events, indicating that the events are a result of upwardly propagating waves.

### 7.2.3 Modulation of Sudden Stratospheric Warmings Surface Impacts

The simulation of SSWs is substantially altered upon the inclusion of an interactive ocean. There is a large reduction in the number of events, a bias towards producing events later in the winter season and the nature of coupling at the tropopause is altered. This leads to the question of whether the differences in anomaly descent has also been altered. Figure 7.8 displays the NAM anomaly composite surrounding

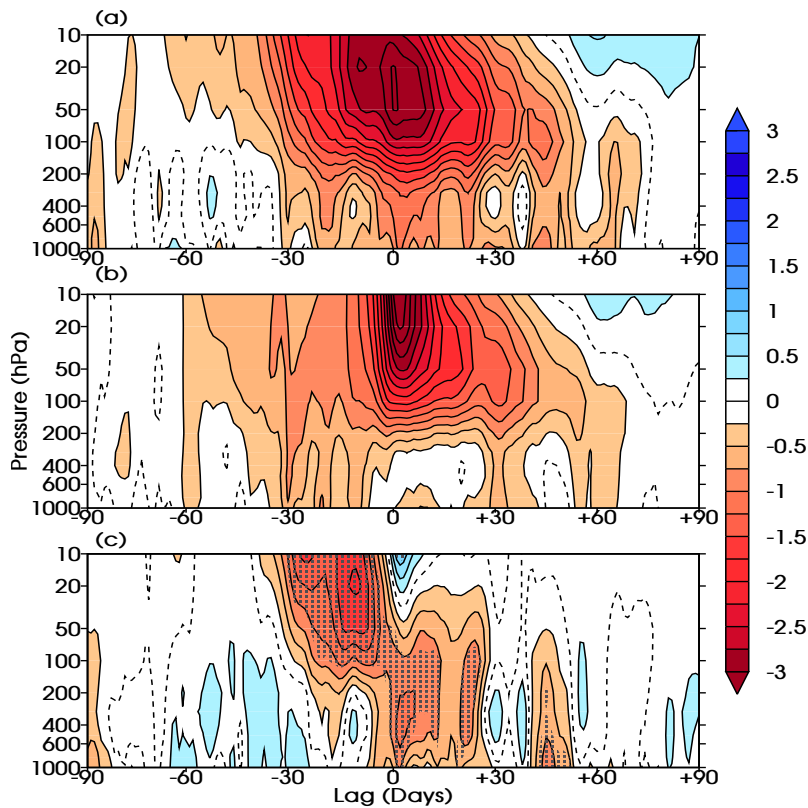


**Figure 7.8:** The NAM anomaly in FORTE for 90 days surrounding identified SSWs as a function of height against time for: (a) 17 splitting events composite and (b) 33 displacement events composite. (c) splitting composite minus displacement composite where stippling represents a  $p$ -value of less than 5%. The dashed line represents the zero contour. The NAM index anomaly is dimensionless.

SSW central dates for splitting events (panel (a)), displacement events (panel (b)) and their difference (panel (c)). These results are directly comparable to Figure 4.2 for events occurring in the IGCM4. As in the stand-alone version of the model splitting events have stronger negative NAM values in the troposphere following event occurrence when compared to displacements. The average surface impact following splitting events in FORTE is now more persistent when compared to the IGCM4 and lasts for approximately 2 months, as is observed in reanalysis [Mitchell et al., 2013a]. In FORTE the onset of negative NAM regime throughout the atmosphere is earlier than in the IGCM4, by approximately 25 days. It is possible that precursors and the state of the stratosphere prior to event occurrence have been altered.

As discussed previously (in section 2.3.2) the NAM regime is a good indicator of difference in surface impacts following SSWs but assessing 2D fields provides further insights. Surface temperature anomaly composites are presented in Figure 7.9 for splitting events (panel (a)), displacement events (panel (b)) and their difference (panel (c)). Paired t-tests (Welch’s test for unequal variances) are performed to

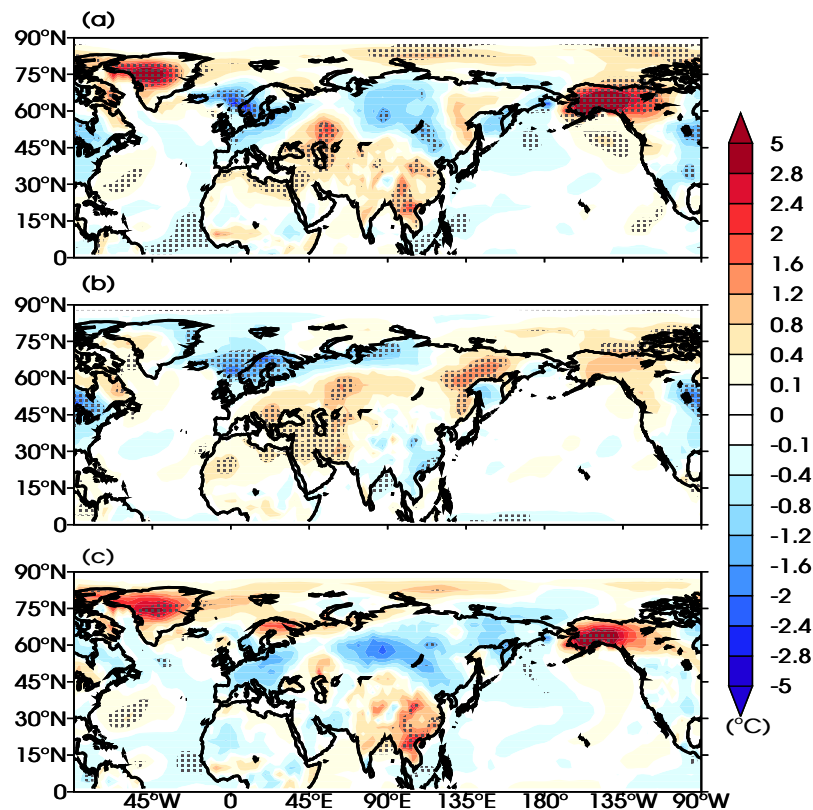


**Figure 7.9:** Surface temperature ( $^{\circ}\text{C}$ ) anomaly composites averaged from event onset (isolated in FORTE) up until 30 days later for: (a) 17 splitting events, (b) 33 displacement events and (c) splitting composite minus displacement composites. *P*-values less than 0.05 stippled.

isolate regions of *p*-values of less than 0.05 (so there is a less than 5% chance that the samples means are from the same population). For the splitting composite there is a warm anomaly over Greenland and cold anomaly over Western Europe, typically associated with a negative NAM regime. This pattern is much stronger than in the displacement composite, in agreement with the NAM anomaly at the surface over the 30 days following event onset (Figure 7.8) and with the conclusions of Chapter 4. In the splitting composite the other strong features (warming over Central Eurasia and Western Alaska and the cooling over Russia) are also present in the 30 days prior to event onset and most likely unrelated to the descent of SSW associated anomalies. The surface temperature response dissipates quickly for the splitting composite and is not present in the period from 30 to 60 days following event onset, unlike in the IGCM4 where anomalies are present during this period.

Expected impacts into the ocean can be assessed via the net-atmosphere surface flux and implied Ekman heat transport. This is similar to the process discussed in Chapter 4 except that now the ocean is able to respond and can directly contribute to the surface fluxes and surface currents can dampen and modify the

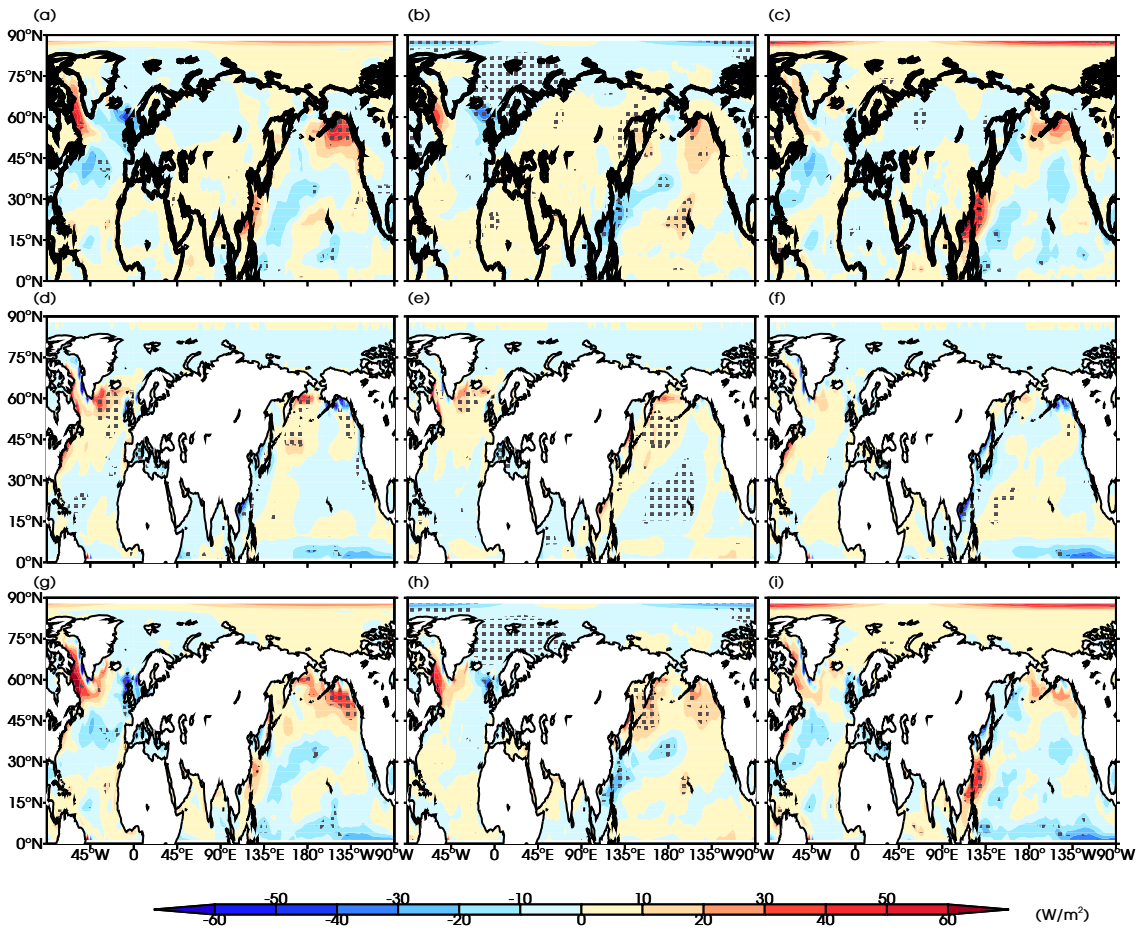


*Figure 7.10: FORTE composites for splitting anomalies, displacement anomalies and their difference (splitting minus displacement events) from event onset up until 30 days later for in columns one, two and three respectively for: (a)-(c) net atmosphere-surface flux, (d)-(f) implied Ekman heat flux and (g)-(i) the combined upper ocean energy flux. Positive fluxes are into the planet (downwards) units are in  $Wm^{-2}$ . There are 17 splitting events (left column) and 33 displacement events (middle column). Stippling represents a  $p$ -value of less than 5%.*

implied-Ekman heat transport. Composites of anomalies following splitting and displacement SSW onset in FORTE are presented in Figure 7.10. This is directly comparable to IGCM4 data presented in Figure 4.6. The implied Ekman heat transport, middle row, displays a warming over the subpolar gyre and a cooling over lower latitudes representing the expected weakening in surface wind stress over the North Atlantic [Marshall et al., 2001, Visbeck et al., 2003, Zhai et al., 2014] in agreement with Reichler et al. [2012]. The pattern is consistent between results calculated from relative and total wind stresses in areas that are stippled. The difference between the splitting and displacement composites, panel (f), indicates a slightly stronger response following splitting events but this difference is weaker than in the IGCM and lacks stippling. Upon repeating the analysis with a relative

wind stress formula [Munday and Zhai, 2015] the differences in panel (f) are found to not be robust, as the statistical testing implies.

The net-atmosphere surface flux anomalies (including longwave and short wave radiation and latent and sensible heat fluxes), top row, display an anomalous flux into the ocean over the Labrador Sea and an anomalous flux out of the ocean over the subtropical gyre. This is again marginally stronger for the splitting composite but lacks stippling. There are local maxima of anomalous heat flux into the atmosphere, for the splitting composite, off the American coast (centered around  $45^{\circ}\text{W}$   $40^{\circ}\text{N}$ ) and, for both composites, to the south of Iceland. These local centres of negative flux are unexpected. Particularly the latter does not appear in the study of Reichler et al. [2012] and most likely is a result of the simple ice dynamics in FORTE.

The combination of implied Ekman heat flux and net-atmosphere surface flux, the combined upper ocean energy flux, directly controls the rate of change of the mixed layer heat budget (see section 4.1.2). For splitting and displacement events and assuming a downward influence, this field indicates oceanic warming over the subpolar gyre and cooling over the subtropical gyre, in agreement with the results of Reichler et al. [2012] and Chapter 4. This signal is stronger for the splitting composite, but the differences lack p-values of less than 0.05. The enhanced tilt in the gyre system is notable in this response pattern.

The expected anomalous change to mixed layer heat budget following SSW events is qualitatively inferred by Figure 7.10(g) and (h) and can now be directly calculated following the simplified framework of Screen et al. [2010], as discussed in Chapter 4 and presented in Equation 4.8. This is conducted over the period from event onset and integrated for the following 120 days to enable time for the signal to impact the ocean system. Anomalous rates of change to the mixed layer heat budget are displayed in Figure 7.11 (a) for splitting and 7.11 (b) for displacement composites. As expected the warming signal over the Labrador Sea does not impact the mixed layer heat budget due to the large winter mixed layer depth here. For the splitting composite there is warming over the subpolar gyre and cooling over the subtropical gyre, in regions where the mixed layer depth is not too large. For the displacement composite the signal is different with a warming centred at  $35^{\circ}\text{N}$ ,  $40^{\circ}\text{W}$ . This is due to an increased net atmosphere-surface heat flux into the ocean over the period from 30 day to 60 days following displacement SSW event onset.

The anomalous rate of change to mixed layer heat budget is directly compared to the actual change in anomalous potential temperature averaged over upper ocean layer (from 0 to 30 *m* depth) anomalies are again calculated as differences from the daily mean climatology so there is no seasonal cycle present. The difference presented is calculated as the 120 day average following event onset minus the 120

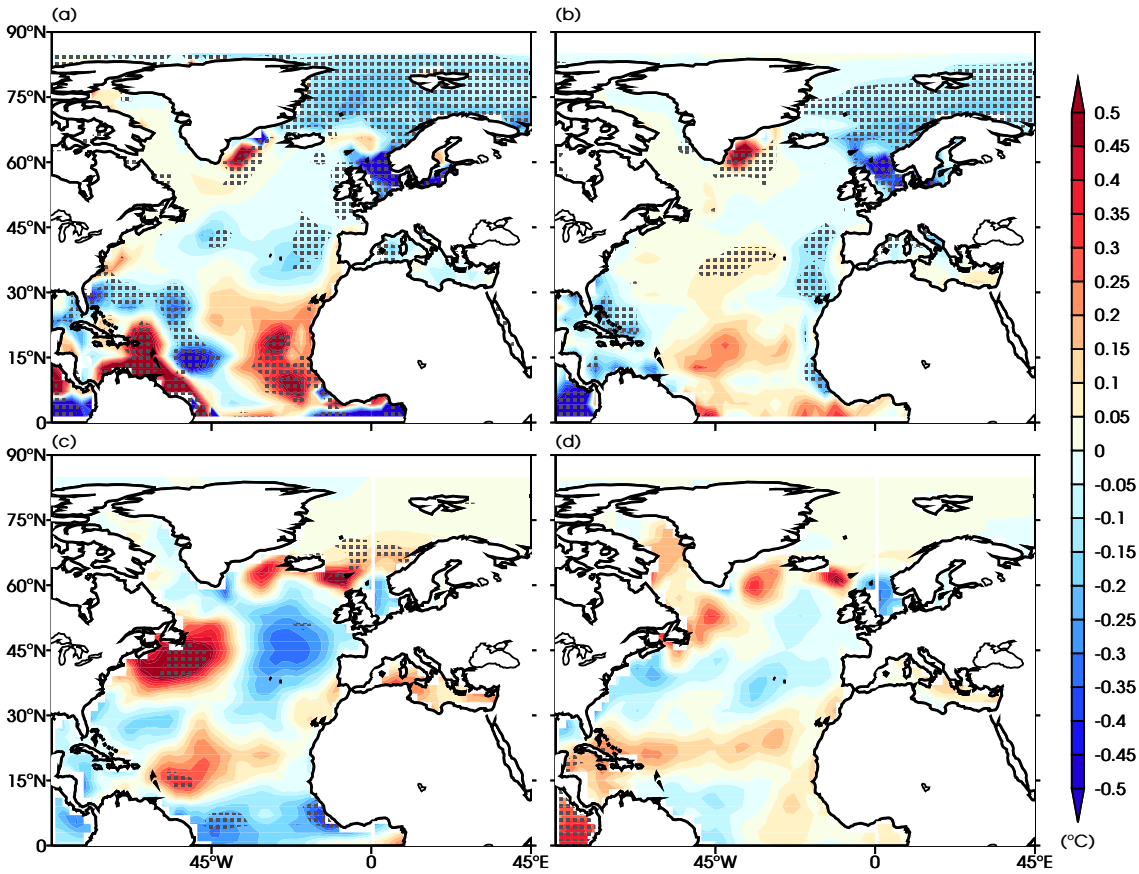


**Figure 7.11:** Anomalous rate of change to mixed layer heat budget ( $^{\circ}\text{C}$ ) for: (a) splitting and (b) displacement composites. Anomalous potential temperature in upper ocean layer (from 0 to 30 m depth,  $^{\circ}\text{C}$ ) for: (c) splitting and (d) displacement composites. Period from 0 to 120 days following event onset. Stippling represents a p-value of less than 5%.

day average before event onset. This isolates the direct oceanic anomalous temperature change following SSWs and removes any precursory signal. Composites for splitting and displacement events are presented in panels (c) and (d) respectively. For displacements there is a warming/cooling following events over the sub-polar/subtropical gyres. The magnitude of this is weak and lacks stippling. For the splitting composite the potential temperature response is interesting. In agreement with the anomalous rate of change to mixed layer heat budget there is warming off the South-East coast of Greenland and cooling over the subtropical gyre. However, there is substantial warming centered at approximately  $40^{\circ}\text{N}$   $55^{\circ}\text{W}$  which does not agree with the results of Reichler et al. [2012] or the theoretical impacts from the atmosphere as presented in panel (a). It is unlikely that this is a result of atmospheric forcing due to the negative atmosphere-surface flux over this region (Figure 7.10(a)).

This oceanic warming off the coast of America/Canada is unexpected and war-

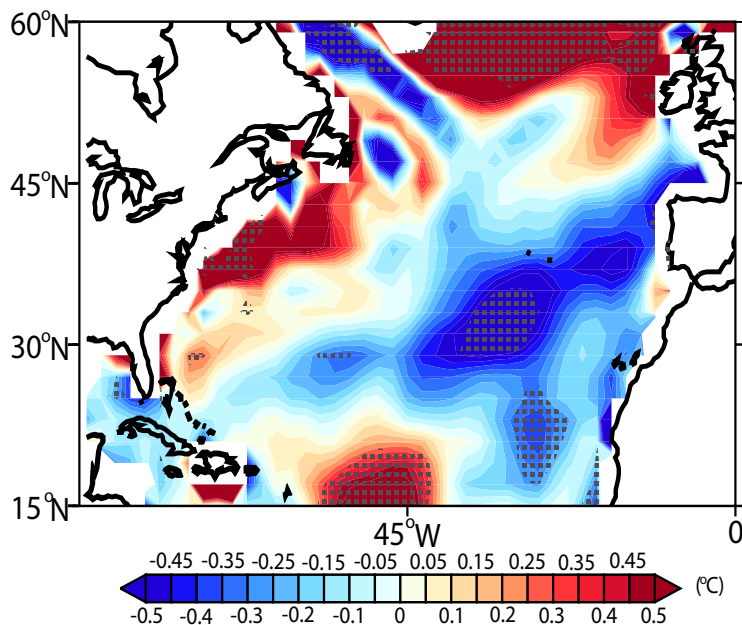


**Figure 7.12:** Anomalous rate of temperature change ( $^{\circ}\text{C}$ ) in the upper ocean layer (from 0 to 30 m depth) due to the full three-dimensional advective terms as outlined in Screen et al. [2010]. From 0 to 120 days following splitting events.  $P$ -values less than 0.1 stippled.

rants further investigation. Following splitting SSWs there is an average anomalous reduction in the sea surface height gradient across the Gulf Stream of approximately  $3/4$  cm. This anomaly is around 30% of the magnitude of the seasonal cycle and could be indicative of an anomalous weakening of the Gulf Stream and/or a shift in its location. Notably, the anomalous changes to mixed layer heat budget presented in Figure 7.11 have been calculated under a simplified framework where it was assumed that advective terms are dominated by the Ekman transport anomalies, which is a good approximation in the absence of a changing circulation. However, it is now evident that in FORTE other processes must be important in the  $40^{\circ}\text{N}$   $55^{\circ}\text{W}$  region. The contribution to anomalous rates of change of the mixed layer heat budget from full advective terms is calculated, as in Screen et al. [2010], for the upper ocean layer and presented in Figure 7.12. Downstream of the region of interest there is an anomalous advective warming and upstream there is cooling. This could be a consequence of reduced heat transport out of this region adds evidence to the hypothesis that there is a weakened Gulf Stream. A proposed mechanism is that the Gulf Stream is weakened in the region between  $40^{\circ}\text{N}$  to  $50^{\circ}\text{N}$  and this leads to less advective heat transport towards the pole. As a consequence of this, there is less poleward heat transport by the Gulf Stream equatorward of  $45^{\circ}\text{N}$  and this leads to heat convergence and warming. Similarly, there is a reduction in advective

heat transport into the region poleward of  $45^{\circ}\text{N}$ , there is a diverge of heat transport and cooling. This hypothesis requires further investigation to validate. Overall, the upper ocean warming centred at  $40^{\circ}\text{N}$   $55^{\circ}\text{W}$  is most likely a result of anomalous advective heat transport which is not Ekman related.

#### 7.2.4 Discussion

Coupling the IGCM4 to an interactive ocean has led to a shift in the atmospheric background climatology and impacted SSW simulation. There are far fewer SSW events, particularly for splitting events and they are biased to occur in late winter. This change is likely to be related to alterations in the climatological upward heat flux at 100 *hPa*.

The descent of anomalies through the troposphere and impacts on surface temperature following SSW onset is stronger for splitting SSWs than displacements. Theoretical impacts into the ocean, via changes to mixed layer heat budget, indicate a warming over the subpolar gyre and a cooling for the subtropical gyre. This agrees with literature and the earlier IGCM4 results presented in Chapter 4. The changes to mixed layer heat budget are stronger for the splitting composites but the differences are smaller than observed in the IGCM4. There are only 17 splitting events in the FORTE 200 year model run. Therefore, it would be beneficial to conduct a longer coupled model integration to enable more rigorous statistical testing to confirm the results.

Upon assessing the actual impacts to oceanic top layer temperature following splitting SSWs there is a cooling over the subpolar gyre as expected. The implied Ekman heat flux should combine with with the net-atmosphere surface flux and induce a cooling off the coast of America. This is not observed in the model, instead there is a strong warming present. This warming is attributed to anomalous changes in advective heat transport over the western boundary current region poleward of  $35^{\circ}\text{N}$ . This warming could be a result of a weakened Gulf Stream. The source of this is unclear and could be potentially related to a reduction in downwelling over the Labrador Sea as a result of negative NAM regime [Zhai et al., 2014]. This hypothesis requires further work to validate. The Atlantic overturning circulation typically reacts to phenomena with low frequency variability and it would be somewhat surprising if the relatively short time scales associated with SSW impacts would be able to impact the overturning circulation [Visbeck et al., 2003, Delworth and Zeng, 2015]. It would be prudent to repeat analysis in a higher resolution coupled model to see if this is related to the coarse resolution of MOMA version utilised here, especially since this warming signal is not seen in the literature [Reichler et al., 2012].

As argued above, it would be beneficial to repeat the analysis in a longer integration due to the small sample size of splitting events.

### 7.3 IGCM4 forced with FORTE SSTs

Upon coupling the IGCM4 to an ocean the nature of SSW simulation is altered, events are less frequent, particularly splitting events, and occur later in the winter season. This change must be due to the presence of the interactive ocean; either through the change in climatological background state, the inclusion of coupling processes or a result of oceanic internal variability.

The change in climatological upward wave propagation would have a direct influence on the number of SSW events since the sensitivity to this flux is unaltered. Questions of interest are; how much of the reduction in event simulation can be attributed to the reduction in climatological upward wave flux and what is the source of this? It would be surprising if the state of the Atlantic Ocean has resulted in this change to SSW simulation given the results of Chapter 6. In FORTE there is a pronounced Western Pacific equatorial cold pool with an annual average magnitude of over  $-2^{\circ}\text{C}$  that is strong compared to the average across CMIP5 models, which have a multimodel mean annual bias of approximately  $-1^{\circ}\text{C}$  [Flato et al., 2013]. This cold equatorial bias could potentially lead to changes in wave dynamics [Winter and Bourqui, 2011].

#### 7.3.1 Experimental design

To test the hypothesis that the background climatological state has impacted SSW simulation the stand-alone IGCM4 is configured to be forced by monthly SST climatologies created from the 200 year FORTE integration. This introduces SST biases without introducing any oceanic internal variability or coupling processes. The new

**Table 7.13:** *Acronyms for each 200 year model integration. If SSTs are from the FORTE monthly climatology the box is ticked, otherwise the default IGCM climatology is used. Fields are applied over the Pacific Ocean or everywhere excluding the Pacific, the latter labelled as ‘Not Pacific’.*

Acronym	FORTE SST	
	Pacific	Not Pacific
IGCM4		
IGCM4-FGL	✓	✓
IGCM4-FEP		✓
IGCM4-FP	✓	

IGCM4 model integrations are configured in a similar manner to the AMO experimental design in section 6.2 with only SST values and saturated vapour pressure values being altered. A total of three experiments are performed and run for 200 years each, see Table 7.13 for experiment acronyms.

If FORTE SSTs are not applied over a domain then the default IGCM SST climatology is utilised. A cosine squared smoothing over 5 grid points is performed where the domain containing FORTE SSTs meets the original SST field (in the South Pacific) to prevent the introduction of artificial gradients. Surface temperature DJF climatologies minus the IGCM4 for each new model configuration is presented in Figure 7.14. This allows for direct comparison of the differences in climatological surface thermal forcing. It is worth noting that the standalone IGCM utilises linear temporal interpolation between monthly forcing fields and this introduces errors. The monthly mean of actual SST climatology the model is forced by deviates slightly from the climatology that is read in. Differences are generally less than  $0.1^{\circ}\text{C}$  and only pronounced at higher latitudes in agreement with Killworth [1995].

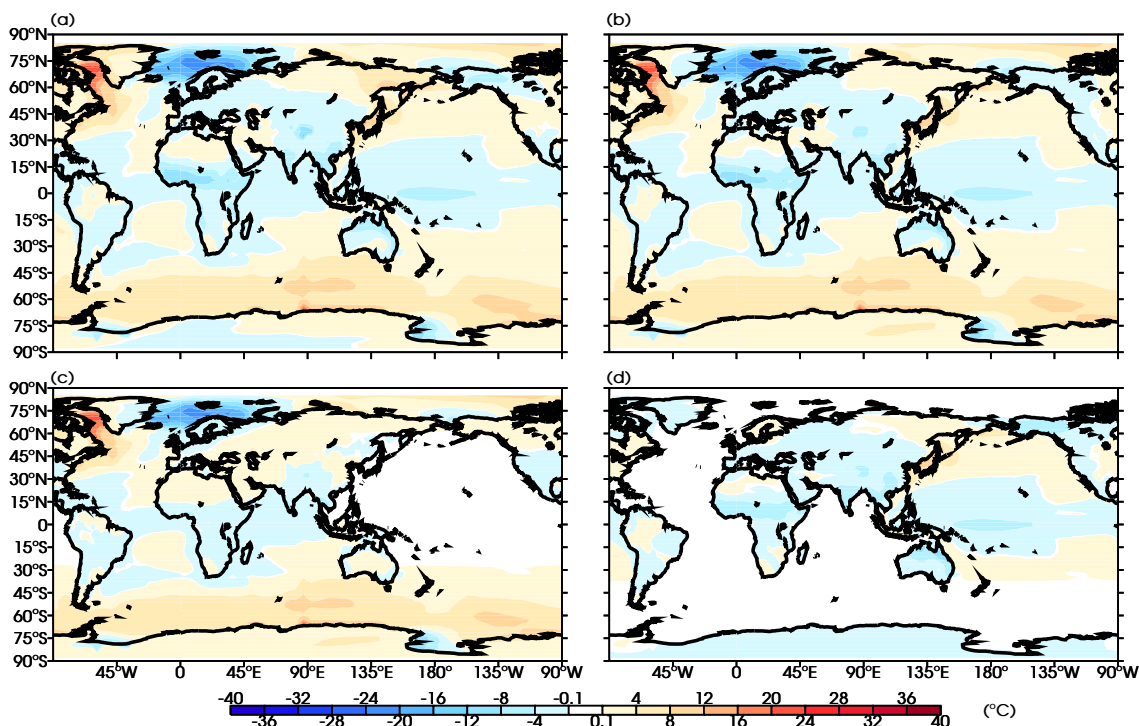


*Figure 7.14: Surface temperature ( $^{\circ}\text{C}$ ) DJF climatologies minus the IGCM4 for: (a) FORTE, (b) IGCM4-FGL, (c) IGCM4-FEP and (d) IGCM4-FP.*

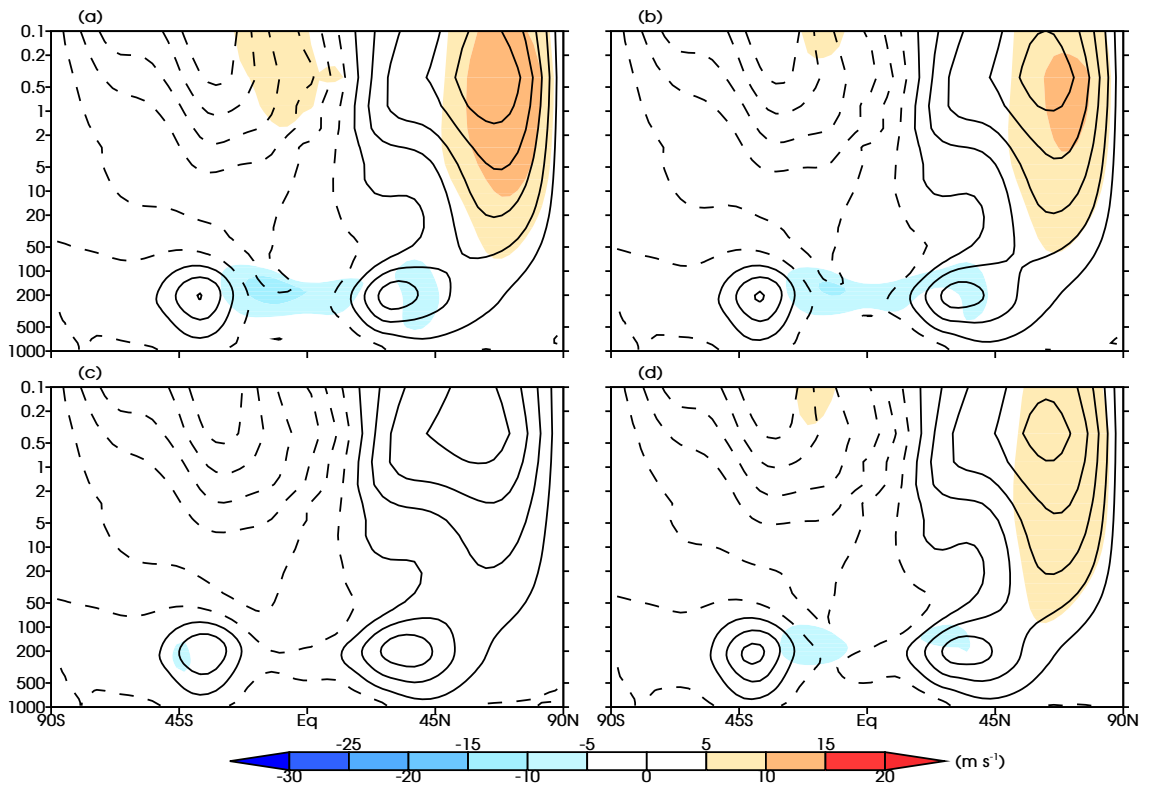


**Figure 7.15:**  $\bar{U}$  ( $m s^{-1}$ ) DJF climatologies minus IGCM4 for: (a) FORTE, (b) IGCM4-FGL, (c) IGCM4-FEP and (d) IGCM4-FP in solid colours. Total field in contour lines. Contour interval  $10 m s^{-1}$  Solid contours for positive values, zero and negative values dashed.

### 7.3.2 Results

$\bar{U}$  winter, DJF, climatologies are presented in Figure 7.15. The total field is presented in contour lines and differences to IGCM4 in solid colours. When forcing the IGCM4 with FORTE based SSTs over all oceans, in IGCM4-FGL Figure 7.15(b), the change in climatological  $\bar{U}$  is very similar to what is observed in FORTE. There is a strengthening of the polar vortex and a similar easterly tendency over the tropical upper-troposphere. This pattern is still present and slightly weaker for the IGCM4 forced with FORTE based SST only over the Pacific, Figure 7.15(d). When the IGCM4 is forced with FORTE SSTs everywhere except from in the Pacific, in IGCM4-FEP Figure 7.15(c), there is no notable change in the DJF  $\bar{U}$ . It appears that the atmospheric state, for the Northern Hemisphere polar vortex and equatorial troposphere, is primarily sensitive to SSTs over the Pacific.

The meridional heat flux, figures omitted, display similar results to  $\bar{U}$  winter climatology. IGCM4-FGL has a early winter reduction in meridional heat flux and stronger flux at lower latitudes, similar to Figure 7.3 and slightly weaker in magnitude. The experiment with FORTE SSTs only over the Pacific has the same

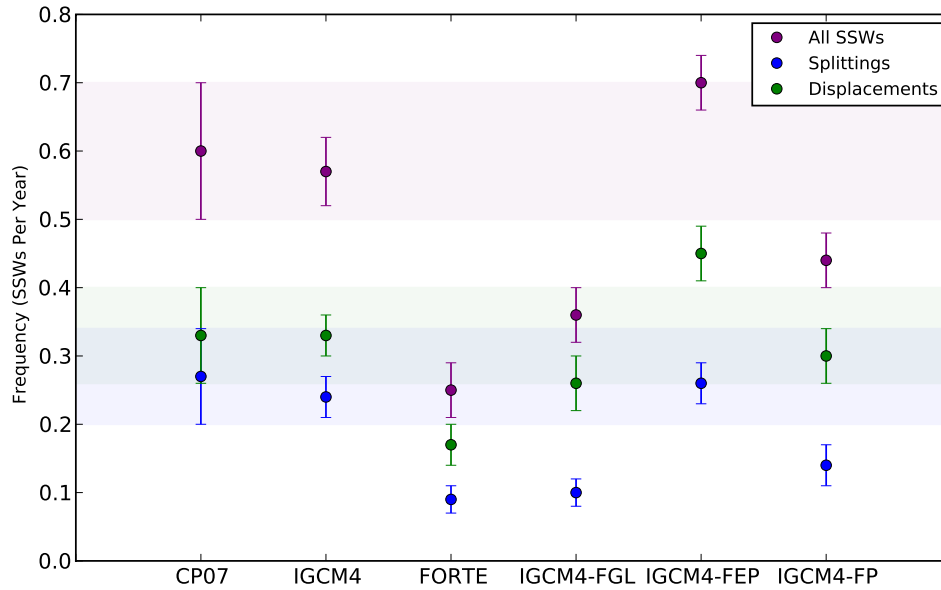


**Figure 7.16:** SSW frequency (events per year) with standard error bars. Limits of Charlton and Polvani [2007] benchmark (from NCEP/NCAR reanalysis data) shaded.

strengthening in heat flux towards the equator and a weaker early winter reduction which is only not insignificant between  $45^{\circ}\text{N}$  and  $60^{\circ}\text{N}$  and up until mid-January. The final experiment, IGCM4-FEP, displays little notable difference to the IGCM4 simulation, there is a slight increase in meridional heat flux towards the end of February between  $40^{\circ}\text{N}$  and  $60^{\circ}\text{N}$ .

The frequency of SSW simulation for each model configuration is presented in Figure 7.16 along with the CP07 benchmark. The coupled model displays a large and not insignificant drop for both splitting and displacement SSWs. Experiments with FORTE SSTs over the Pacific (that is IGCM4-GL and IGCM4-FP) have splitting SSW frequencies below the benchmark lower limit. The number of displacements also reduce, but not as much as in the coupled model. Total SSW frequency is below the CP07 benchmark. IGCM4-FEP has a displacement frequency outside of the benchmark. In this simulation there is an increase in displacement event occurrence. The overall frequency for all SSWs is within the benchmark limits.

The simulation of splitting SSWs is particularly sensitive to climatological Pacific SSTs with a strong reduction in splitting occurrence for both IGCM4 simulations configured with FORTE based SSTs in the Pacific. The overall SSW frequency is outside the CP07 benchmark. Displacement events are less affected in these simulations; the reduction in displacement frequency is larger in magnitude in the coupled

model. When the IGCM4 is forced by FORTE SSTs away from the Pacific the overall SSW frequency remains within the benchmark limits. This is in agreement with the results of Chapter 6 where the stratospheric state of IGCM4 displayed insensitivity to prescribed climatological Atlantic SSTs.

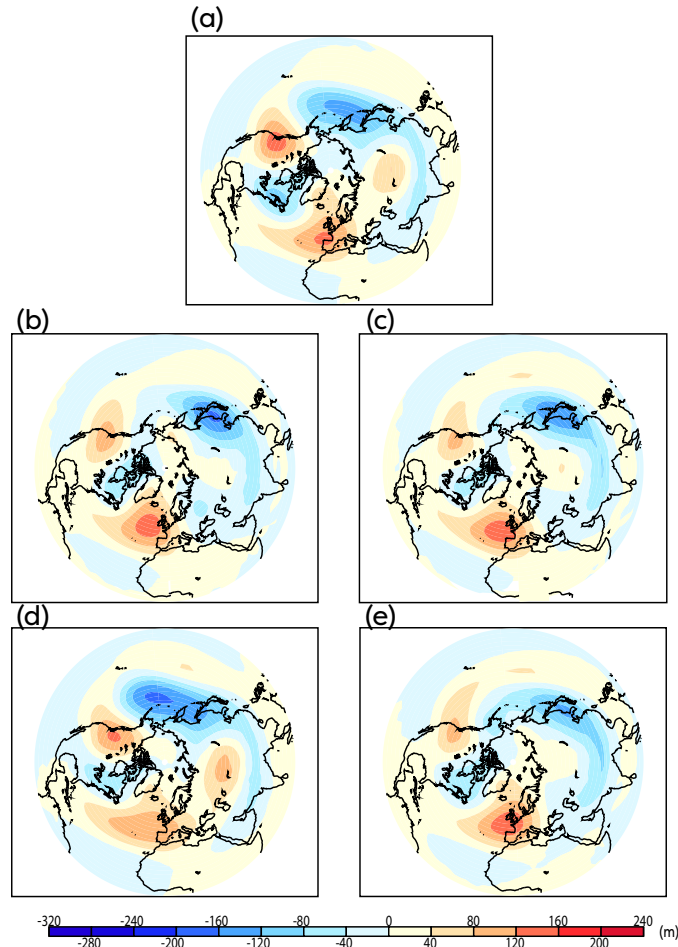


**Figure 7.17:** Geopotential height 500 hPa eddy field (m) for: (a) IGCM<sub>4</sub>, (b) FORTE, (c) IGCM<sub>4</sub>-FGL, (d) IGCM<sub>4</sub>-FEP and (e) IGCM<sub>4</sub>-FP.

To provide two dimensional understanding the DJF geopotential height eddy field is presented in Figure 7.17. The eddy pattern is weaker than the IGCM<sub>4</sub> over the Pacific for FORTE, IGCM<sub>4</sub>-FGL and IGCM<sub>4</sub>-FP. Particularly the local minimum over the Aleutian region is shifted westwards. The eddy pattern is stronger in IGCM<sub>4</sub>-FEP. If the tendency for the model to produce SSW is related to the linear interference between the climatological background eddy field and anomalous behaviour [Omriani et al., 2015, Goss et al., 2015] then this could go some way to consolidate the SSW frequency presented in 7.16. This hypothesis requires further work to validate.

**Table 7.18:** ENSO winters based on the Niño 4 Index in FORTE. An ENSO winter occurs if the index exceeds one standard deviation in DJF, if this is not satisfied the winter is neutral. Splitting and displacement SSWs separated into number of occurrence under ENSO regimes in the third and fourth columns respectively.

	Total Winters	Splittings	Displacements
El Niño	49	4	11
La Niña	46	4	3
Neutral	106	9	19

### 7.3.3 Discussion

Changes in background climatology due to the introduction of Pacific SST biases from FORTE results in a reduction of SSW frequency. Splitting events are more sensitive to changes in climatological thermal forcing over the Pacific. In the coupled model there is a drop in the frequency of both splitting and displacement SSWs. A speculative hypothesis is that other processes related to the introduction of an interactive ocean must be contributing and particularly influencing displacement frequency. These modes are most likely not controlled by the Atlantic given the insensitivity of the IGCM4 to the AMO (Chapter 6).

There are many modes that could be related to SSW occurrence including ENSO, the Madden-Julian Oscillation [Fletcher and Kushner, 2011] and the Pacific Decadal Oscillation [Kren et al., 2015, Woo et al., 2015]. Particularly ENSO modulation of SSW occurrence is an area of active research with the modelling study of Taguchi and Hartmann [2005] reporting an increase of event occurrence under El Niño winters in WACCM. The reanalysis study of Butler and Polvani [2011] reports an increase of SSW frequency in all ENSO winters. There is clearly debate in the literature as to whether SSW events are suppressed or enhanced during ENSO phase. However, it may be feasible that for some climate models SSW frequency is related to ENSO phase. To briefly investigate this hypothesis ENSO winters are isolated in the 200 year FORTE simulation using the Niño 4 Index. Results are presented in Table 7.18. Only 9% of the displacement events occur during La Niña winters whereas splitting events are equally likely to occur under La Niña or El Niño conditions. This provides some support to the hypothesis that a coupled mode of internal variability, that is ENSO, is modulating displacement occurrence. However, the small sample size hinders the robustness of this statement. Further study is required with a much longer coupled model simulation.

## 7.4 Conclusions

This Chapter has focused on how the presence of an interactive ocean in a GCM can affect the atmospheric climatological background state and SSW simulation. In the IGCM4 it was found that the introduction of SST biases over the Pacific resulted in the greatest change to the atmospheric background state. Splitting SSW frequency is particularly sensitive to the climatological Pacific state, with far fewer events occurring in the coupled model. The displacement frequency is also reduced, but appears to be less sensitive to climatological SST biases and is more likely affected by a mode of internal variability. A preliminary investigation suggests event suppression during La Niña, but requires more work to validate. This leads to the caveat that if coupled GCMs are not producing a realistic number of SSW events, or are particularly biased to producing displacements, then the state of the climatological Pacific should be assessed. Improving biases in this region may aid realistic SSW simulation.

It is found that the behaviour of the descent of SSW anomalies and surface impacts are generally similar between the stand-alone and coupled versions of the model, validating the extrapolation of general surface impacts from atmosphere-only GCMs to the coupled climate system, a useful results for the modelling community. For splitting SSWs the simulated anomalous changes to upper ocean temperature is dominated by a warming signal that is a result of non-Ekman transport induced heat advection. There is cooling over the subpolar gyre as expected under the simplified mixed layer heat budget framework. It appears as though there is interaction between splitting SSWs and the strength of the Gulf Stream in FORTE. In the coupled model it is more difficult to clearly isolate differences in ocean impacts for the splitting and displacement subclasses, most likely a result of the small sample sizes here. Next research steps should include: 1) repeating this analysis in a longer coupled model integration to enable larger SSW splitting and displacement samples to assess the robustness of these results; 2) quantification of (and isolation of mechanism behind) the change in Gulf Stream strength in FORTE and 3) repeating analysis in a higher horizontal resolution stratosphere resolving coupled model to assess whether the coarse nature of MOMA is affecting results.



---

## Chapter 8 - Conclusions

The motivation behind this body of work was furthering understanding into the coupled stratosphere-troposphere-ocean system. Focus was on how SSWs impact the surface climate and ocean and their interactions with other climatic modes, specifically the AMO and NAM. This was achieved predominantly through a series of general circulation model experiments.

Improved understanding into the role SSWs play in the coupled climate system has direct applications for model development teams. The results from the models used here demonstrate the importance of simulating both splitting and displacement events with the correct frequency. Ensuring SSWs are realistically simulated has positive implications for medium term weather forecasting due to the strong and sustained impacts SSW can have on the surface climate.

The results of this work also contribute to understanding how the stratosphere can directly impact the Atlantic Ocean; mainly communicated via the induced NAM regime at the surface. There are substantial modifications to the implied Ekman heat transport and air-sea energy flux following SSWs. This demonstrated that if realistic simulations of the climate system are to be achieved then both deep layers of the ocean and stratosphere are necessary.

A brief overview of the key results from this thesis now commences, with scope for further work also outlined.

### 8.1 Simulation Of and Identification Algorithms for SSWs

As highlighted by Palmeiro et al. [2015] different SSW identification techniques can lead to contradiction in the literature. An example is the decadal variability in SSW frequency. Therefore it is important to consider the numerical algorithm being implemented. It is difficult, as highlighted in Chapters 2 and 5, to construct an objective straightforward SSW identification and classification technique. Here a hybrid algorithm was constructed, partially motivated to provide insight into the apparent contradiction between studies that assessed splitting and displacement impacts on the surface climate (Charlton and Polvani [2007] and Mitchell et al. [2013a]). This method utilised zonal mean zonal wind reversal based identification and moment analysis based classification techniques. Benefits included the facts that: it is computationally cheap, easy to implement, based on dynamically relevant criteria and that limitations and error rates are assessed.

Further to this an attempt was made to construct a completely objective EOF based algorithm for SSW identification and classification. The objective was to

isolate modes of spatial variability between SSW events and attribute particular modes of variability to either splitting or displacement subsets which could then be used to construct a classification technique. This was not achieved; issues included the averaging out of data due to disturbed polar vortex rotation and, when an attempt was made to correct this via the rotation of fields, artificial jumps were introduced that limited the validity of physical interpretation of the resulting EOF modes. There is scope to further develop this method and remove artificial jumps in the rotation process.

The IGCM4 is an atmosphere-only, spectral primitive equation global GCM. It is computationally cheap to run, includes a gravity wave drag parametrisation and is relatively straight-forward to manipulate boundary conditions and forcing fields to allow for hypothesis testing. Processes such as: soil moisture, sea-ice formation, evaporation and radiation schemes are simulated in a simplified manner when compared to state of the art models, enabling a quicker run time. It sits within the hierarchy of models as a model with intermediate complexity. SSWs were assessed in the IGCM4, where the gravity wave drag scheme was tuned for a mean zonal climatological state that compares well to NCEP/NCAR reanalysis. Overall it was found that SSWs are simulated well, there was a good ratio of splitting to displacement events and the seasonal distribution was similar to NCEP/NCAR reanalysis. SSWs were a result of upward wave propagation and the winter polar stratosphere had a warming sensitivity to upward wave forcing that was comparable to ERA-40. Average event strength was slightly weak at 10 *hPa*, particularly for splitting events but event magnitude at 100 *hPa* was within the benchmark error. This led to the conclusion that coupling between the middle and lower stratosphere was slightly strong when compared to reanalysis, a common model phenomenon [Charlton et al., 2007]; however, signals communicated into the troposphere were of a similar average strength to reanalysis.

The IGCM4 was combined with a fully-interactive ocean model, MOMA, to form a coupled atmosphere-ocean general circulation model, FORTE. The atmospheric component of this coupled model was configured to be as similar to the stand-alone IGCM4 as possible to enable traceability of changes in atmospheric climatological background state and SSW simulation. One may expect, as in Hansen et al. [2014], an increase in SSW event frequency from the presence of an interactive ocean. This was not observed, in FORTE the average polar night jet strength was stronger and the polar vortex less disturbed, there was less meridional heat flux at 100 *hPa* in early winter and more tropospheric wave breaking poleward of 30°N over DJF. The presence of an interactive ocean led to a dramatic reduction in the number of simulated SSW events, a total of 50 in the 200 years of data. There was also

a change in the seasonality of events with the distribution shifted towards late winter. Statistical testing revealed that it was unlikely the frequency of SSW events occurring in FORTE was similar to that of NCEP/NCAR.

Overall the IGCM4 is capable of simulating SSWs in a manner similar to what is observed in reanalysis. Upon the inclusion of an interactive ocean there is a strong shift in the background atmospheric state that suppresses SSW activity, this is attributed to a lack of wave activity entering the stratosphere during boreal winter.

## 8.2 SSWs Interactions with other Climatic Modes

### 8.2.1 Tropospheric Impacts

In the IGCM4 tropospheric impacts were assessed via the descent of negative NAM regimes and surface temperature anomalies. It was found that, on average, in the IGCM4 splitting SSWs were associated with stronger surface impacts than when compared to displacements. This is a similar result to the work of Mitchell et al. [2013a] but here a zonal mean zonal wind based identification was used, enhancing robustness of the result. It is worth stressing that this work was based on composite analysis and utilised a rather artificial binary classification into either splitting or displacement subcategories. In reality SSW impacts on the surface are not so ‘black and white’. In the stratosphere events can be a mixture of splitting and displacement and, although there may be an enhanced likelihood of splitting events impacting the surface climate in the IGCM4, there is variability between events which should be considered. It would be illuminating to isolate the stratosphere-troposphere coupling mechanisms that promote stronger surface impacts. Overall it is important for models to be able to simulate both splitting and displacement SSWs with the appropriate frequency.

Utilising EOF based analysis to isolate spatial modes of variability between SSW events at 10 *hPa* led to one mode being associated with strong surface anomalies. This was interpreted as events that are shifted towards the Atlantic/W.Europe/Canadian sector being, on average, associated with a negative NAM regime at 1,000 *hPa* over the 30 days following event onset. The statistical nature of EOF analysis and correlations used to assess relationships between 10 and 1,000 *hPa* suggested the need for further independent investigation into this result. An algorithm was developed to isolate SSW events that has a disturbed polar vortex trajectory which passed through the region of variability isolated by the EOF structure. It was confirmed that when events initially tracked into the Atlantic/W.Europe/Canadian sector they were typically accompanied by a negative NAM regime at the surface over the 30 days following events. Events that did not have a trajectory that

travelled through this region were unlikely to impact the surface climate. This is an interesting results that displays promise in isolating a new subcategory of events with enhanced likelihood of impacting the surface climate. This hypothesis requires investigation in other GCMs to determine if this is a model dependent feature and would also benefit from being repeated in a longer IGCM4 integration to assess the robustness of these results. Further research should also include assessment of precursors and the nature of wave forcing prior to event onset and whether splitting SSWs are more likely to track into this region.

### 8.2.2 Pacific

As outlined in section 8.1 there was a reduction in SSW frequency in FORTE and a bias towards events occurring later in the winter season. Further simulations in the stand-alone IGCM4 displayed that the splitting SSW frequency was particularly sensitive to the climatological Pacific state. Two model integrations showed that when the IGCM4 was forced with FORTE based climatological SSTs over the Pacific only and globally there was a drop in splitting SSW frequency. This reduction in frequency was of a similar magnitude to what occurred in the coupled model. When the IGCM4 was forced with FORTE SSTs everywhere except from the Pacific this reduction in frequency was not observed. Changes to upward wave activity reflected the SSW frequency results with less early winter meridional heat flux for IGCM4 simulations forced with FORTE SSTs over the Pacific. Climatological Pacific SST biases introduced from the coupled model appeared to be directly related to splitting SSW frequency. There was a reduction in 200 *hPa* divergence over the western Pacific in FORTE, potentially due to the equatorial cold bias in this model, which could be a cause of the stronger average stratospheric polar vortex [Winter and Bourqui, 2011, Goss et al., 2015]. In the coupled model the displacement frequency was also reduced, but appeared to be less sensitive to climatological SST biases and it was more likely that the displacement frequency was affected by a mode of internal variability. There was a tentative connection to displacement reduction during La Niña phases; however, the small sample size available in this 200 year integration prohibited further investigation. Next research steps require a longer coupled model integration to increase sample sizes and assessment of the robustness of results. Further areas of study should include assessing SSW simulation during El Niño and La Niña winters, including assessment in modification to tropospheric wave generation and any interaction with the Aleutian low structure.

### 8.2.3 Atlantic

Two distinct scientific objectives were undertaken over the Atlantic Ocean. These included the modulation of SSW frequency due to Atlantic SST state and the downward influence SSW events could have on the Atlantic Ocean.

The sensitivity of the stratosphere to Atlantic SST state was assessed under an AMO framework and motivated by studies that argue a NAO/AMO correlation could be related to modulation of SSW frequency [Omrani et al., 2014, Keenlyside and Omrani, 2014, Omrani et al., 2015]. IGCM4 experiments with HadISST anomalies at single, double and quadruple strength for AMO cold and warm phases displayed that the IGCM4's stratospheric state was remarkably insensitive to AMO phase (particularly when considering the strong sensitivity to the Pacific state discussed in the previous section). SSW frequency remained consistent across all model experiments. Benchmarks for SSW event strength at 10 *hPa*, coupling between the middle and lower stratosphere, meridional heat flux at 100 *hPa* prior to event onset and surface impacts showed no significant deviations across the AMO simulations. The results were also insensitive to whether the sea-ice field in the North Atlantic sector was perturbed or if there was smoothing at anomaly boundaries. This is in contrast with the work of Omrani et al. [2014] who proposed a mechanism where there is a shift to increased SSW frequency under AMO warm conditions, thus promoting a more negative NAO regime at the surface in ECHAM5. There is more agreement with the work of Peings and Magnusdottir [2015] who found that a stratospheric response was not necessary to facilitate a shift to negative NAO regime under warm AMO conditions in CAM5.

Expansion of the Omrani et al. [2014] results by Omrani et al. [2015] showed that there could be non-linearity in the response during the AMO negative phase. Omrani et al. [2015] hypothesized that this non-linearity could be related to linear wave interference between the eddy and stationary wave structure over the Aleutian low region. While this mechanism could potentially consolidate the results of Omrani et al. [2015] it could not account for the insensitivity in SSW frequency to AMO phase in the IGCM4. It is more likely that differences in model configuration led to this difference, a multimodel comparison study on the stratosphere's sensitivity to Atlantic SST configuration may go some way to consolidate these results.

Next research steps should include direct assessment of the AMO-NAO relationship in the IGCM4. Although there is a weakened Icelandic low over January-March for the AMO warm single strength simulation when compared to the AMO cold single strength simulation there is no quantification of the presence of an AMO-NAO anti-correlation in the IGCM4. Without direct assessment of whether the IGCM4

can simulate a shift in NAM regime in response to AMO forcing the agreement between these results and that of Peings and Magnusdottir [2015] cannot be unequivocally confirmed.

Impacts on the Atlantic Ocean following SSW events were assessed following the works of Marshall et al. [2001], Visbeck et al. [2003] and Zhai et al. [2014]. In the IGCM4 and in NCEP/NCAR reanalysis there was a weakening of the climatological surface wind stress curl, which was sustained for at least a month. These, for oceanic timescales, short term impacts are communicated into the ocean via modifications to the net atmosphere-surface flux fields (including sensible heat, latent heat, longwave and short wave radiation terms) and wind stress induced modifications to Ekman heat transport. In the IGCM4 following SSW events there was warming over the subpolar gyre and cooling over the subtropical gyre, in agreement with Marshall et al. [2001], Visbeck et al. [2003], Reichler et al. [2012] and Zhai et al. [2014]. This work directly linked SSW events to oceanic impacts and provided a full assessment of the surface fluxes and Ekman induced heat transport. In the IGCM4 it was found that the implied oceanic impacts associated with splitting SSW events were, on average, stronger than those associated with displacement SSWs; as one would expect from the tropospheric impact results, again highlighting the need for splitting and displacement SSWs to be considered as independent events and simulated appropriately.

The above results are qualitative assessments of potential impacts into the ocean. While it was advantageous to assess the SSW impacts in a stand-alone atmospheric model to isolate a clear signal, the full response can only be quantified by repeating analysis in the coupled model. This allowed for identification of how coupling could impact the implied oceanic response to SSW events. Unfortunately the drop in SSW numbers in the coupled model led to small sample sizes. Overall, the implied impacts remained consistent between FORTE and the IGCM4 aiding the robustness of the mechanisms behind SSW impacts into the ocean. The differences between splitting and displacement events were still evident, but weaker and lacked significance. There is a need for a longer integration to allow large enough sample sizes to conduct this analysis with more confidence. The simulated oceanic impacts following splitting SSWs were dominated by a non-Ekman advective heat transport, which could be related to a reduction of the Gulf Stream strength. This response was unexpected and although MOMA has a sophisticated dynamical core the resolution employed in the study was coarse. There is the need for repeat analysis in higher horizontal resolution atmosphere-ocean coupled model to assess the robustness of the simulate ocean results here before further work is conducted.

### 8.3 Concluding Remarks

SSWs are an impressive dynamical phenomena. They greatly perturb the stratospheric state with anomalies potentially descending through the atmospheric column leading to changes in atmospheric flow dynamics and large temperature anomalies in the Northern Hemisphere during boreal winter. This body of work has directly furthered scientific understanding by advancing knowledge on the likelihood of different classes of SSW impacting the surface climate. Furthermore this work has explicitly demonstrated the link between SSWs and their ability to impact the Atlantic Ocean. This is achieved via assessment of anomalous atmosphere-surface energy fluxes and Ekman transport following SSW events. This directly contributes to and expands on previous literature that looked at how strong polar vortex events impact North Atlantic SST [Reichler et al., 2012]. Overall, it is important for SSWs to be accurately simulated to capture their associated surface climate response, particularly both splitting and displacement events should be simulated with appropriate frequencies. There is potential for SSW event simulation to be particularly sensitive to the Equatorial Pacific SST state; which is an important result for modelling groups wishing to simulate SSW in an appropriate manner.

An additional output from this body of work is the technical development of a hybrid algorithm for identifying and classifying SSW events. This algorithm is computationally cheap, straightforward to implement and has been rigorously tested to establish an error rate, allowing for appropriate interpretation of results.

Throughout this thesis there is no attempt to isolate stratosphere-troposphere coupling mechanisms. Ultimately if the mechanisms behind why some SSWs are more likely to impact the surface climate are understood then this would prove valuable to the modelling and forecasting communities.

There is much scope for further work, particularly there is the need for longer coupled model simulations to improve SSW sample sizes. It would be useful to repeat the analysis on SSW impacts on the Atlantic Ocean in different general circulation models. These would need to be fully interactive, high-top coupled models that simulate SSWs well and preferably have higher horizontal resolution oceanic components than FORTE. The key aim would be to test the robustness of the Gulf Stream response to splitting SSWs in FORTE.



## Appendices

### A Moment Analysis Equations

To utilise moment analysis equations as a diagnostic of the temporal evolution of the polar vortex, as in section 2.4.2, polar air must be isolated. The chosen method is outlined in Mitchell et al. [2011] and Matthewman et al. [2009] but will also be included here in the interest of completeness and reproducibility. Moments are presented in Cartesian coordinates obtained from spherical data by utilising Lambert's azimuthal equal-area projection. Following Matthewman et al. [2009] the vortex edge,  $q_b(y)$ , is defined as the average PV poleward of  $45^\circ\text{N}$  9 days before the identified central date. This has the advantage of producing a separate vortex edge for each SSW event (unlike in Waugh and Randel [1999]) and is computationally cheaper than daily formulation of  $q_b$  in Mitchell et al. [2011]. Although it should be noted that the daily computation approach allows for better representation of the vortex edge during the breakdown of a SSW.

Once  $q_b$  is determined the modified PV field,  $q^*(x, y)$ , is calculated as

$$q^*(x, y) = \begin{cases} q(x, y) - q_b(y) & \text{if } q(x, y) > q_b(y), \\ 0 & \text{if } q(x, y) \leq q_b(y). \end{cases}$$

where  $q(x, y)$  is the total PV field.

Using  $q^*(x, y)$  the moments can now be defined. Zeroth and first order moments are calculated using

$$\mu_{ab} = \iint_s q^*(x, y) x^a y^b dx dy, \quad (\text{A1})$$

In this  $a$  is the moment order in the  $x$ -direction and  $b$  is the moment order in the  $y$ -direction such that  $a, b \in \{0, 1\}$ . Higher-order moments are calculated using a centralized formula, this has the benefit of calculating moments relative to the centroid of  $q^*(x, y)$  instead of over the arbitrary coordinate system. The centralized moment formula is given by

$$J_{ab} = \iint_s q^*(x, y) (x - \bar{x})^a (y - \bar{y})^b dx dy, \quad (\text{A2})$$

where  $\bar{x}/\bar{y}$  is the center of the vortex in the  $x/y$ -direction.

Using (A1) and (A2) the vortex parameters can be calculated, recall these are: vortex area, centroid location, aspect ratio and kurtosis. The vortex area is represented using an 'objective area' which is defined in Waugh and Randel [1999] and

also used by Mitchell et al. [2011]. This new area diagnostic was thoroughly examined by Mitchell et al. [2011] and they deduced that it evolves in a similar fashion to area throughout the winter period. A key difference between the area representations is that objective area reacts with a greater amplitude during extreme vortex variability. The objective area,  $A$ , is given by

$$A = \frac{\mu_{00}}{q_b}. \quad (\text{A3})$$

The centroid latitude,  $(\bar{x}, \bar{y})$ , and aspect ratio,  $r$ , equations are used by Waugh and Randel [1999], Matthewman et al. [2009] and Mitchell et al. [2011]. These are

$$(\bar{x}, \bar{y}) = \left( \frac{\mu_{10}}{\mu_{00}}, \frac{\mu_{01}}{\mu_{00}} \right), \quad (\text{A4})$$

and

$$r = \left[ \frac{(J_{20} + J_{02}) + (4J_{11}^2 + (J_{20} - J_{02})^2)^{\frac{1}{2}}}{(J_{20} + J_{02}) - (4J_{11}^2 + (J_{20} - J_{02})^2)^{\frac{1}{2}}} \right]^{\frac{1}{2}}. \quad (\text{A5})$$

The kurtosis, used for distinction between splitting and displacement events, is given by

$$k_4 = \mu_{00} \frac{J_{40} + J_{04} + 2J_{22}}{(J_{20} + J_{02})^2} - \frac{2}{3} \left( \frac{3r^4 + 2r^2 + 3}{r^4 + 2r^2 + 1} \right). \quad (\text{A6})$$

This formula is taken directly from Matthewman et al. [2009]. Once these quantities have been formulated around the central dates they can be used to assess the behaviour of the polar vortex, particularly in the classification procedure of SSWs as outlined in section 2.4.2.

## B SSW Case Studies

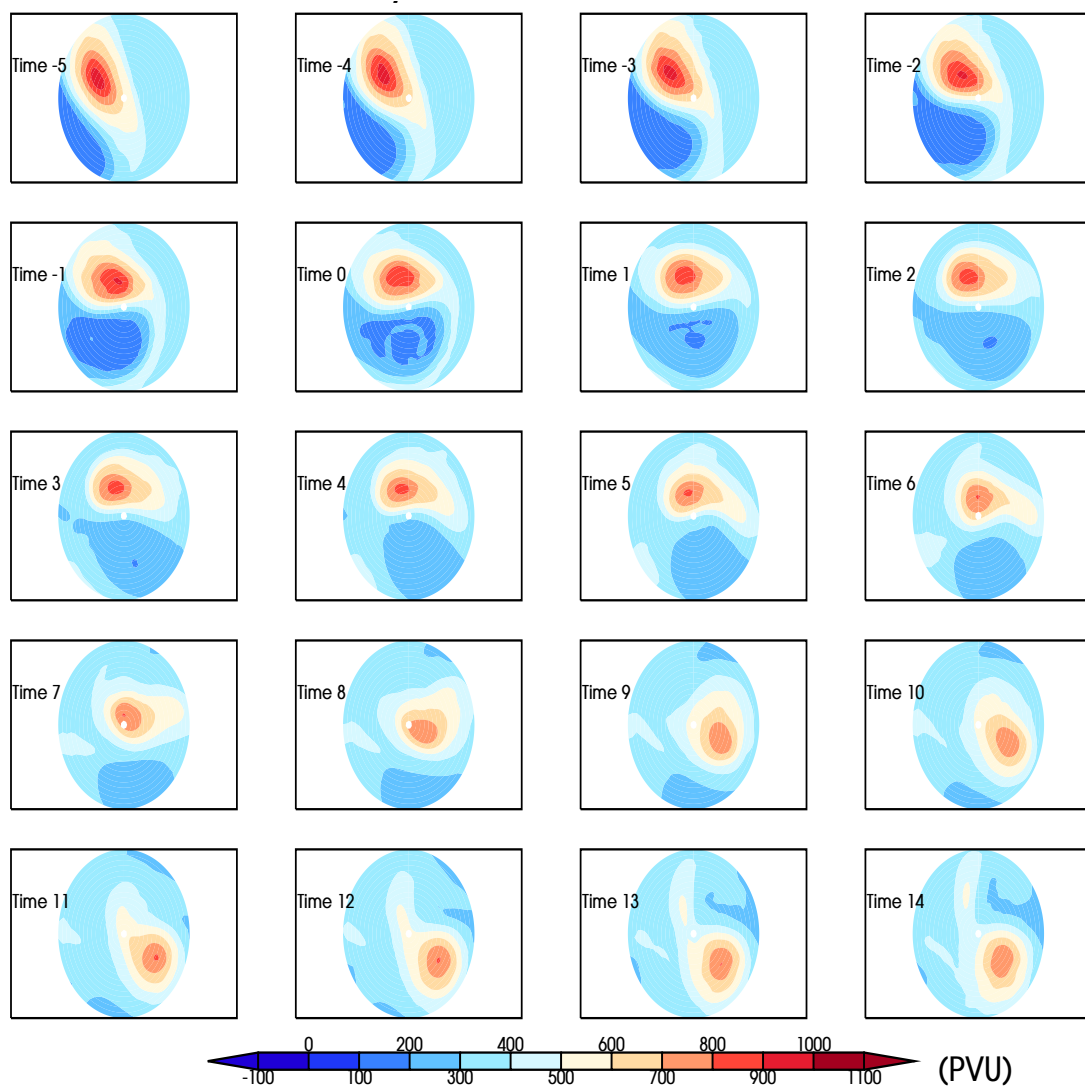


**Figure B1:** Case study of displacement SSW event in Ertel's Potential Vorticity (PVU). Event isolated at time-step 6193, classified as a displacement. Time in days.

Two case studies of the temporal evolution of a displacement and splitting SSW are presented in Figures B1 and B2. This provides a visual representation of the behaviour of the Northern Hemisphere polar vortex during two separate events. These events are captured in the Intermediate General Circulation Model 4, see Chapter 3.

The evolution is depicted in Ertel's potential vorticity (in PVU, defined as  $10^{-6} m^{-2} s^{-1} K kg^{-1}$ ) where red tones indicates high values of potential vorticity and provides a tracer of the polar vortex air mass (a conserved quantity providing diabatic and frictional forcing are known). The plots begin 5 days before the reversal of

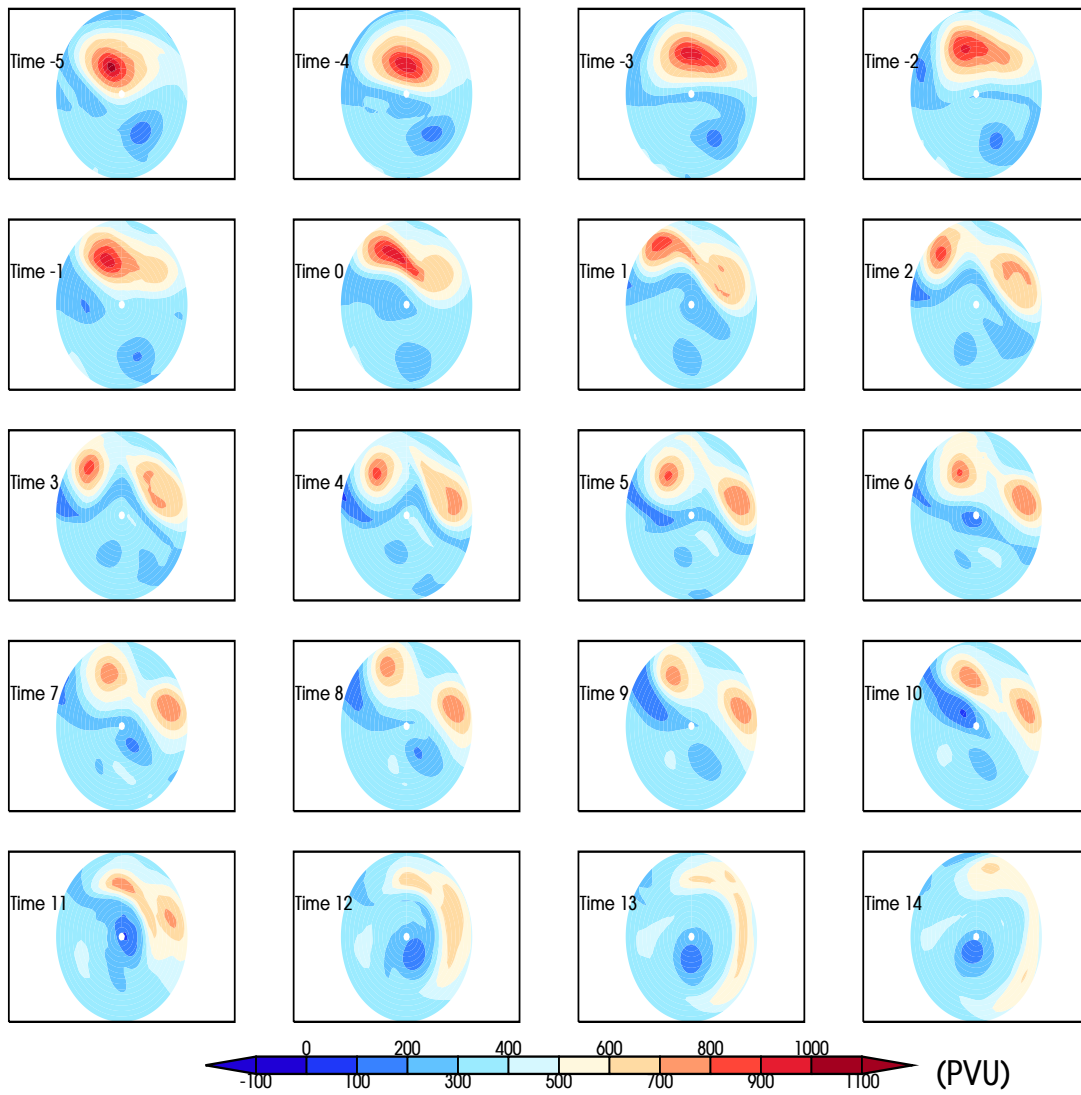


**Figure B2:** Case study of splitting SSW event in Ertel's Potential Vorticity (PVU). Event isolated at time-step 7614, classified as a splitting. Time in days

zonal mean zonal wind at 10 hPa and 60°N and continue until 14 days afterwards.

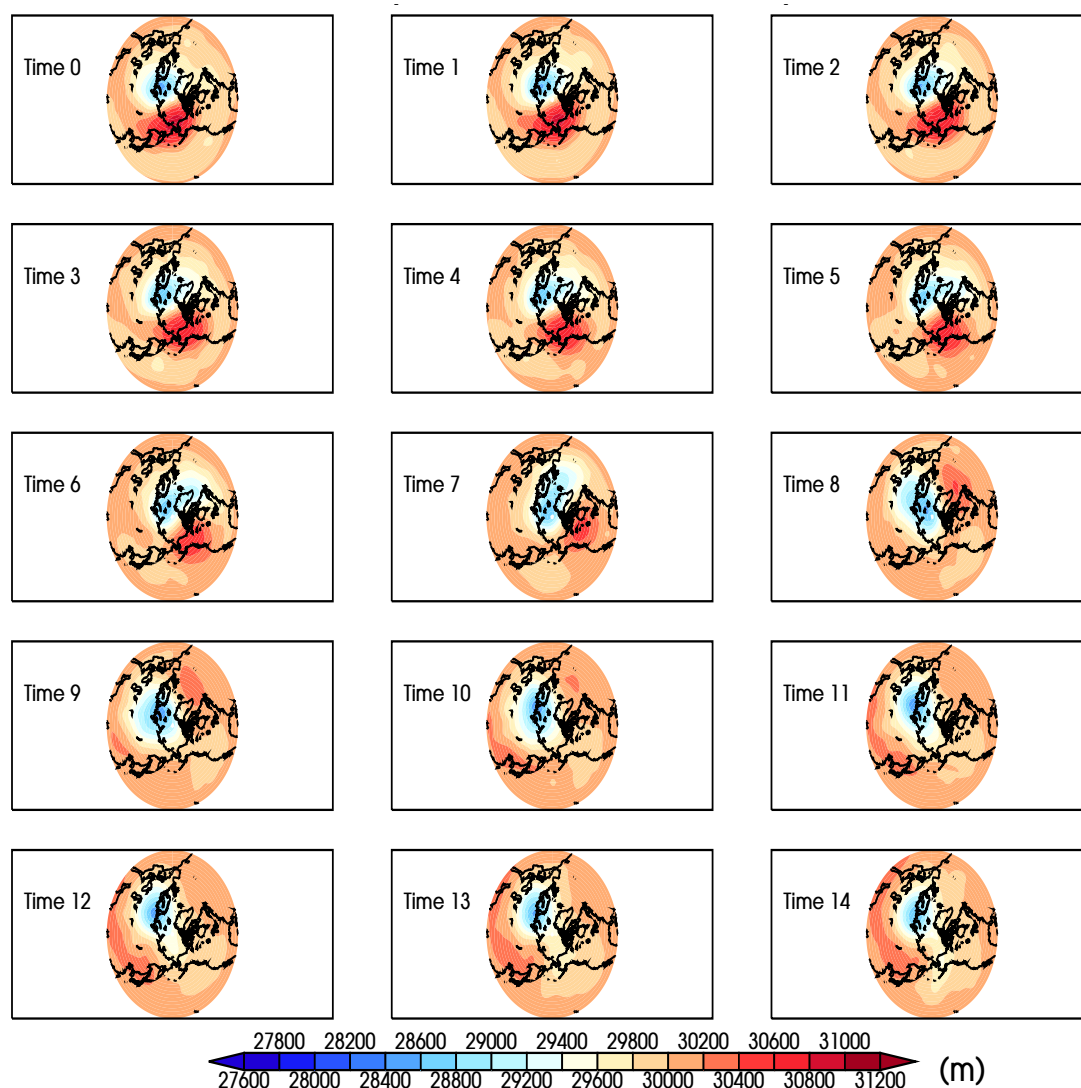


**Figure B3:** Case study of displacement SSW event for rotated EOF analysis. Total geopotential height field at 10 hPa (m) rotated so that the longitude of minimum geopotential height is at  $47^{\circ}\text{E}$ . Event isolated at time-step 6193. Time in days.

Two case studies for the rotated geopotential height field at 10 hPa are presented in Figures B3 and B4. Events are rotated daily so that the vortex centroid remains at  $47^{\circ}\text{E}$  for use in the rotated EOF analysis presented in Chapter 5.

Red tones indicate high geopotential values and blue tones indicate low geopotential height values, indicating where the disturbed polar vortex is located. Time 0 indicates the date where the zonal mean zonal wind reverses at 10 hPa and  $60^{\circ}\text{N}$ .

Event dates are the same as those in Figures B1 and B2 for direct comparison to the original fields (in EPV) and the rotated fields used in EOF analysis.

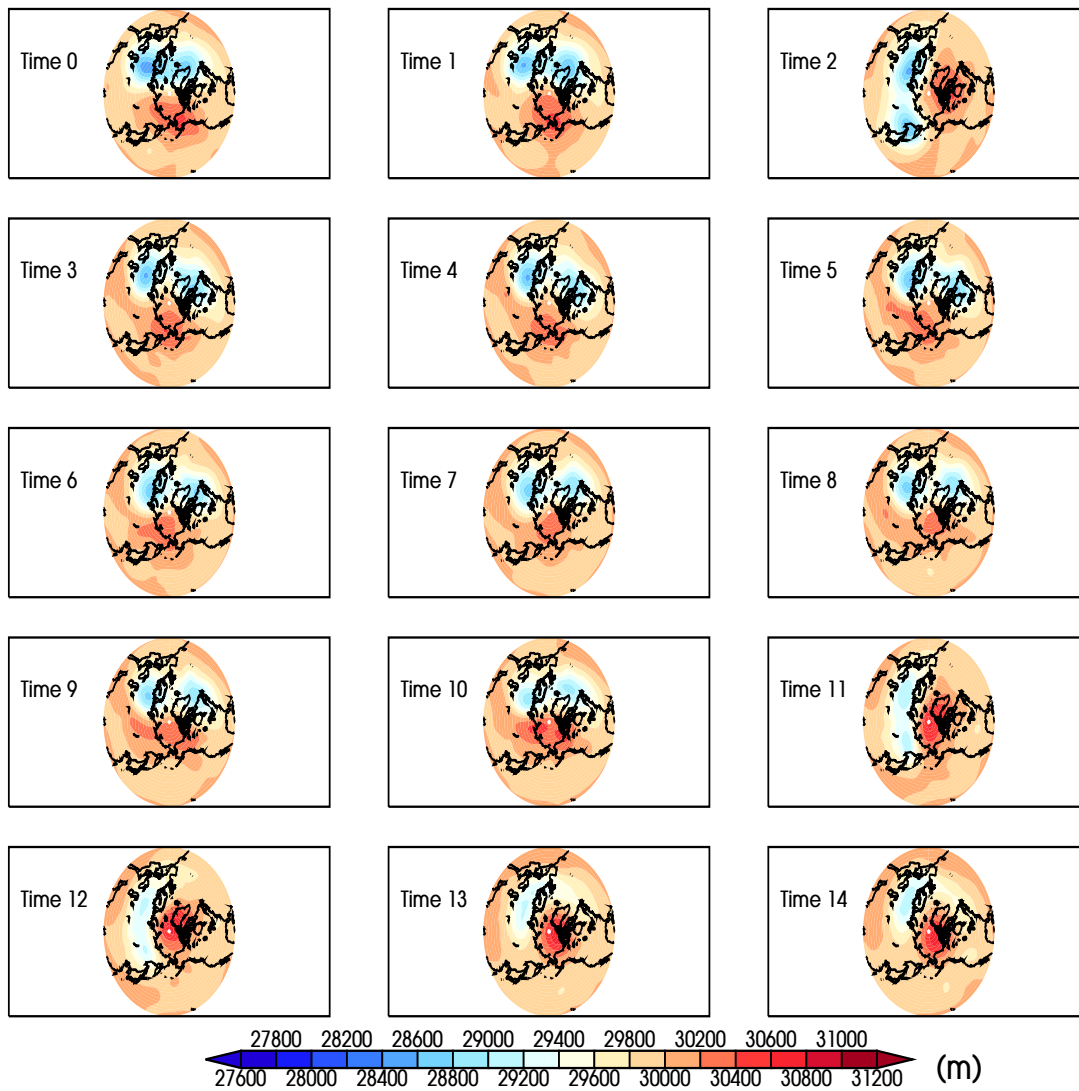


*Figure B4: Case study of splitting SSW event for rotated EOF analysis. Total geopotential height field at 10 hPa (m) rotated so that the longitude of minimum geopotential height is at  $47^{\circ}$  E. Event isolated at time-step 7614. Time in days.*

## C General Circulation Model Vertical Layers

Vertical levels in the general circulation models used in this study are presented in Table C1 for MOMA and Table C2 for the high-top IGCM4 respectively.

MOMA utilises geometric depth with the depth at level mid-points and level thicknesses presented. For the IGCM4, output is on full  $\sigma$ -levels, as utilised in the model code. Corresponding pressure values and conversion to height (in *km*) under a log-pressure approximation [Andrews et al., 1987] are presented in rows 3 and 4 respectively.

**Table C1:** Model layer index for MOMA version coupled to IGCM4.

Model Level Index	Mid-point ( <i>m</i> )	Layer Thickness ( <i>m</i> )
1	15	30
2	53.075	46.15
3	110.615	68.93
4	195.045	99.93
5	315.325	140.63
6	481.695	192.11
7	705.13	254.76
8	996.485	327.95
9	1365.365	409.81
10	1818.825	497.11
11	2360.06	585.36
12	2987.285	669.09
13	3693.035	742.41
14	4464.065	799.65
15	5281.94	836.10

**Table C2:** Model layer index for IGCM4 T42L35 configuration with corresponding  $\sigma$ -level with conversions to pressure and log-pressure height. Mean scale height is assumed to be 7km and surface pressure is assumed to be 1,000 hPa.

Model Level Index	$\sigma$ -level	Pressure (hPa)	Log-Pressure Height (km)
1	0.96000	960.0	0.28
2	0.87762	877.62	0.91
3	0.79176	791.76	1.63
4	0.70557	705.57	2.44
5	0.62249	622.49	3.31
6	0.54524	545.24	4.24
7	0.47565	475.65	5.20
8	0.41469	414.69	6.16
9	0.36248	362.48	7.10
10	0.31848	318.48	8.00
11	0.28166	281.66	8.86
12	0.25070	250.7	9.68
13	0.22424	224.24	10.46
14	0.20101	201.01	11.23
15	0.17994	179.94	12.00
16	0.16026	160.26	12.81
17	0.14152	141.52	13.68
18	0.12351	123.51	14.64
19	0.10624	106.24	15.69
20	0.08988	89.88	16.86
21	0.07463	74.63	18.16
22	0.06073	60.73	19.60
23	0.04837	48.37	21.20
24	0.03764	37.64	22.95
25	0.02859	28.59	24.88
26	0.02115	21.15	26.99
27	0.01522	15.22	29.29
28	0.01061	10.61	31.82
29	0.00715	7.15	34.58
30	0.00463	4.63	37.62
31	0.00285	2.85	41.02
32	0.00164	1.64	44.89
33	0.00086	0.86	49.41
34	0.00038	0.38	55.12
35	0.00010	0.1	64.47

---

## D Acronyms

<b>AMO</b>	Atlantic multidecadal oscillation
<b>CMIP5</b>	Coupled Model Intercomparison Project Phase 5
<b>CP07</b>	Charlton and Polvani [2007]
<b>DJF</b>	December-February
<b>DJFM</b>	December-March
<b>ECMWF</b>	European Centre for Medium-Range Weather Forecasts
<b>ENSO</b>	El Niño Southern Oscillation
<b>EOF</b>	Empirical orthogonal function
<b>EPV</b>	Ertel's potential vorticity
<b>ERA-40</b>	European Centre for Medium-Range Weather Forecasts 45-year reanalysis product
<b>FORTE</b>	Fast Ocean Rapid Troposphere Experiment
<b>GCM</b>	General circulation model
<b>IGCM</b>	Intermediate General Circulation Model
<b>JJA</b>	June-August
<b>M13</b>	Mitchell et al. [2013a]
<b>MOMA</b>	Modular Ocean Model Array Processor Version
<b>MSLP</b>	Mean sea-level pressure
<b>NAM</b>	Northern Annular Mode Index
<b>NAO</b>	North Atlantic Oscillation
<b>NCEP/NCAR</b>	National Centers for Environmental Prediction-National Center for Atmospheric Research
<b>NH</b>	Northern Hemisphere
<b>PC</b>	Principal component

<b>PV</b>	Potential vorticity
<b>QBO</b>	Quasi-biennial oscillation
<b>SH</b>	Southern Hemisphere
<b>SST</b>	Sea surface temperature
<b>SSW</b>	Sudden stratospheric warming
<b>T42</b>	Jagged triangular truncation at wavenumber 42

## References

- M Ambaum and B Hoskins. The NAO Troposphere–Stratosphere Connection. *J. Climate*, 15:1969–1978, 2002.
- D Andrews, J Holton, and C Leovy. *Middle Atmosphere Dynamics*. Academic Press, 1987.
- C Atkinson, N Wells, A Blaker, B Sinha, and V Ivchenko. Rapid ocean wave teleconnections linking Antarctic salinity anomalies to the equatorial ocean-atmosphere system. *Geophys. Res. Lett.*, 36:1–6, 2009.
- M Baldwin and T Dunkerton. Stratospheric Harbingers of Anomalous Weather Regimes. *Science*, 294:581–584, 2001.
- M Baldwin and D Thompson. A critical comparison of stratosphere–troposphere coupling indices. *Q.J.R. Meteorol. Soc.*, 135:1661–1672, 2009.
- J Barnett. Large sudden warming in the Southern Hemisphere. *Nature*, 255:387–389, 1975.
- J Beckers. Selection of a staggered grid for inertia-gravity waves in shallow water. *Int. J. Numer. Meth. Fluids*, 38:729–746, 2002.
- C Bell, L Gray, A Charlton-Perez, M Joshi, and A Scaife. Stratospheric communication of El Niño teleconnects to European winter. *J. Climate*, 22:4083–4096, 2009.
- J Berckmans, T Woolings, M-E Demory, P-L Vidale, and M Roberts. Atmospheric blocking in a high resolution climate model: influences of mean state, orography and eddy forcing. *Atmos. Sci. Lett.*, 14:34–40, 2013a.
- J Berckmans, T Woolings, M-E Demory, P-L Vidale, and M Roberts. Atmospheric blocking in a high resolution climate model: influences of mean state, orography and eddy forcing. *Atmos. Sci. Lett.*, 14:34–40, 2013b.
- M Blackburn. Program Description for the Multi-Level Global Spectral Model, 1985. URL [http://www.met.reading.ac.uk/~mike/dyn\\_models/igcm/doc/rsgup3\\_doc1985.pdf](http://www.met.reading.ac.uk/~mike/dyn_models/igcm/doc/rsgup3_doc1985.pdf).
- A Blaker, B Sinha, V Ivchenko, N Wells, and V Zalesny. Identifying the roles of the ocean and atmosphere in creating a rapid equatorial response to a Southern Ocean anomaly. *Geophys. Res. Lett.*, 33:1–4, 2006.

- B Booth, N Dunstone, P Halloran, T Andrews, and B Bellouin. Aerosols implicated as a prime driver of twentieth-century North Atlantic climate variability. *Nature*, 484:228–232, 2012.
- W Bourke. An Efficient, One-Level, Primitive Equation Spectral Model. *Mon. Wea. Rev.*, 100:683–689, 1972.
- F Bryan, M Hecht, and R Smith. Resolution convergence and sensitivity studies with North Atlantic circulation models. Part I: The western boundary current system. *Ocean Modelling*, 16:141–159, 2007.
- N Butchart. The Brewer-Dobson circulation. *Rev. Geophys.*, 52:1–28, 2014.
- N Butchart, A Scaife, M Bourqui, J Grandpre, S Hare, J Kettleborough, Langematz, E Manzini, F Sassi, K Shibata, D Shindell, and M Sigmond. Simulations of anthropogenic change in the strength of the Brewer–Dobson circulation. *Clim. Dyn.*, 27:727–741, 2006.
- A Butler and L Polvani. El Niño, La Niña, and stratospheric sudden warmings: A reevaluation in light of the observational record. *Geophys. Res. Lett.*, 38:1–5, 2011.
- A Butler, L Polvani, and C Deser. Separating the stratospheric and tropospheric pathways of El Niño–Southern Oscillation teleconnections. *Environ. Res. Lett.*, 9:1–9, 2014.
- A Butler, D Seidel, S Hardiman, N Butchart, T Birner, and A Match. Defining sudden stratospheric warmings. *Bull. Amer. Meteor. Soc.*, 96:1913–1928, 2015.
- A Butler, A Arribas, M Athanassiadou, J Baehr, N Calvo, A Charlton-Perez, M Deque, D Domeisen, K Frohlich, H Hendon, Y Imada, M Ishii, M Iza, A Karpechko, A Kumar, C MacLachlan, W Merryfield, W Muller, A O’Neill, A Scaife, J Scinocca, M Sigmond, T Stockdale, and T Yasuda. The Climate-system Historical Forecast Project: Do stratosphere-resolving models make better seasonal climate predictions in boreal winter? *Q.J.R. Meteorol. Soc.*, In Press, 2016.
- A Charlton and L Polvani. A New Look at Stratospheric Sudden Warmings. Part I: Climatology and Modeling Benchmarks. *J. Climate*, 20:449–469, 2007.
- A Charlton, L Polvani, J Perlwitz, F Sassi, E Manzini, K Shibata, S Pawson, J Nielsen, and D Rind. A New Look at Stratospheric Sudden Warmings. Part II: Evaluation of Numerical Model Simulations. *J. Climate*, 20:470–488, 2007.

- J Cohen, M Barlow, P Kushner, and K Saito. Stratosphere–Troposphere Coupling and Links with Eurasian Land Surface Variability. *J. Climate*, 20:5335–5343, 2007.
- P Davini, C Cagnazzo, and J Anstey. A Blocking View of the Stratosphere–Troposphere Coupling. *J. Geophys. Res. Atmos.*, 119:100–110, 2014. doi: 10.1002/2014JD021703.
- A Dawson. *The Impact of Climate Model Resolution On Tropical–Extra-Tropical Interactions In The Pacific*. PhD thesis, School of Mathematics, University of East Anglia, 2011.
- T Delworth and F Zeng. The Impact of the North Atlantic Oscillation on Climate through Its Influence on the Atlantic Meridional Overturning Circulation . *J. Climate*, 29:941–962, 2015.
- V Ekman. On the influence of the earths rotation on ocean-currents. *Ark. Mat. Astron. Fys.*, 11:1–53, 1905.
- D Enfield, A Mestas-Nunez, and P Trimble. The Atlantic Multidecadal Oscillation and its relationship to rainfall and river flows in the continental U.S. *Geophys. Res. Lett.*, (28):2077–2080, 2001.
- V Eyring, N Butchart, D Waugh, H Akiyoshi, J Austin, S Bekki, G Bodeker, B Boville, C Bruhl, M Chipperfield, E Cordero, M Dameris, M Deushu, V Fioletov, S Frith, R Garcia, A Gettelman, M Giorgetta, V Grewe, L Jourdain, D Kinison, E Mancini, E Manzini, M Marchand, D Marsh, T Nagashima, P Newman, J Nielsen, S Pawson, G Pitari, D Plummer, E Rozanov, M Schraner, T Shepherd, K Shibata, R Stolarski, H Struthers, W Tian, and M Yoshiki. Assessment of temperature, trace species, and ozone in chemistry- climate model simulations of the recent past. *J. Geophys. Res.*, 111:D22308, 2006.
- G. Flato, J Marotzke, B Abiodun, P Braconnot, S.C. Chou, W. Collins, P Cox, F Driouech, S Emori, V Eyring, C Forest, P Gleckler, E Guilyardi, C Jakob, V Kattsov, C Reason, and M. Rummukainen. *Evaluation of Climate Models. In: Climate Change 2013: The Physical Science Basis. Contribution of Working Group I to the Fifth Assessment Report of the Intergovernmental Panel on Climate Change*. Cambridge University Press, Cambridge, United Kingdom and New York, NY, USA., 2013.
- C Fletcher and P Kushner. The Role of Linear Interference in the Annular Mode Response to Tropical SST Forcing . *J. Climate*, 24:778–794, 2011.

- P Forster, M Blackburn, R Glover, and K Shine. An examination of climate sensitivity for idealised climate change experiments in an intermediate general circulation model. *Clim. Dyn.*, 16:833–849, 2000.
- H Garfinkel, T Shaw, D Hartman, and D Waugh. Does the Holton–Tan Mechanism Explain How the Quasi-Biennial Oscillation Modulates the Arctic Polar Vortex? . *J. Atmos. Sci.*, 69:1713–1733, 2012.
- H Garfinkel, D Waugh, and E Gerber. The Effect of Tropospheric Jet Latitude on Coupling between the Stratospheric Polar Vortex and the Troposphere. *J. Climate*, 26:2077–2095, 2013.
- E Gerber, M Baldwin, H Akiyoshi, J Austin, S Bekki, P Braesicke, N Butchart, M Chipperfield, M Dameris, S Dhomse, S Frith, R Garcia, H Garny, A Gettelman, S Hardiman, A Karpechko, M Marchand, O Morgenstern, E Nielsen, S Pawson, T Peter, D Plummer, J Pyle, E Rozanov, J Scinocca, T Shepherd, and D Smale. Stratosphere troposphere coupling and annular mode variability in chemistry climate models. *J. Geophys. Res.*, 115:D00M06, 2010. doi: 10.1029/2009JD013770.
- L Gerber, A Butler, and N Calvo. Assessing and Understanding the Impact of Stratospheric Dynamics and Variability on the Earth System. *Amer. Meteor. Soc.*, 93:845–859, 2012.
- M Goss, S Feldstein, and S Lee. Stationary Wave Interference and Its Relation to Tropical Convection and Arctic Warming . *J. Climate*, 29:1369–1389, 2015.
- L Gray, J Beer, M Geller, J Haigh, M Lockwood, K Matthes, U Cubasch, D Fleitmann, G Harrison, L Hood, J Luterbacher, G Meehl, D Shindell, B Geel, and W White. Sola Influences on Climate. *Rev. Geophys.*, 48:1–53, 2010.
- S Griffies. The Gent-McWilliams Skew Flux. *J. Phys. Oceanogr.*, 28:831–841, 1998.
- J Haigh. The Impact of Solar Variability on Climate. *Science*, 272:981–984, 1996.
- A Hannachi. A Primer for EOF Analysis of Climate Data. Technical report, University of Reading, 2004.
- A Hannachi, D Mitchell, L Gray, and A Charlton-Perez. On the Use of Geometric Moments to Examine the Continuum of Sudden Stratospheric Warmings. *Amer. Meteor. Soc.*, 68:657–674, 2011.
- F Hansen, K Matthes, C Petrick, and W Wang. The influence of natural and anthropogenic factors on major stratospheric sudden warmings . *J. Geophys. Res. Atmos.*, 119:8117–8136, 2014.

- P Haynes. Stratosphere-Troposphere Coupling. SPARC Newsletter 25, Department of Applied Mathematics and Theoretical Physics, Cambridge, UK, 2005.
- P Hitchcock and I Simpson. The Downward Influence of Stratospheric Sudden Warmings. *J. Atmos. Sci.*, 71:3856–3876, 2014.
- D Hodson, R Sutton, C Cassou, N Keenlyside, Y Okumura, and T Zhou. Climate impacts of recent multidecadal changes in Atlantic Ocean Sea Surface Temperature: a multimodel comparison. *Clim. Dyn.*, 34:1041–1058, 2010.
- J Holton. *An Introduction to Dynamical Meteorology*. Elsevier Academic Press, fourth edition, 2004.
- J Holton and J Austin. The Influence of the Equatorial QBO on Sudden Stratospheric Warmings. *J. Atmos. Sci.*, 48:607–618, 1991.
- J Holton and H Tan. The Influence of the Equatorial Quasi-Biennial Oscillation on the Global Circulation at 50 mb. *J. Atmos. Sci.*, 37:2200–2208, 1980.
- B Hoskins and A Simmons. A multi-layer spectral model and the semi-implicit method. *Q. J. R. Meteorol. Soc.*, 429(101):637–655, 1974.
- R Huang. *Ocean circulation: Wind driven and thermohaline processes*. Cambridge University Press, first edition, 2010.
- J Hurrell, Y Kushnir, G Ottersen, and M Visbeck. *An Overview of the North Atlantic Oscillation, in The North Atlantic Oscillation: Climatic Significance and Environmental Impact*. Am. Geophys. Un., 2003.
- S Ineson and A Scaife. The role of the stratosphere in the European climate response to El Niño. *Nature Geosci.*, 2:32–36, 2009.
- S Ineson, A Scaife, J Knight, J Manners, N Dunstone, L Gray, and J Haigh. Solar forcing of winter climate variability in the Northern Hemisphere. *Nature Geosci.*, 4:753–757, 2011.
- M Joshi, M Stringer, K van der Wiel, A O’Callaghan, and S Fueglistaler. IGCM4: A fast, parallel and flexible intermediate climate model. *Geosci. Model Dev.*, 8: 1157–1167, 2015.
- E Kalnay, M Kanamitsu, R Kistler, W Collins, D Deaven, L Gandin, M Iredell, S Saha, G White, J Woollen, Y Zhu, A Leetmaa, R Reynold, M Chelliah, W Ebisuzaki, W Higgins, J Janowiak, K Mo, C Ropelewski, J Wang, R Jenne, and

- D Joseph. The NCEP/NCAR 40-Year Reanalysis Project. *Bull. Amer. Meteor. Soc.*, 77:437–471, 1996.
- A Kaplan, M Cane, Y Kushnir, A Clement, M Blumenthal, and B Rajagopalan. Analyses of global sea surface temperature 1856–1991. *J. Geophys. Res.*, 103:18567–18589, 1998.
- D Karoly and B Hoskins. Three Dimensional Propagation of Planetary Waves. *J. Met. Soc. Jpn.*, 60(1):109–122, 1982.
- N Keenlyside and N.-E Omrani. Has a warm North Atlantic contributed to recent European cold winters? *Environ. Res. Lett.*, 9:061001, 2014.
- P Killworth. Time Interpolation of Forcing Fields in Ocean Models. *J. Phys. Oceanogr.*, 26:136–143, 1995.
- K Kodera, R Thiéblemont, S Yukimoto, and K Matthes. How can we understand the solar cycle signal on the Earths surface? . *Atmos. Chem. Phys. Discuss*, In Review, 2016.
- A Kren, D Marsh, A Smith, and P Pilewskie. Wintertime Northern Hemisphere response in the Stratosphere to the Pacific Decadal Oscillation using the Whole Atmosphere Community Climate Model. *J. Climate*, 2015.
- T Kunz, K Fraedrich, and F Lunkeit. Response of idealized baroclinic wave life cycles to stratospheric flow conditions. *J. Atmos. Sci.*, 66:2288–2302, 2009.
- D Li and K Shine. A three dimensional ozone climatology for use in general circulation models. Ugamp internal report, University of Reading, UK, 1995.
- J Li, C Sun, and F-F Jin. NAO implicated as a predictor of Northern Hemisphere mean temperature multidecadal variability. *Geophys. Res. Lett.*, 40:5497–5502, 2013.
- Y Li and N-C Lau. Influences of ENSO on Stratospheric Variability, and the Descent of Stratospheric Perturbations into the Lower Troposphere. *J. Climate*, 26:4725–4748, 2013.
- D Limpasuvan and D Hartmann. Wave-maintained annular modes of Climate Variability. *J. Climate*, 13:4414–4429, 2000.
- V Limpasuvan, D Thompson, and D Hartman. The Life Cycle of the Northern Hemisphere Sudden Stratospheric Warmings. *J. Climate*, 17:2584–2596, 2004.

- R Lindzen. Turbulence and stress owing to gravity wave and tidal breakdown. *J. Geophys. Res.*, 86:9707–9714, 1981.
- E Manzini. ENSO and the stratosphere. *Nature Geosci.*, 2:749–750, 2009.
- J Marshall, H Johnson, and J Goodman. A Study of the Interaction of the North Atlantic Oscillation with Ocean Circulation. *J. Climate*, 14:1399–1421, 2001.
- J Martin. *Mid-Latitude Atmospheric Dynamics*. Wiley, first edition, 2006.
- T Matsuno. A Dynamical Model of the Stratospheric Sudden Warming. *J. Atmos. Sci.*, 28:1479–1494, 1971.
- N Matthewman, J Esler, A Charlton-Perez, and L Polvani. A New Look at Stratospheric Sudden Warmings. Part III: Polar Vortex Evolution and Vertical Structure. *J. Climate*, 22:1566–1585, 2009.
- R McInturff. Stratospheric warmings: Synoptic, dynamic and general-circulation aspects. Technical report, NASA-RP-1017, 1978.
- D Mitchell, A Charlton-Perez, and L Gray. Characterizing the Variability and Extremes of the Stratospheric Polar Vortices Using 2D Moment Analysis. *J. Atmos. Sci.*, 68:1194–1213, 2011.
- D Mitchell, A Charlton-Perez, and L Gray. The Influence of Stratospheric Vortex Displacements and Splits on Surface Climate. *J. Climate*, 26:2668–2682, 2013a.
- D Mitchell, P Stott, L Gray, M Allen, F Lott, N Butchart, S Hardiman, and S Osprey. The impact of stratospheric resolution on the detectability of climate change signals in the free atmosphere. *Geophys. Res. Lett.*, 40, 2013b.
- G Moore and I Renfrew. Cold European winters: interplay between the NAO and the East Atlantic mode. *Atmos. Sci. Lett.*, 13:1–8, 2012.
- D Munday and X Zhai. Sensitivity of Southern Ocean circulation to wind stress changes: Role of relative wind stress. *Ocean Modelling*, 95:15–24, 2015.
- D Nath, W Chen, C Zelin, A Ivanovich, and K Wei. Dynamics of 2013 sudden stratospheric warming event and its impact on cold weather over eurasia: Role of planetary wave reflection. *Sci. Rep.*, 6:1–12, 2016.
- G North, T Bell, R Cahalan, and F Moeng. Sampling errors in the estimation of empirical orthogonal functions. *Mon. Weather Rev.*, 110(7):669–706, 1982.

- A Norton. Sensitivity of northern hemisphere surface climate to simulation of the stratospheric polar vortex. *Geophys. Res. Lett.*, 30:29–33, 2003.
- N.-E Omrani, N Keenlyside, J Bader, and E Manzini. Stratosphere key for winter-time atmospheric response to warm Atlantic decadal conditions. *Clim. Dyn.*, 42: 649–663, 2014.
- N.-E Omrani, J Bader, N Keenlyside, and E Manzini. Troposphere-stratosphere response to large-scale North Atlantic Ocean variability in an atmosphere/ocean coupled model. *Clim. Dyn.*, 46:1397–1415, 2015.
- Y Orsolini, R Senan, F Vitart, G Balsamo, A Weisheimer, and F Doblas-Reyes. Influence of the Eurasian snow on the negative North Atlantic Oscillation in subseasonal forecasts of the cold winter 2009/2010. *Clim. Dyn.*, pages 1–10, 2015.
- S Orszag. Transform Method for Calculation of Vector-Coupled Sums: Application to the Spectral Form of the Vorticity Equation. *J. Atmos. Sci.*, 27:890–895, 1970.
- F Palmeiro, D Barriopedro, R García-Herrera, and N Calvo. Comparing Sudden Stratospheric Warming Definitions in Reanalysis Data. *J. Climate*, 28:6823–6840, 2015.
- C Pascoe, L Gray, and A Scaife. A GCM study of the influence of equatorial winds on the timing of sudden stratospheric warmings. *Geophys. Res. Lett.*, 33:1–4, 2006.
- Y Peings and G Magnusdottir. Forcing of the wintertime atmospheric circulation by the multidecadal fluctuations of the North Atlantic ocean. *Environ. Res. Lett.*, 9:034018, 2014.
- Y Peings and G Magnusdottir. Wintertime atmospheric response to Atlantic multidecadal variability: effect of stratospheric representation and ocean–atmosphere coupling. *Clim. Dyn.*, pages 1–19, 2015.
- L Polvani and D Waugh. Upward Wave Activity Flux as a Precursor to Extreme Stratospheric Events and Subsequent Anomalous Surface Weather Regimes. *J. Climate*, 17:3548–3554., 2004.
- N. Rayner, D Parker, E Horton, C Folland, L Alexander, D Rowell, E Kent, and A Kaplan. Global analyses of sea surface temperature, sea ice, and night marine air temperature since the late nineteenth century. *J. Geophys. Res.*, 108(D14): 4407, 2003.

- T Reichler, J Kim, E Manzini, and J Kroger. A stratospheric connection to Atlantic climate variability. *Nature Geosci.*, 5:783–787, 2012.
- R Reynolds and T Smith. Improved Global Sea Surface Temperature Analyses Using Optimum Interpolation. *J. Climate*, 7:929–948, 1994.
- J Richter, K Matthes, N Calvo, and L Gray. Influence of the quasi-biennial oscillation and El Niño-Southern Oscillation on the frequency of sudden stratospheric warmings. *J. Geophys. Res.*, 116:1–7, 2011.
- P Ripesi, F Ciciulla, F Mainone, and V Pelino. The February 2010 Arctic Oscillation Index and its stratospheric connection. *Q. J. R. Meteorol. Soc.*, 138:1961–1969, 2012.
- P Sardeshmukh and B Hoskins. The Generation of Global Rotational Flow by Steady Idealized Tropical Divergences. *J. Atmos. Sci.*, 45:1228–1251, 1988.
- A Scaife, N Butchart, C Warner, D Stainforth, W Norton, and J Austin. Realistic Quasi-Biennial Oscillations in a simulation of the global climate. *Geophys. Res. Lett.*, 27:3481–3484, 2000.
- A Scaife, T Woolings, J Knight, G Martin, and T Hinton. Atmospheric Blocking and Mean Biases in Climate Models. *J. Climate*, 23:6143–6152, 2010.
- A Scaife, C Copsey, C Gordon, C Harris, T Hinton, S Keeley, A O’Neill, M Roberts, and K Williams. Improved Atlantic winter blocking in a climate model. *Geophys. Res. Lett.*, 38:1–6, 2011.
- A Scaife, S Ineson, J Knight, L Gray, K Kodera, and M Smith. A mechanism for lagged North Atlantic climate response to solar variability. *Geophys. Res. Lett.*, 40:434–438, 2013.
- A Scaife, A Karpechko, M Baldwin, A Brookshaw, A Butler, R Eade, M Gordon, C MacLachlan, N Martin, N Dunstone, and D Smith. Seasonal winter forecasts and the stratosphere. *Atmos. Sci. Lett.*, 17(51–56), 2016.
- J Screen, N Gillett, A Karpechko, and D Stevens. Mixed Layer Temperature Response to the Southern Annular Mode: Mechanisms and Model Representation. *J. Climate*, 23:664–678, 2010.
- W Seviour, D Mitchell, and L Gray. A practical method to identify displaced and split stratospheric polar vortex events. *Geophys. Res. Lett.*, 40:5268–5273, 2013.

- W Seviour, L Gray, and D Mitchell. Stratospheric polar vortex splits and displacements in the high-top CMIP5 climate models. *J. Geophys. Res. Atmos.*, 121:1–14, 2016.
- G Siedler, J Church, and J Gould, editors. *Ocean Circulation and Climate: Observing and Modelling the Global Ocean*. Academic Press, 2001.
- S. Solomon, M. Manning D. Qin, Z. Chen, M. Marquis, K.B. Averyt, M. Tignor, and H.L. Miller, editors. *Contribution of Working Group I to the Fourth Assessment Report of the Intergovernmental Panel on Climate Change, 2007*. Cambridge University Press, 2007.
- M Taguchi and D Hartmann. Increased Occurrence of Stratospheric Sudden Warmings during El Niño as Simulated by WACCM. *J. Climate*, 19:324–332, 2005.
- L Terray, S Valcke, and A Piacentini. The OASIS Coupler User Guide Version 2.3. *Tech. Rep. TR/CMGC/99-37*, CERFACS, 1999.
- D Thompson and J Wallace. Annular Modes in the Extratropical Circulation. Part I: Month-to-Month Variability. *J. Climate*, 13:1000–1016, 2000.
- D Thompson, M Baldwin, and J Wallace. Stratospheric Connection to Northern Hemisphere Wintertime Weather: Implications for Prediction. *J. Climate*, 15:1421–1428, 2001.
- S Tibaldi and F Molteni. On the operational predictability of blocking. *Tellus A*, 42:343–365, 1990.
- O Tripathi, A Charlton-Perez, M Sigmond, and F Vitart. Enhanced long-range forecast skill in boreal winter following stratospheric strong vortex conditions. *Environ. Res. Lett.*, 10:1–8, 2015.
- S Uppala, P Kallberg, A Simmons, U Andrae, V Bechtold, M Fiorino, J Gibson, J Haseler, A Hernandez, G Kelly, X Li, K Onogi, S Saarinen, N Sokka, R Allan, E Andersson, K Arpe, M Balmaseda, M Beljaars, L Van De Berg, J Bidlot, N Bormann, S Caires, F Chevallier, A Dethof, M Dragosavac, M Fisher, M Fuentes, S Hagemann, E Holm, B Hoskins, L Isaksen, P Janssen, R Jenne, A McNally, J Mahfouf, J Morcrette, N Rayner, R Saunders, P Simon, A Sterl, K Trenberth, A Untch, D Vasiljevic, P Viterbo<sup>1</sup>, and J Woollen. The ERA-40 re-analysis. *Q.J.R. Meteorol. Soc.*, 131:2961–3012, 2005.

- C Varotsos. The extraordinary events of the major, sudden stratospheric warming, the diminutive antarctic ozone hole, and its split in 2002. *Environ. Sci. Pollut. Res. Int.*, 11:405–411, 2004.
- M Visbeck, E Chassignet, R Curry, T Delworth, R Dickson, and G Krahnmann. The oceans response to North Atlantic Oscillation variability, in the North Atlantic Oscillation: Climatic significance and environmental impact. *Am. Geophys. Un. Mon.*, 134:113–145, 2003.
- C Wang and L Zhang. Multidecadal Ocean Temperature and Salinity Variability in the Tropical North Atlantic: Linking with the AMO, AMOC, and Subtropical Cell. *J. Climate*, 26:6137–6162, 2013.
- W Washington and C Parkinson. *An Introduction To Three-Dimensional Climate Modelling*. University Science Books, second edition, 2005.
- D Waugh. Elliptical diagnostics of stratospheric polar vortices. *Q. J. R. Meteorol. Soc.*, 123:1725–1748, 1997.
- D Waugh and W Randel. Climatology of Arctic and Antarctic Polar Vortices Using Elliptical Diagnostics. *J. Atmos. Sci.*, 56:1594–1613, 1999.
- D Webb. An Ocean Model Code for Array Processor Computers. *Computers and Geosci.*, 22:569–578, 1996.
- J Wilcox and A Charlton-Perez. Final warming of the Southern Hemisphere polar vortex in high and low-top CMIP5 models. *J. Geophys. Res. Atmos.*, 118:1–12, 2013.
- C Wilson, B Sinha, and R Williams. The effect of ocean dynamics and orography on atmospheric storm tracks. *J. Climate*, 22:3689–3702, 2009.
- B Winter and M Bourqui. Sensitivity of the Stratospheric Circulation to the Latitude of Thermal Surface Forcing. *J. Climate*, 24:5397–5415, 2011.
- S-H Woo, M-K Sung, S-W Son, and J-S Kug. Connection between weak stratospheric vortex events and the Pacific Decadal Oscillation. *Clim. Dyn.*, 45:3481–3492, 2015.
- X Zhai, H Johnson, and D Marshall. A Simple Model of the Response of the Atlantic to the North Atlantic Oscillation. *J. Climate*, 27:4052–4069, 2014.
- W Zhong and J Haigh. Improved broad-band emissivity parameterization for water vapor cooling calculations. *J. Atmos. Sci.*, 52:124–138, 1995.